Measuring the Thermal Response of Small Asteroids via the YORP Effect

A thesis submitted for the degree of
Doctor of Philosophy

by

Tarik Joseph Zegmott

School of Physical Sciences

University of Kent
Canterbury
United Kingdom

March 2021

Declaration

This thesis has not been submitted as an exercise for a degree at any other university.

Except where stated, the work described therein was carried out by me alone.

I give permission for the Library to lend or copy this thesis upon request.

SIGNED:

Dedicated to my parents,
Elizabeth Ann and Omar

Acknowledgements

First and foremost, I am very grateful to all those who have helped me to succeed along this path. Overall, it has been a challenging, yet rewarding journey.

I would like to offer enormous thanks to my supervisor, Stephen Lowry, for all of your help, teaching, and guidance over these past five years. For your encouragement in pursuing my studentship with the ING, and for sending me on many observing runs. I also thank Agata Rożek for her teaching and patience, showing me how to use SHAPE and convexinv, and in helping me to resolve the many issues I've had.

Thank you to the Science and Technology Facilities Council for providing me with studentship funding for the duration of my PhD. Thank you to the School of Physical Sciences for providing me with the workspace I required. I would also like to thank all of the academic and administrative staff at the University of Kent. Thank you particularly to Tim for all of your computer wizardry.

Thank you to Jamie, Luke, Lord, Justin, Vassi, and all of my officemates for the thoughtful and interesting discussions and also for the fun evenings of games. Also to all the folks that made my time in Canterbury such a memorable experience. Steve, thank you for all of the fun trips, help, and the relaxing mornings fishing.

Gracias al Grupo del Telescopio Isaac Newton por un año inolvidable en La Isla Bonita, tanto por la oportunidad de trabajar con el Telescopio Isaac Newton como por enseñarme español. Gracias también a las personas que me dio la bienvenida en Santa Cruz, ademàs a mis compañeros.

I thank my parents for all of their encouragement and support over the many years that I have now been in education. You have always pushed me to achieve my best. Lastly, a massive thank you to Helen Felemegos for the countless hours you spent proof-reading my thesis, you are one of a lucky handful to read it :-)

Abstract

As part of the European Southern Observatory Large Programme (ESO LP), a selection of over 40 asteroids have been monitored photometrically since 2010, primarily, from the New Technology Telescope and Very Large Telescope facilities. These objects were chosen based on conditions which made them likely candidates to experience YORP accelerations. The principal aim of the ESO LP is to detect YORP-induced rotational period variations in order to further the understanding and development of YORP theories. Of these 40 asteroids, three were chosen for investigation in this thesis: (29075) 1950 DA, (68346) 2001 KZ66, and (89830) 2002 CE.

Light curves were collected via the ESO LP for the asteroid (29075) 1950 DA and combined with published radar and optical data. Utilising the published shape models, it was not possible to fit our light curve dataset leading to attempts to remodel the asteroid. In the early stages of analysis, initial modelling indicated a deceleration in the asteroid's rotation rate; however, the cause of this deceleration could not be definitively attributed to YORP. In 2019, an additional set of light curves were obtained, with which the best-fit models indicated that the asteroid is experiencing negative YORP accelerations. This is a first-of-its-kind finding, which will have a profound significance for YORP theory.

For asteroid (68346) 2001 KZ66, both optical and radar observations were obtained. The optical dataset allowed a comprehensive analysis of the asteroid's rotation period and pole orientation. While the radar observations were utilised to produce a detailed shape model of the object. The asteroid was determined to be a retrograde rotator with the pole located near the southern ecliptic pole and a rotation period of 4.985997 ± 0.000042 hours. By combining the radar-derived shape model with the optical light curves, a solution was developed which fit all available data by requiring a YORP strength of $(8.50 \pm 0.11) \times 10^{-8}$ rad/day^2. Moreover, possible mechanisms by which this asteroid could've been formed are explored in addition to the stability of its present shape.

For the final object, a light-curve-only analysis was performed for the asteroid (89830) 2002 CE. The investigation of this object utilised 25 light curves obtained by the ESO LP and its auxiliary campaigns. These observations allowed the accurate determination of the asteroid's rotation period and pole orientation, which is located at $(94^\circ \pm 5^\circ, 47^\circ \pm 5^\circ)$ in ecliptic coordinates. Constraints on the asteroid's shape were also developed using convex inversion techniques, producing two shape models capable of fitting the majority of the light curves. Attempts to define bounds for possible YORP accelerations produced several potential values equal in their ability to fit the data. This indicates that more data is required to determine meaningful constraints on YORP.

With the number of direct YORP detections only in the single digit range, the work performed in this thesis adds an additional detection which is crucial in order to calibrate and further the field of YORP theory. Moreover, the indications of negative YORP acting on DA are the first of their kind. Before which, only positive accelerations were measured, which spurred the development of additional forms of YORP to explain the statistically unlikely non-binarity of detections hitherto. Beyond the scope of YORP, the shape models produced within this thesis can be used in further studies. For example, in studies aiming to determine the formation mechanisms capable of contact-binaries such as KZ66.

Contents

Declaration i

Acknowledgements i

Abstract ii

List of Tables vii

List of Figures xiv

Publications xv

1 Evolution of asteroids in the Solar System 1

1.1 The Solar System and its formation 1

1.2 Asteroids in the Solar System 4

1.2.1 Sizes, spin-states, and morphologies of asteroids 4

1.2.2 Near-Earth Asteroids 9

1.3 Thermal drivers of asteroid evolution 11

1.3.1 The Yarkovsky effect 12

1.3.2 The YORP effect 19

2 Observations of near-Earth asteroids for YORP detections 31

2.1 Photometric light curves of asteroids from optical imaging 32

2.1.1 Overview of optical light curve observations 32

2.1.2 ESO Large Programme and supporting campaign 33
2.1.3 Observation planning and image acquisition of NEAs 37
2.1.4 Post-processing of CCD Images 40
2.1.4.1 Data Reduction 42
2.1.4.2 Relative photometry of asteroids 45
2.2 Radar observations 52
2.2.1 Overview of radar observations 52
2.2.2 Types of radar observations 55
2.3 Preparation of observational data for modelling 58

3 Shape and spin-state modelling of NEAs to detect YORP accelerations 60

3.1 Inversion of optical light curves photometry 60
3.1.1 Introduction 60
3.1.2 Modelling shape, spin-state and YORP with `ConvexInv` 61
3.2 Modelling radar observations 69
3.2.1 Introduction 69
3.2.2 Modelling asteroids with `SHAPE` 72
3.2.2.1 Procedure to optimise model with `SHAPE` 78
3.3 Spin-state analysis with an existing model 82
3.3.1 Generating synthetic light curves 83
3.3.2 Determining changes in rotation period from phase offsets 90

4 First direct detection of a YORP 'spin-down': the case of (29075) 1950 DA 92

4.1 Introduction 92
4.2 Observations of (29075) 1950 DA 95
4.2.1 Optical light curves 95
4.2.2 Radar-derived shape models 100

4.2.3 Radar Observations 101

4.3 Combining the published radar shape models and new optical light curves 103

4.3.1 Searching for YORP with the published models 103

4.3.2 Revision of the published shape models 104

4.4 Remodelling (29075) 1950 DA with combined radar and optical observations 107

4.4.1 Pre-2019 shape and spin-state analysis of (29075) 1950 DA . . . 107

4.4.2 Addition of 2019 light curve data 119

4.5 Summary of main conclusions and discussion 123

5 Detection of YORP on the contact-binary (68346) 2001 KZ66 from radar and optical observations 127

5.1 Introduction 127

5.2 Observations of (68346) 2001 KZ66 129

5.2.1 Optical light curves 129

5.2.2 Asteroidal radar observations 133

5.3 Modelling shape and spin-state 134

5.3.1 Period and pole search with light curve data – convex inversion results 134

5.3.2 A radar shape model – `SHAPE` results 136

5.3.3 Surface structure of KZ66 141

5.4 Direct detection of YORP 143

5.4.1 Convex inversion 144

5.4.2 Phase-offset spin-state analysis 144

5.5 Discussion 147

5.5.1 Direct detection of YORP spin-up 147

5.5.2 Gravitational slopes and topographic variation on (68346) 2001 KZ66 148

5.5.3 Bifurcated shape of (68346) 2001 KZ66 151

5.6 Conclusions 154

6 Optical observing campaign and modelling of asteroid (89830) 2002 CE 156

6.1 Introduction 156

6.2 Optical datasets obtained from the observing campaign of (89830) 2002 CE 158

6.3 Shape modelling of (89830) 2002 CE 161

6.3.1 Determination of the sidereal rotation period 161

6.3.2 Grid search for the pole orientation using `convexinv` 163

6.3.3 Spin-state modelling of (89830) 2002 CE 166

6.4 Summary and discussion of the analysis of (89830) 2002 CE 172

7 Final conclusions and future work 175

7.1 Final comments on the modelling results 175

7.2 Thoughts to the future of asteroidal studies and YORP theory 184

Bibliography 190

A Supplementary figures and tables 218

B Formatting of the input data files 251

C Acronyms 262

List of Tables

1.1 YORP detections to date. 30

4.1 Optical light curves of asteroid (29075) 1950 DA 97

4.2 Radar observations of asteroid (29075) 1950 DA 102

4.3 Summary of models of asteroid (29075) 1950 DA 126

5.1 Optical photometry datasets of asteroid (68346) 2001 KZ66 131

5.2 Radar observations of asteroid (68346) 2001 KZ66 134

5.3 Summary of geometric parameters of (68346) 2001 KZ66 142

5.4 Summary of spin-state model parameters for asteroid (68346) 2001 KZ66 143

6.1 Optical lightcurves of asteroid (89830) 2002 CE 162

7.1 YORP non-detections from our ESO LP 185

A.1 Summary of the moments of inertia and the orientation of the principal axes (PA) for the (68346) 2001 KZ66 model 220

List of Figures

1.1 Distribution of inner Solar Systerm asteroids - eccentricity vs semi-major axis . . . 3

1.2 Polar view of asteroids and planets in the inner Solar System . . . 5

1.3 Size frequency distribution of Main Belt Asteroids . . . 6

1.4 Rotation frequency size distribution of asteroids . . . 7

1.5 Example of an asteroid with an equatorial ridge . . . 9

1.6 Illustration of the Yarkovsky effect . . . 14

1.7 Yarkovsky detection with the Karin cluster . . . 16

1.8 Yarkovsky detection for (6489) Golevka . . . 18

1.9 Illustration of the YORP effect . . . 20

1.10 Dependency of the YORP torque components on obliquity . . . 21

1.11 Affect of thermal conductivity on YORP torque . . . 23

1.12 YORP detection via linear change in rotation period for asteroid (54509) YORP . . . 28

1.13 YORP detection via rotation phase offsets for asteroid (54509) YORP . 28

2.1 Image of the NTT, La Silla Observatory, Chile. . . . 34

2.2 Image of the Isaac Newton Telescope, Spain. . . . 36

2.3 Image of the Nordic Optical Telescope, Spain. . . . 37

2.4 Image of the robotic Liverpool Telescope, Spain. . . . 38

2.5 Charts used in preparation of an observing run . . . 41

2.6 Basic image reduction frames 44
2.7 Marking the reference stars with circular apertures 47
2.8 Point spread function of a star 48
2.9 Continuous wave spectrum showing both circular polarisations 53
2.10 Image of Arecibo Observatory 54
2.11 Image of DSS-14 (aka Mars Station) of the Deep Space Network 55
2.12 Relationship between asteroid's shape and Doppler spectrum 57
2.13 Demonstration of the mapping between a delay-Doppler image and the plane-of-sky view 59

3.1 Example of periodogram 65
3.2 Example of χ^2-plane output from pole scan 67
3.3 Grid-like nature of a pole scan 67
3.4 Example of convex shape output by `convexinv` 68
3.5 Schematic of YORP planes 70
3.6 Example of 'YORPogram' 70
3.7 Illustration of linear offsets applied to two component `SHAPE` model . . . 74
3.8 Visualisation of `SHAPE` vertex 75
3.9 Example of various `SHAPE` component types 75
3.10 Masking delay-Doppler images 80
3.11 `SHAPE` model vertices and facet 84
3.12 Example of the various scattering laws 87
3.13 Illustration of a pair of potentially blocking facets. 88
3.14 Illustration of ray tracing. 89
3.15 Example of phase offset fitting using (3103) Eger. 91

4.1 Orbit of (29075) 1950 DA 93
4.2 Observing geometries of (29075) 1950 DA 96

4.3 Published shape models of (29075) 1950 DA 101

4.4 Artificial light curves produced with the published models of asteroid (29075) 1950 DA 105

4.5 Illustration of the pole orientations used for the modified Busch models 106

4.6 Overview of the analysis undertaken during the investigation of DA . . 108

4.7 `convexinv` pole scan for (29075) 1950 DA with a $5° \times 5°$ resolution . . . 109

4.8 `convexinv` pole scan for (29075) 1950 DA with a $2° \times 2°$ resolution . . . 110

4.9 `convexinv` model of (29075) 1950 DA 110

4.10 `SHAPE` YORPogram utilising radar observations and optical light curves 114

4.11 Resulting best-fit spherical harmonic model for (29075) 1950 DA for the -2.075×10^{-6}rad/d^2 YORP plane 115

4.12 Subset of synthetic light curves produced with the best-fit spherical harmonic model of (29075) 1950 DA 115

4.13 Fit of (29075) 1950 DA to delay-Doppler images taken 3 March 2001 from Goldstone 116

4.14 Phase offset measurements for the best-fit spherical harmonic model of asteroid (29075) 1950 DA using 2010 to 2014 light curves 118

4.15 Phase offset measurements for the best-fit spherical harmonic model of asteroid (29075) 1950 DA using 2010 to 2019 light curves 120

4.16 Subset of artificial light curves produced with the best-fit spherical harmonic model of asteroid (29075) 1950 DA 120

4.17 `convexinv` YORPogram utilising 2001 to 2019 optical light curves . . . 121

4.18 -3.6×10^{-6} rad/d^2 YORP plane from YORPogram 122

4.19 Subset of synthetic light curves produced with the best-fit YORP scan model of (29075) 1950 DA 123

4.20 Orbital geometry of asteroid (29075) 1950 DA between 2020 and 2025 . 126

5.1 Orbit of (68346) 2001 KZ66 128

5.2 Observing geometries of asteroid (68346) 2001 KZ66 132

5.3 Rotation period scan for (68346) 2001 KZ66 135

5.4 Pole orientation scan results for (68346) 2001 KZ66 137

5.5 Best-fit convex inversion model of (68346) 2001 KZ66 138

5.6 Best-fit vertex model of (68346) 2001 KZ66 140

5.7 Fit of (68346) 2001 KZ66 to delay-Doppler images for 28 October 2003 . 141

5.8 Fit of (68346) 2001 KZ66 to delay-Doppler images for 29 October 2003 . 142

5.9 Continuous wave observations of (68346) 2001 KZ66 143

5.10 Phase offset analysis of (68346) 2001 KZ66 146

5.11 Comparison of model (68346) 2001 KZ66 with(out) YORP 147

5.12 Gravitational slopes and topographic variation on asteroid (68346) 2001 KZ66 150

6.1 Orbit of (89830) 2002 CE 157

6.2 Observing geometries of (89830) 2002 CE 159

6.3 Results of the period scan for asteroid (89830) 2002 CE 163

6.4 Results of the pole orientation scan for the asteroid (89830) 2002 CE . . 165

6.5 Results of the high resolution pole orientation scan for the asteroid (89830) 2002 CE 166

6.6 Best-fit convex shape model of asteroid (89830) 2002 CE 167

6.7 Second-best-fit convex shape model of asteroid (89830) 2002 CE 167

6.8 Phase-offset analysis for Models A and B 168

6.9 Convex inversion YORP scan for asteroid (89830) 2002 CE 169

6.10 Best-fit convex shape model of asteroid (89830) 2002 CE from the -3.4×10^{-6} rad/day^2 YORP-plane 170

6.11 Comparison of models' ability to reproduce light curves 171

6.12 Future observing geometry of asteroid (89830) 2002 CE between 2020 and 2030 174

7.1 Distribution of ecliptic latitudes for main-belt and near-Earth asteroids 177

7.2 Theoretical phase-offset values for the asteroid (29075) 1950 DA over the 2021 observing campaign 179

7.3 Observer ecliptic latitude of (29075) 1950 DA during 2021 180

7.4 Theoretical phase-offset values for the asteroid (29075) 1950 DA extended into 2023 180

7.5 Visual magnitude of (68346) 2001 KZ66 until 2030 182

7.6 Theoretical phase-offset values for the asteroid (68346) 2001 KZ66 extended through to 2030 183

7.7 New planetary radar proof-of-concept image of the Moon's surface . . . 189

A.1 Synthetic light curves generated using the (29075) 1950 DA prograde published model 219

A.1 (Continued.) 220

A.2 Synthetic light curves generated using the (29075) 1950 DA retrograde published model 221

A.2 (Continued.) 222

A.3 Synthetic light curves generated using the `convexinv` model of (29075) 1950 DA 223

A.3 (Continued.) 224

A.4 Additional YORP plane results from global scan of (29075) 1950 DA . . 225

A.5 Additional YORP plane models from the extended YORP scan of (29075) 1950 DA 226

A.6 Radar observations of (29075) 1950 DA on 3 March 2001 from Goldstone 227

A.7 Radar observations of (29075) 1950 DA on 4 March from Goldstone . . 227

A.8 Radar observations of (29075) 1950 DA on 7 March from Goldstone . . 228

A.9 Radar observations of (29075) 1950 DA on 3 March from Arecibo 228

A.10 Radar observations of (29075) 1950 DA on 4 March from Arecibo 229

A.11 Synthetic light curves generated using spherical harmonic model of (29075) 1950 DA 230

A.11 (Continued.) 231

A.12 Synthetic light curves generated from convex inversion YORPogram model of (29075) 1950 DA Pro 232

A.12 (Continued.) 233

A.13 Synthetic light curves from convex-inversion model of (68346) 2001 KZ66 234

A.13 (Continued.) 235

A.14 Synthetic light curves from radar-derived model of (68346) 2001 KZ66 with YORP 236

A.14 (Continued.) 237

A.15 Synthetic light curves from radar-derived model of (68346) 2001 KZ66 with constant period 238

A.15 (Continued.) 239

A.16 Synthetic light curves from the `convexinv` Model A of (89830) 2002 CE with constant period 240

A.16 (Continued.) 241

A.17 Synthetic light curves from the `convexinv` Model B of (89830) 2002 CE with constant period 242

A.17 (Continued.) 243

A.18 Synthetic light curves from `convexinv` model of (89830) 2002 CE with YORP strength of -3.4×10^{-6}rad/day^2 244

A.18 (Continued.) 245

A.19 Synthetic light curves from `convexinv` model of (89830) 2002 CE with YORP strength of 4×10^{-7}rad/day^2 246

A.19 (Continued.) 247

A.20 Synthetic light curves from `convexinv` model of (89830) 2002 CE with YORP strength of 4.2×10^{-6}rad/day^2 248

A.20 (Continued.) 249

A.21 Additional best-fit convex inversion shape models of (89830) 2002 CE . 250

B.1 Excerpt of `convexinv` input file 252

B.2 Excerpt of `MATLAB` input file 252

B.3 Excerpt of a `SHAPE` obs file containing light curve observations 254

B.4 Excerpt of a `SHAPE` light curve data file 255

B.5 Excerpt of a SHAPE obs file containing delay-Doppler observations 256

B.6 Excerpt of a SHAPE obs file containing Doppler spectra 257

B.7 Excerpt of a SHAPE mod file 260

B.8 Excerpt of a SHAPE par file 261

Publications

Refereed Publications

O. Vaduvescu et al. including T.J. Zegmott Ready for EURONEAR NEA surveys using the NEARBY moving source detection platform.
New Astronomy, 2021, Volume 88, 101600

M. Monguió et al. including T.J. Zegmott IGAPS: the merged IPHAS and UVEX optical surveys of the northern Galactic plane.
Astronomy & Astrophysics, 2020, Volume 638, A18

A. Rożek et al. including T.J. Zegmott Shape model and spin-state analysis of PHA contact binary (85990) 1999 JV6 from combined radar and optical observations.
Astronomy & Astrophysics, 2019, Volume 631, A149

D. Froebrich et al. including T.J. Zegmott A survey for variable young stars with small telescopes: First results from HOYS-CAPS.
Monthly Notices of the Royal Astronomical Society, 2018, Volume 478, Page 5091

D. Froebrich et al. including T.J. Zegmott Variability in IC5070: Two Young Stars with Deep Recurring Eclipses.
Research Notes of the American Astronomical Society, 2018, Volume 2, A61

C. Snodgrass et al. including T. J. Zegmott The 67P/Churyumov- Gerasimenko observation campaign in support of the Rosetta mission.
Philosophical Transactions of the Royal Society A, 2017, Volume 375, Issue 2097

D. Froebrich et al. including T.J. Zegmott Optical brightness and colours of V2492Cyg before, during and after the recent record peak in brightness.
The Astronomer's Telegram, 2017, No. 10259

A. Sicilia-Aguilar et al. including T.J. Zegmott The 2014-2017 outburst of the young star ASASSN-13db: A time-resolved picture of a very low-mass star between EXors and FUors.
Astronomy & Astrophysics, 2017, Volume 607, A127

Submitted Publications

T.J. Zegmott et al. Shape model and spin-state analysis of contact-binary (68346) 2001 KZ66 from combined radar and optical observations.
Monthly Notices of the Royal Astronomical Society, 2021
(Based on Chapter 5 of thesis).

In Preparation

T.J. Zegmott et al. Physical characterisation of asteroid (29075) 1950 DA.
(Based on Chapter 4 of thesis).

1 Evolution of asteroids in the Solar System

1.1 The Solar System and its formation

Initially, the Solar System started as a molecular cloud of gas. Composed mostly of hydrogen and helium, but also containing some dust grains including silicates, hydrocarbons, and ices (Montmerle et al., 2006). The gas cloud had some angular momentum at the onset of its collapse, this lead the falling matter to form a disk surrounding the protostar in order to conserve its initial angular momentum. The timescale over which the disk disappears for Solar-like stars is 6 Myr (Haisch et al., 2001), by which point the planets will have formed. In the core-accretion paradigm of planetary formation, the process of formation is divided into three stages: (I) the coagulation of dust to form planetesimals, (II) the formation of terrestrial planets and the cores of the gas giants, (III) the accretion of gas to form giant planets.

During the critical "disk-era" of planet formation, tiny dust grains coagulate growing in size to eventually form planetesimals. During the initial growth, micron-sized grains stick together via slow collisions and form fractal structures (Kempf et al., 1999). Once at the millimetre to centimetre size range, further growth becomes stunted due to catastrophic collisions and particles bouncing off each other (Zsom et al., 2010). However, this is overcome in turbulent regions where particles become trapped in vor-

tices allowing further growth to continue (Lyra et al., 2009). These vortices are able to operate like planetesimal factories, quickly producing kilometre sized bodies which decouple from the gas trapped in the vortex (Lyra et al., 2009).

The composition of the planetesimals will contain an indication of the location within the Solar System at which they formed. As each volatile species condenses at a different temperature, they each have a 'snow line' - the distance from the Sun beyond which it is cold enough for them to condense. Due to this, the inner Solar System is mostly comprised of material with a high melting point, such as metals and silicates. These rocky and metallic planetesimals lead to formation of the terrestrial planets. Beyond the water snow line, more material is found in the solid phase. As the proto-Jovian planets grow in size, the depth of their gravitational potential wells grow with them. Eventually, growing large enough to accumulate a gaseous envelope. By mass, Jupiter and Saturn are composed predominantly of hydrogen and helium. Both of which are unable to condense under the conditions of the protoplanetary disk. Therefore, the Jovian planets must have formed before the disk dissipated.

Under this picture of planetary formation, with planets forming and remaining within the same location of the Solar System, models of terrestrial planet formation are unable to form Mars as seen today. Instead, they systematically produce a planet five to ten times larger than Mars at its location (Raymond et al., 2009). In the Grand Tack model, this issue is prevented by the migration of Jupiter inwards which reduces the amount of planetesimals available to Mars for accretion. The migration Sun-ward was stopped by a faster migrating Saturn when it fell into Jupiter's exterior 2:3 mean motion resonance (Walsh et al., 2011). Both Jupiter and Saturn then began to migrate outwards, slowing and eventually stopping as the disk dissipated (D'Angelo and Marzari, 2012).

During the migration of Jupiter and Saturn, planetesimals - both interior and exterior to Jupiter - were scattered. Many of these were ejected from their orbits (Petit et al., 2001), but many others survived on stable orbits within the Main Belt (Raymond

and Morbidelli, 2014). To this day, asteroids in the belt still feel the effects of Jupiter's gravitational field, this is evident from the Kirkwood gaps that can be seen in the belt. These gaps are emptied by powerful gravitational resonances that inject asteroids into near-Earth orbits. These gaps can be seen in the distribution of asteroids shown in Fig. 1.1.

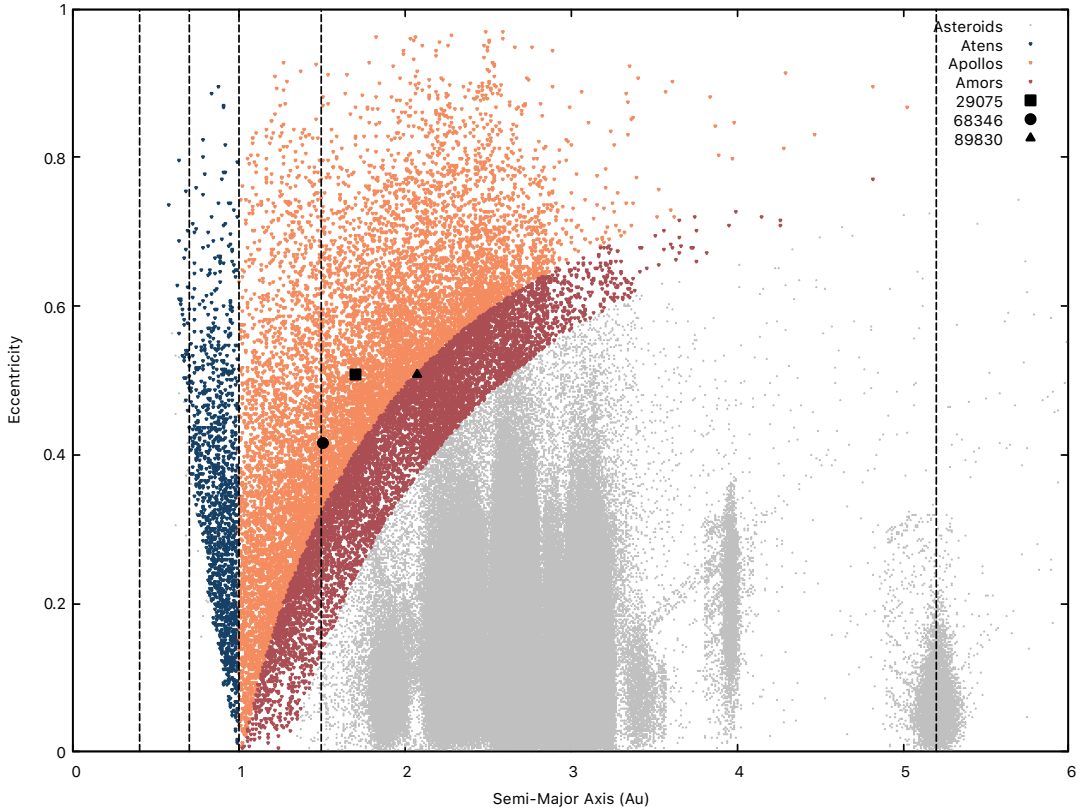

Figure 1.1: Distribution of asteroids within the inner Solar System. All asteroids are marked by grey circles, with the near-Earth asteroids marked in colour according to their orbital classification. Aten class asteroids are shown in blue, Apollos with orange, and Amors with red. The asteroids that were investigated in this thesis are marked with black shapes. The semi-major axis of the planets are also highlighted with black dashed lines. The data used to produce this plot was obtained from JPL (`https://ssd.jpl.nasa.gov/?sb_elem`) on 1 September 2020

1.2 Asteroids in the Solar System

Asteroids and other small-body populations are the surviving remnants of the formation of the planets in the Solar System, they are living relics that contain a record of the initial environment of the Solar System in addition to its conditions post planet-formation. They are small bodies that are usually irregular in shape, too small to individually dominate the region of space in which they orbit. The majority of asteroids are considered to be "rubble piles", weakly bound by self-gravity with high bulk porosity, and range in size from 0.2 to 10 km (Walsh, 2018). There are also large asteroids that have undergone internal heating leading to the differentiation of their internal composition. On the opposite scale, there also exist small monolithic asteroids, these are typically fast rotators. Asteroids differ from comets in that they do not contain ices, they do not undergo outgassing and therefore have no coma. However, this distinction has been challenged recently with the detection of volatiles on asteroids (Rivkin et al., 2015) and the observation of active asteroids (Jewitt et al., 2015).

The vast majority of asteroids reside in the Main Belt, which is a region in the Solar System that is found between the orbit of Mars and Jupiter between 2.0 and 4.0 AU. Though numerous, by mass, asteroids in the Solar System are negligible. The total mass of the Main Belt is approximately 3% that of the Moon, with half of that mass accounted for by the four largest asteroids: (1) Ceres, (4) Vesta, (2) Pallas, (10) Hygiea. Outside of the Main Belt, the other groups of asteroids are the Jupiter trojans, Hilda asteroids, and near-Earth asteroids. As of 1 September 2020, there were a total of 990,933 asteroids and comets that have been discovered and reported to the Minor Planet Center, these objects are shown in Fig. 1.2

1.2.1 Sizes, spin-states, and morphologies of asteroids

From most telescopes, asteroids are too small to measure their sizes directly, only powerful telescopes with adaptive-optics are able to resolve large objects (Vernazza

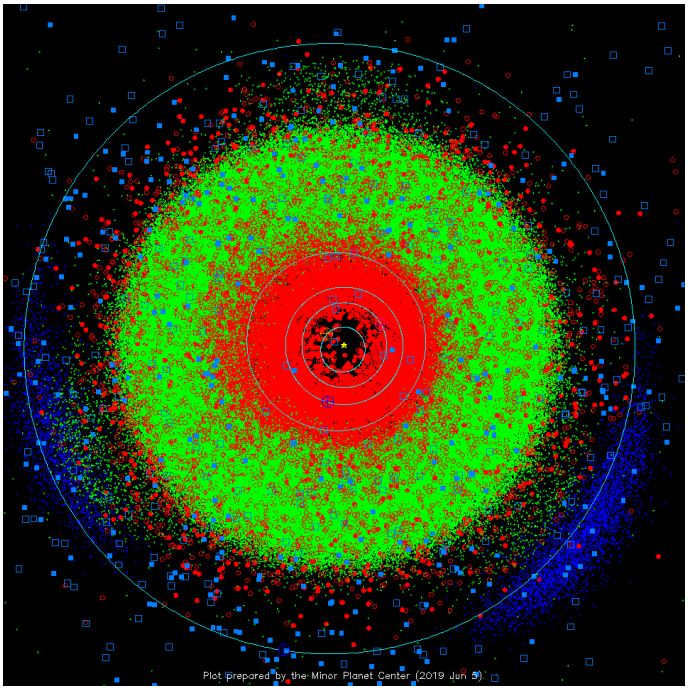

Figure 1.2: The orbits of the major planets are shown in light blue. The locations of the minor planets are indicated by green circles. Near-Earth objects are shown by red circles. The two "clouds" of objects 60° ahead and behind Jupiter are the Jupiter Trojans, here coloured deep blue. Comets are shown as light-blue squares. *Reprinted from the Minor Planet Center*

et al., 2020). However, even from facilities where these objects cannot be resolved, it is still possible to measure or estimate their sizes. This can be performed by measuring the brightness of the asteroid using a technique called photometry (this technique is discussed in Chap. 2). This is due to the dependence of an asteroid's brightness on its distance from the Sun, size, and albedo. The effective diameter D, if the asteroid was a sphere, is given by:

$$D = \frac{1329}{\sqrt{p_v}} 10^{-0.2H} \tag{1.1}$$

Where, the absolute magnitude H is the magnitude when the asteroid is both 1 AU from the Sun and observer, and at an orbital phase angle of zero. The geometric albedo p_v is defined as the ratio of light reflected directly back, which is also measured at zero phase angle. The surface properties of the asteroid are not always known, so a representative albedo is sometimes chosen (as done in Bottke et al. (2005)).

As previously mentioned, asteroids contain a record of the initial conditions in the Solar System, however, they have since undergone collisional, compositional, and dy-

namical evolution. In order to interpret the record they contain, we need to be able to disentangle the effects of their subsequent evolution. By placing constraints on the asteroid population, such as the present day size-frequency distribution (see Fig. 1.3), known asteroid families, and large asteroids such as (4) Vesta, collisional evolution models can be produced to infer the size distribution of the primordial Main Belt. Analysis along this approach has lead to the belief that asteroids were born large (100 km or larger) (Morbidelli et al., 2009), a claim which has been supported by the investigation of a primordial asteroid family (Delbo et al., 2017). It is also believed that the current shape of the size-frequency distribution of the largest asteroids is a fossil feature representative of the primordial distribution at that size range (Bottke et al., 2005).

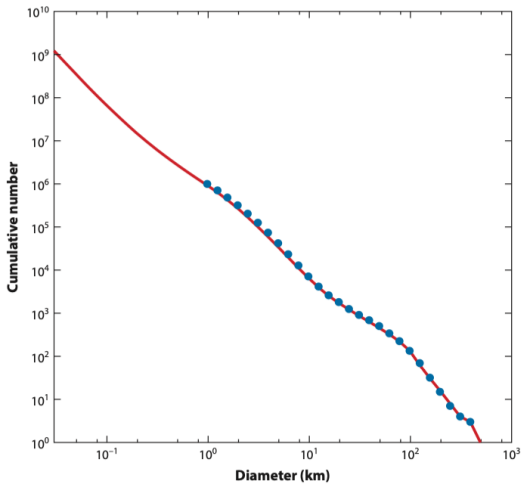

Figure 1.3: The size frequency distribution of asteroids within the Main Belt. The diameter of asteroids has been calculated from their absolute magnitude assuming a geometric albedo of 0.092. Absolute magnitudes are results of the Sloan Digital Sky Survey. *Reprinted from Walsh (2018), originally printed in (Bottke et al., 2005).*

Photometry can also be used to determine the rotation period of an asteroid. By linking together a series of photometric measurements, typically over several hours of a night, a light curve can be obtained from which the period can be measured. Currently, in the Asteroid Lightcurve Database (LCDB) there are a total of 7942 asteroids with a known rotation period and size. The distribution of these asteroids' rotation frequencies and sizes reveal an important characteristic: the lack of fast rotators with a period smaller than 2.2 hours. This spin barrier, first discovered by Harris (1996), provided evidence for the rubble-pile structure of asteroids larger than 200 metres. Pravec and Harris (2000) revisited this with a larger sample size, this sample showed that small

asteroids were able to pass this barrier. These asteroids are thought to be monolithic. The spin barrier can be seen visually in Fig. 1.4, created using data from the LCDB.

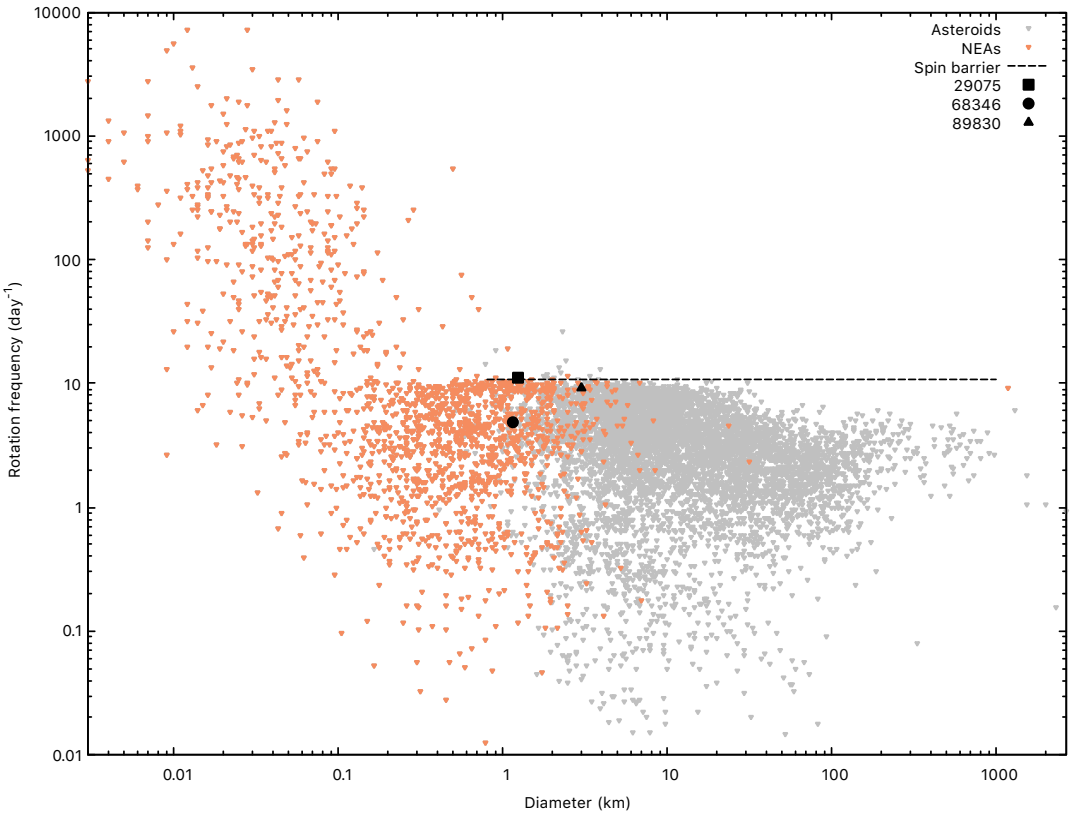

Figure 1.4: Rotation frequency and size distribution for 7942 asteroids published in Asteroid Lightcurve Database (LCDB). Rotation frequency given per day, and the diameter is in kilometres. Asteroids are marked with small grey circles, with NEAs highlights in orange. The asteroids investigated in this thesis are marked with unique black shapes. The data used to produce this plot was obtained from the LCDB (Warner et al., 2009)

Further work by Holsapple (2007) investigated the role of tensile and cohesive strength on the spin-barrier, finding two limiting regimes: a strength regime and a gravity regime. The gravity regime dominates for large bodies, with a diameter >10 km, where the strength of the asteroid is of no consequence and the maximum rotation period is determined by gravity and spin stresses. This is the regime that was discovered by Harris (1996). For smaller bodies, with diameters <10 km, even a trace amount of cohesive strength can allow for faster rotation rates. The transition zone from the gravity regime to strength regime covers a narrow range, a factor of three in size. In the

strength regime, where asteroids have a diameter <3 km, the cohesive/tensile strength of the asteroid determines the asteroid's rotation rate limit and gravity is of no consequence. The spin limit in this regime can be given by $\omega_{strength} = C\sqrt{\frac{\kappa}{\rho}}(\bar{r})^{-5/4}$, where C is a coefficient that depends on the asteroid's shape and friction coefficient, κ is the strength coefficient, ρ is the bulk density, and $\bar{r}$ is the average radius. This $\propto r^{-5/4}$ dependency in the strength regime means that smaller asteroids are able to spin faster, which is what is seen in Fig. 1.4.

Even an asteroid's morphology can indicate the evolutionary mechanisms that have shaped them. Distinct amongst small ($\lesssim$1 km) asteroids are those with equatorial ridges, sometimes called top-shape asteroids. This feature is common in populations of asteroids with a fast rotation rate, many of them also have satellites orbiting them. This shape is thought to be an end-state of a rotationally accelerated asteroid (Harris et al., 2009). Interestingly, in the case of asteroids (162173) Ryugu and (101955) Bennu their geological characteristic suggest that they either formed directly as top-shapes, or attained their ridges soon after their formation (Michel et al., 2020). Once past the spin barrier, asteroids that continue to be accelerated break apart and can form a binary system (Walsh et al., 2008; Harris et al., 2009; Walsh, 2018). Binaries account for 15% of population of near-Earth and Main Belt asteroids (Pravec and Harris, 2007). Another distinctive shape are bifurcated contact binary asteroids which are composed of two lobes. Benner et al. (2006) estimated that approximately 10% of the NEA population with diameters larger than 200 m are contact binaries. Several mechanisms are able to produce bifurcates asteroidal shape. These include catastrophic collisions between unbound pairs (Sugiura et al., 2018; Schwartz et al., 2018), sub-catastrophic collision (Jutzi, 2019), and the collapse of an aggregate with a weak core (Sánchez and Scheeres, 2018).

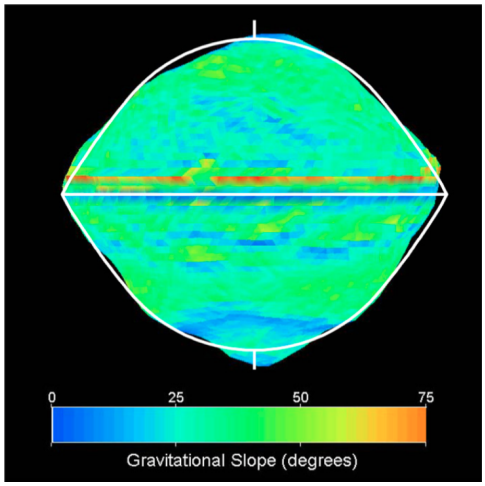

Figure 1.5: This figure depicts the asteroid (66391) 1999 KW4. This asteroid has a spherical shape with an equatorial ridge, the slope from the equator is 37°. The colour of each facet describes the gravitational slope.k *Reprinted from Harris et al. (2009).*

1.2.2 Near-Earth Asteroids

Near-Earth Asteroids (NEAs) are a population of asteroids on orbits that approach or intersect that of Earth. They have perihelia q of 1.3 AU or less. This population is further divided into four named classes: Amors (1.017 <q <1.3 AU), Apollos (semi-major axis a >1.0 AU, q <1.017 AU), Atens (a <1.0 AU, aphelion Q >0.983 AU), and Atiras (0.718 <Q <0.983 AU). Amors and Atiras do not cross the orbit of Earth, but they do approach it, where as Apollos and Atens do cross the Earth's orbit at perihelion and aphelion respectively.

The source of NEAs is the Main Belt. Particularly, regions within the Main Belt where asteroids experience strong perturbations from both Jupiter and Saturn. Asteroids within these regions are in one of several mean motion resonances or secular resonance. The strongest resonances are the 3:1 and 5:2 mean motion resonance with Jupiter, and the ν_6 secular resonance with Saturn. Gravitational interactions between the gas giants and the asteroids slowly alter the orbital parameters of asteroids within the resonance orbits. Continually pumping up their eccentricity, until eventually, these asteroids enter near-Earth space.

Once an asteroid is in a near-Earth orbit, they have a mean lifetime of $\lesssim$10 Myr (Granvik et al., 2018). The end of an NEAs lifetime is described as a 'sink'. The most

common sink of a NEA is a collision with the Sun (Granvik et al., 2018). Other large sinks include ejection from the Inner Solar System via a close encounter, destruction of the asteroid by thermal effects (Granvik et al., 2016), or a collision with terrestrial planets.

Interest in the study of NEAs is multifaceted. Like other asteroids, NEAs also provide evidence about the formation of planetesimals in the early Solar System (Johansen et al., 2015). However, NEAs are much more easily accessible for exploration. In the past two decades, there have been several missions to explore and collect samples from near-Earth objects. Recently, there were two missions: JAXA's Hayabusa 2, a sample return mission to asteroid (162173) Ryugu which returned to Earth with a sample of subsurface material in December 2020, and NASA's on-going OSIRIS-REx mission to monitor asteroid (101955) Bennu for two years before collecting a sample and returning in 2023. In addition to the scientific value that NEAs have, there is also a growing interest in mining asteroids (Elvis, 2014).

Perhaps more practically, is understanding and mitigating the threat that near-Earth asteroids pose to us as humans. This is highlighted by the Tunguska event of 30 June 1908 over the remote Siberian taiga, when an impactor exploded releasing an energy equivalent of 10 megatons of TNT and flattened over 2000 km^2 of forest (Jenniskens et al., 2019). More recently on 15 February 2013, a smaller asteroid exploded over the Russian city of Chelyabinsk. The bolide released an estimated energy equivalent of 500 kilotons of TNT (Popova et al., 2013), the resulting shock wave shattered glass in the surrounding area injuring approximately 1600 people (Brown, 2013). Since these impacts, strategies to deflect an asteroid have been discussed. Including the use of a nuclear explosion, pulling it with the gravity of a massive spacecraft, and even impacting it with a spacecraft (Cheng et al., 2016). However, none of these mitigation methods have ever been tested on a NEA. The experiment to demonstrate one of these strategies will be the joint ESA and NASA Asteroid Impact and Deflection Assessment (Cheng et al., 2018; Michel et al., 2018). This mission aims to impact the secondary

member of the (65803) Didymos binary and alter the binary orbit period by 4 minutes (Cheng et al., 2016). In the following section, I will discuss two thermal forces and their influence on asteroidal evolution.

1.3 Thermal drivers of asteroid evolution

Conventionally, the motion of all objects within the Solar System is considered to be due to the effects of gravity. Thus the orbital evolution of asteroids has been attributed to gravitational interactions between bodies and collisions. With just these two forms of interaction, the history and evolution of asteroids in the inner Solar System can be described with moderate success. However, there are some aspects that can't be explained solely by collisions and gravitational interactions.

The source of NEAs is accepted to be the Main Asteroid Belt, from which objects are thrown into the inner Solar System by powerful resonance orbits with Jupiter. An asteroid within one of these resonances has a typical dynamic lifetime of a few million years (Gladman et al., 1997). Conventionally, these resonance zones were thought to be repopulated by the ejecta, resulting from collisions between asteroids. However, there are issues with this theory. Dating of asteroids via cosmic-ray exposure (CRE) ages show that most stony meteorites have CRE ages between ∼10 and 100 million years, while iron meteorites have CRE ages between ∼0.1 and 1 billion years (Marti and Graf, 1992). Additionally, collisions between asteroids should produce a wide range of spin states, roughly following a Maxwellian frequency distribution (Binzel et al., 1989; Davis et al., 1989), but there is an excess of both fast and slow rotators (Pravec and Harris, 2000; Pravec et al., 2002).

These discrepancies can be alleviated with the addition of an important physical mechanism: the affect of non-gravitational forces on the evolution of asteroids. These forces are a result of the reflection, absorption, and re-emission of solar radiation by the surface of an asteroid. They manifest in two distinct effects, an orbital effect and a

spin-state effect called the Yarkovsky and YORP effects respectively. The Yarkovsky effect, discussed in Sec. 1.3.1, plays a non-negligible effect in the long-term evolution of an asteroid's orbit. The YORP effect, discussed in Sec. 1.3.2, plays an important role in the evolution of an asteroid's spin-state.

1.3.1 The Yarkovsky effect

The Yarkovsky effect was discovered, and first published in a pamphlet circa 1900, by Ivan Osipovich Yarkovsky, however, it received no interest until 1951 when it was included in a discussion paper by Opik (1951). Yarkovsky is caused by the transfer of momentum during the absorption of solar radiation, which is ultimately re-radiated into space by the asteroid in the infrared region of the spectrum. The photons interacting with the asteroid impart the momentum $p = E/c$, where E is the photon's energy, and c is the speed of light. Due to the thermal inertia of the body, there is a delay between the absorption of a photon and its re-emission. The thermal inertia, Γ, describes a material's ability to conduct and store heat. It is given by $\Gamma = \sqrt{K\rho C}$, where K is the thermal conductivity of the asteroid's surface, ρ is its density, and C is the specific heat capacity of the surface material. This tiny force, while small, could lead to large secular changes in the orbits of small bodies, especially small asteroids. The magnitude of the force depends on the asteroid's proximity to the Sun, the orientation of its spin-axis, its size, and thermal inertia. There are two ways in which this effect can manifest. The diurnal component, related to the day-night cycle of the asteroid, and the seasonal component, related to the passing of seasons on the asteroid's surface.

The diurnal Yarkovsky effect arises from the temperature difference between the asteroid's day and night side. This concept is illustrated in Fig. 1.6a, where a circular asteroid is shown orbiting the Sun. To simplify the situation for the purpose of clarity, the asteroid's pole orientation is perpendicular the plane of its orbit. If the asteroid had no thermal inertia, then the sub-solar point would be the hottest part of the asteroid, and the temperature across the rest of the surface would be symmetrical

about this point. This would act to counter the gravitational pull of the Sun, leading to a secular increase in the semi-major axis. However, all bodies have thermal inertia, so the hottest part of the asteroid would in fact be in the asteroid's afternoon hemisphere, not the sub-solar point. Thus the asteroid experiences a force that not only has a radial component, as in the zero thermal inertia example, but also in the direction tangential to the asteroid's orbit along its direction of motion. The latter component causes a secular change in the semi-major axis, and eccentricity to a lesser degree, over time. For a prograde rotator like that shown in the figure, with it rotation in the same direction as its orbital motion, the Yarkovsky effect causes an increase in the semi-major axis. However, for a retrograde rotator that rotates in the opposite direction to its orbital motion, the force will cause a decrease in the semi-major axis.

The seasonal Yarkovsky effect is dependant upon the orbital motion of the asteroid, but still has a dependency on its spin-axis. This is illustrated in Fig. 1.6b for a simplified configuration where the asteroid is in a circular orbit with its spin-axis in the orbital plane. The strongest insolation of the northern (or southern) hemisphere occurs when the asteroid is at point A (C) of its orbit. Like the diurnal effect, there is delay due to thermal inertia and so the northern (southern) hemisphere is hottest at point B (D). Averaged over an entire orbit, the along-track force is non-zero. Unlike the diurnal effect, the seasonal effect only acts to decay the orbit of the asteroid, reducing its semi-major axis. It is also unaffected by the sense of rotation, the effect applies equally for both prograde and retrograde rotators.

Yarkovsky's effect on asteroidal evolution

The Yarkovsky effect is an important factor in the dynamics of small Solar System bodies, essential in explaining the distribution of asteroid family orbits, delivery of asteroids and meteors to near-Earth space, and useful in determining physical properties of asteroids.

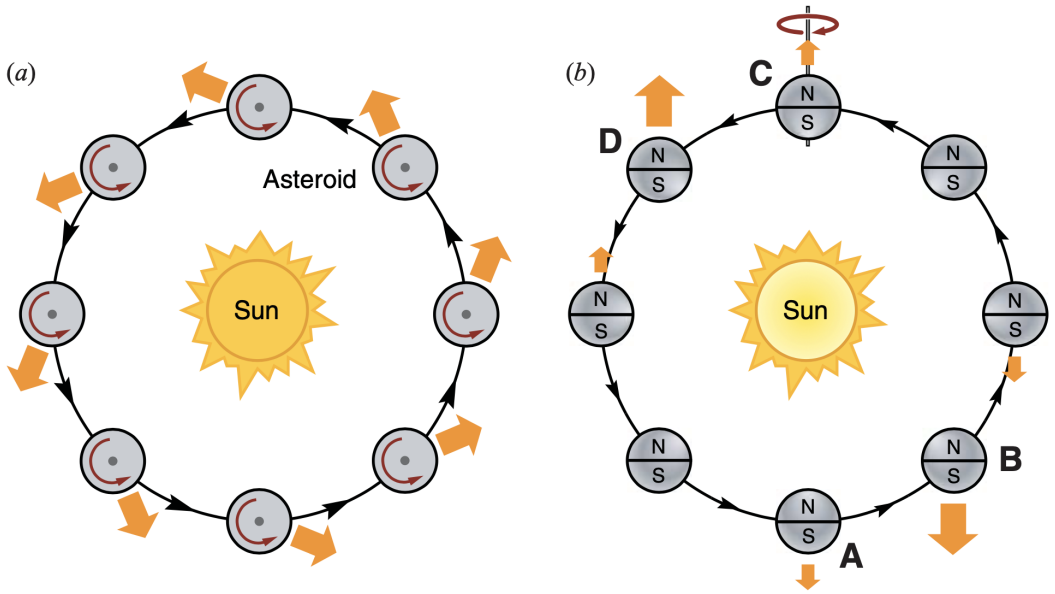

Figure 1.6: (a) The diurnal Yarkovsky effect for an asteroid with its spin-axis perpendicular to the orbital plane. A fraction of the solar radiation is absorbed and later re-emitted causing a net-force shown by the wide arrows. The delay in re-emission is due to a non-zero thermal inertia, and so the hottest part of the asteroid is its afternoon side. This force causes a secular increase in the asteroid's semi-major axis. For a retrograde rotator, the force would cause a decay in the semi-major axis. (b) The seasonal Yarkovsky effect for an asteroid in a circular orbit with its spin-axis in the orbital plane. The difference in insolation of the northern and southern hemisphere over an orbit cause a net force along the spin-axis. Due to the thermal inertia the poles are hottest at points B and D of the asteroid's orbit, and not the points with the largest insolation, points A and C. The result averaged over an orbit always causes the object to spiral towards the Sun. *Reprinted from Bottke et al. (2006).*

The first proposed application of the Yarkovsky effect was to explain the transportation of small bodies from the Main Belt to Earth (Opik, 1951). It was proposed that the decay of an object's semi-major axis due to the Yarkovsky effect would bring an object directly from the Main Belt to Earth. The time-scales involved with this were far too long. However, combining the Yarkovsky effect, and mean-motion and secular resonance in the Main Belt resolves this issue (Farinella et al., 1998). The Yarkovsky effect is responsible for the slow delivery of asteroids to the resonance regions of the Main Belt. This slow drift allows the bodies to be bombarded by cosmic rays. The difference in thermal conductivity between stony and iron asteroids is also able to explain the difference seen in their CRE ages, as the iron asteroids will drift much slower. Not only

does Yarkovsky elegantly explain the continual replenishment of the resonance zones, but it also provides a natural explanation for the lack of short CRE ages. Nowadays, the Yarkovsky effect is routinely included in numerical studies of asteroidal dynamical evolution (Granvik et al., 2017; Zain et al., 2020).

The strength and magnitude of the Yarkovsky effect, as mentioned earlier, depends not only on an asteroid's orbital parameters, but also its physical characteristics. Therefore, a direction measurement of an asteroid's Yarkovsky drift can allow insights into its physical properties. Even with only a measurement of da/dt and the absolute magnitude, meaningful constraints can be placed on the obliquity of the asteroid. The sign of da/dt instantly indicates whether the asteroid has a prograde or retrograde rotation (Vokrouhlický et al., 2015). If the spin-state and diameter are already known from light curve and radar observations, then constraints can be placed in terms of the bulk density ρ and the thermal inertia Γ. A characteristic peak in the ρ vs Γ relationship allows an upper bound to be placed on ρ, as obtained for (6489) Golevka (Chesley et al., 2003). In the best cases, where a shape model, spin-state, and thermal properties are available, the local gravitational strength of the body can be constrained or even the measurement of cohesive forces acting on rubble-pile asteroids (Rozitis et al., 2014).

The Yarkovsky effect has an important influence on the evolution of asteroid families. Asteroid families are comprised of the fragments from a catastrophic impact of their parent body. For young asteroid families (< 10 million years old), a fine determination of the age of the family is possible by finding the point in the past where the positions of members of the family converge. The role of Yarkovsky in this is important due to its effect on the evolution of the orbital secular angles (the ascending node and the argument of periapsis), which are sensitive to the semi-major axis value (Nesvorný et al., 2002). For older asteroid families (> 100 million years old), the effect of Yarkovsky pushes small asteroids towards extreme values of semi-major axis. When an old asteroid family is plotted in semi-major axis and absolute magnitude space, they display a characteristic V-shape (Vokrouhlický et al., 2006b). The distinct shape of these 'V-plots' allows for the determination of the age of an asteroid family (Vokrouhlický et al., 2006c,a; Carruba and Morbidelli, 2011). This phenomenon has also been used to identify new asteroid families (Delbo et al., 2017; Bolin et al., 2017). Fig 1.7 shows an example V-plot, in which the characteristic 'V'-shaped spread is clearly shown.

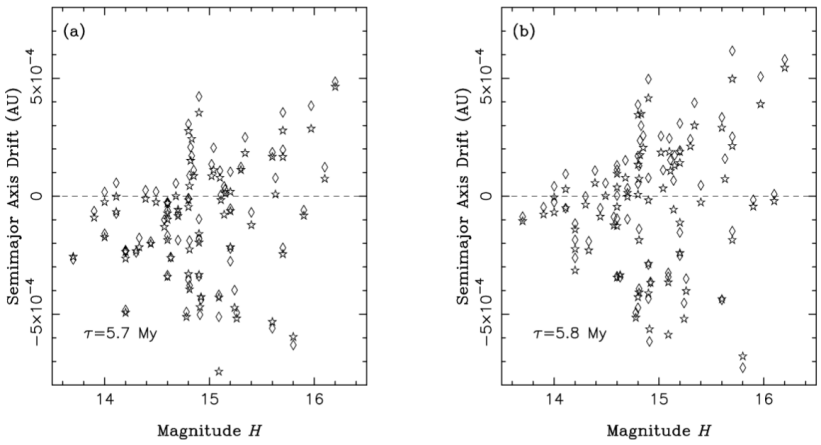

Figure 1.7: Measurements of the semi-major axis drift of 70 Karin family asteroids. The drifts were computed from two secular angles: the argument of periapsis and the longitude of the ascending node, represented by the diamonds and stars. This figure represents direct evidence of semi-major axis drift due to non-gravitational effects of asteroids within the Karin family. The two panels are for different ages of the family (a) is 5.7 My and (b) is 5.8 My. These values bracket the age uncertainty of the family. *Reprinted from Nesvorný and Bottke (2004).*

Current detections and detection methods

The earliest detection of the Yarkovsky effect acting on an asteroid was measured for the asteroid (6489) Golevka (Chesley et al., 2003). Extensive radar observations meant that the orbital determination for Golevka was precise enough to test for the presence of non-gravitation effects. Two orbital predictions were made: one accounting for gravitational perturbations and the other with the addition of non-gravitational effects. The error ellipses for each prediction are shown in Fig. 1.8. The error ellipses show the 90% confidence areas in delay-Doppler space. The ellipse showing the gravitational model, which includes perturbations from both planetary and small body masses, is labelled SUM1. The second ellipse, labelled SUM2, includes the additional offset and associated error for the Yarkovsky effect. The strength of which was computed using a non-linear numerical model that incorporated both the asteroid's shape and spin-state. The new astrometric measurement taken in 2003 from Arecibo is plotted as a diamond. It can clearly be seen to reside within the predicted error ellipse that includes the effects of Yarkovsky. Based on the magnitude of the detection Chesley et al. (2003) were able to determine a bulk density of $2.7 \pm 0.2 \mathrm{gcm}^{-3}$ and a surface thermal conductivity of $0.01 \mathrm{Wm}^{-1}\mathrm{K}^{-1}$.

A different approach was taken by Nesvorný and Bottke (2004), who used the orbital distribution of the members of the Karin family to determine the drift speed of ∼70 asteroids. They assumed that the spread in the fragments' argument of periapsis and longitude of ascending node at the time of the parent breakup were small ($< 1°$), and that the semi-major axis drifted at a constant rate. Using the current day values of the secular angles for each of the family members and the age of the family, they were able to integrate backwards to obtain two measurements of the semi-major axis drift (one for each of the secular angles). From this, they were able to calculate the drift speed required to produce the semi-major axis drifts seen. They found larger drifts in semi-major axis for objects with larger absolute magnitude, as would be expected for the Yarkovsky effect.

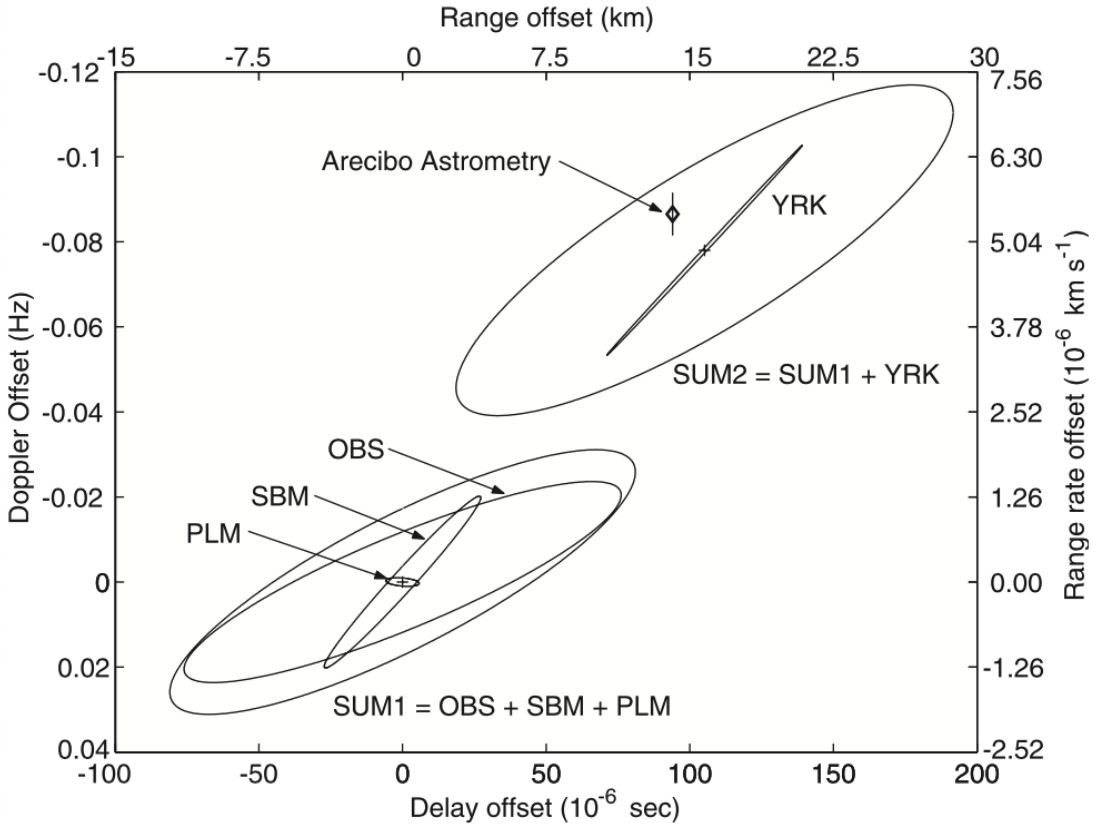

Figure 1.8: Image depicting the first detection of the Yarkovsky effect acting on asteroid (6489) Golevka. Predicted Yarkovsky-induced offset based on astrometric data from the 90's apparition. An error ellipse with 90% confidence is shown the prediction made with purely gravitational perturbations (SUM1). This is comprised of contributions from astrometric uncertainties (OBS), small body masses (SBM), and planetary masses (PLM). Another error ellipse (SUM2) represents the 90% confidence region which includes the uncertainty of the Yarkovsky modelling (YRK). The x-axis represents the delay offset in μs, which can be interpreted as a range offset in km. The y-axis shows the Doppler offset in Hz, which can be interpreted as a range rate offset or radial velocity measured in 10^{-6}km/s. The actual measurement of the delay and Doppler offsets of the 2003 Arecibo observation is marked by a diamond. *Reprinted from Chesley et al. (2003).*

The signature of a Yarkovsky drift can also be found directly from astrometric data without the need for extensive modelling. As the key manifestation of the Yarkovsky effect is a drift in the semi-major axis, a formulation can be chosen that depends on a single parameter that is determined concurrently with the orbital elements. This is achieved by defining an arbitrary transverse acceleration that is dependant on the parameter A_2 (Farnocchia et al., 2013). This simple model derives a mean semi-major

axis drift rate which is proportional to A_2, the advantage of this method is that it bypasses the need for physical characteristic of the object. The measurement of A_2 will have an accompanying error σ_{A_2}, the ratio of the two will give the signal-to-noise of the detection which can be used as a gauge for the measurement's reliability. A list of Yarkovsky detections can be found within Farnocchia et al. (2013); Vokrouhlický et al. (2015); Greenberg et al. (2020).

1.3.2 The YORP effect

The Yarkovsky-O'Keefe-Radzievskii-Paddack effect, commonly shortened to YORP, is the sister effect of the Yarkovsky effect discussed in Sect. 1.3.1. Yarkovsky's contributions to the advancement to this field is reflected in the name along with the other prominent scientist who made significant contributions. Where the Yarkovsky effect alters the orbital state of asteroids, the YORP effect alters an asteroid's spin-state, namely the angular frequency or rotation period and the obliquity (Rubincam, 2000). The YORP effect arises from the absorption and re-emission of thermal photons from the asteroid's surface, this can produce a torque that alters its spin-state if it has the correct shape. Unlike the Yarkovsky effect, the YORP effect does not work for spherical bodies, as the symmetry of the body will lead to the solar torque averaging to zero.

To experience a YORP torque, a body must have a degree of "windmill" asymmetry in its shape, such as the body shown in Fig. 1.9. To simplify the scenario, the asteroid is in a circular orbit with its spin axis perpendicular to its orbital plane and the asteroid is a blackbody radiator with zero thermal conductivity. The torque imparted by the incident photons striking the blackbody asteroid will be zero, as the body presents a symmetric silhouette to the Sun. For a Lambertian radiator, the re-radiated energy from the spherical parts of the body do not impart a net torque. From the wedges, however, a torque is produced as the wedge faces are not co-planar. For the body shown in Fig. 1.9, the result is an increase in the spin rate. If the body was rotating in the opposite sense this would lead to a spin down.

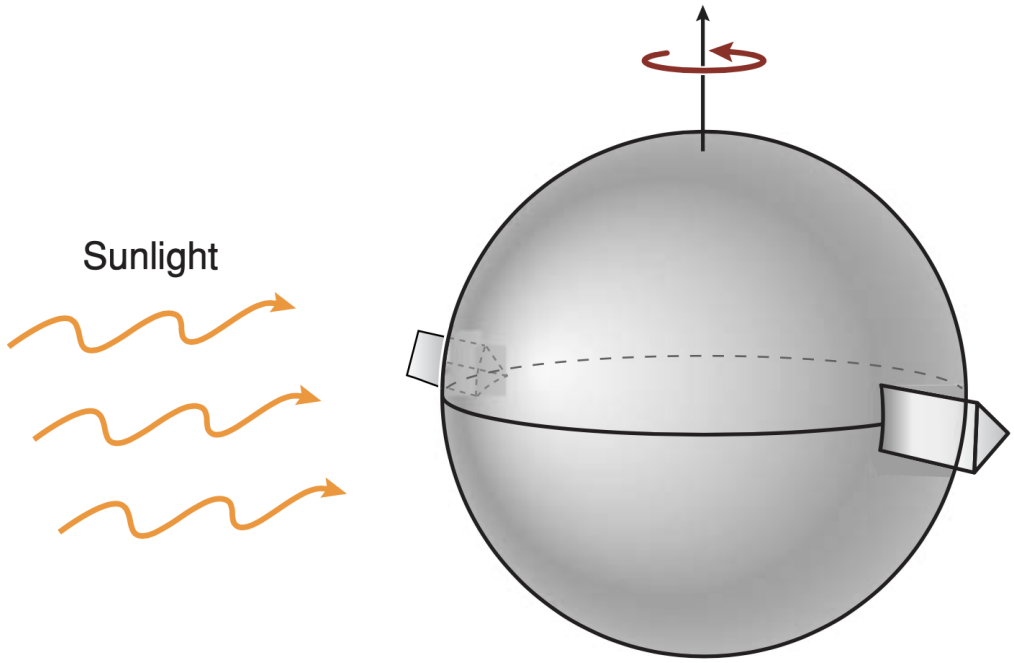

Figure 1.9: The asteroid depicted has an asymmetrical shape, it is modelled as a sphere with two wedges on opposites sides of its equator. The asteroid is a blackbody, so that it absorbs all incident sunlight. Upon re-emission, the asteroid will experience an impulse from the departing radiation. The impulse from the spherical part of the body cancels each other due to the symmetry. However, the photons leaving the wedges are in different directions and so a net torque is produced. This torque leads to the spin-up of the asteroid. *Reprinted from Bottke et al. (2006).*

The torque $\vec{\tau}$ imparted on the asteroid, can be split into two components: one that acts along the axis of maximum moment of inertia which changes the rotation rate τ_ω, and the other which acts to change the obliquity τ_Θ. The obliquity Θ is defined as the angle between the normal to the orbital plane $\hat{N}$ and the unit spin vector $\hat{\omega}$. Assuming principal axis rotation, the rate of change of both the rotation rate and the obliquity are:

$$\frac{d\omega}{dt} = \frac{\tau_\omega}{C}, \qquad \frac{d\Theta}{dt} = \frac{\tau_\Theta}{C\omega}. \tag{1.2}$$

Where C is the principal axis of inertia about the spin-axis, $\tau_\omega = \vec{\tau} \cdot \hat{\omega}$, and $\tau_\Theta =$

$\vec{\tau} \cdot (\hat{\omega} \cos\Theta - \hat{N}) / \sin\Theta$ (Rubincam, 2000; Vokrouhlický and Čapek, 2002). The change in spin rate for some asteroids is sufficiently large that it can be directly measured from high-precision optical light curves (see Chap. 3).

An investigation of the behaviour of YORP was performed by Vokrouhlický and Čapek (2002). Using a statistical approach they calculated the components of the YORP torques for a variety of asteroid shapes and over varying obliquity. How the evolution of their spin-states were affect was used to classify them into four asteroid "types". The asteroid shapes that were used included real shapes of NEAs and Mars' moon Deimos, and also randomly generated asteroid shapes. They found that obliquity component of the YORP torque, τ_Θ, pushes the asteroids towards certain values of obliquity, these values are dependant upon the asteroid's shape. Once in the preferred obliquity, the value of the spin component, τ_ω, leads the asteroid to continually accelerate or decelerate until it either breaks apart or begins to develop an unstable spin-state and tumble. Tumbling is an excited rotation state, where the motion is governed by two periods: one about one of the two extremal principal axes, and a quasi-period of precession about the asteroid's angular momentum vector. For certain values of obliquity, it was also found that the spin component of YORP vanishes. This can be seen in the reprinted in Fig. 1.10 for Eros-like (Type I) and Deimos-like (Type II) objects.

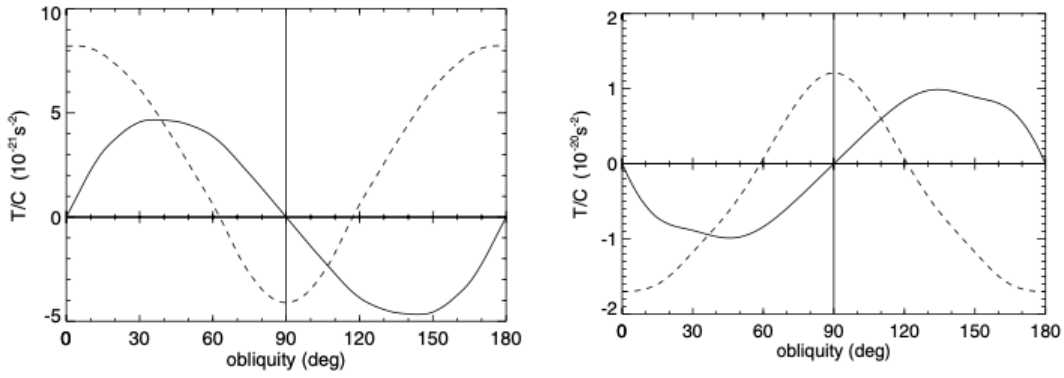

Figure 1.10: Obliquity dependency of the spin (dashed line) and obliquity (solid line) components of the YORP torque for objects with Eros-like (left panel) and Deimos-like (right panel) shapes. *Reprinted from Vokrouhlický and Čapek (2002).*

In the case of Eros-shaped objects, they found that the strength of τ_Θ was antisym-

metric about 90°, such that the YORP evolution always leads these objects towards a final obliquity value of 90°. For this final state, the value of τ_ω is negative, corresponding to a perpetual decrease of the rotation rate. Across the whole range of obliquities, the value of τ_ω is symmetric about 90°, with τ_ω having a positive value until about 62°. For the case of Deimos-shaped objects, the results revealed an inverted case to the Eros-like objects. That the value of τ_Θ leads the obliquity away from 90° to a final value of either 0° or 180° depending upon the initial obliquity of the object. Again, the value of τ_ω is such that it leads to a perpetual de-spin of the object for either of the terminal obliquities. From the investigation of their randomly generated shapes, they found that the two YORP evolution types discussed here were the dominant types.

In the early years of the numerical study of the YORP effect, to simplify computations, investigations were only carried out for the case of objects with zero thermal conductivity K. Following the study of Vokrouhlický and Čapek (2002), Čapek and Vokrouhlický (2004) expanded upon this work by including several values of thermal conductivity when investigating the YORP evolution of asteroids. The results of this study demonstrated a near-independence of τ_ω with K. However, the obliquity component, τ_Θ, has a very strong dependence on K. Shown in Fig. 1.11, are the results of the study for the asteroid (6489) Golevka. Each colour in the figure represents a different value of K, with the black line, $\log K = -9$, replicating the zero thermal conductivity case of Vokrouhlický and Čapek (2002). For the near-zero case, the results show three possible asymptotic values of obliquity 0°, 90°, and 180° corresponding to a Type IV in Vokrouhlický and Čapek (2002). However, as the thermal conductivity increases, a transition occurs leading to the asteroid now having a single asymptotic state at 90°, which would correspond with a Type I.

Effects of YORP

At the inception of the YORP effect, its was only theorised to have a significant effect on asteroids of 5-km-radius or smaller (Rubincam, 2000). Although, at the discovery of the first indirect evidence of YORP acting on the Koronis asteroid family, the asteroids

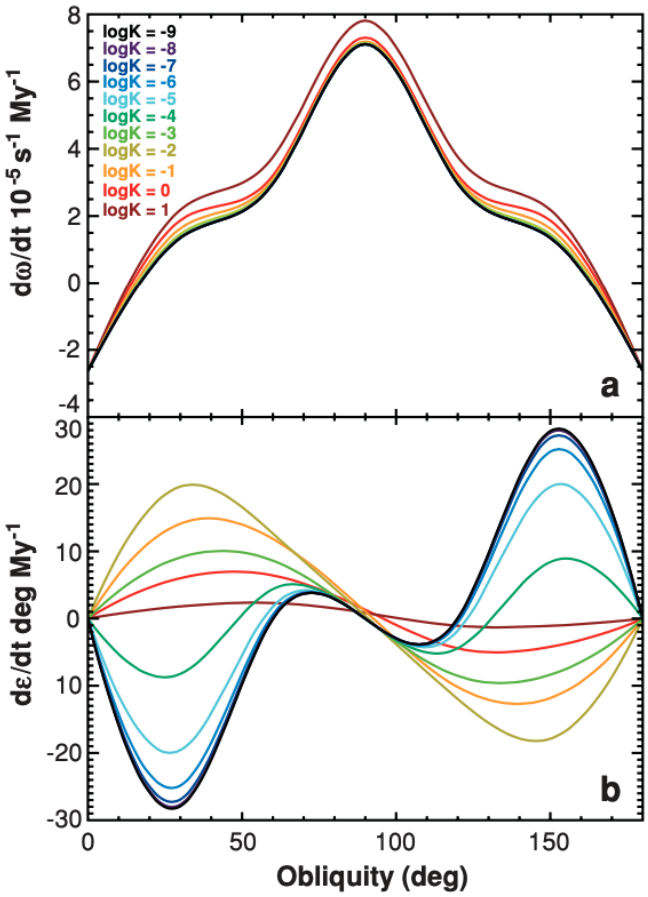

Figure 1.11: Rate of change in rotation rate and obliquity due to YORP torques as a function of obliquity for varying values of thermal conductivity. In this figure, these values are show for the asteroid (6489) Golevka. Note that the lowest value is identical to the zero thermal conductivity case from Vokrouhlický and Čapek (2002). The rotation rate displays a near independence to the thermal conductivity, while the obliquity (given the symbol ϵ in this figure) has a strong dependence. *Reprinted from Bottke et al. (2006), originally printed in Čapek and Vokrouhlický (2004).*

were a factor of two to four times larger with diameters between 20 - 40 km (Slivan, 2002). The Koronis family is thought to have formed from the collisional disruption of a parent body, which modelling had shown should result in fragments with stochastic spin-vectors (Michel et al., 2001). However, the Koronis family was found to have two distinct 'spin-clusters' (Slivan, 2002; Slivan et al., 2003). Those with prograde spins had obliquities between 42° and 50°, and those with retrograde spins had obliquities between 154° and 169°. Clustering such as this would be difficult to explain in terms of collisional and gravitational evolution, however, the secular effect of YORP are able to produce non-random pole orientations and spin rates (Vokrouhlický et al., 2003).

The effect that YORP has on not only the spin rate, but also the spin orientation also allows it to indirectly influence the evolution of an asteroid's orbital parameters. This is due to a pairing with the Yarkovsky effect, which alters an asteroid's semi-major

axis over time with the magnitude and direction dependant on the asteroid's obliquity. Within an asteroid family, the outcome of this can be a depletion of objects in the central part of the family when observed in a 'V-plot' (Paolicchi and Knežević, 2016) - see Sect. 1.3.1 for a description of V-plots. The size of the void in the V-plots can then be used to obtain an estimate of the asteroid family's age (Paolicchi et al., 2018). By the nature of this analysis of age, families that are so young that no significant YORP evolution has occurred cannot be dated. Additionally, due to the manner in which this method is calibrated it is also not possible to measure the ages of families younger than 50 Myr.

The interplay between obliquity and spin can lead to YORP cycles, where asteroids alternate between periods of acceleration and deceleration. As discussed earlier, YORP's effect on the obliquity pushes the asteroid towards its preferred value. Once at the preferred obliquity, the spin component may lead the asteroid to continually decelerate (Vokrouhlický and Čapek, 2002). This slow rotation will lead to the asteroid into a tumbling state, which will shut off YORP. In some cases, principal axis rotation can be established through internal energy dissipation with the spin axis oriented in arbitrary direction (Rubincam, 2000). At which point, YORP is able to operate again, beginning the cycle anew.

In some cases, the completion of the YORP cycle may be interrupted. The acceleration provided by YORP can lead to asteroidal aggregates slowly reshaping (Sánchez and Scheeres, 2012). The centrifugal force resulting from the acceleration leads to the disruption of the body causing the appearance of an equatorial ridge (Walsh et al., 2008; Sánchez and Scheeres, 2016). As YORP is highly sensitive to shape, this reconfiguration of its shape will begin a new cycle. However, if the acceleration continues asymmetric deformation of the asteroid can occur, stretching the asteroid to form a non-ellipsoidal shape with a distinct bifurcation (Scheeres, 2018). Further acceleration of the body eventually leads to fission producing a binary asteroid (Walsh et al., 2008; Scheeres, 2018).

Beyond our Solar System, a large fraction of white dwarf stars have been reported to be surrounded by rocky debris (Zuckerman et al., 2010). It has been proposed that these debris fields had formed during the giant branch phases of stellar evolution, during which the stellar luminosity can exceed the Sun's by orders of magnitude. YORP-based rotational fission in these systems has been shown to easily fragment exo-asteroids, producing large debris fields (Veras and Scheeres, 2019).

Developments of YORP theory

The paper by Rubincam (2000) showed the importance that YORP has on the spin-state evolution of asteroids. However, in doing so, several assumptions were made in the interest of simplifying the scenario. The most prominent was the assumption that asteroids behaved as blackbodies, in reality asteroids have non-zero albedos and so the YORP effect will also have a reflective component to it. This has since been included in subsequent modelling software (Rozitis and Green, 2011).

Additionally, the shapes of the asteroids were approximated using spherical harmonic representations of the asteroids. YORP has been shown to be extremely sensitive to small scale surface topography (Statler, 2009), this makes the prediction of YORP difficult. As the models obtained by light curve inversion usually resolve structures spanning hundreds of metres, the smallest structures resolved by radar are usual of the order of tens of metres. Taking this sensitivity down to the centimetre to decimetre scale, shows how small scale structures on the surface of an asteroid are able to create a recoil force parallel to the surface. Due to the thermal conductivity of the boulders, under certain conditions this leads to a temperature gradient across the east-west direction of the boulder. This gradient produces a tangential thermal torque from the boulders which increases the asteroid's rotation rate, this effect is called tangential YORP or T-YORP (Golubov and Krugly, 2012; Golubov et al., 2014; Golubov, 2017; Golubov and Scheeres, 2019).

Numerical studies of T-YORP have been performed for simple geometries including:

a one-dimensional wall (Golubov and Krugly, 2012), and a spherical boulder (Golubov et al., 2014; Ševeček et al., 2016). These numerical studies have shown that the torques produced by T-YORP are comparable to the N-YORP torques, and therefore are an important factor in the evolution of an asteroid's rotation state. More complex scenarios are also being modelled. These are aiming to investigate the torque produced from irregular boulders, and effects of shadowing and self-heating for various arrangements of boulders (Golubov et al., 2019).

Further improvements to the modelling of YORP include the consideration of the small scale surface roughness of the asteroid and the self-heating that occurs within the concavities of asteroids Rozitis and Green (2011). The roughness of an asteroid's surface is able to alter the effective Bond albedo of the asteroid in addition to its thermal inertia. YORP is sensitive to the thermal-infrared beaming caused by the surface roughness, which causes significant damping of the rotational acceleration (Rozitis and Green, 2012). The effect of global self-heating on the asteroid's surface tends to produce an offset in the rotational acceleration when measured as a function of obliquity, the direction of the offset is opposite to the offset produced by the effect of shadowing (Rozitis and Green, 2013).

A related effect to YORP occurs within binary systems, this effect is called binary YORP or B-YORP. B-YORP acts to modify the orbit of a synchronously orbiting secondary, as the locked secondary is in essence an asymmetric appendage of the primary (Ćuk and Burns, 2005). The effect of B-YORP can lead to inward or outward migration of the secondary, which also decreases or increases the mutual orbit's eccentricity, respectively. Inward migration of the secondary contracts the orbit until it passes the stability limit, at which point the orbit will continue to contract until the secondary impacts the primary, forming a contact-binary asteroid. On the other hand, outward migration does not always to lead to the dissociation of the binary system. As the system separates, it is possible that the secondary enters a chaotic rotation state, from which, re-establishment of synchronous rotation in the opposite orientation is the

most likely outcome, which then leads to inward migration (Ćuk and Nesvorný, 2010). Hence, it is very unlikely that migration alone is capable of producing heliocentric asteroid pairs.

Current detections of YORP

The first direct detection of YORP was reported jointly by Lowry et al. (2007) and Taylor et al. (2007) on asteroid (54509) 2000 PH5, which was subsequently renamed YORP. (54509) YORP is a small (∼100m in diameter) NEA, that was discovered by the Massachusetts Institute of Technology's Lincoln Near-Earth Asteroid Research (LINEAR) project on 3 August 2000. The asteroid orbits with a semi-major axis of 1 AU, allowing annual monitoring of the target. Additionally, (54509) YORP has a fast rotation period of 12 minutes, making it conductive to observations with the aim of obtaining light curves as multiple rotations can be observed in a single hour.

An optical observing campaign monitored (54509) YORP for a duration of four years, beginning in 2001. Using the group of light curves observed between 2002 and 2003, Lowry et al. (2007) were able to determine a sidereal rotation period of 0.20290020 hours. This rotation period was subsequently set as the initial rotation period P_0 from which they searched for changes in the period of later light curves. The light curve sets were grouped together such that each group had a one year timebase, for each group a Fourier analysis was performed to determine the yearly averaged sidereal rotation period. These rotation periods are displayed in Fig. 1.12 as fractional changes from P_0, $\Delta P/P_0 = (P - P_0)/P_0$, from which they measured an increase in the asteroid's rotation rate of $(2.0 \pm 0.2) \times 10^{-4}$ °/day^2, or $(3.49 \pm 0.35) \times 10^{-6}$ rad/day^2 as it is more commonly reported now.

This YORP detection was confirmed in a twin paper by Taylor et al. (2007) using a different method, in which the utilisation of radar observations was crucial. These observations allowed the authors to create a model of the asteroid's three-dimensional

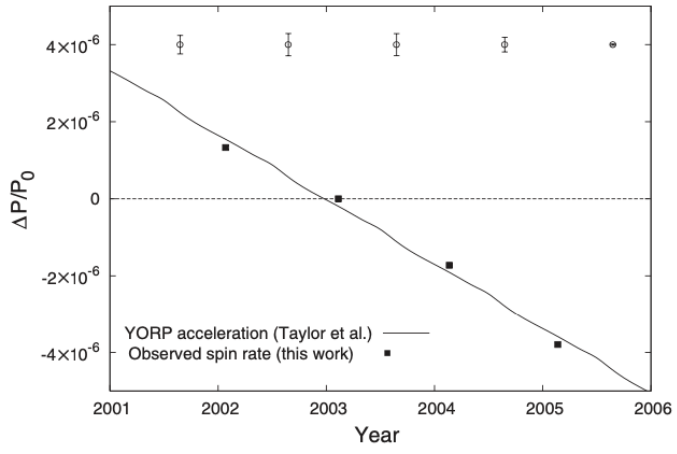

Figure 1.12: Measurements of the rotation period of asteroid (54509) 2000 PH5 over four years. Shown here as a fractional change in period $(P - P_0)/P_0$ marked by black squares. The black line is the numerical prediction of the YORP strength, while the dotted line displays the case of a constant rotation period. The open circles toward the top show the change in rotation period due to the close encounters with Earth (offset for clarity). *Reprinted from Lowry et al. (2007).*

shape. Which in turn, allowed the generation of synthetic light curves for each of the epochs of the observed light curves. By measuring the required offset in rotation phase to align the synthetic and observed light curves, they were able to detect a trend that confirmed the acceleration of the asteroid's spin-state by YORP. The phase offsets that were measured are shown in Fig. 1.13. The quadratic trend that is shown in the figure is the signature of YORP, arising from the linear increase in rotation rate produced by the continuous torque.

Figure 1.13: Rotation phase offset required to align the synthetic light curves with the observed light curves of (54509) 2000 PH5. Each cluster of light curves has their corresponding year labelled above them. The phase offsets are measured from the initial epoch which was set to 27 July 2001. The solid black line is a quadratic fit whose coefficient reveals the YORP strength acting on the asteroid . *Reprinted from Taylor et al. (2007).*

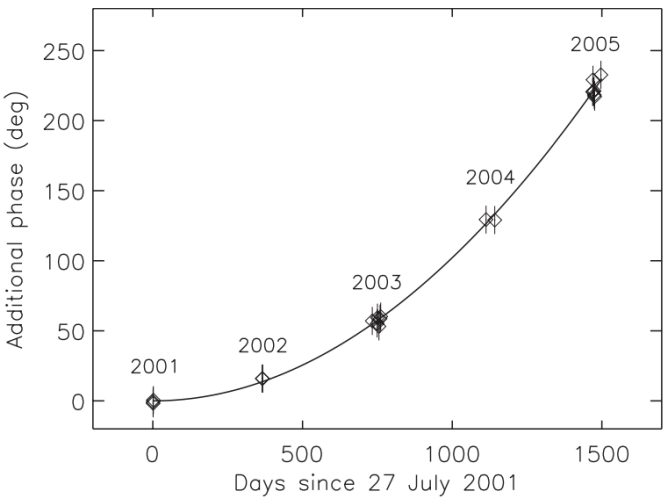

The focus of this thesis has been the observation of NEAs with the aim of determining their physical characteristics, particularly, their shape and spin-state. This work was undertaken with the aim of enabling the direct detection of a change in an asteroid's spin-state due to the YORP effect. Since the first detection of YORP, there have been detections for six more asteroids: (1862) Apollo (Kaasalainen et al., 2007), (1620) Geographos (Ďurech et al., 2008), (3103) Eger (Ďurech et al., 2012, 2018), (25143) Itokawa (Lowry et al., 2014), (161989) Cacus (Ďurech et al., 2018), and (101955) Bennu (Nolan et al., 2019). So, to date there have been seven detections of YORP, the aim of this thesis is to add to the number of those detections. My contribution to this number is a positive YORP detection for the asteroid (68346) 2001 KZ66 (Zegmott et al. [in prep], see Chap. 5). All of the detections to date, including the work of this thesis, are listed in order of YORP strength in Table 1.1, additionally the asteroids' spin-state and sizes are given. Curiously, all eight detections to date have been YORP accelerations.

In order to further improve YORP theory, it is important to continue to increase the number of detections of YORP and also, to publish YORP non-detections. These will help by providing a "ground-truth" from which YORP theory can be calibrated. Especially given the amount of indirect evidence of YORP and the lack of any spin-down detections, there ought to be more YORP detections that encompass both the spin-up and spin-down modes of YORP.

Asteroid	Period [h]	ν [$\times 10^{-8}$ rad/day^2]	d [km]	Pole [°]	Obliquity [°]	Reference
YORP	0.20283333(1)	$349 \pm 10\%$	0.113	(180, -85)	174.3	Lowry et al. (2007) Taylor et al. (2007)
Apollo	3.0654476(30)	$5.3 \pm 25\%$	1.4	(50, -71)	159.6	Kaasalainen et al. (2007)
Bennu	4.2960477(19)	$4.61 \pm 40\%$	0.492	(87, -65)	159.6	Nolan et al. (2019)
Itokawa	12.132371(6)	$3.54 \pm 11\%$	0.33	(128.5, -89.7)	178.4	Lowry et al. (2014)
Cacus	3.755067(2)	$1.9 \pm 16\%$	1.0	(254, -62)	143.2	Ďurech et al. (2018)
Eger	5.710156(7)	$1.4 \pm 43\%$ $1.1 \pm 55\%$	$\sim$1.5	(226, -70)	155.6	Ďurech et al. (2012) Ďurech et al. (2018)
Geographos	5.223336(2)	$1.15 \pm 13\%$	2.56	(58, -49)	149.9	Ďurech et al. (2008)

Table 1.1: All detections of YORP as of August 2020 in order of YORP strength. The table lists: Asteroid's name, rotation period (with uncertainty given in parenthesis), YORP strength (ν), diameter of a sphere of equivalent volume, pole orientation (λ, β), orbital obliquity, and reference to published work. All obliquities were calculated using the pole orienations determined by the authors and the best oribtal solution from JPL Horizons as of Jan 2020.

2 | Observations of near-Earth asteroids for YORP detections

In order to understand the formation of our Solar System, it is crucial to probe the secrets that asteroids can reveal to us. To do so, we need to understand their physical nature, distribution, formation mechanisms, as well as their evolutionary processes. This includes determining their sizes, shapes, and rotational properties. There are many different available data sources that can reveal these characteristics: optical photometry, remote sensing disk-resolved images, space missions, stellar occultations, interferometry, radar, and thermal infrared spectra.

The most valuable source of data when characterising asteroids are space missions, such as the Hayabusa sample return mission to (25143) Itokawa or the ongoing sample return missions Hayabusa 2 to (162173) Ryugo and OSIRIS-REX to (101955) Bennu (Fujiwara et al., 2005; Yoshikawa et al., 2014; Lauretta et al., 2017). With their suite of instruments, these in-situ observations allow us to produce extremely detailed models of the asteroid visited, however, missions like these are costly which severely limits the number of asteroids that can be investigated in this manner. Ground based observatories, although they are unable to resolve asteroids, are able to monitor thousands of asteroids per year. Additionally, decades worth of archival data is also available. Ground-based optical observations are by far the most abundant data source, particularly, photometry. Perhaps then, it is no surprise that the majority of data used in this

thesis is optical photometry data.

This chapter will therefore discuss the sources of data used in this thesis: light curves and radar observations. As such, an overview of asteroidal light curves will be given, starting with the facilities used to obtain them to the method utilised to extract them. The chapter will detail the planning required to obtain optical observations of asteroids and the steps required to processes the images, in addition to the considerations that must be made when observing the asteroids. This chapter will also give an overview of asteroidal radar observations, detailing the radar facilities from which data has been used in this thesis and the types of observations. Finally, an overview of the formatting required of the data to be understood by the software will be given.

2.1 Photometric light curves of asteroids from optical imaging

2.1.1 Overview of optical light curve observations

Although not the most detailed type of observation when trying to probe the shape and structure of asteroids, photometry, as previously mentioned, is by far the most abundant source of data. A sequence of photometric measurements of an asteroid that covers a full or partial rotation, a light curve, can be utilised to determine its rotational properties. When multiple light curves are combined which cover a range of aspect angles, the angle between the asteroid's pole and the sub-observer point, we can use convex inversion techniques (discussed in detail later in Sect. 3.1) to produce a convex hull of the shape that will reproduce the light curves. By combining photometric light curves with other data sources, such as radar observations, we are able to develop much more detailed models of an asteroid.

The majority of photometric data that is used in this thesis, was obtained through the ESO Large Programme and its auxiliary campaigns at a range of facilities. We also

make use of lightcurves publicly available from the LCDB. The LCDB collects and stores formatted light curves for over 14700 objects on their site which is hosted by the Minor Planet Center (Warner et al., 2009).

2.1.2 ESO Large Programme and supporting campaign

The ESO LP, lead by PI Prof. Stephen Lowry, is a long-term campaign to photometrically monitor a large sample of NEAs that are strong candidates for YORP detections. The aim of the overall programme is to detect YORP-induced rotational period variations of NEAs so that we may constrain the physical and thermal properties that determine the strength of the YORP effect (Taylor et al., 2007; Lowry et al., 2007, 2014). This programme and its supporting campaigns are the source of the vast majority of the data used in this thesis. Since its inception in April 2010, a selection of over 40 asteroids have been monitored via this programme. The objects that are selected fulfil three conditions that make them likely candidates to experience YORP accelerations: they orbit close to the Sun, are of small sizes, and have short rotation periods. Their short rotation periods allow us to obtain full coverage of the rotation phase over a few nights of observing.

Observatories used in the Large Programme

New Technology Telescope – The 3.58 m New Technology Telescope (NTT), which saw first light in March 1989, was built to demonstrate new technology. The telescope pioneered Active Optics and also had a new revolutionary enclosure (Tarenghi and Wilson, 1989). It has a thin monolithic mirror that has over 70 actuators that adjust the primary mirror to maintain an optimal reflective surface that accounts for the deformation of the mirror at different pointings and for the inhomogeneities of the air temperature in the dome.

The NTT has an altitude-azimuth mount and hosts two Nasmyth foci. At the time

Figure 2.1: A view of the NTT, La Silla Observatory, Chile taken in October 2018. Picture taken by T. Zegmott during an observing run in Oct 2018.

of writing, two instruments are available on the NTT. However, only one was used in our programme, the ESO Faint Object Spectrograph and Camera - version 2 (EFOSC2) a 2048 x 2048 CCD with a 4.1' x 4.1' field of view and pixel scale of 0.12"/pix mounted at Nasmyth B (Buzzoni et al., 1984). This instrument has a large variety of filters, grisms, and slit that can be combined to observe in multiple configurations.

Very Large Telescope – The Very Large Telescope (VLT) consists of four 8.2 m Unit Telescopes (UTs) that can work together as an interferometer or individually. Each of the four UTs has a monolithic primary mirror that is equipped with Active Optics and is capable of hosting three instruments: one at each of the Nasmyth foci and another at the Cassegrain focus (Gray, 2000) The instrument of interest to the ESO LP is the VLT Imager and Spectrometer for mid-Infrared (VISIR) mounted at the Cassegrain focus of UT3, which is named Melipal (Lagage et al., 2004). A single

1024x1024 CCD instrument that has multiple objectives: the small field with a 38' x 38' FOV and 0.045"/pix pixel scale, and the intermediate field with a 1' x 1' FOV and 0.076"/pix. Another instrument used in the programme was the VIsible MultiObject Spectrograph (VIMOS) (Le Fèvre et al., 2003), which is made up of four 2048 x 2440 CCDs each with a field of view of 7' x 8', 0.205"/pix pixel scale, and each separated by 2'. It was mounted at Nasmth B of UT3, however, this instrument is now decommissioned.

Observatories used in auxiliary campaigns

Isaac Newton Telescope – The Isaac Newton Telescope (INT) has a 2.54 m primary mirror and has an equatorial mount. Having originally started operations at what was then the Royal Observatory in Herstmonceux in 1967. The INT was later moved and underwent significant changes so that it could operate in its new location at the Observatorio del Roque de los Muchachos (ORM), La Palma, Spain. Amongst other things that were changed and upgraded, the mount in particular needed to be adapted for the latitude of the INT's new home. These modifications were completed and the telescope resumed operations in 1984.

The INT has three focal stations: the Prime focus which houses the Wide Field Camera (WFC), the Cassegrain focus with the Intermediate Dispersion Spectrograph (IDS), and the Coudé focus which has never been used. The WFC is the only instrument used by the ESO LP with its four 2154 x 4200 CCD mosaic large field of view, 34' x 34', and 0.33"/pix scale(Ives et al., 1996).

Nordic Optical Telescope – The Nordic Optical Telescope (NOT) is another 2.56 m class telescope also located at the ORM, La Palma, Spain. Its has altitude-azimuth mount, which allows it to be tightly enclosed by its dome. The instrument Alhambra Faint Object Spectrograph and Camera (ALFOSC), mounted at the Cassegrain focus (Aspin, 1998). This instrument has a 2048 x 2064 CCD with a 6.4' x 6.4' field of view and 0.214"/pix scale in imaging mode, additionally it can be used

Figure 2.2: An image of the author and Isaac Newton Telescope at the Observatorio del Roque de los Muchachos. Picture taken by T. Zegmott during Isaac Newton Group Support Astronomer studentship in March 2018.

for low resolution spectroscopy, and also has a polarimetry mode. However, only the imaging mode was used to gather data for this thesis.

Palomar Observatory: Hale Telescope – The 200-inch (5.1 m) Hale Telescope is located in California, USA on the Palomar mountain range. This telescope combined new technologies that allowed it be the world's largest telescope for 27 years from its commissioning in 1949 until 1976. Its large mirror was mounted on a horseshoe equatorial mount. The telescope has an optical wide-field camera, the Large Format Camera (LFC) (Gunn et al., 1987). This instrument is a mosaic of six 2048 x 4096 CCDs that is mounted at the prime focus of the telescope, it has a field diameter covering 24' and a pixel scale of 0.18"/pix.

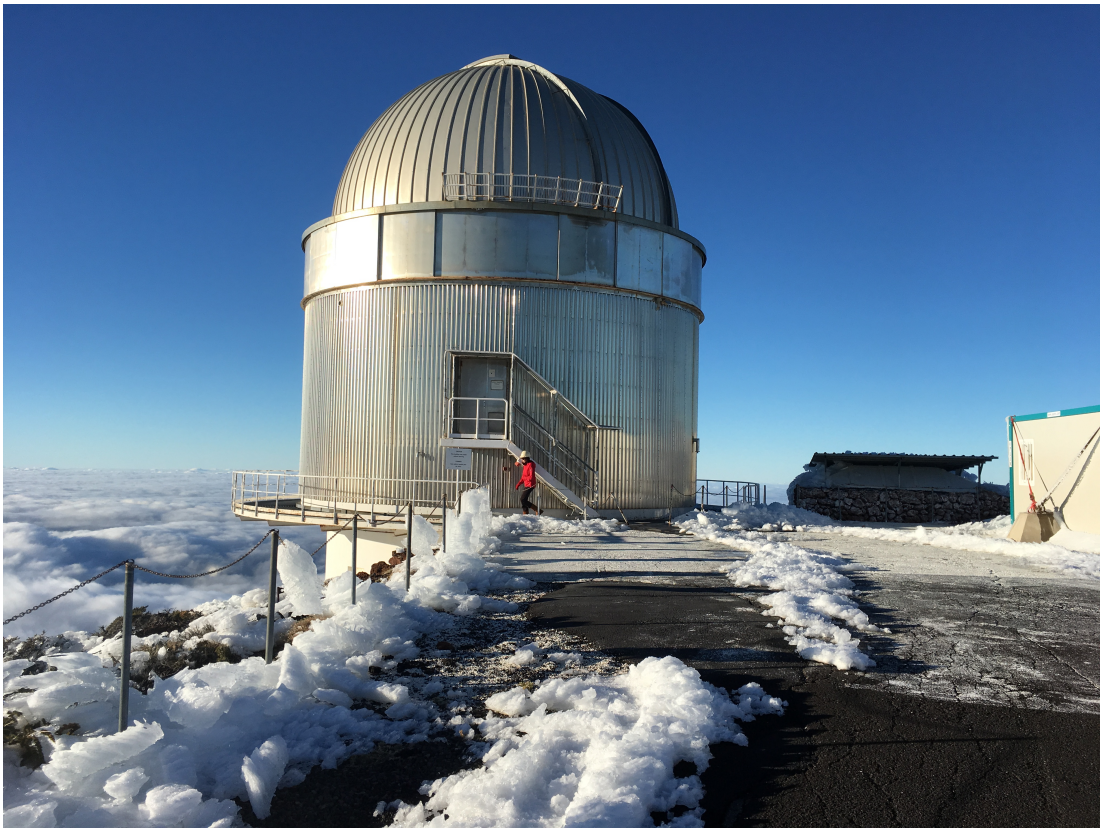

Figure 2.3: An image of the Nordic Optical Telescope taken after a night of bad weather and wintery conditions. Picture taken by T. Zegmott, February 2018.

Liverpool Telescope – The Liverpool Telescope is a 2 m fully robotic telescope located close to the INT at the ORM, La Palma, Spain. This telescope has an alt-az mount and is able to mount up to nine instruments at the Cassegrain focus, one in the straight-through position and eight more mounted on side ports which are accessible by a rotating tertiary mirror. Our programme used the now decommissioned RATCam an optical camera, a 2048 x 2048 CCD with a 4.6' x 4.6' field of view and 0.135"/pix pixel scale (Steele, 2001).

2.1.3 Observation planning and image acquisition of NEAs

The preparation work to observe NEAs starts long before arriving at the telescope. There are a variety of extra considerations to make when planning the observations of moving objects compared to stationary objects. As asteroids do not emit their own

Figure 2.4: An image of the Liverpool Telescope at dawn, taken after a long night's observing. Picture taken by T. Zegmott, June 2018.

light but reflect and re-emit that of the Sun, their position relative to that of the Earth around the Sun is important when planning observations. The angle between the Sun-Earth-object system is called the solar elongation. Generally, observations are not made below a solar elongation of $\sim 75°$. Below this angle, asteroids that are observable only appear close to the horizon, at high air masses, and are not observable for long. In order to select times when the asteroid would be in geometrically favourable parts of its orbit we create geometry plots. These usually consist of parameters such as heliocentric and geocentric distance, orbital phase angle, solar elongation, visible magnitude, right ascension and declination plotted against time. An example of such a plot is shown in Fig. 2.5(a). For the purpose of determining which observatory to observe the asteroid with, our attention turns to the plots showing the visible magnitude and declination. The visible magnitude will indicate the size of telescope required and the declination will limit the latitudes on Earth from which the asteroid could be observed, narrowing

down the choice of suitable telescopes.

Once a list of potential telescopes has been chosen, the observability of the asteroid can be further investigated. For each of the observatories, the object's airmass each night for each site over the dates that it is observable is plotted. Although it is known that the asteroid is observable, it is important to determine how long the asteroid will be visible each night. This step is important in order to informatively choose nights that maximise the length of time that the asteroid will be in the sky. These airmass plots are also of use within an individual night when observing multiple objects, they assist in establishing the order in which the object should be observed. An example of an airmass plot is shown in Fig. 2.5(b).

The preparation up to now has been about selecting which telescope should be chosen to observe NEAs of interest. Planning of the order in which to observe the asteroids was touched on when talking about airmass plots. Another step to inform the order of observations is the creation of finder charts. Primarily, these will help locating the asteroid once some images have been acquired, but they can also be useful when choosing the order to observe asteroids in as they show us when the asteroids will make star passages. Star passages can be difficult to handle and in most cases usually result in the image not being used. This can be avoided by planning observations such that they are avoided. An example finder chart can be seen in Fig. 2.5(c).

An important decision to make when imaging asteroids is choosing the exposure time for the images. For all objects in the sky it is important to make sure that the chosen exposure time is such that your object of interest will have a sufficient signal-to-noise in the images. Each telescope will usually provide a tool on their webpage to calculate this. These tools take in to account factors such as the object's brightness, the sky conditions, the filter used, and of course the instrument used too. Asteroids come with unique considerations in this regard, as they are moving and rotating objects. An exposure time for an asteroid has the additional constraint that the exposure time is set to be below 5% of the asteroid's rotation period in order to resolve light curve

features. The asteroid is also in continual motion through the sky, so if the exposure time is too high the asteroid or stars will trail in the image. Generally, an exposure time that contains the motion of the asteroid within the seeing disk is chosen.

Depending on the asteroid's rates of motion, there are two ways that the telescope can track the asteroid as it move through the sky. If the asteroid is moving slow enough that it's motion can be contained in the seeing disk for the selected exposure time a sidereal tracking rate can be used. This moves the telescope at the same rate that the stars move across the sky by accounting for the Earth's rotation. However, if the asteroid's motion is fast enough that the asteroid would trail outside of the seeing disk, then the telescope can be set to track differentially. The telescope can be set to move at the rate that the asteroid moves through the sky so that the asteroid appears stationary and the stars appear to move. To ensure correct tracking the asteroid's position and rates of motion are periodically updated throughout the night using values from an ephemeris. In some cases, the motion of the asteroid can be larger than the field of view of the telescope, in such cases it is important to plan the observations such that there are common stars between the changing fields. Lastly, it is good practice to dither between images. This process involves making small adjustments to the pointing of the telescope, this allows for stationary pixel artefacts to be removed when stacking images. It is also useful in case the object of interest falls on an artefact that isn't removed during the post-processing of the images. If tracking differentially, this would lead to the asteroid falling on bad pixels in all frames!

2.1.4 Post-processing of CCD Images

Since the 1980s, Charge Coupled Devices (CCDs) have become the standard detector used in observational astronomy and have revolutionised the practise. A CCD is composed of an array of photo-sensitive pixels that collect photons. As a photon strikes the pixel, it interacts with the silicon surface, exciting and releasing an electron. As these electrons are produced, they're stored in the pixel until the end of the image exposure.

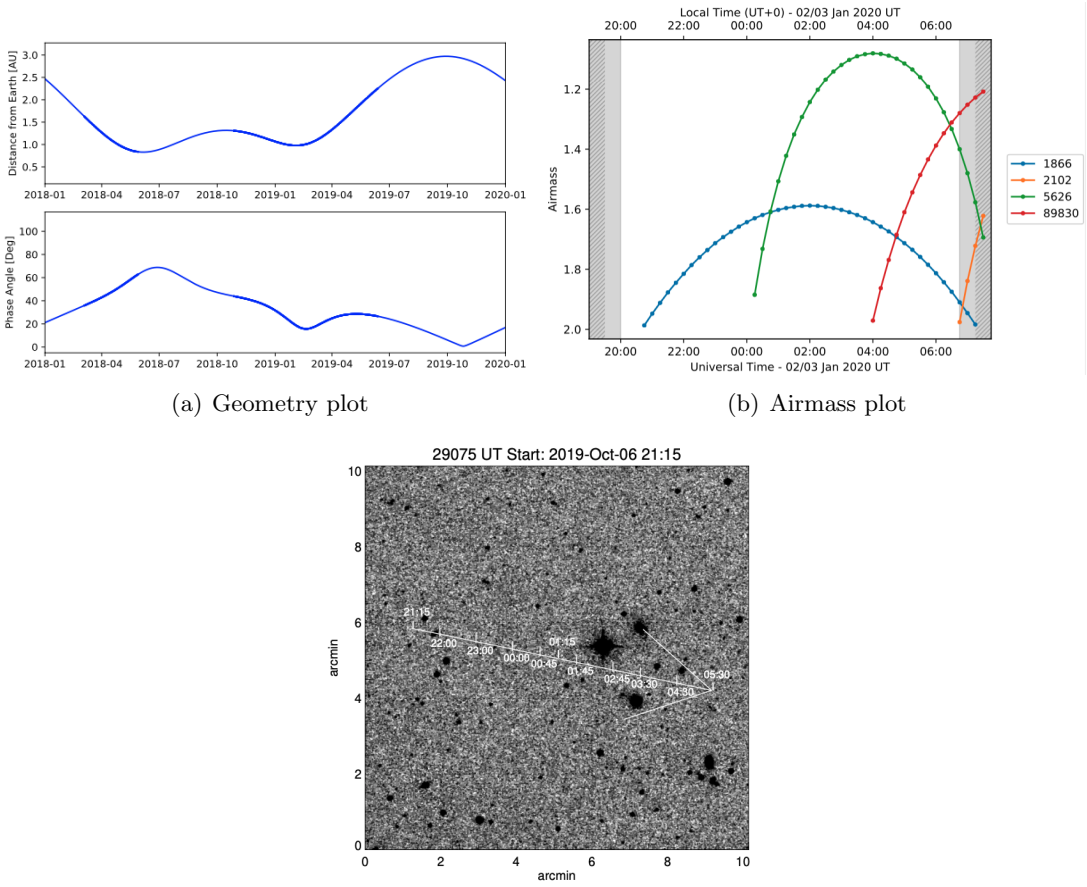

(a) Geometry plot

(b) Airmass plot

(c) Finders' chart

Figure 2.5: Collection of figures generated in preparation of observing an asteroid. Sub-figure a) is an excerpt of a geometry plot for the asteroid (68346) 2001 KZ66 plotted between the years 2018 and 2020. This figure shows the asteroid's geocentric distance and orbital phase angle during this period with the solid blue line, the bold parts of the line correspond to the times when the asteroid's solar elongation is larger than 75°. Sub-figure b) shows the airmass of four asteroids at the ORM for the night of 2 January 2020. Sub-figure c) is a finder chart for the asteroid (29075) 1950 DA on the night of 6 October 2019 observed from the INT using a 10' x 10' window.

At which point the CCD is read-out by transferring the charge column-by-column to the edge of the CCD where the pixels are read individually and the packet of electrons held by each pixel is converted from an analogue quantity to a digital value (ADU) that is proportionally related to the number of photons. Once the CCD has been fully read, the ADU value for each pixel is written to an array, resulting in the raw image.

2.1.4.1 Data Reduction

Data reduction is a necessary stage in the processing of astronomical images as they are not immediately ready for measurements after they've been obtained. Within a raw image there remain artefacts from the electrical noise when reading out images, from the non-uniform optical path of the telescope, as well as other sources. The procedure to correct all of these artefacts are well known and have been described in much detail by many, such as Berry and Burnell (2005). There are several steps involved in this process: bias subtraction, flat-fielding, de-fringing, dark correction, cosmic ray removal, and the correction of bad pixels. It is important to collect calibration images while at the telescope to correct each of these, which are all discussed in detail below. Unless stated otherwise, all data reduction for this thesis was performed by the author.

Bias Corrections – The bias is caused by a constant voltage being applied across the CCD detector. Ideally, it should appear as a constant value added across the whole image. But in reality, it is non-uniform due to noise. Bias images can be obtained by taking images with a zero second exposure time. Several of these images are taken so that they can be averaged together to make a "master bias" image. The effect of the bias on images is additive and so to remove this the master bias is simply subtracted from each of the flat and science images.

Dark Corrections – Even when left in complete darkness, CCDs will accumulate electrons that will be interpreted as photons falling on the detector. This is actually a temperature effect, as electrons can be thermally excited and released in the pixels that make up the detector, this is the dark current. The amount of electrons thermally excited will depend on the amount of time that the image is left to expose for and so the exposure time of these frames are set to match those of the science images. If this was not the case, they can also be scaled to match the exposure time. Like the biases, this effect is additive and so a master frame can be created in the same manner and

subtracted from the science images. However, in professional telescopes the detectors are usually cooled well below zero degrees and so the thermal current in these detectors are usually negligible and so this step can often be ignored.

Bad Pixel Corrections – Each of the pixels in a CCD camera have their own characteristics. Over time the CCD will degrade, this can lead to some of the pixel being either over- or under-sensitive to light, appearing as light or dark spots in the images. These artefacts in the image are easily removed by interpolating across the bad pixels. This can be done either manually or with the use of a pixel map, sometimes provided by the observatory. Care must be taken, when dealing with bad pixels that lay over objects of interest, however, it is best to plan the observations such that this does not occur. Note that this step is not always required, for example, if there are no obvious defects in the image.

Flat Field Corrections – All the pixels making the CCD surface are similar, but not identical. They will all have slightly varying sensitivity to light, i.e. some will convert photons to electrons more efficiently than others. There will also be variation in the path that light takes to reach each of the pixels due to dust that has collected on the mirrors and filters. The result of all of these effects is that an image of a uniformly illuminated source will appear to be non-uniform in the image taken by the CCD. This effect can be corrected by taking several images of a uniform source, a *flat field*. A uniform source could be either an evenly illuminated section of the inside of the dome or a clear twilight sky. These images normally vary in the average number of counts and so must be scaled before they can be combined together using the median average, which is used as it is much less susceptible to skewing from anomalous values. Once they have been median combined they are normalised. This master flat field image is a map of the sensitivity variation across the detector. The science images are then corrected by dividing them by the normalised master-flat.

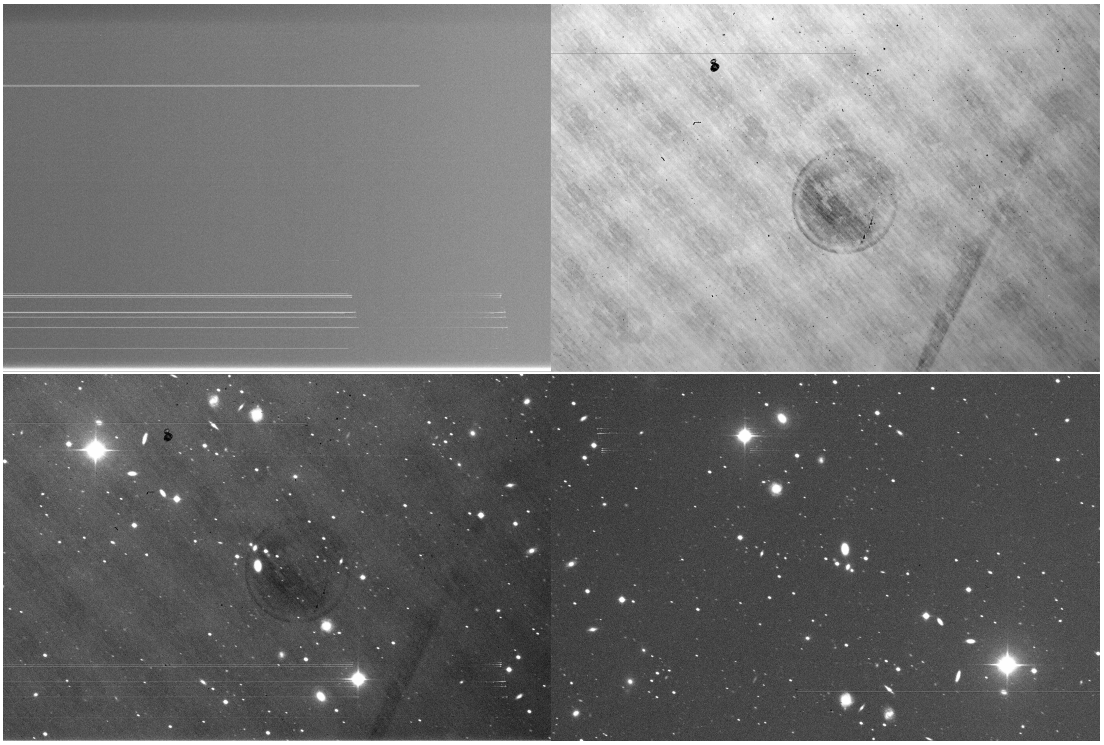

Figure 2.6: **Top Left:** Master bias image. **Top Right:** Master flat image. **Bottom Left:** Raw science image. **Bottom Right:** Reduced science image. These images were taken by Lord Dover on the INT, 6 October 2019. The instrument used was the WFC with the Harris V-band filter.

Fringe Corrections – CCD images can often be affected by fringe patterns, typically for narrow-band filters but also for broad-band filters which contain strong sky emission lines. Fringing is caused by constructive and destructive interference of light that is reflected between the back and front surfaces of the CCD several times before finally being absorbed. Fringes add only a small amount of flux to the image, but it is important to remove them to obtain uniform photometry across the frame. As they are caused by the sky emission lines, dome and twilight flats cannot be used to remove these. Instead, fringe maps must be created from deep exposures of a sparse field taken during the night. The intensity of the fringes depend on the amount of flux collected from the sky, they differ depending on the conditions of the sky and the exposure time in each image. The fringe map must be scaled to match the intensity of the peaks and troughs in each image. However, the pattern of the fringe is a function of the thickness of the CCD and so should be fixed. Once the fringe map has been scaled for an image

it can simply be subtracted from the science images to remove the fringes.

Images from the NTT's EFOSC2 instrument taken with the R Bessell filter were the most affected by this. For these datasets a fringe map was provided for the instrument from the ESO website, in addition to this, Snodgrass and Carry (2013) created an automatic fringe correction tool which was used to correct these images. The tool automates the process using control pairs to determine the amplitude of the fringe in each image which in turn are used to scale the fringe map before subtracting it.

Cosmic Rays Corrections – Cosmic rays are high-energy particles that lose their energy by interacting with the atoms of the CCD. This high-energy interaction excites many electrons, which appears as a sharp bright spot in the image. When cosmic rays appear with the photometric aperture of an object of interest, it must be removed. This can be done in a similar manner to the removal of bad pixels, however, due to the nature of cosmic rays this can't be done automatically with a map. The most reliable way is to mark out the regions effected by them manually in each image and interpolate across them.

2.1.4.2 Relative photometry of asteroids

Once the images have been reduced and the artefacts have been removed, the images are ready to be processed for light curve extraction. The fundamental concept of light curve extraction requires a measurement of the brightness of the asteroid and background stars in a series of images. Simply measuring the brightness of the asteroid in each image will build up the raw rotational light curve. Since the asteroid is in orbit around the Sun, its motion in the sky is much larger than the stars that make up the celestial sphere, which have such a small proper motion that they can be assumed to be stationary. The asteroids have to be manually located in each image, and the position given to `IRAF` in order to measure its brightness. For large numbers of images this can be time consuming and tedious, even more so if the user has to type the same command

repeatedly. The analysis between datasets can vary greatly, therefore it is not easy to create a one-size fits all program to extract light curves. With this is mind, a modular approach to this process was taken.

The first step is to mark the positions of the asteroid and several background stars in each image. This stage can be very time consuming, especially when handling large datasets with hundreds of images per night. In order to locate the asteroid at the beginning of the image sequence, a finder chart can be used by locating the backgrounds stars that surround the asteroid's predicted path. Or a more rudimentary method is to simply blink a series of images aligned on a star and look for the moving object. Care must be taken with the latter approach to make sure that the correct asteroid is selected, as it is possible that there may be more than one in the field. The background stars chosen should be brighter than the asteroid and spread throughout the field. However, they should not be so bright that they saturate the CCD. Blooming in an image is an indication that a star is heavily saturated. As the pixels the star falls on fills up the charge starts to fill adjacent pixels creating streaks leading away from the star. Not all saturated stars are so easy to spot, so if there is doubt as to whether or not a star is saturated use a tool such as `IRAF`'s `imexamine` to plot a photometric profile. The profile of a saturated star has a plateaued top rather than curved as expected. The reason that saturated stars, or even those close to saturation, are not used in photometry is because they enter the non-linear response region of the CCD. In this region the charged induced in the pixels is no longer proportional to their illumination. It is best to select as many suitable stars as possible at this stage, as if a star is later found to be variable, it must be rejected.

Marking so many stars per image in the same order done completely manually would be an error-prone process. To ease and accelerate this process partial marking of the stars was automated with a script. This script functioned by marking the background stars in a reference image. Typically, this was chosen to be the first image of the sequence, following the selection of stars the user would then be required to mark only

the first star in all of the images. The shift required to align the first star with its position in the reference frame would then be calculated so that the position of all stars in the frame could be obtained by applying that shift to their coordinates in the reference frame. The positions of all of the stars could then be overlaid on the image to ensure that they were correctly calculated. An example of this is shown below in Fig. 2.7.

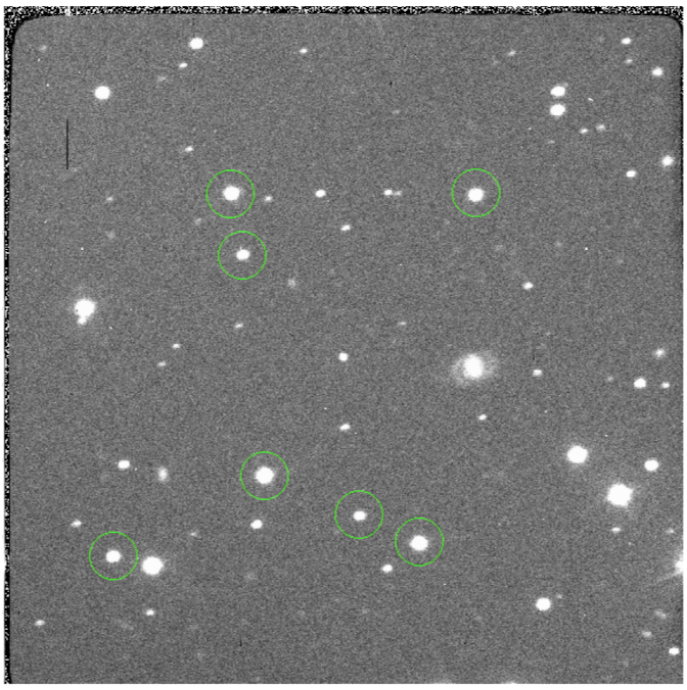

Figure 2.7: This figure shows the marking of background stars for one image in a sequence taken on 28 January 2019 of asteroid (68346) 2001 KZ66. The seven green circles highlight the stars chosen to perform the differential photometry, the sizes of the apertures were set to a fixed size of 30 pixels.

Asteroids and stars observed with ground-based telescopes appear as point sources. However, during the light's passage through the atmosphere and telescope's optics the light is dispersed. The light will be spread over multiple pixels, and the degree of spreading is described by the Point Spread Function (PSF). A cut through a well sampled source reveals that the PSF has a Gaussian shape (see Fig. 2.8). The measurement of the width of a point source at the point were its intensity is at 50% of the maximum, Full Width at Half Maximum (FWHM), is a straight forward way to characterise the PSF. The minimum FWHM possible is determined by diffraction and is inversely proportional to the telescope's diameter. This would be for an image taken without the Earth's atmosphere. However, all ground based telescopes suffer from atmospheric blurring, otherwise known as seeing. The seeing can be measured by converting the

FWHM from pixels to arc-minutes, and is generally used as an indicator of the image quality. The effects of this atmospheric blurring increase as the light travels through more of the atmosphere, this is part of the reason why telescopes are built on high altitude sites.

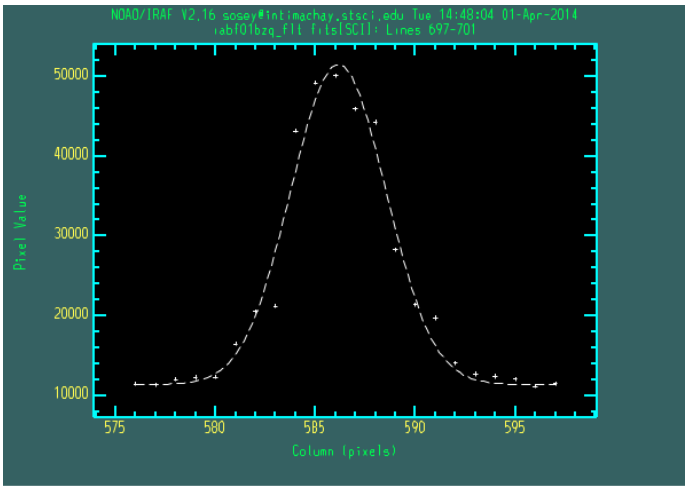

Figure 2.8: This figure is the measurement of a star's Point Spread Function (PSF). It shows the pixel values for a constant row across several columns. The Gaussian shape, which appears like a bell, it typical of point source objects that are not saturated. The Full Width at Half Maximum (FWHM) of the star can be determined by measuring the width of this PSF at half of the maximum value, in this case a pixel value around 30,000.

All photometry in this thesis is performed using `IRAF` (Tody, 1986). The photometry procedure used, `phot`, calculates instrumental magnitude following Eqn. 2.1. An aperture defines the area within which the object's brightness is calculated, a variety of different shapes can be used to describe an aperture. However, the apertures used for the photometry in this thesis are all described by circles, their radius set to a multiple of the FWHM of the asteroid in the image. Multiple apertures were used in the photometry performed within this thesis, these were $\times 1$, $\times 1.5$, $\times 2$, and $\times 3$ of the FWHM. Each of these apertures were inspected, with the best signal-to-noise aperture size being applied to the entire set of images – usually this was $\times 1.5$ but varies for some datasets. An example of an aperture can be seen in Fig. 2.7, where apertures are used to mark the background stars.

$$m_i = m_{zp} - 2.5 log_{10} \frac{I}{t_{exp}} \tag{2.1}$$

where:

m_i	instrumental magnitude of the targeted object,
m_{zp}	zero-point magnitude - for relative photometry this is arbitrarily chosen and kept the same throughout the dataset,
I	total counts of the object recorded within the aperture in ADUs,
t_{exp}	exposure time of the image in seconds.

The total flux, I, accounts for the sky background counts. An annulus with the inner radius larger than that of the aperture is used to determine the average background counts per pixel. When the sky is subtracted from the number of counts with in the aperture, it is scaled by the area of the aperture. Each measurement of the instrumental magnitude will also have a corresponding uncertainty. The `phot` procedure defines this uncertainty as given by Eqn. 2.2.

$$\Delta m_i = \frac{1.0857}{I}\sqrt{\frac{I}{g} + A\sigma^2 + \frac{A^2\sigma^2}{n_{sky}}} \tag{2.2}$$

where:

Δm_i	error in the instrumental magnitude,
g	gain of the CCD in electrons per ADU,
A	area of the aperture in square pixels,
σ	standard deviation of the sky pixel value,
n_{sky}	number of sky pixels in annulus.

The raw magnitudes obtained at this point will not be ready to be used for the light curves as they contain variations in them due to the observing conditions. Conditions such as the change in airmass as the telescope tracks the object throughout the night, or any temporal changes in the weather conditions like passing cirrus clouds. To account for the changing conditions the background stars are used as a reference, as the stars should have a consistent brightness throughout the dataset. By looking at the frame-to-frame changes in their instrumental magnitudes, the temporal changes can be corrected for the asteroid.

For each night of images a reference frame is chosen, typically this is the first image in the dataset. The instrumental magnitude of each background star is compared with their corresponding instrumental magnitude in the reference frame for each of the images. The magnitude shifts of all the background stars should all vary in the same way, if this is not the case this could be due to a cosmic ray falling on the star. In that case, the star can be temporarily ignored for that frame. Or, if one star's magnitude shifts consistently varies from the others in multiple frames, this could be an indication that the star is variable. In which case, the variable star should be removed in all frames. All of the magnitude shifts are then combined to determine the weighted average magnitude shift, $\bar{m_s}$. They are combined following Eqn. 2.3 and are weighted by the inverse squared of their magnitude error. By using the magnitude shift of the background stars as opposed to their instrumental magnitude, it is possible to easily combine both faint and bright stars. It also allows the changing of background stars part way through the night, should the tracking of the asteroid require a change of field.

$$\bar{m_s} = \frac{\sum_j w_j m_j}{\sum_j w_j}; \qquad w_j = \frac{1}{\sigma_j^2} \tag{2.3}$$

where:

$\bar{m_s}$ average magnitude shift of the stars in one frame,

w_j weight of the magnitude shift of the j-th star,

m_j magnitude shift of the j-th star,

σ_j error of the magnitude shift of the j-th star.

The average shift in magnitude of the background stars is then subtracted from the magnitude of the asteroid. These corrected magnitudes for the asteroid are the values that are used for the final light curve. Although these are not absolute magnitudes, these relative light curves show how the magnitude of the asteroid changes through out the night. Which is sufficient for the purpose of shape and spin-state modelling of asteroids.

Finally, in some cases, the asteroid may not be bright enough to obtain a clean light curve with an adequate signal-to-noise ratio. In those cases, it can be necessary to stack frames. The frames would be grouped into sets to be stacked and they would be added in two ways. For the first series, the frames would be aligned on the asteroid so that it falls on the same location in all frames, then grouped sets of frames would be summed. The asteroid's instrumental magnitude would be calculated using these images. In the second series, the stars are aligned in each of the frames and summed. The photometry of stars is performed using this series of images. The photometry is performed in exactly the same way as previously described for both series of images. However, the observation time for the summed images must be carefully calculated using the exposure times of the sets of images stacked together. Unless stated otherwise, all light curves extracted for this thesis was performed by the author, included the re-extraction of published light curves where the data could be obtained.

2.2 Radar observations

2.2.1 Overview of radar observations

Radar is a unique type of observation, in that the illumination of the object is under human control. Where all other techniques rely on passive observation of a reflected or naturally emitted radiation, the transmitted signal used in radar uses a coherent illumination with a chosen frequency and polarisation. This manipulation of the illumination source enable radar observations a resolved glance of an asteroid's morphology. This is an important factor in helping to determine the YORP acceleration that an asteroid may be experiencing. This thesis uses radar observations to compliment the light curves in search of YORP.

The basic strategy when observing asteroids with radar is to measure the intensity of the transmitted signal reflected off the asteroid in both time delay and Doppler frequency. The monochromatic wave will experience Doppler shifting as the wave meets the proceeding and receding limbs of the rotating asteroid, altering the reflected signal's wavelength. In addition, a delay in the signal will be detected due to the difference in time taken by the radio wave to reach different parts of the asteroid's surface. The resolution of the delay can be measured down to decimetre scales, but is dependant of the wavelength of the signal. The returning wave is recorded and processed by Fourier transform to obtain the delay-Doppler image or Doppler spectrum. Both types of radar observations are discussed further and in more detail later in this section.

Radar observations of nearby passing NEAs with sufficient rotation phase coverage can be used to determine the asteroid's rotation state and also to construct a detailed shape model. This has been performed for many asteroids to date, some examples include: (4769) Castalia, (8567) 1996 HW1, and (89830) 1999 JV6 to name a few (Hudson and Ostro, 1994; Magri et al., 2011; Rożek et al., 2019a). The accuracy of radar models becomes more apparent when looking at asteroids which have since

been visited in situ. This is highlighted when comparing radar and in-situ models for asteroids such as (25143) Itokawa and (101955) Bennu (Ostro et al., 2004; Nolan et al., 2013).

The reflected echo power is measured in both polarisations, in the opposite sense (OC) of the circular polarisation that was transmitted and in the same sense (SC) - this can be seen in Fig. 2.9. If the target object had no structure at the wavelength scale (between centimetres to a decimetre for Arecibo and Goldstone facilities), mirror-like backscattering would mean that the SC component of the echo would be missing. The SC echo becomes more important when the near-surface structure of the asteroid is at the wavelength scale or when multiple scattering occurs. By comparing the intensity ratio of these two polarisation components the circular polarisation ratio, SC/OC, can be determined. This ratio reveals insights into an asteroid's near-surface structure at scales near the wavelength.

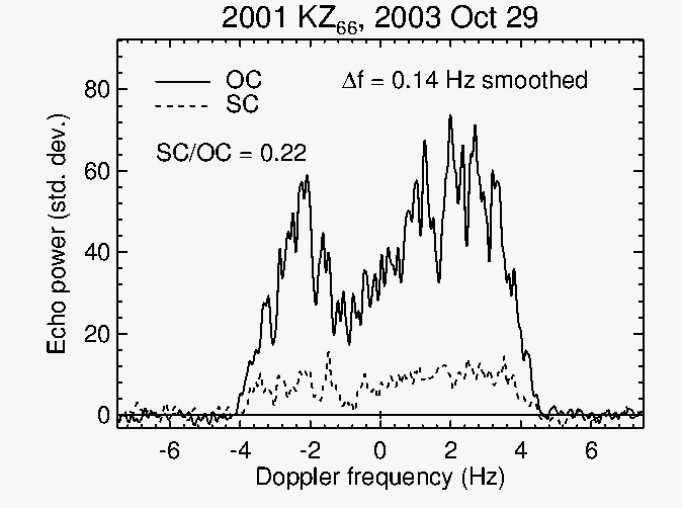

Figure 2.9: A continuous wave spectra of the asteroid (68346) 2001 KZ66 taken on the 29 October 2003 at Arecibo Observatory. The echo power was recorded in both polarisations: same sense (the dotted line) and opposite sense (the solid line). The spectrum was smoothed using frequency bins of 0.14 Hz.

A radio telescope requires physical manipulation to change between transmitting and receiving modes. The amount of time to switch is influenced by the observer, but is usually on the order of tens of seconds. The integration time of images needs to account for the time it takes to switch between modes. Additionally for close passing NEAs, the integration times will be limited by the time taken by the transmitted signal to reach the asteroid and return, this is called the round-trip time (RTT), when

observing with a single dish. However, by using two telescopes this limitation can be over come, one telescope is used to continuously transmit while the other is receiving. This mode of observations is called bi-static observing.

In this thesis, pre-processed radar data was provided by our collaborators which was co-added by the author to improve the signal-to-noise ratios of the datasets. This data was then also fully modelled by the author. The provided data originated from two telescopes:

Arecibo Observatory – The William E. Gordon radio telescope at the Arecibo Observatory in located in Puerto Rico (Altschuler and Salter, 2013). The telescope has a single 305 m aperture, for more than 50 years it was the world's largest single-aperture telescope until the completion of the Five hundred metre Aperture Spherical Telescope (FAST) in southwest China. The 540 m fixed spherical primary dish was constructed inside a sinkhole. The receiver is mounted in a platform suspended above the dish. The receiver is moved above the dish to intercept the reflected signals from the dish. This allows the telescope to observe 20° about the local zenith - between −1° and 39° in declination. The telescope is equipped with an S-band Planetary Radar transmitter centred at 2380 Mhz, roughly 13 cm in wavelength.

Figure 2.10: An image of Arecibo Observatory, a radio telescope located in Puerto Rico. The telescope is equipped with an S-band transmitter, which is centred at 2380 MHz - roughly 13 cm in wavelength. This facility is the second largest single aperture telescope with an aperture of 305 m. Image reprinted from NAIC Arecibo Observatory webpage.

Goldstone Solar System Radar – Part of the NASA Deep Space Network, Goldstone Observatory hosts nine parabolic antennas located in the Mojave Desert, California, USA, which are used to maintain communication with spacecraft (Slade et al., 2011). When they are not needed for spacecraft communication, the antennas are used for astronomical research. Of particular interest is DSS-14 or the "Mars Station", it is the largest antenna at the complex, a 70 m fully steerable dish. Originally 64 m, it was later expanded to support communications with the Voyager missions. The station is equipped with a X-band transmitter centred at 8560 MHz or roughly 3.5 cm wavelength.

Figure 2.11: An image of DSS-14 of the Deep Space Network, a network of radio antennas used to maintain communication with spacecraft. Outside of spacecraft communication, this 70 m fully steerable dish is also used for astronomical research. The station is equipped with a X-band transmitter centred about 8560 MHz, approximately equivalent to a wavelength of 3.5 cm. Image credit NASA/JPL-Caltech.

2.2.2 Types of radar observations

There are two types of radar observation: continuous wave (cw) spectrum and delay-Doppler imaging. The method for both type of observation is carried out in the same manner. A directed signal is transmitted towards the object being observed; the transmission length is equal to the length of time that it takes the signal to reach the object and return to the telescope. The recorded echo is processed and converted from ana-

logue to digital.

Continuous-wave spectrum

– In continuous-wave spectra, a monochromatic polarised signal is transmitted for the duration of the RTT (Pettengill and Jurgens, 1979). The frequency of the transmitted signal or the returning echo is adjusted for the radial velocity of the object's centre of mass using ephemeris predictions. The returning signal will be Doppler shifted around this centre of mass frequency, f_0, depending on the motion of the asteroid: higher for the parts that are approaching Earth and lower for those that are receding from Earth. The total broadening of the signal, or the bandwidth, is a function of the asteroid's size and spin state in addition to the wavelength of the observations and the observational aspect angle. Therefore, cw observations are able to give an indication of an asteroid's size and rotation period. With observations covering enough of the rotation phase an estimation of the convex-hull of an asteroid's pole-on silhouette can also be determined (Ostro et al., 1988, 1990). The convex-hull can be thought of as the shape resulting by gift wrapping the asteroid's shape, this can be seen in Fig. 2.12.

The returning echoes induce an continuous voltage in the receiver, this is called an analogue voltage time series, which is sampled at a frequency of f_s to convert it into a digital signal. The number of samples taken, n_s, is related to the integration time, τ, of the observations by $n_s = \tau \cdot f_s$. The digital signal is then reduced using an n-point Fourier transform, where n is chosen to be a divisor of n_s. The resolution of the signal is given by f_s/n, this is highest when n is chosen to be n_s giving a resolution of $1/\tau$. Typically full-resolution spectra are spiky due to background noise, which confuses the modelling software as it tries to fit the noise. Therefore, spectra are smoothed prior to their input into modelling software.

Delay-Doppler imaging

In a delay-Doppler image the transmitted signal is phase-modulated with a pseudo-random binary code (Harmon, 2002). The binary code contains 0's and 1's, which are

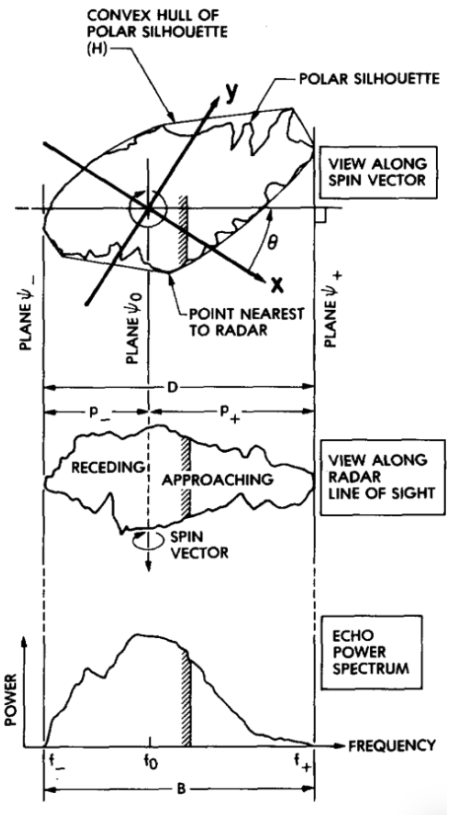

Figure 2.12: This figure visualises the relationship between an asteroid's Doppler spectrum and shape, it shows a view along both the radar line of sight and the spin vector. The plane ψ_0 contains the line of sight and the asteroid's centre of mass about which the asteroid rotates on its spin axis. An echo from any part of the asteroid within this plane has a Doppler frequency of f_0. The hatched area of the echo spectrum corresponds to the hatched areas highlighted on the asteroid. The asteroid's shape as seen along the spin vector is labelled polar silhouette. The convex-hull of the polar silhouette can be thought of as the shape that would be given by placing an elastic band around the polar silhouette. *Figure reprinted from Ostro et al. (1988).*

instructions to invert, or not invert, the phase of the emitted sinusoidal signal. Each inversion code lasts a duration of b seconds, where b is referred to as baud length. After a number of binary elements, L, the code is repeated; thus the code repeats every p seconds, where $p = Lb$. The pseudo-random binary code is chosen to minimise the self-correlation of the code; the elements cannot shift less than an integer multiplier of the code-length to create the same code. For example, for a code with $L = 4$, a bad binary code would be 1010 as this repeats twice per code length. Where as a good example, 0001, cannot repeat more than once per code length. The returning echoes are received as analogue signals and converted to digital, taking s samples every baud length.

The echoes have to be decoded in delay, as each sample will contain contributions from multiple delay lags. In other words, a signal transmitted earlier but reflected off a distant part of the asteroid will arrive back at the same time as an element transmitted later and scattered off a closer part of the asteroid. It is for this reason that the signal

is encoded with the binary phase code. Decoding each delay lag by multiplying the received time signal with a suitably lagged version of the phase code and taking the average value of the product will lead to the sum of contributions from a different delay lag equalling zero. The maximum number of lags that can be decoded is Ls, the total number of samples taken over a code repetition time. If the number of samples taken per baud was greater than 1, then it is possible to decode only a subset within each baud length. The number of decoded lags per baud is denoted as χ. Once each of the N delay lags - where $N = L\chi$ - have been decoded, like the continuous wave spectra, each delay lag is recorded as a voltage time series. An n-point fast Fourier transform is performed on each delay, where n is limited by the division of the transmission time by the code duration, p. This results in N continuous-wave spectra, one for each delay lag. Their combination gives a $n \times N$ delay-Doppler image.

It is important to note that delay-Doppler images differ from optical images. For a radar image, two or more points on the asteroid's surface can share the same delay and Doppler value. This means that the mapping from the plane-of-sky to a delay-Doppler image is many-to-one, by contrast, the mapping of the plane-of-sky to an optical image is one-to-one (see Fig. 2.13). This is because the dimensions of a radar image are not both spatial; the delay dimension is proportional to the Earth-target distance, but the Doppler dimension is proportional to the radial velocity - a function of the position of the scattering element and the target's spin-state.

2.3 Preparation of observational data for modelling

In order for the observations to be used in the analysis stages, they also require formatting. This thesis uses three different formats for each of the modelling software: `convexinv`, `SHAPE`, and customised software based on `MATLAB`, developed at the University of Kent. `Convexinv` performs the inversion of light curves to obtain an asteroid's spin state and convex shape (Kaasalainen et al., 1992b; Kaasalainen and Torppa, 2001).

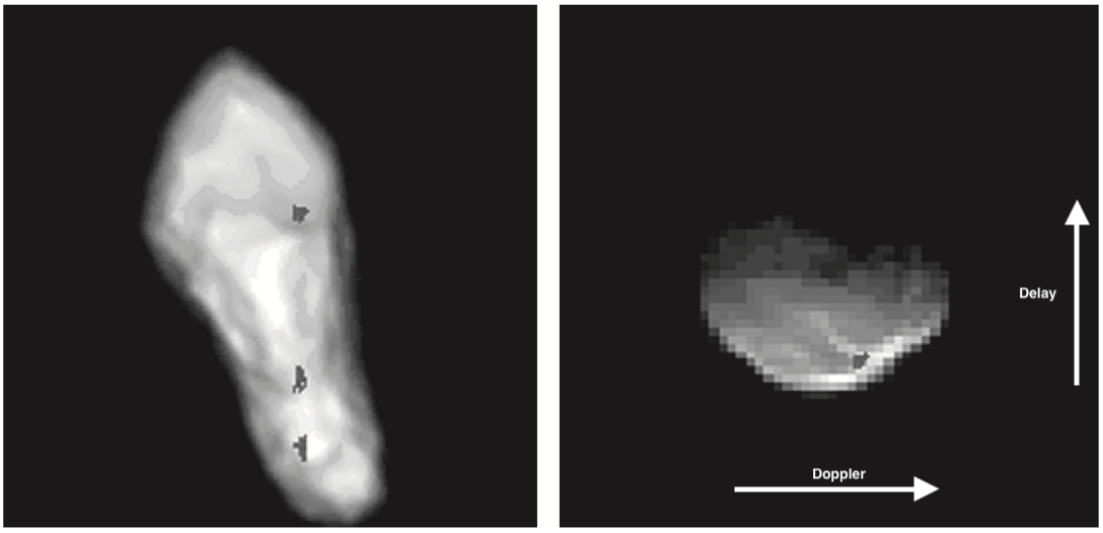

Figure 2.13: Mapping between delay-Doppler images and the plane-of-sky. On the left is a plane-of-sky view of the asteroid (4179) Toutatis. The grey dots lay on a line with a single delay value and a single Doppler value. To the right, is the delay-Doppler image. Oriented such that range increases from the bottom to top, and Doppler increases from left to right. The three grey dots marked on the plane-of-sky image all fall on the single grey point marked on the delay-Doppler image. *Figure reprinted from (Ostro et al., 2002).*

`SHAPE` is able to accept the input of both light curves and radar observations, which is is able to invert to model the non-convex shape of asteroids (Magri et al., 2007). The custom `MATLAB` software is able to detect spin-state changes and measure the YORP strength required to produce them. Each of these software have a unique formatting requirement which is described in detail in Appendix B. Also, detailed discussion of the workings of the modelling software is carried out in the subsequent chapter (Chap. 3).

3 | Shape and spin-state modelling of NEAs to detect YORP accelerations

3.1 Inversion of optical light curves photometry

3.1.1 Introduction

As previously mentioned in Chap. 2, photometric light curves are the most abundant source of observational data on asteroids. Light curves will likely remain a major source of information for asteroids whose size and/or distance prevent disk-resolved images from being obtained. As such, it is important that we are able to maximise the amount of information that we are able to extract from light curves. Russell (1906) was the first to analyse the inverse problem of obtaining an asteroid's pole orientation, rotation period, and shape from its light curves. Russell approached the problem by limiting the observation geometry to the opposition situation, this was an important assumption, as during the early twentieth century asteroids were mostly observed at opposition. However, in restricting the observing geometry at a zero solar phase angle, it was found that an infinite variety of shapes and albedo variegations are able to reproduce the observed light curves. Ultimately, this lead Russell to the conclusion that the effect

of shape and albedo variegation on a light curve's form were inseparably linked; only the *possible* existence of a non-spherical shape or albedo variegation could be obtained. This preconception that shape and albedo effects are inseparable remained for many decades. As observing techniques evolved and the possible observation geometries of asteroids increased, interest in revisiting the inversion of light curves grew. Several authors have since approached the inverse problem by employing various methods. A typical approach is to simplify the problem by minimising the number of free parameters. This was implemented by placing constraints on the shape by describing them as either triaxial ellipsoids or merging eight octants from different ellipsoids (Magnusson et al., 1989; Cellino et al., 1989; Barucci et al., 1992). However, not all efforts were focused solely on determination of the shape. Fourier analysis methods were developed to study the pole orientation and define rotation phase more formally. Harris et al. (1989) demonstrated that it was possible to extract an asteroid's synodic rotation period from a single light curve of sufficient quality using Fourier transforms.

The largest breakthrough in the inversion of light curves is the work of Kaasalainen et al. (1992b,a). Kaasalainen developed the theory which demonstrates that a dataset with sufficient coverage of observing geometries and reasonable assumptions, allows the obtention a solution to the inverse problem. These assumptions require the observing geometry to be known and that the asteroid must be a principal axis rotator. This theory has been used extensively in the work contained within this thesis in the form of the `convexinv` software, which is described in detail in the following section.

3.1.2 Modelling shape, spin-state and YORP with `ConvexInv`

The inversion of light curves facilitates the approximation of an asteroid's shape with either a convex or non-convex model. A convex model represents the hull of the asteroid which is commonly described as a 'gift-wrapped' model of the asteroid's real shape. In contrast, non-convex models are able to produce concave features of the asteroid, however, their results are more qualitative than quantitative. In other words, they

can reveal the presence of a valley on an asteroid, but they will not reliably describe its depth. The main drawback for non-convex models is that their parameter space is plagued with local minima, therefore the non-convex solutions are degenerate. As such, in this thesis, preference is given to the convex shape models as these are unique.

The software applied in this work is a modified version of the program, `convexinv`, written in C by Ďurech et al. (2010). Originally, the software was written in Fortran by Mikko Kaasalainen, which is based on earlier theoretical work (Kaasalainen et al., 1992b,a). They posed the inverse problem in the form:

$$\mathbf{L} = A\mathbf{g} \tag{3.1}$$

where:

$\mathbf{L}$	the vector of the asteroid's observed brightnesses,
$\mathbf{g}$	the vector that contains the parameters to be solved,
A	the matrix describes the relation between $\mathbf{L}$ and $\mathbf{g}$.

The vector $\mathbf{g}$ can describe the asteroid's shape, its albedo variegation, or a mixture of both. Usually, $\mathbf{g}$ represents the former. Using relative light curves, the solution to Eqn. 3.1 can be obtained by minimising the square norm, χ^2_{rel}, defined as

$$\chi^2_{rel} = \sum_i \left\| \frac{\mathbf{L}^{(i)}}{\bar{L}^{(i)}} - \frac{A^{(i)}\mathbf{g}}{\langle A^{(i)}\mathbf{g} \rangle} \right\|^2 \tag{3.2}$$

where:

i	an index refering to each light curve,
$\bar{L}^{(i)}$	the mean brightness of the i-th light curve,
$\langle A^{(i)}\mathbf{g} \rangle$	the mean brightness of the i-th model light curve.

This is iteratively solved using the conjugate gradient method to create a model, $\mathbf{g}$, whose light curve, $A\mathbf{g}$, matches the observed light curve, $\mathbf{L}$. The conjugate gradient method acts to minimise the square norm by searching for the downhill direction as the parameters are varied. The downhill direction is followed until the parameter value that minimises the square norm is found. The unit of brightness in `convexinv` is described in terms of intensity opposed to magnitude. Note that Eqn. 3.2 does not include reference to the uncertainty of the observed brightnesses; this drawback leads to poor quality light curves being given equal weight to high quality ones. Therefore, care must be taken when deciding which light curves to input.

The matrix A contains a description of the observational geometry and albedo of each component constituting the shape model represented by $\mathbf{g}$. It is written as

$$A_{ij} = S_j \left(\mu_{\oplus}^{(ij)}, \mu_{\odot}^{(ij)} \right) \bar{\omega}_j \tag{3.3}$$

S_j and $\bar{\omega}_j$ are the scattering law and albedo for the j-th facet. The illumination and visibility of the asteroid are described by $\mu_{\oplus}^{(ij)} = \mathbf{E}_{\oplus,i} \cdot \mathbf{n}_j$ and $\mu_{\odot}^{(ij)} = \mathbf{E}_{\odot,i} \cdot \mathbf{n}_j$ respectively. $\mathbf{E}_{\oplus}$ and $\mathbf{E}_{\odot}$ are unit vectors in the asteroid's frame of reference that point to the observer (usually the Earth, but can be any position e.g. a spacecraft) and Sun, and $\mathbf{n}_j$ is the facet normal of the j-th facet. If either $\mu_{\oplus}^{(ij)}$ or $\mu_{\odot}^{(ij)}$ are equal to or less than zero, then the contribution from the j-th facet is zero.

The asteroid's shape is represented within `convexinv` initially as an exponential spherical harmonic series, which has fewer parameters describing the shape and thus reduces the numbers of parameters to be solved for. Allowing a quick optimisation towards an initial solution which can then be discretised to represent the facets of a polyhedron and further optimised. The shape of the polyhedron, $\mathbf{g}$, is described by a set of facet normals ($\mathbf{n}_j$) and facet normal areas (g_j). For $\mathbf{g}$ to describe a convex polyhedron the following constraints must be true: the facet normal areas must be positive ($g_j \geq 0$) for all facets and the surface must be closed ie:

$$\sum_j \mathbf{n}_j g_j = \mathbf{0} \tag{3.4}$$

To ensure positivity each g_j is represented exponentially by $g_j = \exp(a_j)$, where the values of a_j are unconstrained. Because the exponential function is monotonic, the smallest χ^2_{rel} solution is unique. During the minimisation of Eqn. 3.2 the resulting solution for $\mathbf{g}$ could be such that Eqn. 3.4 is not satisfied, i.e. there is a non-zero residual. This is corrected by introducing a 'dark' facet to account for features that cannot be reproduced with a purely convex shape. The 'dark' facet is of a corresponding size such that Eqn. 3.4 is satisfied, but is usually very small. Finally, in order for the shape to be utilised it must be converted from `convexinv`'s internal representation to a triangulated polyhedron mesh. The manner is which this software has been applied in the modelling of asteroids and the search for YORP within this thesis will be discussed in the following paragraphs.

Determination of the rotation period

The determination of an asteroid's rotation period is not always a required step, as a value may be available from the literature. However, in the case where there is no literature period, or there are conflicting periods reported, there are two methods available to obtain an estimate of the rotation period. The first is to employ a fast Fourier transform of one or more light curves with a similar observational geometry (Harris et al., 1989). This method will result in a synodic rotation period, that can be refined in the subsequent stages. An alternative method is to perform a period scan over the entire data set using the `period_scan` package included in `convexinv`. This package performs the scan for a selection of periods between two periods specified by the user. The number of periods probed within the period range, N_{per}, is given by

$$N_{per} = \frac{2\Delta t(P_1 - P_0)}{P_0 P_1} \frac{1}{p} \tag{3.5}$$

where P_0 and P_1 are the minimum and maximum periods specified by the user, Δt is the full epoch range of the light curves utilised for the scan, and p is the coefficient of the period scan which should be less than one and is usually set to 0.8. The step size for the interval scanned is then $p\Delta P$, where ΔP is the smallest separation of local minima in the period parameter space roughly given by

$$\Delta P \approx 0.5 \frac{P^2}{\Delta t} \tag{3.6}$$

For each of the periods scanned, six models are probed, each model has a unique pole orientation which are initially uniformly scattered over the entire celestial sphere. The pole orientation and ellipsoid shape are optimised for each model with the chi squared for the best of the six models being recorded, in addition to the rms deviation, the number of iterations performed, and the dark facet area (as a percentage). However, the shape of the asteroid is *not* recorded. The results are output in a log file that can be used to display the results graphically, in a periodogram, as in Fig. 3.1.

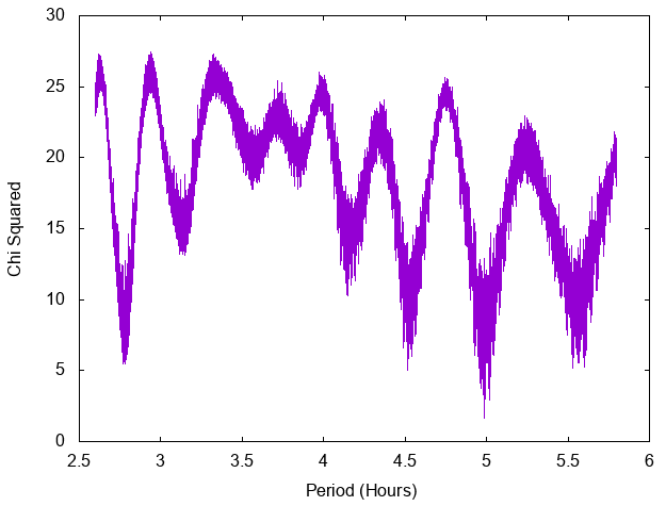

Figure 3.1: Results of a period scan, or periodogram, for the interval 2.6 - 5.8 hours. The goodness-of-fit, or χ^2, is plotted for each of the periods scanned. Smaller values indicate a better fit to the observed data. This graph suggests that the period for this asteroid is about 5 hours.

Grid search to determine pole orientation

An asteroid's pole gives its orientation in space, it is described in the ecliptic reference frame by the ecliptic polar angle, $\tilde{\beta}$, and longitude, λ. $\tilde{\beta}$ is measured from the asteroid's positive z-axis and varies between $[0, \pi]$, $\tilde{\beta}$ is related to the ecliptic latitude, β, by

$\beta = 90° - \tilde{\beta}$. For a principal axis rotator, the object's z-axis should also be aligned with the largest principal axis of inertia and its pole orientation will remain fixed with respect to the ecliptic plane. Note however, that the x- and y-axes of the object are not aligned with the other principal axes.

The vectors input to `convexinv` pointing to the Earth and Sun, with the asteroid at their origin, are transformed from ecliptic coordinates, $\mathbf{r}_{ecl}$, to the asteroid's body-centric coordinates, $\mathbf{r}_{ast}$, by a series of rotations

$$\mathbf{r}_{ast} = R_z(\phi_0 + \omega(t - t_0))R_y(\tilde{\beta})R_z(\lambda)\mathbf{r}_{ecl} \tag{3.7}$$

where t is time, t_0 is the initial epoch, ω is the angular velocity, and $R_i(\theta)$ is the rotation matrix rotating the vector by the angle θ about the i-axis. This equation allows the parameters β, λ, and ω to be included in the inverse problem by describing the Earth and Sun vectors as seen from the asteroid. By allowing the pole orientation to be a free parameter that is optimised, this will introduce several local minima in χ^2. To avoid the equivocacy created by this, the pole is determined in this thesis by scanning over a grid of fixed poles. This still allows an accurate determination of the pole orientation, but reduces the risk of the fitting procedure falling into a local minima. The pole orientations are chosen to cover the entire celestial sphere and have a fixed resolution, typically $5° \times 5°$ but this can be decreased for a finer resolution scan. For each pole orientation a model is created with an initial shape and period, all of the models will have the same initial shape and period, but vary only in pole orientation.

This method of scanning for the pole leads to a large number of models for which period and shape need to be optimised, therefore the scan is performed on a cluster of computing nodes. This optimisation process is configured to run concurrently on several computing nodes in order to reduce the amount of time that the scan requires. Once the scan has been completed, the χ^2 recorded for each pole orientation can be plotted to create a χ^2-plane as shown in Fig. 3.2. The grid-like nature of the pole scan

is shown in Fig. 3.3, which also highlights the number of models that are optimised. Contours denoting increases of 1%, 5%, and 10% of the χ^2 value above the minimum value can be used to group equally valid solutions. Additionally, the uncertainty can also be derived from these figures, with the standard 1σ error corresponding to an increase of one to χ^2_{min} above the minimum value.

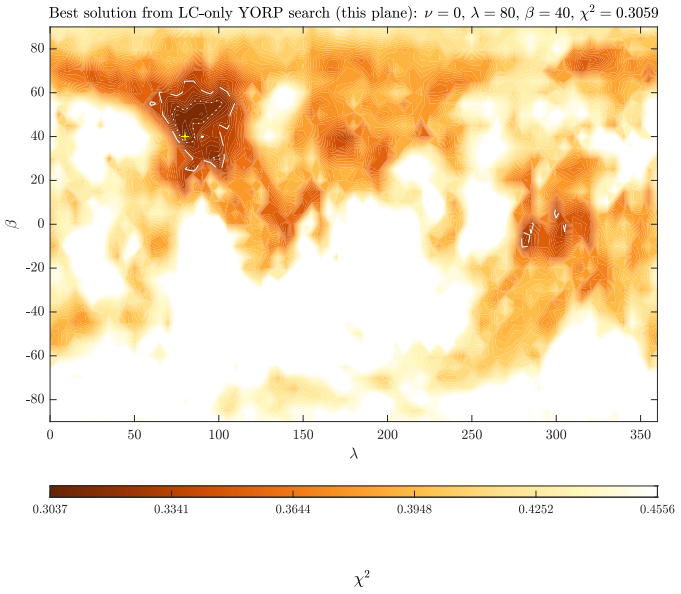

Figure 3.2: An example χ^2-plane generated from the output of the pole scan for asteroid (89830) 2002 CE. χ^2 values represent the goodness-of-fit of the model's optimised rotation period and shape at each of the fixed pole orientations. Darker colours represent lower χ^2 values, which in turn represent better fits between the observations and model. Values of χ^2 50% above the minimum value are all plotted white.

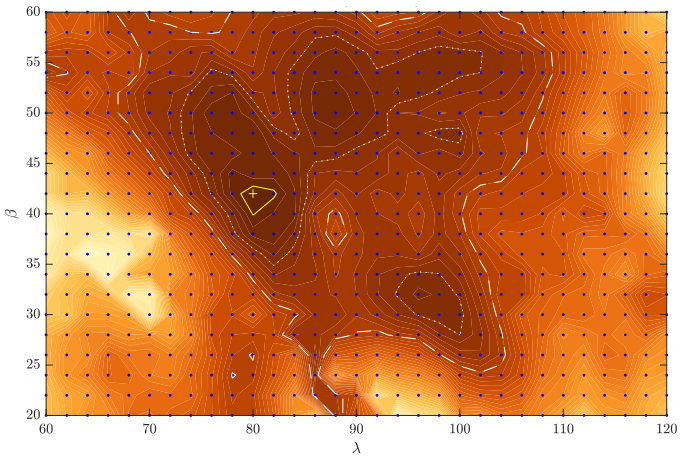

Figure 3.3: A inflated view of the region surrounding the best model in Fig. 3.2, which is marked by the yellow cross. For each of the blue dots a model with the corresponding pole orientation has been optimised. In this figure a total of 651 pole orientations were optimised.

The pole scan may be iterated over several times and may include or exclude various data sets or the resolution of the pole scan may be increased in order to obtain the best solution for the object's pole orientation. Once the best solution has been obtained, `convexinv`'s internal description of the model can be converted into a polyhedral model

to obtain the final convex model. Additionally, the optimised spin-state parameters of this model can be output.

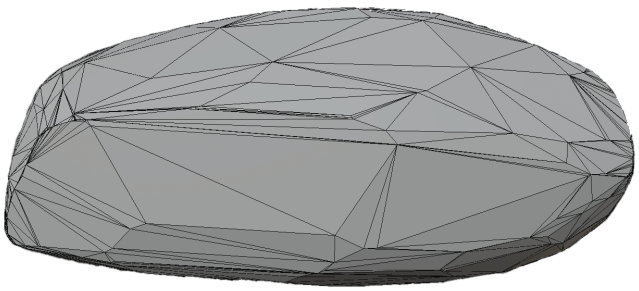

Figure 3.4: Example of the resulting polyhedral model output by `convexinv`. This figure displays the convex model for the asteroid (68346) 2001 KZ66. This shape is described by two arrays, one listing the vector components of each vertex and another listing the vertices that make up each facet.

Inclusion of the YORP factor

The `convexinv` software does not natively allow changing rotation rates to be investigated, it only allows the modelling of fixed rotation periods. As discussed in Chap. 1, the axial component of YORP induces a continuous torque that drives changes in an asteroid's spin-state, which consequently leads to a linear change in an object's rotation rate (Rubincam, 2000). The addition of a continuous rotational acceleration to the `convexinv` software was performed by a past post-doc at the University of Kent, Sam Duddy. The linear changes in rotation rate translate to quadratic changes in an asteroid's rotation phase, which can be described by

$$\varphi(t) = \varphi\left(T_0\right) + \omega\ \left(t - T_0\right) + \frac{1}{2}\nu\ \left(t - T_0\right)^2\ , \tag{3.8}$$

where:

$\varphi(t)$	rotation phase in radians,
t	the time of observation (JD),
$\varphi(T_0)$	initial rotation phase in radians,
T_0	time (JD) at which the X-axis of the body crosses the plane-of-sky, also the epoch from which the model is propagated,
ω	rotation rate in rad day^{-1}; $\omega \equiv 2\pi/P$, P is rotation period in days,
ν	the change of rotation rate in rad day^{-2}; $\nu \equiv \dot{\omega}$ (the YORP strength).

With YORP acceleration integrated into the software, it is possible to scan the light curves for indications that their rotation period is changing. Note however, that the integration of YORP only allows fixed values; the value of YORP cannot be optimised during the fitting process. This limitation requires the scanning of YORP values to be performed in a grid, much like the search for the optimum pole orientation described earlier. The modified software allows us to create multiple χ^2-planes for non-zero YORP values (visualised in Fig. 3.5). By extracting the χ^2-value of each YORP plane's best model, it is possible to display how the goodness-of-fit varies with YORP strength. Allowing us to create a 'YORPogram' such as the one shown by Fig. 3.6. These YORPograms give an overview of the possible YORP strengths that best fit the observations. As with the pole scan, the best solution can be converted to a polyhedral model for further investigation.

3.2 Modelling radar observations

3.2.1 Introduction

There are two types of radar observation that can be made: continuous-wave spectra or delay-Doppler imaging. Both can be utilised to constrain an asteroid's shape, spin-state, and radar-scattering properties. Until 1987, only ranging and continuous-wave

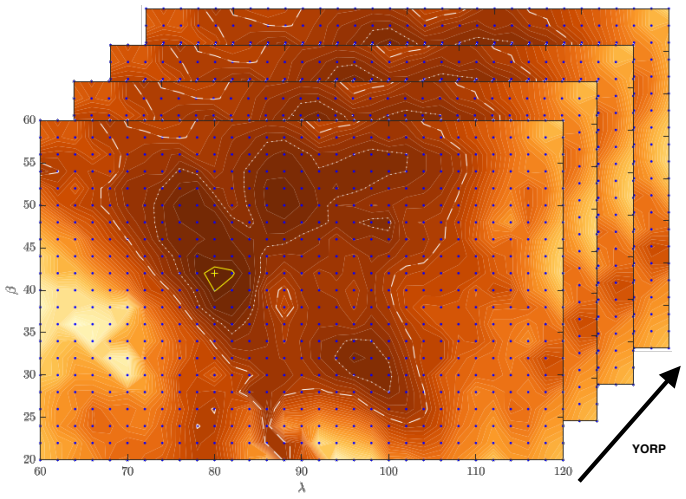

Figure 3.5: A visualisation of the multiple YORP planes that are produced when YORP is integrated into the scan. Each YORP plane is a pole scan that has a fixed YORP strength, where the asteroid's shape and rotation period are optimised for each pole orientation.

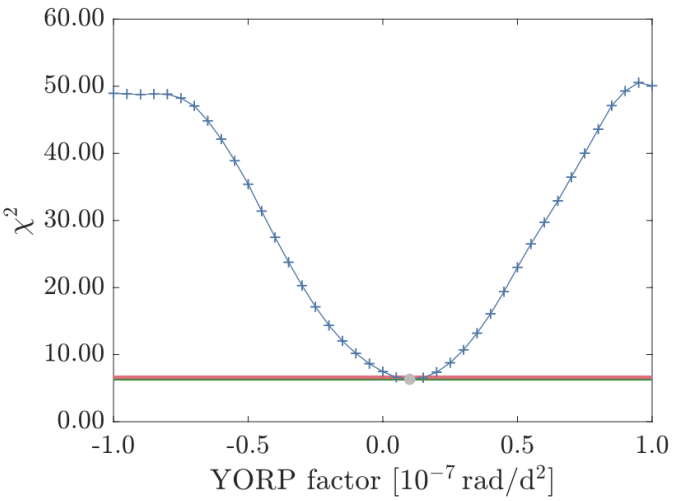

Figure 3.6: An example of a 'YORPogram' generated by scanning over discreet YORP values. Each cross in this figure represents the best solution from a χ^2-plane for a given YORP value, in which the asteroid's shape and period were optimised. The multiple YORP planes are visualised in Fig. 3.5, each plane contributes a single cross in this figure. The global χ^2 minimum across all YORP strengths is marked here by a grey dot. The green and red horizontal lines indicate increases of +1% and +5% above the global minimum χ^2 value.

spectra were possible with radar facilities (Snyder, 1987). A continuous-wave spectrum measures the Doppler shift of the returning signal's frequency from that of the transmitted signal (examples shown previously in Figs. 2.9 & 2.12). However, even with these Doppler-only images it is possible to obtain the convex-hull of an asteroid's polar silhouette. This requires that the spectra have suitable coverage of the asteroid's rotation phases. That is to say, that if the asteroid was covered by elastic bands this

would cover up all concavities, this is the convex-hull, and from these spectra we could obtain the silhouette of this hull from a polar view. This is possible as the echo's bandwidth, $B.$ is proportional to the asteroid's apparent diameter, D, the two are related by $B = 4\pi D \cos\delta/\lambda P$ (Ostro et al., 1988), where δ is the sub-radar latitude, λ is the wavelength of the transmitted radar signal, and P is the asteroid's rotation period.

With the advent of delay-Doppler images, which included range as a component of the images, radar could now be inverted to yield three-dimensional models of the target (Hudson, 1993). This became possible as the inclusion of range leads to each surface element now having a unique delay and Doppler value as the target rotates. The exception to this being when the sub-radar latitude falls on the asteroid's equator. This case causes an aliasing called the north-south ambiguity, which cannot be broken without additional data from a non-equatorial sub-radar latitude. The ambiguity is caused by the lack of temporal difference between signals reflected from the northern and southern hemisphere with the same angular distance from the equator, as both points would have the same delay. This can happen in individual images from a non-equatorial sub-radar latitude, but as the rotation phase changes the aliasing will be broken. Although, with equatorial images it is possible to obtain the unambiguous pole-on silhouette of an asteroid (Ostro et al., 1995). This is because the silhouette will be traced out by the point with the shortest delay value with zero Doppler shift.

To produce the best physical models of asteroids, multiple data sources are combined together. For instance, radar observations are often combined with light curves (Magri et al., 2007, 2011; Busch et al., 2007). This helps to determine an asteroid's size and spin, which are degenerate for radar observations alone. The inclusion of the light curves allows a unique determination of the rotation period, thus breaking this degeneracy as only the size will need to be determined from the width of the Doppler spectrum. The inversion of radar observations yields non-unique solutions. Therefore, it is important that the starting point of a radar model is a good approximation of the data, roughly reproducing features in the delay-Doppler images. The modelling of radar observations

is a highly iterative process that requires a lot of user interpretation and alteration.

3.2.2 Modelling asteroids with SHAPE

The software used in this thesis to invert radar observations is SHAPE, written by Chris Magri (Magri et al., 2007). The software is more complex than convexinv, as it allows for the inversion of a mixture of data types; for this thesis these are radar observations and optical light curves. The software also allows the inclusion of 'penalty functions', the purpose of which are to discourage certain types of improbable physical features from arising in the model. However, it applies the same principle: attempting to minimise χ^2 between model and observations. In this context, 'model' includes a combination of the three-dimensional shape of the asteroid, its spin-state, reflective properties, and ephemeris corrections. Where the ephemeris corrections act to rectify any inaccuracies in the prediction of the asteroid's location by applying a delay correction.

Each call to SHAPE requires three files which describe: the action to be taken by SHAPE, the model of the asteroid, and the observations to be utilised. Respectively, these files are called the parameter file, model file, and observation file. A summary of each of these files are discussed in the paragraphs below, with the detailed description and excerpts to be found in appendix B.

Parameter (par) file

This file contains not only the action to be performed by SHAPE, but also a list of parameter values required in order to run. Additionally, this file contains weighting factors for any penalty functions that may have been applied. The parameter file is split into two headings: 'PARAMETERS', which indicate the action to be taken, and 'PENALTIES'.

Following the latter heading, 'PENALTIES', an integer is stated that indicates the number of penalty functions that are to be applied when using the 'fit' action which are

listed below. The purpose of the penalty functions are to discourage certain behaviours from appearing in the model that `SHAPE` produces. Penalty functions depend solely on the asteroid model, and are given weights with larger numbers leading to stronger discouragement of features. However, the weights given are arbitrary and what is considered a larger penalty weight will vary with asteroid and datasets used. Penalties functions are an important tool required to ensure that the resulting model is physical. There are many penalty functions that can be applied and a completed list can be found in the documentation (Magri et al., 2007). Though, there are several important penalties that were utilised in the work of this thesis, which are summarised here:

- *nonsmooth* - discourages facet-scale topography, which inhibits unphysical spiky (hedgehog-like) models from appearing.
- *pa3tilt* - discourages misalignment between the third principal axis, which for a principal axis rotator corresponds the maximum moment of inertia, and the spin-axis (z-axis).
- *inertiadev_uni* - an alternative to *pa3tilt*. This penalty tries to align the principal axes by using the model's inertia tensor.
- *nonpa_uni* - discourages non-principal axis rotators by insuring the first and second principal axes are smaller than the third.
- *comdev* - discourages misalignment between the model's centre of mass and the origin of the body-fixed coordinates.

Model (mod) file

This file describes the 'model' which includes the shape of the asteroid, its spin-state and photometric parameters. The description of a model's shape can be comprised of multiple components. For instance, when modelling a contact-binary, two components would be used to describe the object's shape. For each component, there are three linear offsets applied describing shifts along the body-fixed x-, y-, z-axes away from the

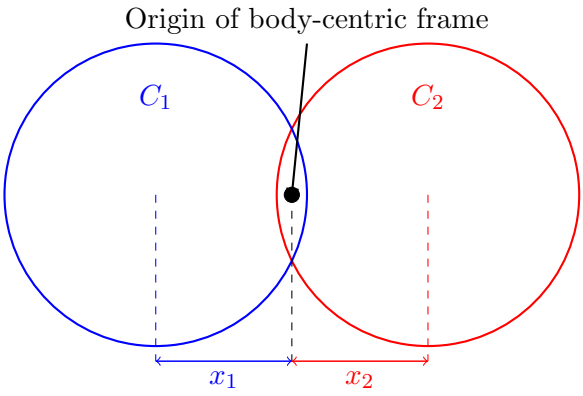

Figure 3.7: An illustration of the linear offsets applied to two component model to form a basic contact binary shape. The offset applied to the first component C_1 is x_1, where x_1 is a negative value. Similarly, an offset is applied to the second component C_2, where the offset x_2 is positive. This figure simplifies the scenario by displaying only a one-dimensional offset, but offsets can be applied also in the y- and z-axis within `SHAPE`.

origin, there are also three rotational offsets describing rotations about the body-fixed axes. Modelling a one-component model, each of the linear offsets and the rotational offsets would be held at zero. However, for a contact-binary one component might have a offset in the +x direction while the other component is offset in the -x direction (see Fig. 3.7 for an illustration). The shape of each component can be described using one of three types: ellipsoid, spherical harmonic, or vertex. Only the vertex type is described in the following paragraph. The other types and an excerpt of a mod file can be found in appendix B.

Vertex components – The component type used in the final models within this thesis are vertex components, these are the most computationally intensive components to model due the high number of parameters they are able to have. As such, they are able to generate fine resolution models. For this reason, the final shape model is usually comprised of a vertex component(s). The format for the description of these components start by declaring the number of vertices that the model is comprised of. This is followed by scaling factors like those described for spherical harmonic components. After which the vertices are specified, these are composed of two lines per vertex. The *second* line contains the three body-fixed coordinates of the base vertex displacement ($\vec{v_b}$ in Fig. 3.8, variables given in brackets for the remainder of the paragraph also relate to the figure). The *first* line contains a unit displacement direction ($\hat{v_d}$) for a

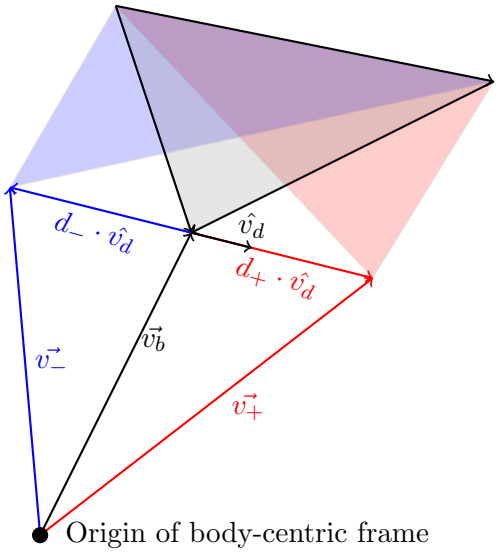

Figure 3.8: A visualisation of how a vertex of a triangular facet is described within SHAPE. The location of the vertex is given as a combination of a base vector $\vec{v_b}$ plus a unit displacement $\hat{v_d}$ that is scaled by $d_\pm$. The vertex is initialised in a way such that initial $d_\pm$ is zero.

deviation from the base vertex, and a coefficient that modifies the scale of the vertex displacement in km ($d_\pm$). Following the specification of all of the vertices, the number of facets is stated. Each facet is described by a single line that lists the vertex numbers of the three vertices that make up the corners of that facet.

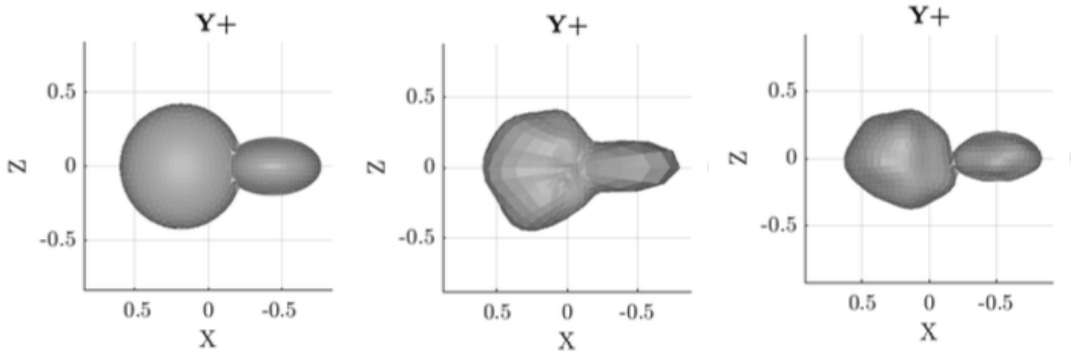

Figure 3.9: An example of a bilobed asteroid optimised using various component types available within SHAPE. The left panel shows the asteroid comprised of two ellipsoidal components, the center panel shows the same asteroid using two spherical harmonic components, and the right panel shows the same asteroid again using one vertex component. As the model progresses through the component types from left to right, the number of parameters describing the shape increases along with the detail of the model.

The second section of the model file describes the photometric properties used to calculate the synthetic images. First, the radar scattering law(s) is given. Several choices are available for this: 'Cosine', 'Hagfors', and a hybrid of the two 'hagfors+cosine'. The 'Cosine' scattering law is the simplest applicable law, and can be utilised for scattering

angle from 0° to 90°. It is described mathematically by (Ostro, 2007)

$$\frac{d\sigma}{dA} = R(C+1)\cos^{2C}\theta \tag{3.9}$$

where:

σ the radar cross section,

A the target surface area,

R the Fresnel reflectivity at normal incidence,

C is related to the r.m.s. slope angle; larger values indicate more specular scattering,

θ the scattering angle.

'Hagfors' is a quasi-specular law, in addition to the R and C parameters, it also has a cut-off angle. For scattering angles above this value the echo power is zero. Note that the cut-off angle is not a fitted parameter, it is a fixed value given in degrees. The form of the 'hagfors' scattering law is given by (Ostro, 2007)

$$\frac{d\sigma}{dA} = \frac{CR}{2}[\cos^4\varphi + C\sin^2\varphi]^{-3/2} \tag{3.10}$$

Where φ is the radar incidence angle. Within a single model file multiple radar scattering laws can be given, but only one can be applied per data set. Like most parameters in `SHAPE` the radar scattering law parameters R and C can either be set to fixed values or be fit for.

Following the radar scattering law(s), the optical scattering law(s) are given. Again there are several choices for the optical scattering law, these are: Lambertian, Lommel-Seeliger, and Kaasalainen. The optical scattering law determines how much intensity each visible facet contributes to the total intensity. For a facet to contribute any intensity both $\cos(\phi) > 0$ and $\cos(\theta) > 0$ must be true. Where ϕ is the optical incidence

angle, and θ is the optical scattering angle. In other words, the facet must be both illuminated by the Sun, and visible to the observer. For the Lambertian scattering law, the intersity contribution from each visible and illuminated facet is given by

$$sf(R)I_0\cos(\varphi) \tag{3.11}$$

And for the Lommel-Seeliger scattering law, each facet contributes

$$sf(R)I_0\frac{cos(\varphi)}{\cos(\varphi)+\cos(\theta)} \tag{3.12}$$

Where $sf(R)$ is a scaling factor that is a function of the albedo, R, I_0 an intensity factor dependant on the asteroid's location in its orbit. Within `SHAPE` all scattering laws include a parameter to describe the albedo of the asteroid, R, this is only used with absolute light curves. However, this work relies on relative light curves, so this parameter was always held at a fixed value. The final optical scattering law is 'Kaasalainen', this law is a mixture of the Lambertian and Lommel-Seeliger laws. Note however, that its implementation within `SHAPE` differs from the published law (Kaasalainen et al., 2001). The published law uses a weighting factor 'c' that varies from 0 to ∞, whereas `SHAPE` uses 'wt' which varies from 0 (purely Lommel-Seeliger) to 1 (purely Lambertian).

Observation (obs) file

This file contain both metadata that provide descriptions of the data and the paths to the data files themselves. Observation files comprise of all of the data to be utilised in the modelling procedure, which can be a mixture of light curves, delay-Doppler images, and continuous wave spectra. A detailed description of these files and their contents is discussed in appendix B.

3.2.2.1 Procedure to optimise model with SHAPE

The method that SHAPE uses to optimise the parameters of the asteroid model is constrained-least-squares. The software searches for the 'best-fit' by cycling through the parameters, optimising one parameter while holding all other parameters constant. The term 'best-fit' signifies that the objective function, which is a combination of the reduced-χ^2 and any penalties applied, is at a local minimum. For each parameter, SHAPE starts by calculating the objective function for the unchanged parameter value, then again for the parameter plus the user specified step-size taken from the parameter file. The software uses both of these measurements of the objective function to apply increasingly larger steps in the direction that minimises the objective function. It does so until the objective function begins to rise again, at which point the minimum has been bracketed. SHAPE then pinpoints the minimum that has been bracketed, although there is the danger that it will pinpoint a local minimum that might not be the best one. The final value best-fit value of a parameter x will fall between $\pm(fractol|x| + abstol)$ of the value x_{min} that would truly minimise the objective function. Where $fractol$ is the fractional tolerance and *abstol* is the absolute tolerance, both of which are specified by the user in the parameter file. This process is repeated until the termination criteria is achieved; either the maximum number of iterations is reached or the change in the objective function between iterations is smaller than the precision stated in the parameter file.

The modelling procedure used by the author in this thesis is based on the methods of Magri et al. (2007, 2011). Each asteroid is unique, as such, so are the steps and decisions taken while modelling them. For some asteroids, a basic shape model and rough spin-state may already be known and so it will not be necessary to create a model from scratch. For other asteroids, multiple models may have to be investigated simultaneously as they cannot be ruled out. However, presented below are the general steps that are applicable to any asteroid.

Generating initial model

It is important when modelling with `SHAPE` that the initial model is able to approximate the data. In practice, this could be achieved via several methods: (i) a published model can be input as the starting point, (ii) a model generated with `ConvexInv`, or (iii) hand-craft an initial ellipsoidal model estimating the size from the delay-Doppler images and using the period determined from earlier `ConvexInv` modelling. To ensure that the initial model is an acceptable starting point, the 'write' action is used to generate synthetic images that can be compared with a couple of delay-Doppler images. If the model doesn't approximate the data to a satisfactory standard, the model can be altered to better reproduce the data and then use the 'write' action once more. This process may have to go through several iterations.

Once a satisfactory starting point has been established, the model can begin to be optimised. Due to the computing intensity of modelling, the initial stages of modelling are performed with a representative subset of data and it is not until the final stages that the entire dataset is utilised. This typically means limiting the light curves that are input to one or two from every unique observing geometry available. For delay-Doppler images, a subset sampling the variety of rotation phases and sub-radar latitudes are input, where possible also giving preference to lower resolution images. Additionally, masks can be applied to the data to further reduce computing time. The most important information provided by the continuous-wave spectra is the bandwidth of the echo, the surrounding background provides no additional information but will increase the computation time. The continuous-wave spectra contains recording of the echo power in a range of frequency bins. The mask is a logic filter that indicates which of these frequency bins are important (mask value of 1) and which are not (mask value of 0). The mask is applied when calculating the χ^2 value between the model and the data, only frequency bins with a non-zero mask value are included in the calculation. Similarly for delay-Doppler images, the delay-Doppler bins considered in the χ^2 calculation can be restricted with a mask. These images can be very large if the full bandwidth and delay range are utilised, and so masking delay-Doppler images provides a greater saving of

computing time than continuous-wave spectra. The initial mask applied is usually a generously buffered rectangle, as the model improved and any ephemeris corrections are applied, the mask can be further refined to tightly outline the echo (Fig. 3.10). The light curves can also be simplified for the improvement of computing time. This is achieved by binning them in rotation phase. This limits the amount of rotation phases that the model brightness needs to be calculated for, while maintaining the accurate phasing information that the light curve provides.

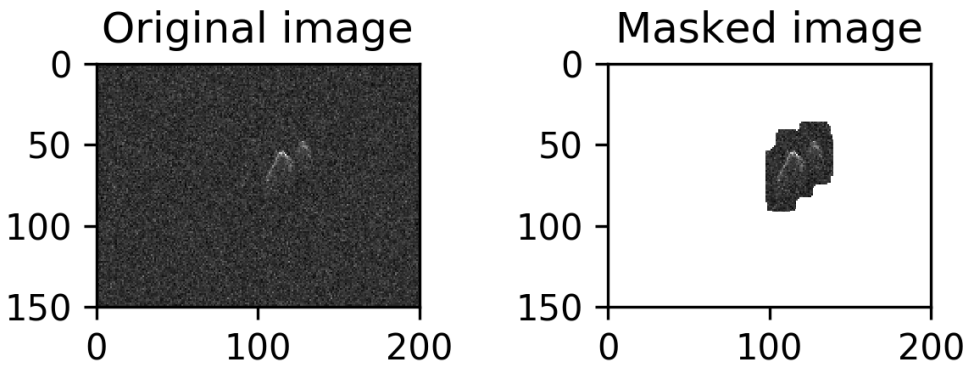

Figure 3.10: An example of a delay-Doppler image, taken on 28 October 2003 at the Arecibo Observatory of (68346) 2001 KZ66. The left panel shows the original image captured at Arecibo, the y-axis shows delay and the x-axis shows Doppler shift. The right panel shows the same image but masked. This masked image would be used as an input to `SHAPE` as there is less superfluous data to parse.

When modelling an asteroid for the very first time, the asteroid is best expressed with ellipsoidal components as these shapes are parametrised by the least variables. This low number of variables leads to a quicker computation. The model generated from the `ConvexInv` analysis could also be utilised at this stage in the modelling as it is able to reliably reproduce the light curves that were used in its creation. However, the disadvantage of this model is that it is described by hundreds or thousands of vertices. These types of vertex models are computationally expensive to model and are usually used as the final stage of modelling.

Refinement of the spin-state

The initial model is only valid for the spin-state that it was modelled for: either selected from the `ConvexInv` analysis, or chosen arbitrarily. Therefore, a grid of fixed pole orientations will need to be scanned. If the pole orientation was well constrained to a particular region of the celestial sphere, a grid of poles evenly spaced by a fixed angular step-size encompassing that region can be probed. If the pole was not well constrained, the entire celestial sphere may have to be scanned. The grid can be constructed such that each pole orientation is evenly spaced across the whole celestial sphere. By spacing them in this way a lower number of models will need to be optimised.

For each of the fixed pole orientations, the sidereal rotation period and the initial rotation phase are optimised. The point from which the rotation phase is calculated from is T_0, unlike `ConvexInv` the initial rotation phase is not required to be zero. Although it is defined differently, `SHAPE` defines the moment that the initial phase rotation is zero as the moment when the model's x-axis crosses the plane-of-sky. If the model is described by ellipsoidal components, the shape of the asteroid can also be optimised in addition to the spin-state. Else if it has a more complex description, it should be held fixed in the interest of computing time.

Shape and rotation period refinement

Once the pole orientation has been determined, the focus can now shift to the optimisation of the shape. The pole orientation is now held fixed and the shape is allowed to vary. If the shape of the asteroid was described by ellipsoidal components in the previous stage, it can be upgraded to either a spherical harmonic or low-resolution vertex representation. Further refinements are also made to both the rotation period and initial rotation phase during this stage. At the end of this stage, the 'write' and 'moments' actions should be utilised to assess the model, insuring that there are no unphysical characteristics developing in the model and that the data is reproducing the observation satisfactorily. This stage could be repeated several times, each time altering the resolution of the shape, the penalties or penalty weights applied, or the

termination precision for the parameters. The penalties and their weights in particular will require multiple iterations as they are highly dependant on the datasets and model, there is no way to determine these *a priori*.

At this stage, it could be necessary to repeat the earlier stage of the modelling process to refine the pole orientation with a finer grid of poles, and/or using a refined description of the shape as the initial model. The delay-Doppler masks can also be refined at this stage.

Polishing the shape model

Once the simplified model has reached a satisfactory level with the chosen subset of data, the final set of fine adjustments can be made to the model. At this stage the entire dataset is utilised, and the resolution of the triangulated model is increased to match the range resolution of the observations. This iteration of the modelling process will likely be the longest stage of the process to compute due to the large number of parameters that describe the asteroid's shape. However, this high-resolution model will enable insights into the surface features present on the asteroid. The final result of this modelling procedure is the spin-state and a detailed shape model which can be used for further spin-state analysis in search of indications of YORP accelerations.

3.3 Spin-state analysis with an existing model

One method to analyse an asteroid's spin-state has already been touched upon in this chapter, the global approach. This method included the YORP acceleration as a fixed value that is scanned over in a grid. This was discussed using the `convexinv` software in Sec. 3.1.2 (see also Fig. 3.6), but can also be applied in the same manner with `SHAPE`.

The methods to detect YORP are not constrained to derivation concurrently with an asteroid's shape, a published shape model can be utilised along with an ample set

of optical light curves. There exists databases containing a wealth of published shape model, which include a mixture of both light-curve-only and radar derived models. The DAMIT database (Ďurech et al., 2010), specialising in light-curve-only models, contained 4,213 models for 2,408 asteroids during July 2020. There is also JPL's "Asteroid Radar Research" page, which host approximately 30 asteroid models derived from radar observations[1].

Another method to detect changes in the spin-state, is a rotational phase offset analysis (Taylor et al., 2007; Lowry et al., 2014). This technique involves using the pre-existing shape model to generate an artificial light curve for each observed light curve. If there is a change in the spin-state due to YORP, there will be a difference in rotation phase between the observed and synthetic light curves that increases over time, which if large enough can be measured. The constant torque induced by YORP produces a quadratic trend in those phase offsets, a fit of the phase offset is therefore able to determine the strength of YORP required to align the observations and model. This method is discussed further in this section.

3.3.1 Generating synthetic light curves

Artificial lightcurves are generated numerically from shape models using ray-tracing code. This makes use of the fact that the model is comprised of triangular facets. The format of the shape is usually an `obj` file, which contain four columns: in the first column is either a 'v' or an 'f', indicating whether the line describes a vertex or a facet respectively. For lines describing a vertex, the following three columns are the v_x, v_y, and v_z vector components of the vector $\vec{v_n}$ that points to the vertex V_n. For lines describing a facet, the three columns are a list of vertices that comprise the corners of that triangular facet, for example V_1, V_2, V_3. An example of this is shown in figure 3.11. Both of these are read into corresponding arrays, `v` and `f`.

For each facet, its normal vector and area are also calculated for future use. Two

[1] `https://echo.jpl.nasa.gov/asteroids/shapes/shapes.html`

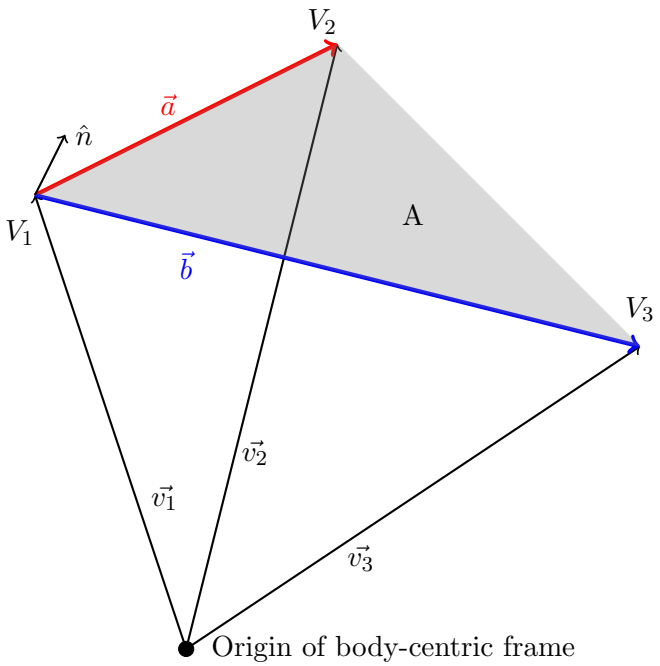

Figure 3.11: The models used to generate artificial light curves are comprised of a list vectors, $\vec{v_n}$, pointing to their corresponding vertices, V_n, and a list of vertices which describe the corners of triangular facets. This figure displays an example facet and the vectors that point to the vertices that constitute its corners. Also drawn, are the vectors $\vec{a}$ and $\vec{b}$ that are used to calculate the facet normal, $\hat{n}$. The vectors are in Cartesian coordinates and in the asteroid's body-centric reference frame.

additional vectors, $\vec{a}$ and $\vec{b}$, are defined from the facet's vertices. $\vec{a}$ is defined as the path from V_1 to V_2 and $\vec{b}$ is the path from V_1 to V_3. Using these the area of the facet, A, is given by:

$$A = \frac{1}{2}\left|\vec{a} \times \vec{b}\right| \tag{3.13}$$

And the facet normal, with its origin from V_1, is given by:

$$\hat{n} = \frac{\vec{a} \times \vec{b}}{2A} \tag{3.14}$$

For a facet to contribute to the brightness of the asteroid, it must be both illuminated and visible to the observer for a given orbital geometry and rotation phase. To determine whether a facet meets these conditions, the asteroid's position relative to both the Sun and Earth must be known. This information can be found in ephemerides, usually given in the ecliptic reference frame, from services such as the JPL HORIZONS

system[2]. Both of these vectors are inverted so that they point from the asteroid to the Sun and Earth. These vectors are included in the light curve data file described in Sect. 2.3. For each light curve, the Sun and Earth vectors are averaged and normalised to give the unit vectors $\hat{E_{\odot}}$ and $\hat{E_{\oplus}}$. This is performed under the assumption that the observational geometry does not change significantly over the duration of a single light curve.

The Sun and Earth unit vectors are then transformed from the ecliptic reference frame to the body-fixed reference frame, so that they are in the same frame of reference as the previously calculated facet normal vectors. This is performed by applying a series of rotation matrices:

$$\hat{E}' = \begin{pmatrix} \cos\phi_0 & \sin\phi_0 & 0 \\ -\sin\phi_0 & \cos\phi_0 & 0 \\ 0 & 0 & 1 \end{pmatrix} \begin{pmatrix} \cos\tilde{\beta} & 0 & -\sin\tilde{\beta} \\ 0 & 1 & 0 \\ \sin\tilde{\beta} & 0 & \cos\tilde{\beta} \end{pmatrix} \begin{pmatrix} \cos\lambda & \sin\lambda & 0 \\ -\sin\lambda & \cos\lambda & 0 \\ 0 & 0 & 1 \end{pmatrix} \hat{E} \tag{3.15}$$

where:

$\hat{E}$	represents both $\hat{E_{\odot}}$ and $\hat{E_{\oplus}}$,
$\hat{E}'$	Sun or Earth vector rotated by asteroid's pole orientation,
λ	ecliptic longitude of the asteroid's pole orientation,
$\tilde{\beta}$	$90 - \beta$, where β is the ecliptic latitude of the asteroid's pole orientation,
ϕ_0	initial rotation phase at t_0.

The Sun and Earth unit vectors are finally rotated by the asteroid's rotation phase at each epoch of observations. Using Eqn. 3.8 to determine that asteroid's rotation phase. This angle is then utilised in the final rotation matrix giving the final unit

[2] `https://ssd.jpl.nasa.gov/horizons.cgi`

vectors for the Sun and Earth direction:

$$\hat{E}'' = \begin{pmatrix} \cos\phi & \sin\phi & 0 \\ -\sin\phi & \cos\phi & 0 \\ 0 & 0 & 1 \end{pmatrix} \hat{E}' \tag{3.16}$$

As previously stated, for a facet of the shape model to contribute to the lightcurve, it must be both illuminated by the Sun and visible to the observer on Earth. Mathematically, this is expressed by $\mu_\oplus = \hat{E_\oplus} \cdot \hat{n} > 0$ and $\mu_\odot = \hat{E_\odot} \cdot \hat{n} > 0$. If the facet of area dA meets both of these conditions then its brightness contribution dL to the total brightness is

$$dL = S(\mu_\oplus, \mu_\odot)\bar{\omega}dA \tag{3.17}$$

where S and $\bar{\omega}$ are the scattering law and albedo respectively. If a uniform albedo is assumed, then the factor $\bar{\omega}$ is removed from the equation. There are various scattering laws that can be applied at this stage: Lambertian, Lommel Seeliger, or Kaasalainen. The Lambert scattering law is $S_L = \mu_\oplus\mu_\odot$, Lommel Seelinger law is $S_{LS} = S_L/(\mu_\oplus + \mu_\odot)$, and the Kaasalainen empirical scattering law is a weighted sum of the Lambert and Lommel-Seelinger laws, $S_K = S_{LS} + cS_L$ (Kaasalainen et al., 2001; Kaasalainen and Torppa, 2001). In the last step, once the artificial light curve has been generated it is adjusted so that it has a mean value of zero. For convex shapes there are no further steps or considerations to make. However, for a non-convex shape, facets must also be checked to ensure that they are not blocked by, nor block, another facet.

Self-shadowing of non-convex shapes

Assuming that the shape of the asteroid is a constant over the epochs of the obtained light curves, a map of the facets that could potentially block another can be created for that shape model. The condition for a facet i to block facet j is that not only must facet i be above the local horizon of facet j, but facet j must be below the local horizon

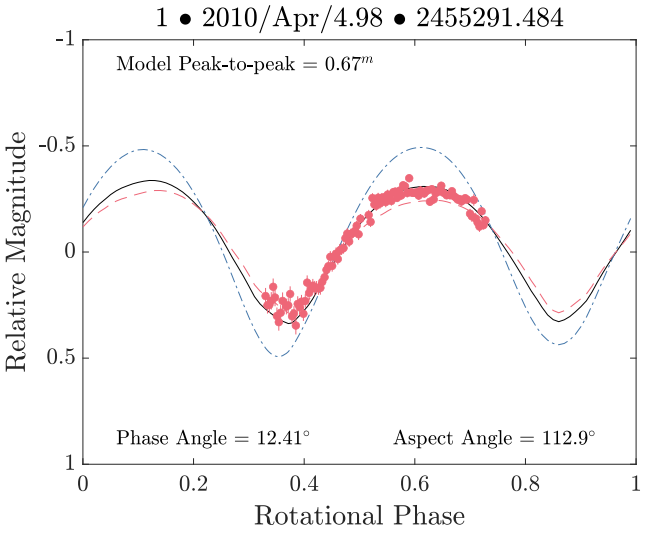

Figure 3.12: This figure demonstrates the different scattering laws that are utilised in the generation of synthetic light curves. These light curves were generated using a non-convex model of the asteroid (68346) 2001 KZ66. The red dots show the observed light curves. The blue dash dot line is the artificial light curve generated using the Lambertian scattering law. The red dashed line was generated with the Lommel Seeliger scattering law. Finally, the black solid line was generated using the Kaasalainen scattering law.

of facet i, as only the front of any facet can be used to block another.

To create a list of possible blocker facets, every possible pair of facets must be checked. For each pair of facets, the centre of each facet must be determined; the centre of the facet i can be defined using the vectors that point to each of the facet's vertices by $\vec{v}_{C,i} = \frac{1}{3}(\vec{v}_{1,i} + \vec{v}_{2,i} + \vec{v}_{3,i})$. With this vector, a new vector, $\vec{p}_{ji}$, that points from the first vertex of facet j to the centre of facet i is defined by $\vec{p}_{ji} = \vec{v}_{C,i} - \vec{v}_{1,j}$. A schematic showing this description is given in Fig. 3.13. With the direction of facet i relative to facet j, we can now determine whether facet i is above the local horizon of facet j using the dot product: $\hat{n_j} \cdot \vec{p}_{ji} > 0$. And so mathematically, the two conditions for facet i to be a potential blocker of facet j are: $\hat{n_j} \cdot \vec{p}_{ji} > 0$ and $\hat{n_i} \cdot \vec{p}_{ij} < 0$.

For a given observing geometry, the facet j is first checked to determine whether it is both visible and illuminated. Only if both are true, then the map of blocker facets is checked for any potential blockers of facet j. If facet j could potentially be blocked by facet i, then geometry of the Sun and Earth are considered. The mathematics are the same for both the Sun and Earth, and so $\hat{E''}$ is used to represent both $\hat{E_\odot}$ and $\hat{E_\oplus}$.

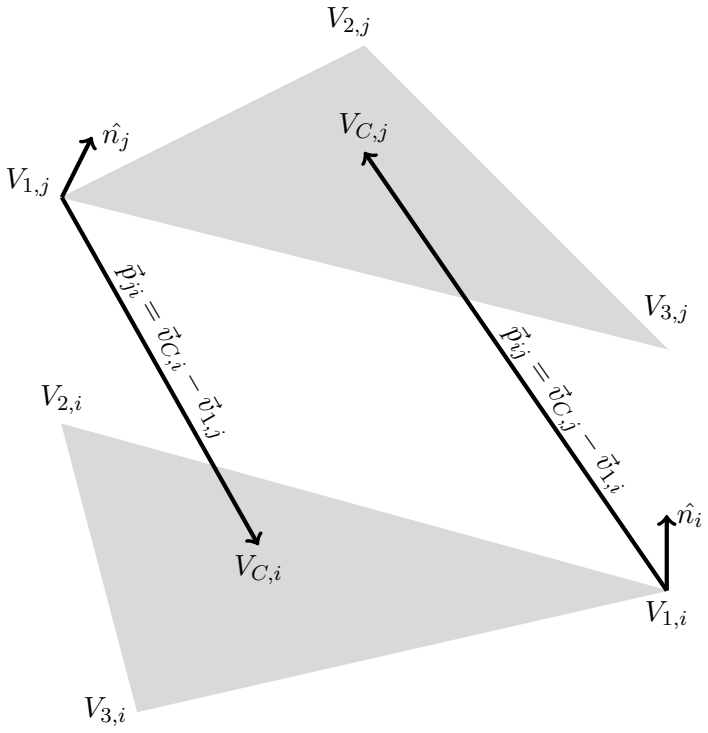

Figure 3.13: This figure displays a pair of facets that could potentially block one another. For one of these facets to cast a shadow over the other, it must be above the local horizon of the facet it is blocking. The vectors required to determine this are drawn in the figure with black arrows. The centre of the facet j is marked by $V_{C,j}$ and the vector $\vec{v}_{C,j}$, not drawn, points to this point from the origin of the asteroid. The vector $\vec{p}_{ij}$ points from the first vertex of the facet i to the centre of facet j.

For facet j to be blocked by facet i, facet j must be within line-of-sight of the centre of facet i. To determine this a ray is traced from the centre of facet i, $\vec{v}_{C,i}$, in the direction of $\hat{E}''$. This ray will intercept the plane of facet j at the point R_{ji}, which has a position $\vec{r}_{ji}$ from the first vertex of the facet j, $V_{1,j}$. The position of the interception point will be $\vec{r}_{ji} = \vec{p}_{ji} - \dfrac{\hat{n_j} \cdot \vec{p}_{ji}}{\hat{n_j} \cdot \hat{E}''}\hat{E}''$. Where $\hat{n_j} \cdot \vec{p}_{ji}$ was computed for each pair of facets when creating the map of blocker facets, and $\hat{n_j} \cdot \hat{E}''$ was also computed when determining if the facet is both illuminated and visible.

The vector $\vec{r}_{ji}$ can also be expressed as $\vec{r}_{ji} = s_{ji}\vec{a_j} + t_{ji}\vec{b_j}$, where s_{ji} and t_{ji} are coefficients of the non-orthogonal basis vectors, $\vec{a_j}$ and $\vec{b_j}$. Taking the dot product of the vector $\vec{r}_{ji}$ with respect to both $\vec{a_j}$ and $\vec{b_j}$ gives

$$\vec{r}_{ji} \cdot \vec{a_j} = s_{ji}(\vec{a_j} \cdot \vec{a_j}) + t_{ji}(\vec{b_j} \cdot \vec{a_j}) \tag{3.18}$$

$$\vec{r}_{ji} \cdot \vec{b_j} = s_{ji}(\vec{a_j} \cdot \vec{b_j}) + t_{ji}(\vec{b_j} \cdot \vec{b_j}) \tag{3.19}$$

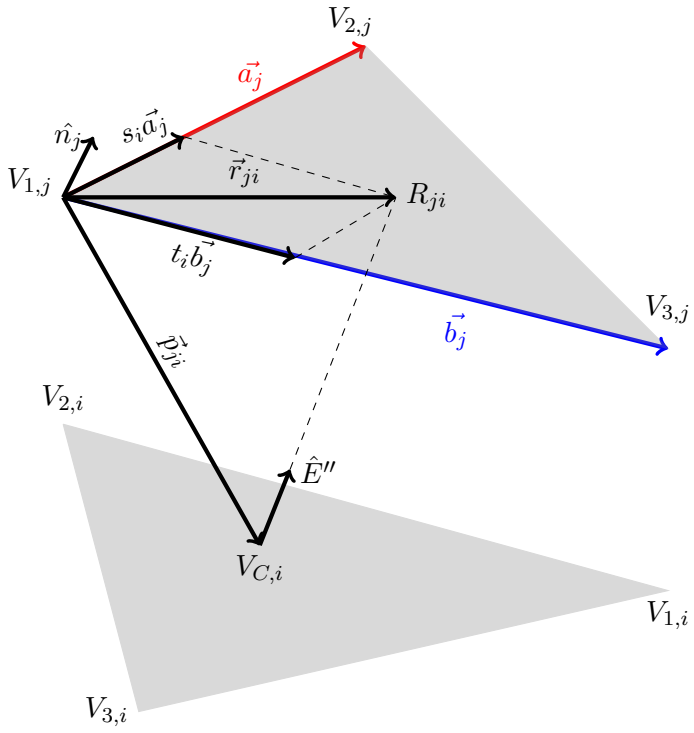

Figure 3.14: This figure displays a pair of facets, it highlights how the ray-tracing procedure determines whether or not the facet j is obstructed by facet i. A ray is traced from the centre of facet i in the direction of the vector $\hat{E}''$, which intercepts the plane of facet j at the point R_{ji}. If R_{ji} falls with in the facet j then it is obscured from either illumination or observation.

These simultaneous equations can be solved to give

$$t_i = \frac{(\vec{r}_{ji} \cdot \vec{a_j})(\vec{a_j} \cdot \vec{b_j}) - (\vec{r}_{ji} \cdot \vec{b_j})(\vec{a_j} \cdot \vec{a_j})}{(\vec{a_j} \cdot \vec{b_j})^2 - (\vec{a_j} \cdot \vec{a_j})(\vec{b_j} \cdot \vec{b_j})} \tag{3.20}$$

$$s_i = \frac{(\vec{r}_{ji} \cdot \vec{a_j})(\vec{b_j} \cdot \vec{b_j}) - (\vec{r}_{ji} \cdot \vec{b_j})(\vec{b_j} \cdot \vec{a_j})}{(\vec{a_j} \cdot \vec{b_j})^2 - (\vec{a_j} \cdot \vec{a_j})(\vec{b_j} \cdot \vec{b_j})} \tag{3.21}$$

The advantage of expressing the problem in this way is that the majority of the terms in these two equations are not reliant on the geometry, hence they can be pre-computed and recorded to improve the efficiency of the procedure. If both s_{ji} and t_{ji} are between zero and one (inclusive), then traced ray will intercept facet j and thus facet i is a blocker of facet j. If a facet is blocked then its contribution is excluded from the total brightness by setting the corresponding cosine, $\mu_\odot$ or $\mu_\oplus$, to zero. From this point the computation of the artificial light curve is the same as for convex shapes.

3.3.2 Determining changes in rotation period from phase offsets

By comparing the observed light curves with their synthetic counterparts, changes in the rotation period can be determined by measuring the phase offset, if any, required to align the two. The initial phase of the artificial light curves are calculated using Eqn. 3.8. Typically, this process is performed for a constant period model, ie a YORP strength of zero.

A range of phase offsets are applied to the artificial light curves, these phase offset cover one whole rotation with the step-size chosen by the user. For each phase offset applied the chi squared is recorded. The phase offset that results in the best alignment between the observations and synthetic light curve is recorded for each light curve in the dataset, in addition to its corresponding uncertainty.

The recorded phase offsets are then plotted against the number of days since t_0. A non-linear relation indicates a change in rotation period, with a quadratic trend being the signature of YORP. In order to measure the YORP strength, the phase offsets are fit to a curve of the form

$$\Delta\phi(t) = \Delta\phi_0 + \Delta\omega(t - t_0) + \frac{1}{2}\nu(t - t_0)^2 \tag{3.22}$$

where:

$\Delta\phi(t)$ the observed rotation phase offset [rad],

$\Delta\phi_0$ the error in the model's initial phase offset [rad],

$\Delta\omega$ the error in the model's rotation rate [rad/day],

ν the change in rotation rate [rad/day^2]; $\nu \equiv \dot{\omega}$ (YORP acceleration).

To stress, the phase offset is a measurement of the difference in rotation phase between the observed phase and the expected rotation phase for a constant period model. Hence one value is recorded per light curve. In other words, Eqn. 3.22 is equal

to Eqn. 3.8 for a non-zero YORP minus Eqn. 3.8 for a constant rotation period and zero YORP.

In the absence of YORP, if the recorded phase offsets form a linear trend, this indicates a non-zero value for $\Delta\omega$ which can be used to refine the model's rotation period. With the new rotation period, a new set of phase offsets can be calculated. This can be iterated until the $\Delta\omega$ becomes zero or becomes sufficiently small enough that it is negligible. Thus, the phase offsets are also able to perform refinements to the rotation period.

A non-zero $\Delta\phi_0$ indicates an error in the t_0 value chosen to propagate the model forward from. This can be remedied by converting the angular error measure into a time using the asteroid's rotation period, which can be used to correct the t_0 value. For the optimal determination of the YORP strength, both $\Delta\phi_0$ and $\Delta\omega$ should be either zero or negligibly small, so that only the quadratic term remains (see Fig. 3.15). This method to detect has been in the direct detection of YORP in the cases of: (54509) YORP, (25143) Itokawa, and (68346) 2001 KZ66 (Taylor et al., 2007; Lowry et al., 2007, 2014; Zegmott [submitted], see also Chap. 5).

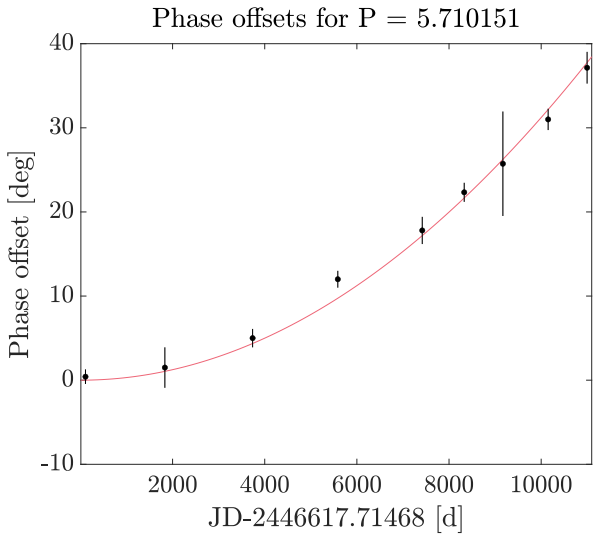

Figure 3.15: An example of the results of the phase offset analysis for the asteroid (3103) Eger. The measured phase offsets are shown by the black circles, in this figure they have been averaged for each year. The solid red curve is a purely quadratic fit to measure the YORP strength. The YORP measured here has a value of $(\nu = 1.1 \pm 0.1) \times 10^{-8} rad/d^2$, which is in agreement with Ďurech et al. (2018). The light curves and model were obtained from the DAMIT database.

4 First direct detection of a YORP 'spin-down': the case of (29075) 1950 DA

4.1 Introduction

The asteroid (29075) 1950 DA (hereafter DA) is an Apollo type NEA that was discovered on the 22 February 1950 by Carl A. Wirtanen at Lick Observatory (Wirtanen, 1950). Shortly after its discovery, it was lost until it was rediscovered on 31 December 2000 at Lowell Observatory as 2000 YK66, where it was promptly recognized as DA (LONEOS, 2001; Bardwell, 2001). DA has an Earth Minimum Orbit Intersection Distance (MOID) of 0.0401 AU[1] and so it is considered a Potentially Hazardous Asteroid - see Fig. 4.1 for a visualisation of the asteroid's orbit. DA has been observed in infrared wavelengths, in which it lacked thermal emissions about 2.5μm region. This was suggested by Rivkin et al. (2005) to indicate a high albedo (> 0.25) or a high thermal beaming η. The asteroid's spectrum was a close match to (3103) Eger, a known X-class asteroid. Ultimately, Rivkin et al. (2005) suggested a classification of an E or M type asteroid within the Tholen taxonomic system based on the high albedo constraint. However, observations since by NEOWISE suggest that DA has a low geometric albedo

[1] `https://ssd.jpl.nasa.gov/sbdb.cgi`

of 0.07 ± 0.02 (Mainzer et al., 2011), this in addition to the asteroid's low radar circular polarisation ratio (Busch et al., 2007) rule out the E-type classification (Rozitis et al., 2014). The observations by NEOWISE also suggested a diameter of 2.0 ± 0.2km for DA (Mainzer et al., 2011).

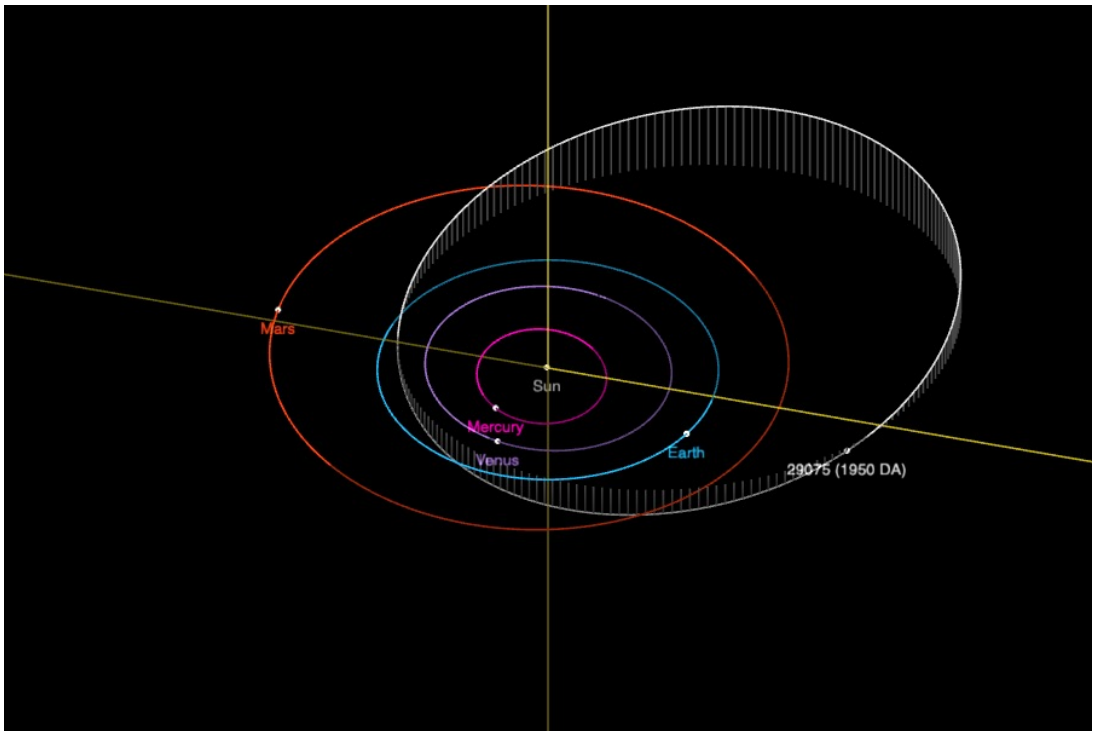

Figure 4.1: Diagram of the orbit of asteroid (29075) 1950 DA also showing the orbits of Mercury, Venus, Earth, and Mars. Positions of all objects are for the date 2020-09-01 00:00 UTC. Image produced using `https://ssd.jpl.nasa.gov/sbdb.cgi`

The first available optical light curves for DA are from 2001. There are four R-band light curves taken by P. Pravec between 29 January and 28 February 2001 (Pravec et al., 1998). These light curves revealed a rotation period of 2.12158 ± 0.00006 h, which was later reinforced by Busch et al. (2007) while modelling the shape of the asteroid. The shape modelling efforts resulted in two potential models for DA, one prograde solution with a pole orientation of $88.6° \pm 5°$ in ecliptic longitude and $77.7° \pm 5°$ in ecliptic latitude and a diameter of 1.16 ± 0.12km. The other solution is a retrograde model with the pole orientation $(187.4° \pm 5°, -89.5° \pm 5°)$ and diameter of 1.30 ± 0.13km.

With a rotation period of 2.1216 h, DA is just past the critical spin limit for a

cohesion-less rubble-pile asteroid held together by gravity and friction (Pravec and Harris, 2000). Past which, rubble pile asteroids are expected to undergo mass-lofting and structural disruption. Without cohesive forces acting on DA, a minimum bulk density of 3.5 g cm^{-3} would be required to prevent a loss of surface material due to centrifugal forces. But as an M-type asteroid with a similar radar albedo to (21) Lutetia, DA likely has a similar composition to Lutetia, the best meteorite analogue for which has a grain density of 3.55 g cm^{-3}. This would suggest that to achieve the required bulk density of 3.5 g cm^{-3}, DA would need to be quasi-monolithic with a near zero porosity. However, by combining the Busch retrograde model with a measured Yarkovsky drift of 44.1 ± 8.5 m yr^{-1}, Rozitis et al. (2014) used their Advanced Thermophysical Model to derive a bulk density of 1.7 ± 0.7 g cm^{-3} for DA. With a rotation period of 2.1216 h, this means that DA is rotating faster than possible to be held together by gravity and friction alone. Rozitis et al. (2014) concluded that cohesive forces, in the form of small Van de Waals forces, are preventing the rotational break up of DA.

An investigation of DA's orbit revealed a 20 minute window where the asteroid has a non-negligible probability of impacting the Earth. In 2880, this asteroid has a probability between $0 - 0.33\%$ of colliding with the Earth (Giorgini et al., 2002). However, this window of intersection is dependant on the influence of non-gravitational forces on DA's orbit. In other words, the probability of a collision is dependant upon the physical characteristics of the asteroid. Although the probability of a collision is low, the size of DA means that the implications of such a collision would have a catastrophic effect. Cases such as this highlight the importance of characterising NEAs. Further work in 2012, using two new Arecibo range measurements of DA suggest that the retrograde model was in fact the correct model (Farnocchia and Chesley, 2014). Using the new range measurements, the orbit of DA was refined and Yarkovsky predictions using the retrograde model reduced the probability of a 2880 collision to one in 4000, or 0.025%.

As an asteroid of interest in our ESO LP, we have been monitoring DA for nine

years between July 2010 and October 2019. The majority of our observations were carried out on the NTT - a 3.6 m telescope located in La Silla, Chile. During our observation campaign we obtained 19 light curves primarily in the R-band. Also in our dataset are published light curves, which extend our time-baseline back to 2001. Radar observations of DA are included in our data, these observations were taken from both Arecibo and Goldstone Observatories. A description of the telescopes used in our campaign and their configuration is discussed in Sect. 4.2. Additional details of the optical light curves are given in Table 4.1.

In this chapter, we will present the results and analysis of a long-term photometric monitoring programme to investigate changes in the object's rotation rate that could be due to YORP. The format of this chapter is the following: Sect. 4.2 thoroughly describes our observing campaign of DA. In Sect. 4.3 and 4.4, the analysis performed for this asteroid is reported. Finally, Sect. 4.5 provides a discussion of the results.

4.2 Observations of (29075) 1950 DA

4.2.1 Optical light curves

The complete optical dataset for DA covers a 19 year period from 2001 to 2019, of those light curves our observations cover the period from 2010 to 2019. However, initially our light curves only the period from 2010 to 2014, during the analysis of this object an additional set of light curves were obtained in 2019. A summary of all of the light curves used in this work is given in Table 4.1. Also included in the table are the details of the observing conditions: observer ecliptic latitude and longitude, orbital phase angle, and geocentric distance. Additionally, the observing geometries are displayed graphically in Fig. 4.2.

Our observations were taken using our standard observing strategy. An exposure time was selected such that the asteroid does not trail and also that the FWHM profile

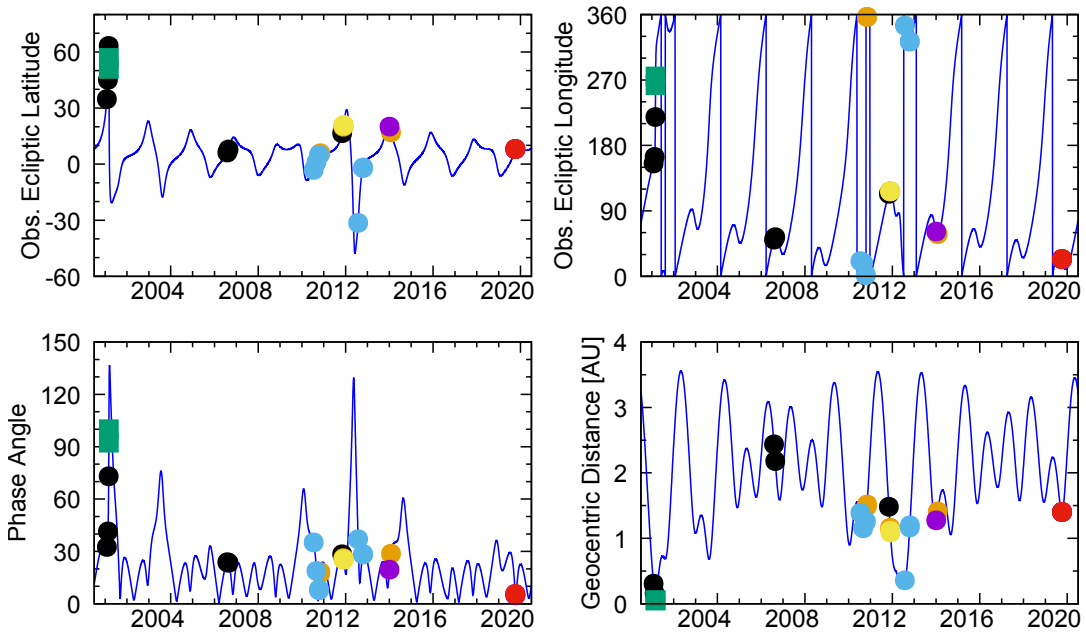

Figure 4.2: Asteroid (29075) 1950 DA observing geometries during the optical and radar observations over the period 2001 to 2019. The top two panels show the position of the object in the ecliptic coordinate system, latitude and longitude, as observed from Earth. The bottom two panels show the phase angle and geocentric distance to the target. Optical light curve data from the NTT are marked with filled blue circles, data from the INT are marked with filled purple circles, those from PAL are marked with orange filled circles, those from LT are marked by yellow filled circles, those from NOT are marked by red filled circles. Black circles represent the published light curve data. The green filled squares mark when the Arecibo radar data were collected. The blue continuous line represents the object's observational ephemeris.

of the asteroid falls within the seeing disk. However, the exposure time could not be a significant fraction of the rotation period. Sidereal vs differential tracking was chosen on a case-by-case basis depending on the asteroid's motion in each apparition. Differential photometry was used to extract light curves of the asteroid from the images. By comparing the asteroid to the average brightness of background stars, we are able to remove temporal variations in the observing conditions. In some cases, the signal-to-noise ratio of the images were low, thus requiring the co-addition of subsequent images to improve it. Datasets that required this additional step are noted later. All datasets were reduced using the standard CCD reduction procedures, unless otherwise stated. The light curves that were observed as part of our programme are those with IDs 7-12

and 14-26 in Table 4.1.

ID	UT Date [*dd/mm/yyyy*]	$R_\odot$ [AU]	$\Delta_\oplus$ [AU]	α [°]	λ_O [°]	β_O [°]	Total [hour]	Filter	Observing facility	Reference
1	29/01/2001	1.235	0.313	32.46	155.1	34.6	1.6	R	Ond	Pravec et al. (1998)
2	15/02/2001	1.104	0.162	41.00	163.7	44.6	3.4	R	Ond	Pravec et al. (1998)
3	16/02/2001	1.097	0.154	42.03	164.7	45.5	8.1	R	Ond	Pravec et al. (1998)
4	28/02/2001	1.011	0.067	70.51	212.7	62.9	2.1	R	Ond	Pravec et al. (1998)
5	03/08/2006	2.481	2.441	23.78	50.3	6.2	4.2	R	PAL	Busch et al. (2007)
6	24/08/2006	2.516	2.186	23.52	53.8	7.8	2.6	R	PAL	Busch et al. (2007)
7	16/07/2010	1.759	1.392	35.26	20.9	-3.1	2.5	R	NTT	
8	31/08/2010	2.027	1.155	19.12	18.6	1.0	2.5	R	NTT	
9	12/10/2010	2.222	1.248	7.50	2.3	4.8	1.9	R	NTT	
10	13/10/2010	2.226	1.256	8.05	2.0	4.9	1.6	R	NTT	
11	04/11/2010	2.309	1.498	17.66	356.8	5.7	3.2	R	PAL	
12	06/11/2010	2.315	1.524	18.29	356.6	5.8	1.1	R	PAL	
13	03/11/2011	2.007	1.489	28.36	113.3	16.5	0.6	R	KPNO	Gwyn et al. (2012)
14	24/11/2011	1.889	1.167	26.24	116.8	19.9	3.1	R	PAL	
15	26/11/2011	1.877	1.139	25.89	116.9	20.3	1.4	R	PAL	
16	27/11/2011	1.871	1.125	25.71	117.0	20.5	2.8	V	LT	
17	27/07/2012	1.274	0.356	37.65	345.4	-31.6	2.1	R	NTT	
18	17/10/2012	1.854	1.158	28.19	322.6	-2.1	2.5	V	NTT	
19	19/10/2012	1.866	1.190	28.42	323.0	-1.9	1.7	V	NTT	
20	03/01/2014	2.089	1.273	19.34	61.7	20.1	1.6	r'	INT	
21	30/01/2014	1.948	1.414	28.87	58.1	16.9	2.2	R	PAL	
22	06/10/2019	2.384	1.401	5.89	24.2	8.0	4.1	V	NOT	
23	06/10/2019	2.384	1.401	5.89	24.2	8.0	6.5	V	INT	
24	07/10/2019	2.387	1.402	5.45	23.8	8.1	7.2	V	NOT	
25	07/10/2019	2.387	1.402	5.45	23.8	8.1	6.6	V	INT	
26	08/10/2019	2.389	1.403	5.03	23.4	8.1	6.6	V	INT	

Table 4.1: A chronological list of optical lightcurves of asteroid (29075) 1950 DA used in this study. Each light curve has a numerical "ID" listed, then the Universal Time (UT) "Date" of the beginning of the night is given as well as the heliocentric ($R_\odot$) and geocentric ($\Delta_\oplus$) distances measured in AU, the solar phase angle (α), the observed ecliptic longitude (λ_O), the observed ecliptic latitude (β_O), and the "Observing facility" used to obtain the light curve. Where relevant a "Reference" to published work is given. Each line represents a single light curve (sometimes a few segments were observed on a single night). Observing facility key: Ond – 2 m telescope at the Ondřejov Observatory (Czech Republic), PAL – Palomar Observatory 5 m Hale Telescope (California, USA), NTT – European Southern Observatory 3.5 m New Technology Telescope (Chile), KPNO – Kitt Peak National Observatory 4 m Telescope (Arizona, USA), LT – 2 m Liverpool Telescope (La Palma, Spain), NOT – 2.5 m Nordic Optical Telescope (La Palma, Spain), INT – 2.5 m Isaac Newton Telescope (La Palma, Spain).

New Technology Telescope – 2010 and 2012

The majority of observations of DA come from the NTT and were obtained with the EFOSC2 instrument (Buzzoni et al., 1984). For a detailed description of this telescope and the others mentioned below, please refer to Sect. 2.1. The full 2048 x 2048 CCD array was used in imaging mode with a 2 x 2 binning, giving a field of view of 4.1' x

4.1'. A total of seven light curves were obtained: four nights in 2010 and three nights in 2012. The Bessel R filter was used in the 2010 observations and also in July 2012. However, for the two nights in October 2012, the Bessel V filter was used. The decision to switch to the Bessel V filter was multi-faceted, the largest benefit was in terms of image reduction. As images taken in the Bessel R filter required the additional step of de-fringing the images during the CCD reduction, a description of how this was performed is given in Sect. 2.1.4. Asteroids reflect a solar spectrum, so they are brightest in V. Additionally, the sky is darker in V than R. Finally, as this work only requires relative light curves, there were no calibrations needed to account for the change in filter. Light curves with IDs 7, 9, and 10 from Table 4.1 required co-addition of the image frames to improve the signal-to-noise ratio.

Isaac Newton Telescope – 2014 and 2019

Auxiliary campaigns made use of four other telescope facilities. The first is the INT and its WFC instrument (Ives et al., 1996) with which multiple runs were performed. For the 2014 observations, the CCD was not windowed making full use of CCD 4's 23' x 12' field of view. During these observations, it was observed for one night on the 3rd January using the Sloan-Gunn r filter. For the 2019 observations, a proposal which I led, the CCD was windowed to a field of view of 15' x 10' to decrease the read out time. During these observations the asteroid was observed for three nights in October using the Harris V filter. Light curves with IDs 20, 23, 25, and 26 required co-addition.

200-inch Hale Telescope – 2011 and 2014

DA was also observed from the Hale Telescope using the LFC (Gunn et al., 1987). DA was imaged two nights in August 2010, two nights in November 2011, and one night in January 2014. All images were taken using the R filter, with the CCD not windowed giving a field of view of 24' x 9'. The light curve with ID 11 required co-addition of the images.

Liverpool Telescope – 2012

The robotic Liverpool Telescope (LT) was used for one night to observe DA with the now decommissioned RATCam. A single light curve was obtained from this facility on the night of 27 November 2011. The images were taken using the Bessel V filter and the CCD was not windowed giving a field of view of 4.6' x 4.6'. This light curve, with the ID 16 in table 4.1, required the co-addition of subsequent images in order to improve the signal-to-noise.

Nordic Optical Telescope – 2019

The last telescope that we obtained data from was the NOT using ALFOSC in the imaging mode. DA was observed for two nights in October 2019 in the Bessel V filter. The CCD was not windowed for these observations, giving the images a 6.4' x 6.4' field of view. All of the light curves from this telescope required co-addition, their IDs are 22 and 24.

Published Light Curves

Previously published data for DA is also available, these include four nights of data from the Ondrejov Observatory, two nights from the 200-inch Hale Telescope, and one night from the Mayall 4-Meter Telescope. These light curves have IDs 1-6, and 13 in Table 4.1. The observations from Ondrejov Observatory comprise of four light curves taken across January and February 2001 with an R-band filter, these light curves were obtained pre-extracted. The Hale Telescope R-band observations were taken on two non-consecutive nights in August 2006 this data was provided by Michael Busch (private communication). Finally, the Mayall Telescope observations contain a short light curve segment from one night of observations taken in November of 2011. This data set was obtained from the Canadian Astronomical Data Centre (Gwyn et al., 2012).

4.2.2 Radar-derived shape models

As mentioned in the introduction, this asteroid has been previously modelled by Busch et al. (2007). They inverted a combination of both radar observations (discussed below) and a single epoch of optical light curves using `SHAPE`. Using a combination of grid searching and iterative fitting they searched for possible pole orientations which fit the observations. Their efforts revealed two potentially pole orientations, a prograde and a retrograde solution. The prograde solution has an ecliptic longitude and latitude of $(89°, +78°)$, and the retrograde solution is $(187°, -89°)$.

Further modelling of the asteroid's shape was performed for both of the potential pole orientations, increasing the number of vertices that describe each until the small-scale structure did not significantly improve. The final models are described by 1020 and 510 vertices for the prograde and retrograde models respectively. The prograde model has the appearance of a rough spheroid, it has a diameter of 1.16 km. The retrograde model's appearance in contrast is a relatively smooth oblate sphere, with a larger diameter of 1.30 km. However, the authors noted that discernable deviations remained between the models and the observations (Busch et al., 2007). The optimisation of both models resulted in the same rotation period of 2.12160 ± 0.00004 hours and their shapes are displayed below in Fig. 4.3.

With the increased range of observing geometries covered by the new light curves obtained by the ESO LP and auxiliary campaigns, the analysis within this chapter will reanalyse all of the available data to define a single pole orientation for DA. Additionally, with an extensive light curve dataset covering several epochs, a comprehensive investigation of the asteroid's spin-state will be performed in order to determine if any changes are occurring in DA's rotation rate which could be due to the YORP effect.

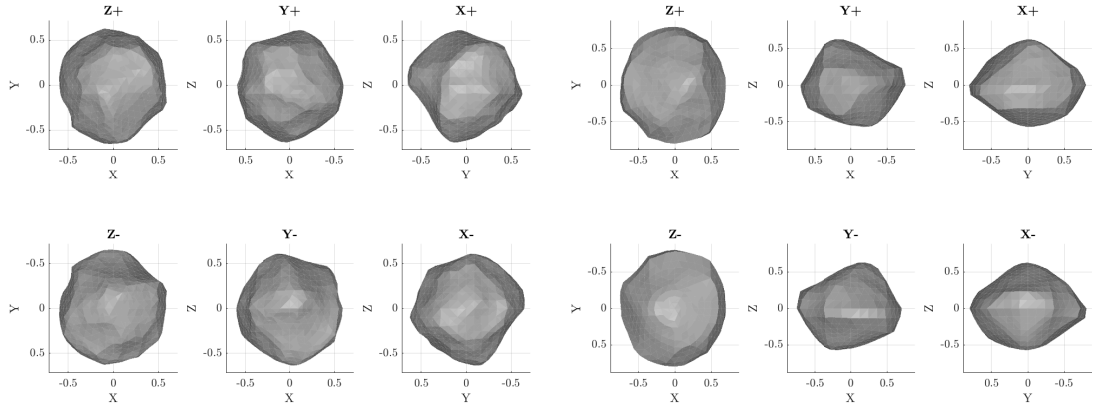

Figure 4.3: Two published shape models for the asteroid (29075) 1950 DA. The models were both produced by Busch et al. (2007) using a combination of both radar observations and optical light curves. The left panel of six images displays the prograde model, and the six on the right show the retrograde. The axes are given in units of km.

4.2.3 Radar Observations

Radar observations are a powerful tool in determining an asteroid's shape. However, the advantage of actively illuminating the target with a controlled radio signal comes with the drawback of a greater inverse dependence on the distance to the target, as the signal must travel to the target and back. Due to this dependence, objects making a close approach are good observing targets as they provide observational data with a higher signal-to-noise ratio. During March of 2001, DA made a such an approach passing by at 0.05 AU from Earth. This made the asteroid a strong target for radar observations and as such, DA was observed from both Arecibo and Goldstone. These data were provided by Michael Busch (private communication) and an overview of them is given below.

Arecibo Observatory – 2001

Observations of DA were performed with Arecibo Observatory on two nights: 3 and 4 March 2001. Delay-Doppler imaging was performed on both nights. On the first night, the baud length was set to 0.2 μs and sampled twice per baud. For the second

night the baud length was changed to 0.1 μs but only sampled once per baud. This results in both nights' image resolution corresponding to 15 m in delay. Additionally, continuous wave spectra were taken on the 4 March 2001. A detailed overview of the radar observations can be found in Table 4.2.

Goldstone Observatory – 2001

Observations of DA were also performed during the same period at Goldstone Observatory. These observations were carried out on three nights: 3, 4, and 7 March 2001. Solely delay-Doppler imaging was performed from this observatory. A mixture of two baud lengths were used, 0.25 μs and 1.00 μs and all observations were sampled once per baud. These baud lengths correspond to delay resolutions of 37.5 m and 150 m respectively. Although the Goldstone observations are coarser, the manoeuvrability of DSS-14 allowed the observation of DA to continue for a longer duration. The details of the Goldstone observations are also included in Table 4.2.

UT Date [*yyyy-mm-dd*]	Telescope	Baud [μs]	Spb	Resolution [m]	Start-Stop [*hh:mm:ss-hh:mm:ss*]	Runs
2001-03-03	A	0.2	2	15	11:27:51-11:59:32	18
	G	1.0	1	150	15:32:56-15:55:54	13
	G	0.25	1	37.5	16:04:47-18:14:45	61
2001-03-04	G	0.25	1	37.5	10:09:56-11:30:38	36
	A	cw	N/A		10:39:41-11:08:17	13
	A	0.1	1	15	11:10:41-12:00:04	28
2001-03-07	G	1.0	1	150	12:11:30-16:31:17	115

Table 4.2: Radar observations of asteroid (29075) 1950 DA from March 2003. "UT Date" is the universal-time date on which the observation began. "Telescope" indicates from which observatory the observations were performed: A - Arecibo, G - Goldstone. "Baud" is the delay resolution of the pseudo-random code used for imaging; baud does not apply to cw data. "Spb" is the number of complex samples per baud giving an effective delay resolution of baud/spb. The delay "Resolution" is dependant upon the baud and the number of samples taken per baud. For a baud of 0.1 μs and one sample taken per baud this corresponds to a delay resolution of 15 m. The timespan of the received data is listed by the UT *start* and *stop* times. "Runs" is the number of completed transmit-receive cycles.

4.3 Combining the published radar shape models and new optical light curves

4.3.1 Searching for YORP with the published models

As DA has been previously modelled, the first step of analysis in this work was to utilise the shape models generated by Busch et al. (2007) and combine them with the extensive newly obtained set of optical light curves. This extended dataset, covering multiple epochs, obtained by the ESO LP enabled an investigation of the asteroid's spin-state with the aim of directly detecting YORP. Due to YORP's quadratic nature when described in terms of rotation phase, the additional epochs sampled by the new light curves would allow the measurement of YORP strength acting on the asteroid via the measurement of phase-offsets. As discussed in the introduction, Busch et al. (2007) produced two viable shape models for DA: the prograde model and the retrograde model. Neither model has since been ruled out, however, indirect evidence has lead to the preference of the retrograde model (Farnocchia and Chesley, 2014). Therefore, both models were examined to investigate whether the additional light curves were able to rule out one of the models and to search for any traces of a YORP acceleration via phase-offsets.

As described in Sect. 1.3.2, the YORP effect produces a miniscule torque, which leads to a secular change in an asteroid's rotation period. The direct detection of this effect requires long-term monitoring of an asteroid's rotation rate over an extended period of time. The longer that the asteroid is monitored the greater the opportunity of detecting YORP. This is due to the quadratic signature that YORP has on rotational phase, which can be measured by investigating the phase offset required to align an asteroid's light curves with synthetic light curves generated using a shape model (see Sect. 3.3.2). The ESO LP observing campaign had been monitoring DA for four years, between 2010 and 2014. This was later extended by new data obtained in 2019, however,

that data was not yet available during this stage of analysis. Although, additional published light curves taken in 2001 and 2006 extend the duration to 14 years (Busch et al., 2007). For the analysis, this gives a total baseline of 4749 days. Over this period, a YORP acceleration larger than 2.32×10^{-8}rad/d^2 would be required to produce a measurable shift in rotation phase larger than 15°.

Synthetic light curves for both models were created at epochs matching the observations using our customised `MATLAB` software (described in Sect. 3.3). The initial time from which the models are propagated, T_0, was fit for as this was not published for the Busch models. This was performed by selecting a Julian Date near the time of the first light curve which resulted in the best alignment, as this light curve was also the first in Busch's modelling of DA (Busch et al., 2007). For each model, a single T_0 was produced. From which each model was propagated forward in time with a fixed rotation period of 2.12160 ± 0.00004 hours. A subset of the resulting synthetic light curves are shown below in Fig. 4.4.

Figure 4.4 shows that both models are able to reproduce the light curves from the 2001 epoch, as expected due to the fact that they were used in the creation of both models. However, for the ESO LP light curves from later epochs (particularly for 2012), two issues are noted: firstly, the light curves do not align, but it is not just an issue of a misalignment in phase. Secondly, and more significantly, the artificial light curves have a different shape to the observed light curves. This could indicate that the asteroid has undergone a change in spin-state or that the shape of the asteroid has changed. To investigate this, new attempts to model the asteroid's shape and spin-state are required.

4.3.2 Revision of the published shape models

As the published shape models were unable to reproduce the new light curves obtained by our observing campaign, the first attempt to address this problem was to make minor edits to both the models' shape and pole orientation. The dataset used to perform this modelling includes all of the published data on DA and also includes

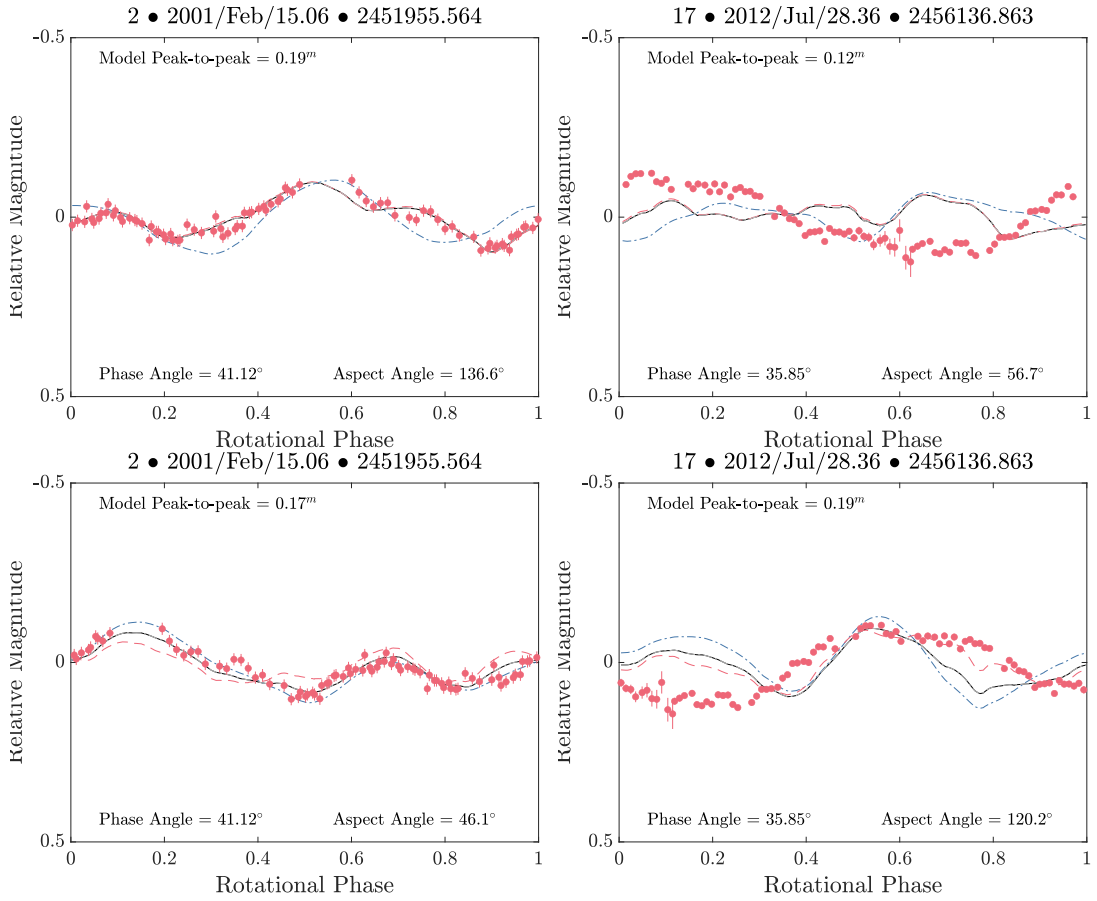

Figure 4.4: Artificial light curves for both the prograde and retrograde published models (Busch et al., 2007). The top two panels are produced using the prograde model and the bottom two with the retrograde model. Shown here is a subset of the light curves, the full set are shown in the appendix (see Figs. A.1 and A.2). The artificial light curves were produced using a variety of scattering laws. The blue dash dot line is the artificial light curve generated using the Lambertian scattering law. The red dashed line was generated with the Lommel Seeliger scattering law. The black solid line was generated using the Kaasalainen scattering law. Finally, the red dots show the observed light curves.

the new light curves obtained as part of the ESO LP and supporting campaigns. For each model, a several new pole orientations surrounding the original pole orientation were investigated. The pole orientations were spread out equally, within $\sim 10^\circ$ of each model's original pole. For the prograde model, the poles were arranged in a square grid around a longitude of 90° and a latitude of 80° (note the original pole is located at longitude of 88.6° and latitude of 77.7°) with $\pm 10^\circ$ added to either the longitude or latitude. For the retrograde model, as its pole is within a few degrees of the ecliptic

south pole, the poles were chosen to form rings around this point. The first ring was at a latitude of $-85°$ and with three different longitudes increasing in steps of 120° starting from a longitude of 0°. The second ring was at a latitude of $-80°$ and with four longitudes increasing in increments of 90° from 0°.

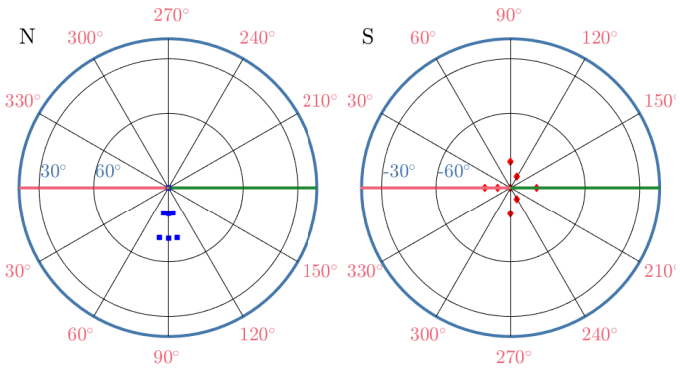

Figure 4.5: Illustration of the pole orientations used for the modified shape models, generated by making small edits to the published shape models. The blue dots mark pole orientations used for the edits of the prograde model and the red mark those for the retrograde model edits.

Fitting the adjustments was performed in two stages. In the first stage, the scaling which allowed alteration of the model's axial ratios, in addition to the rotation period and the initial rotation phase were all set as free parameters to be optimised. For the second stage, the scaling was held constant and this time the shape of the model was optimised. The number of vertices that represented each model were kept the same as when the models were published, 1020 vertices for the prograde model and 510 for the retrograde. This results in the prograde and retrograde models having a mean facet edge length of 75 m and 137 m respectively, much larger than the maximum resolution of the delay-Doppler image (15 m).

The results of these edits produced minute changes in the shape of the models. The resulting best-fit model for the prograde group has a pole orientation of (80°,+80°). Although, a second solution at (90°,+80°) has a negligible difference in chi-squared, less than 1%. Note that both of these pole orientations bracket the original prograde pole orientation at (88.6°,77.7°). Similarly, for the retrograde model the resulting best-fit model has a pole orientation of (0°,−85°), but again several other pole orientations also have similar chi-squared values. This is not unexpected as the original pole orientations were reported in the literature with uncertainties of ±5° (Busch et al., 2007). Given that

the resulting shapes had minimal changes to their morphology, these models produce similar synthetic light curves to the originals and thus are unable to replicate our additional light curves.

4.4 Remodelling (29075) 1950 DA with combined radar and optical observations

The modelling undertaken in this chapter is extensive, up to this point the analysis performed has been focused on using the published Busch models to reproduce the newly obtained light curves. Here on begins the development of a new models for DA starting from scratch. This is the point in Fig. 4.6 where the flowchart branches. The left branch contains the light-curve-only analysis, in contrast, the right branch lists the combined radar and optical analysis. The different colours and shapes of the fields in Fig. 4.6 are used to highlight their differences. The rounded boxes indicate the input of data into the analysis, with red indicating published data sources and blue listing the input of data obtained as part of the ESO LP and auxiliary programmes. The orange fields indicate the steps that were taken at each stage of the analysis of DA. The majority of the analyses performed do not include the 2019 light curves, as these stage of analysis were performed before that year.

4.4.1 Pre-2019 shape and spin-state analysis of (29075) 1950 DA

Search for pole orientation using light curve inversion

As the new light curves could not be reproduced by the published models of DA or their edited versions, all of the light curves available at this point in time (IDs 1-21 listed in table 4.1) were inverted using `convexinv` in an effort to discover if a single pole orientation would be able to reproduce them all. The entire celestial sphere was scanned over using a $5° \times 5°$ grid of pole orientations in ecliptic coordinates. For each fixed pole orientation, the shape and rotation period of the asteroid were optimised (as

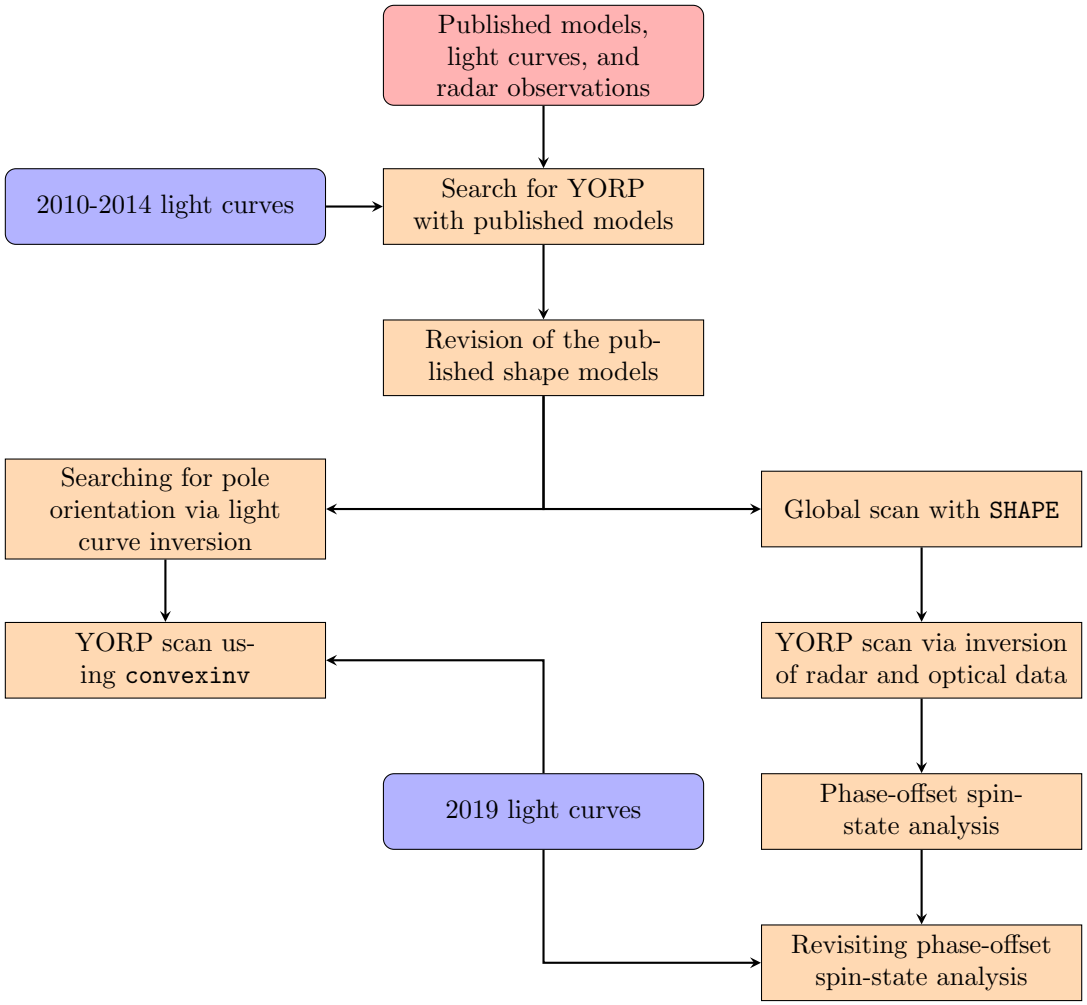

Figure 4.6: Overview of the analysis undertaken during the investigation of DA. The red rounded field lists the published data that has been input into this work and the blue rounded fields list the data obtained by the ESO LP and auxiliary programmes that were input. Orange fields indicate the steps taken at each stage of the analysis, splitting into two branches; the left branch contains the light-curve-only analyses and the right branch contains the combined radar and optical analyses.

discussed in Sec. 3.1). In addition, the chi-squared value at each pole was recorded and this was used to produce Fig. 4.7. The scan reveals a single region that is within 1% of the minimum chi-squared value, which is located about a ecliptic longitude of 185° and latitude of 35°. Note that this pole orientation is located near the celestial equator, away from both of the pole orientations reported in the literature.

A second pole scan was performed with the same dataset, this time focusing on the region containing the chi-squared minimum which was scanned at a higher resolution.

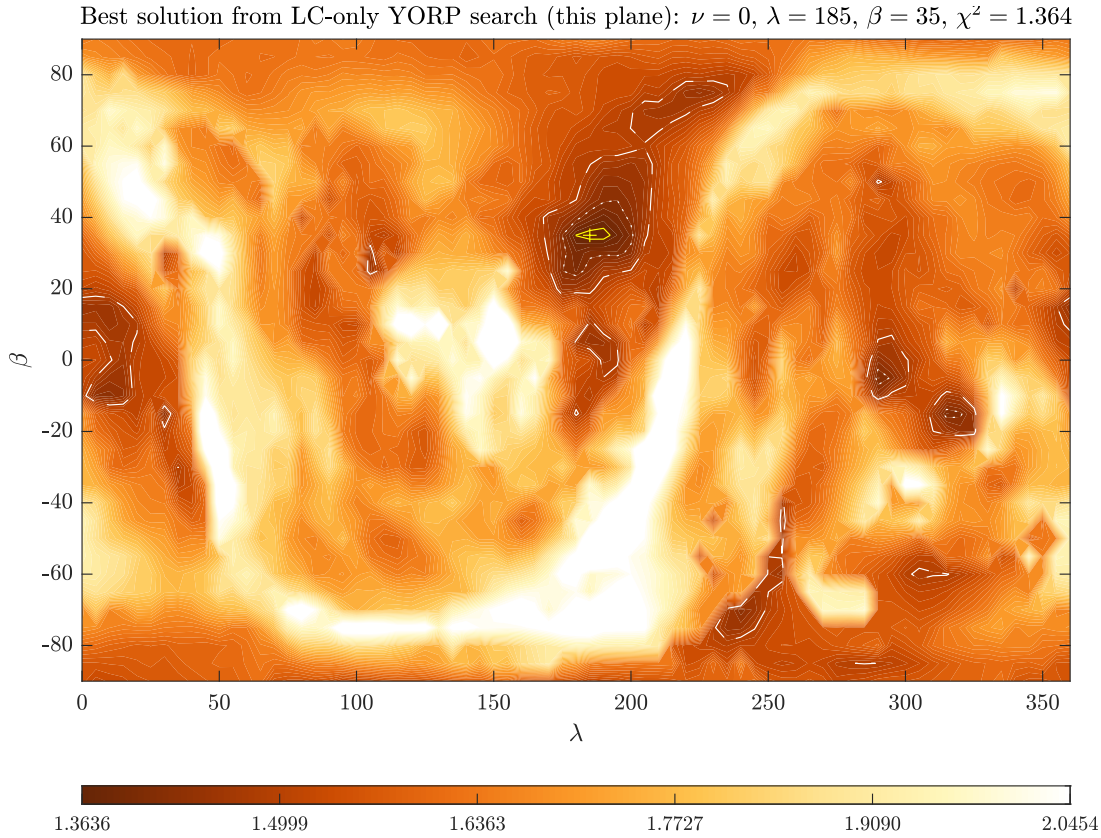

Figure 4.7: Results of the `convexinv` pole scan. This scan utilised the light curves from 2001 to 2014, probing fixed pole orientations covering the entire celestial sphere with a resolution of 5° × 5° in ecliptic coordinates. The resulting chi-squared value from the optimisation of each pole's model shape and rotation period are displayed here. With darker colours indicating a better fit, the pole with the lowest chi-squared is marked by a yellow cross and the solid yellow, dotted white, and dashed white contours show an increase of 1%, 5%, and 10% respectively.

A grid of poles was setup over the region 160° to 240° in longitude and 10° to 80° in latitude with a resolution of 2° × 2°. Again, at each fixed pole the shape and rotation period were optimised and the chi-squared value was recorded. The results of the second scan are displayed in Fig. 4.8.

The result of the scan indicates the best pole orientation to be within a 20° radius of ecliptic longitude 190° and latitude 34°. The model produced for this pole orientation has a quasi-triangular shape when viewed from the x-axis and has an almost circular pole-on silhouette. None of the shape's features appear non-physical and the degree of flattening seen from the negative z-axis is not excessive. See Fig. 4.9 for a panel

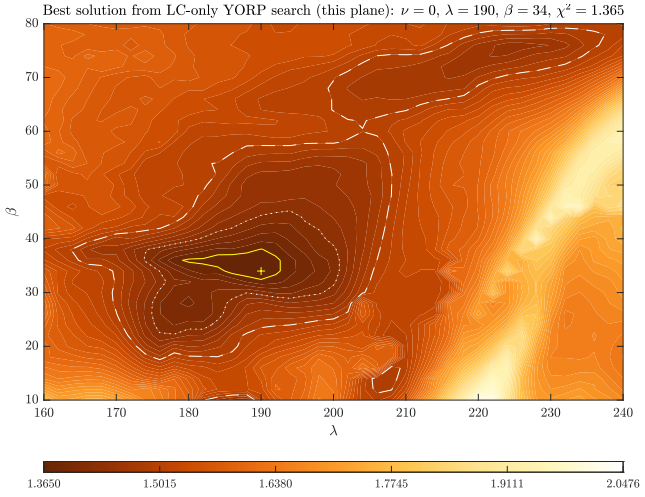

Figure 4.8: Results of the subsequent `convexinv` pole scan. This scan probed fixed pole orientations covering a region celestial sphere surrounding the solution in Fig. 4.7. The resolution of this scan is $2° \times 2°$ in ecliptic coordinates. The resulting chi-squared value from the optimisation of each pole's model shape and rotation period are displayed here. With darker colours indicating a better fit, the pole with the lowest chi-squared is marked by a yellow cross and the solid yellow, dotted white, and dashed white contours show an increase of 1%, 5%, and 10% respectively.

of images showing the convex model along its body-fixed axes. The `convexinv` model is able to reproduce more of the light curves than the published models, particularly those that are of higher quality. All of the synthetic light curves can be found in the appendix in Fig. A.3.

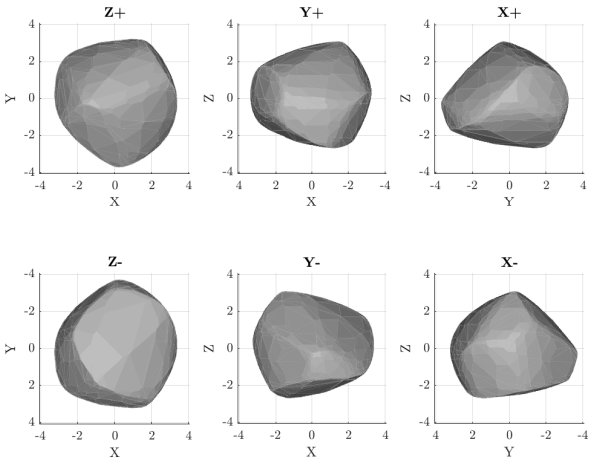

Figure 4.9: The convex shape model of (29075) 1950 DA. The model was produced from a pole search using light curve data only, assuming a constant period, the pole is located at $\lambda = 190°$, $\beta = 34°$. *Top row* (left to right): views along the Z, Y and X axes of the body-centric coordinate frame from the positive end of the axis. *Bottom row* (left to right): views along the Z, Y and X axes from their negative ends. The model's z-axis is aligned with the rotation axis and axis of maximum inertia. The light curve convex inversion model is not scaled and the units shown are arbitrary.

Global scan - simultaneous optimisation of the shape, period, pole, and YORP strength with SHAPE

Another method used to model DA was to utilise a global approach, this involved inverting all of the data available at the time (pre-2019) - both radar observations and the 2001-2014 optical light curves (IDs 1-21). This approach modelled the asteroid in two stages: those where the asteroid is represented first by ellipsoidal components, and the second where the descriptions are then converted spherical harmonic components (these component descriptions are described in Sect. 3.2.2). The advantage of this two-stage approach opposed to a single-stage is the reduction of required computing time, as a reduced number of parameters describe an ellipsoid which allows the general axial ratios of the model to be optimised quickly. The following spherical harmonic stage then further optimises the shape allowing the model to reflect more detail of the asteroid's morphology.

As the retrograde model is the preferred model in the literature, the shape's starting point is an ellipsoid component with the same axial ratios as Busch's retrograde model (Busch et al., 2007; Farnocchia and Chesley, 2014; Rozitis et al., 2014). Copies of this ellipsoidal model are setup with fixed pole orientations covering the entire celestial sphere, the poles are separated by 30° in both longitude and latitude. This coarser grid of pole orientations was chosen due to the increased computing time required to invert the combined radar and optical data. Additionally, this was repeated for multiple YORP strengths: $\pm 5 \times 10^{-7}\,\mathrm{rad/d^2}$, $\pm 1 \times 10^{-6}\,\mathrm{rad/d^2}$, and a constant period or zero YORP. The parameters that are optimised include the shape's axial ratios, the rotation period, and the initial rotation phase.

Upon completion of the optimisation of the ellipsoidal models, the models are converted to a spherical harmonic description. The shape of the spherical harmonic models were described by 81 parameters, in contrast to the three parameters that describe an ellipsoidal component. For each of the pole orientations, these spherical harmonic models were then optimised with the free parameters including their shape, rotation

period, and initial rotation phase. The resulting chi-squared value for each pole orientation was recorded and used to produce a chi-square plane for each YORP value, these are displayed in Fig. A.4 of the appendix.

The results of this scan revealed three different pole orientations over the five YORP strengths. Two YORP planes obtained a pole of (300°,0°) and another plane reported a similar pole of (270°,0°). The final two planes obtained (210°,30°) as the best-fit pole orientation, which is in a region close to the pole from the `convexinv` analysis reported in Fig. 4.8. Due to the coarseness of the scan, these poles are all reported with an uncertainty of ±30°.

A reliable determination of preferred YORP strength from this scan was not possible due to the lack of data points produced by this scan. Across the range of YORP strengths probed the chi-squared values are all fairly flat, with all points in this scan within ∼5% of the chi-squared minimum. In order to probe YORP, the resolution of YORP strengths in the scan would have to be increased. However, this scan required significant computing time for only five YORP planes with a coarse grid of poles. Unfortunately, a higher resolution scan over both pole orientation and YORP was not possible, as that would require an unreasonable amount of computing time.

Generating YORPogram from inversion of combined radar and optical data

As mentioned at the end of the last section, a significant amount of computing time was required to perform the global scan. However, the resolution of the YORP planes in this analysis was not sufficient to obtain any useful insight. In order to increase the number of YORP planes scanned while not requiring an impractical amount of computing time, the number of pole orientations probed was reduced. The poles chosen contained two poles determined from the earlier analysis and both of Busch's poles from the literature. From the previous analysis, the pole (270°,0°) was omitted due to its proximity to the more prevalent pole located at $(300°, 0°)$. As such, the two poles utilised from the

previous analysis are (210°,30°) and (300°,0°).

The scan was configured to increase the resolution of the shape's description during the fitting process by using two different descriptions: both ellipsoidal and spherical harmonic components, as done during the global scan. The parameters optimised during the fitting include the rotation period, initial rotation phase, and shape of the asteroid. Additionally, penalty functions were also employed to discourage non-physical features (see Sect. 3.2.2). The penalties applied were used to keep the asteroid's centre of mass aligned with the origin of the body-fixed frame and also to keep the z-axis aligned with the largest inertial axis. Initially, this scan probed YORP strengths between $\pm 1.5 \times 10^{-6}$rad/d^2 with a resolution of 1.25×10^{-7}. In subsequent phases of the scan, the range was extended and resolution of YORP strengths probed were chosen in reaction to the results of the previous phase. For instance, if a phase of the scan displayed a minima that was starting to emerge between the region -10 to -20, then the subsequent phase would be focused on improving the resolution within this region and bracketing the minima. This resulted in the final phase of the YORP scan ranging from -3×10^{-6}rad/d^2 to 1.5×10^{-6}rad/d^2 with a variable resolution. The results of the initial and final phases of this scan are shown in the left and right panels of Fig. 4.10 respectively.

Crucially, the result of the final phase of this scan indicate, firstly, that our poles from the previous stages of analysis are the best-fit pole orientation for the majority of YORP strengths probed. Secondly, that solutions with negative YORP provide the best-fit to the data. There are three YORP strengths that are with 1% of the chi-squared minimum value, these values are -1.203×10^{-6}, -1.541×10^{-6}, and -2.075×10^{-6}rad/d^2. It is worth noting that there are also solutions in the positive YORP region that are about 5% above the chi-squared minimum. These are located at 5.00×10^{-7} and 9.75×10^{-7}rad/d^2.

Inspection of the models produced by this scan show that the shape of the positive YORP models appear very oblate in shape, flattened in the z-axis. The shapes of

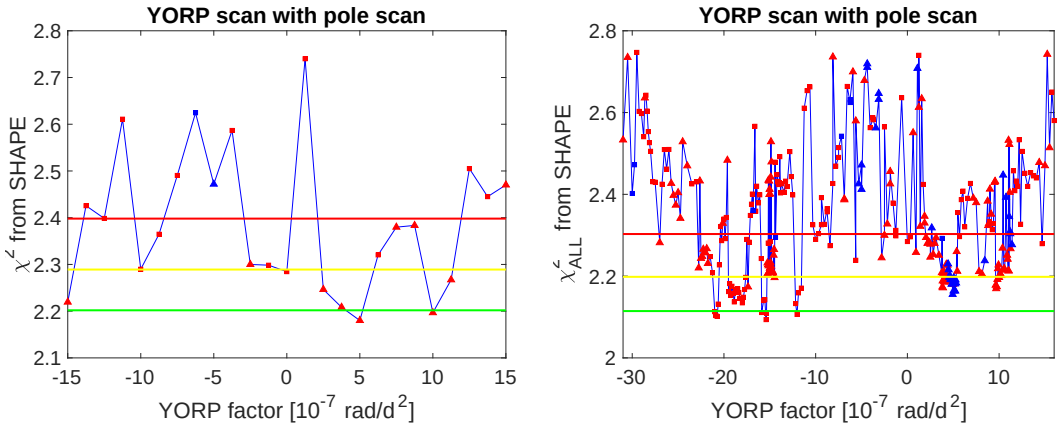

Figure 4.10: Chi-squared value of the best-fit model for each YORP strength probed. The markers signify the pole orientation of the best-fit model, with red signifying our poles and blue representing the Busch model poles: red triangle = $(210°, +30°)$, red square = $(300°, +0°)$, blue triangle = $(360°, -90°)$, and blue square = $(85°, +75°)$. For each model, the shape, rotation period, and the initial rotation phase was optimised. The green, yellow, and red lines mark 1%, 5%, and 10% above the overall chi-square minimum of the scan. The left panel show the initial phase of the scan and on the right the final phase is displayed.

the negative YORP solutions appear more plausible with a less oblate morphology. The resulting shape of the best-fit spherical harmonic model for a YORP strength of -2.075×10^{-6}rad/d^2 is shown below in Fig. 4.11 and other models are shown in appendix Fig. A.5. Focusing on the -2.075×10^{-6}rad/d^2 model, the maximum extent of the model along its body-fixed axes is $1.317 \times 1.256 \times 1.086$ km for the x-,y-, and z-axis respectively. The diameter of the model's equivalent-volume sphere has a value of 1.209 km. These dimensions are in agreement with those reported by Busch et al. (2007), but smaller in diameter than the 2.0 ± 0.2km recorded by the NEOWISE survey (Mainzer et al., 2012). Using this model with a YORP strength of -2.075×10^{-6}rad/d^2 to create synthetic observations, the model is able to reproduce the majority of the light curves and delay-Doppler images - a subset of these are shown in Figs. 4.12 and 4.13. When the other models were used to generate synthetic light curves, they were all unable to reproduce as many of the light curves as the model from the -2.075×10^{-6}rad/d^2 YORP plane. Hence, based on the visual inspection of models' ability to reproduce the data, the -2.075×10^{-6}rad/d^2 YORP plane model was considered the preferred model

henceforth. Although the model is able to generally reproduce the data, it should be noted that the model doesn't perfectly reproduce all of the delay-Doppler images, this is particularly prominent in the figure below. The model is able to reproduce the height and width in delay and Doppler shift, but it struggles to reproduce the sharper features displayed in the data.

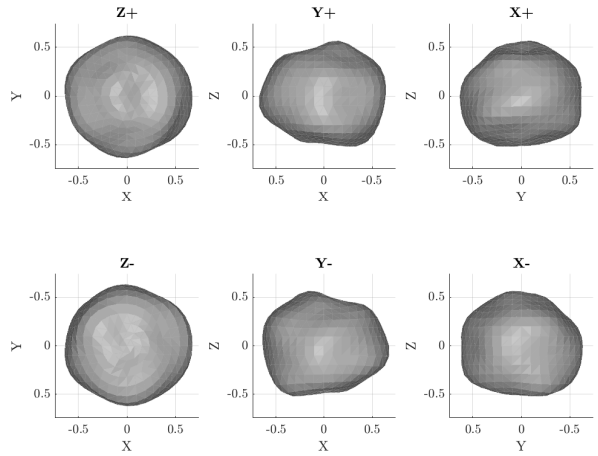

Figure 4.11: The resulting best-fit shape model of DA from a combined radar and optical data inversion for the -2.075×10^{-6}rad/d^2 YORP plane. The model has a pole orientation of $(300°, 0°)$. *Top row* (left to right): views along the Z, Y and X axes of the body-centric coordinate frame from the positive end of the axis. *Bottom row* (left to right): views along the Z, Y and X axes from their negative ends. The axes scales are shown in kilometres.

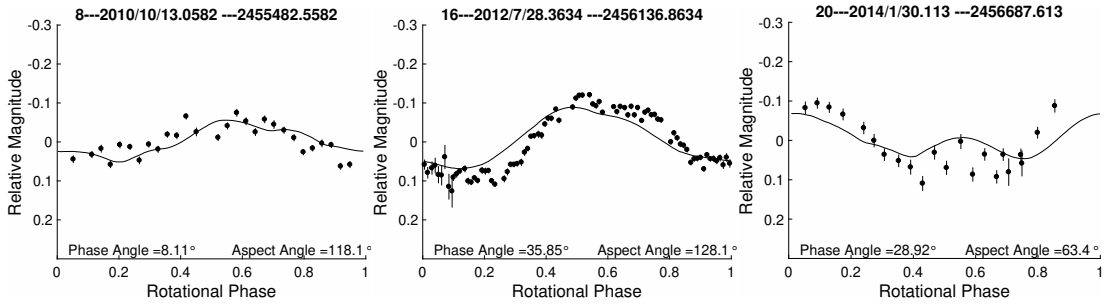

Figure 4.12: Synthetic light curves generated with the best-fit spherical harmonic model of (29075) 1950 DA. The model was propagated forward with a rotation period of 2.1216 hours and a YORP strength of -2.075×10^{-6}rad/d^2 (corresponding to the YORP strength the model was optimised with).

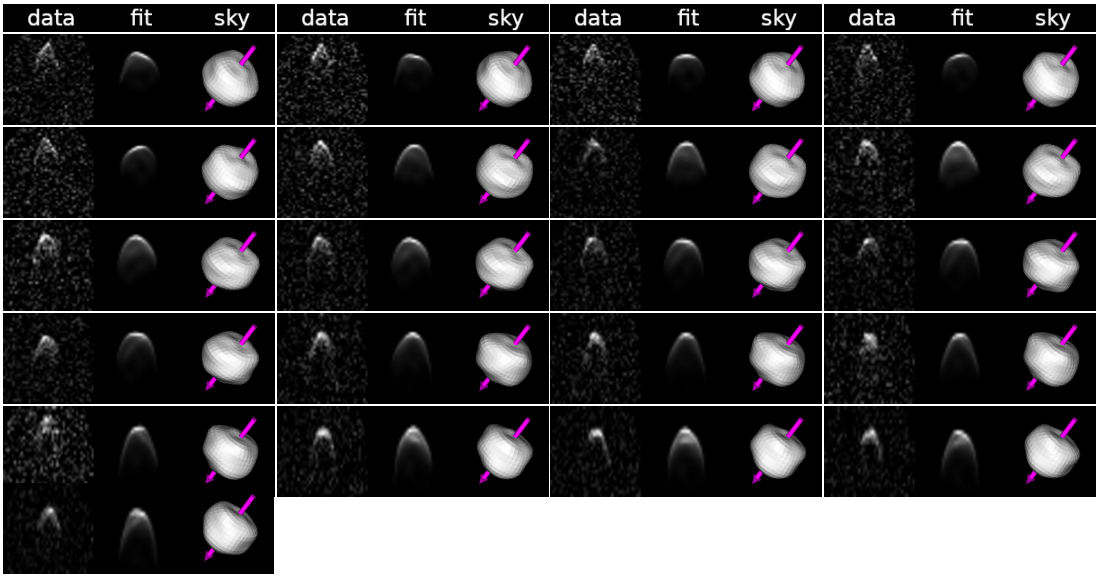

Figure 4.13: Fit of the best-fit spherical harmonic model of asteroid (29075) 1950 DA to the radar data. Each three-image sub-panel is comprised of: the observational data (left panel), synthetic echo (middle panel), and plane-of-sky projection of the best-fit model (right panel). On the data and synthetic-echo images the delay increases downwards and the frequency (Doppler) to the right. The plane-of-sky images are orientated with celestial north (in equatorial coordinates) to the top and east to the left. The rotation vector (Z-axis of body-fixed coordinate system) is marked with a pink arrow. This sequence of images corresponds to Goldstone data collected on 3 March 2001.

Phase-offset spin-state analysis

In an attempt to confirm the negative YORP strength of -2.075×10^{-6}rad/day^2 identified in the YORP scan, a phase-offset analysis was performed using the shape model derived using radar observations and optical light curves but removing the YORP strength and using a constant period. A phase-offset analysis probes an asteroid for changes in its spin-state by measuring the difference in rotation phase between the observations and synthetic light curves - an in depth description of this can be found in Sect. 3.3.

Over the period from 2001 to 2014, a baseline of 4749 days, if the asteroid does have a YORP strength of -2.075×10^{-6}rad/day^2 then a phase offset of 1340° is expected. This is an extremely large phase offset, as only values within one rotation or 360° are able to be directly measured. This is due to the fact that phase-offsets separated by 360°

will have the same chi-squared value, ie a phase-offset of 90° or 450° would result in the same goodness-of-fit. In order to reduce the expected phase-offsets to fall within 360°, a restricted light curve set was used in the phase-offset analysis spanning 2010 to 2014. With the reduced dataset and the expected YORP strength of -2.075×10^{-6}rad/day^2, the resulting expected phase-offset should be 130°. Additionally, by restricting the light curves to those taken between 2010 and 2014, the dataset utilised is limited to those light curves that were reduced and extracted by the author.

To perform a phase-offset analysis requires that the first observed light curve and its synthetic counterpart are aligned. This is done by determining a suitable T_0 value close to the time of first data point of the first light curve. From this initial epoch, the model was propagated using the constant rotation period, 2.121596 hours, determined during the model's optimisation. At the epoch of each light curve, a synthetic light curve is generated using the method described in Sect. 3.3.1. The difference in rotation phase between the observed and synthetic light curve is then measured by measuring the goodness-of-fit between them when applying a range of phase offsets. The range of phase offsets applied ranged from −180° to +180° in steps of 0.5°. Lastly, the individual phase-offsets were grouped by epoch. This is done by taking the average phase-offset of the group and the uncertainty is the standard deviation of the group. If the constant rotation period utilised to propagate the model is sufficient to align all of the light curves, then the measured phase-offsets should all fall on a straight line at zero degrees. However, if the period is incorrect or YORP is acting on the asteroid, then the phase-offsets should be fit by a straight line with non-zero gradient or a quadratic curve respectively.

The results of the phase-offset analysis are shown in Fig. 4.14. The figure suggests that the asteroid's rotation rate is slowing down, a phenomenon that has never been observed for an asteroid. One possible explanation for this is the movement of regolith across the asteroid's surface. Being past the spin-barrier, it is possible that DA is undergoing structural changes, where material from the pole migrates towards the

equator (Hirabayashi and Scheeres, 2019). As the material slides down to the equator this would produce a change in rotation period, caused by the slow down of the asteroid to conserve angular momentum. Another possible interpretation of this slow down could be due to a YORP spin-down, a mode of YORP not yet detected.

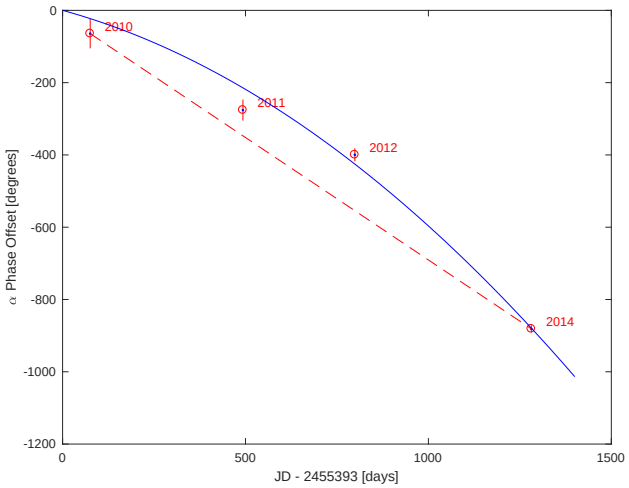

Figure 4.14: Phase offset measurements for the best-fit spherical harmonic model of asteroid (29075) 1950 DA, with $\lambda = 300°$, $\beta = 0°$, period $P = 2.121600$ hours, and starting point $T_0 = 2455393.8$ (July 2010). The red circles represent averaged phase offset measurements for light curves grouped by year, and the associated uncertainties are given by the standard deviation of the individual light curves within each year. The blue solid line marks the potential YORP solution, $\nu = (-1.9 \pm 0.4) \times 10^{-5} rad/d^2$. The red dotted line is a straight line that highlights the divergence from a linear trend.

In order to be able to distinguish between these two scenarios, an investigation is required to analyse how the rotation rate is changing over time. In the first possible scenario, concerning the migration of surface material, a sporadic change in rotation period would be expected, which would be seen as sporadic changes in rotation phase-offset with time. In the second scenario, the YORP torque provides a continuous acceleration that produces a linear change in the rotation rate, which equates to a distinctive quadratic trend in the phase-offsets compared to those expected for a constant rotation period model. This scenario is shown in Fig. 4.14 by the solid blue line, which was obtained by fitting a curve of the form $y = \frac{1}{2}ax^2$ weighted by the error of the phase offsets. Where, a represents the YORP acceleration, and it's uncertainty is the statistical 1-sigma error. However, with the 2010-2014 dataset it is not possible to distinguish between the sporadic change indicative of regolith movement or the quadratic signature of YORP. The reason for this is that the earlier epochs from 2010-2012 all lay

near a straight line (see Fig. 4.14). The 2014 data point is significantly offset from this trend, but taken together with the 2010-2012 data is not enough to establish a robust quadratic trend in rotational phase-offset with time. To determine the cause of the observed slow down requires an additional set of observations at the next observable apparition of DA (at the time of analysis this was 2019).

4.4.2 Addition of 2019 light curve data

Revisiting the phase-offset spin-state analysis

Based on the results of Fig. 4.14, an observing run was lead by the author at the INT and NOT in 2019 to obtain an additional epoch of data. Three nights of observations were obtained between 6 and 8 October 2019, all three nights with the INT and the first two with the NOT. From these observations, additional light curves were extracted which were subsequently included in the phase-offset analysis to determine the source of deceleration observed.

Figure 4.15 shows the results of the new phase-offset analysis, including the newly obtained 2019 light curves. It can be seen in the figure that the phase-offsets of new light curves forms a clean quadratic curve. Although, the YORP strength $\nu = (-2.0 \pm 0.1) \times 10^{-5}\mathrm{rad/d}^2$ is slightly different to that in Fig. 4.14, it is still well in agreement with the previous value of $(-1.9 \pm 0.4) \times 10^{-5} rad/d^2$.

The synthetic light curves generated with a YORP strength of $-2.0 \times 10^{-5} rad/d^2$ are able to roughly reproduce the observed light curves. In particular, they reproduce their turning points. The full set of synthetic light curves are shown in the appendix A.11. Based on these results, the favoured scenario for the slowing of DA rotation rate is negative YORP effect. This is the first ever indication of YORP acting in this mode, as all other detections of YORP to date are spin-ups (see Table 1.1).

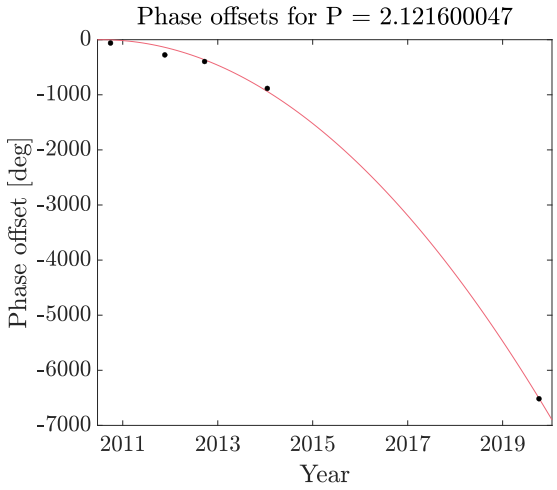

Figure 4.15: Phase offset measurements for the best-fit spherical harmonic model of asteroid (29075) 1950 DA, with new 2019 light curves. The black circles represent averaged phase offset measurements for light curves grouped by year, and the associated uncertainties are given by the standard deviation of the individual light curves within each year. The red solid line marks the potential YORP solution, $\nu = (-2.0 \pm 0.1) \times 10^{-5} rad/d^2$.

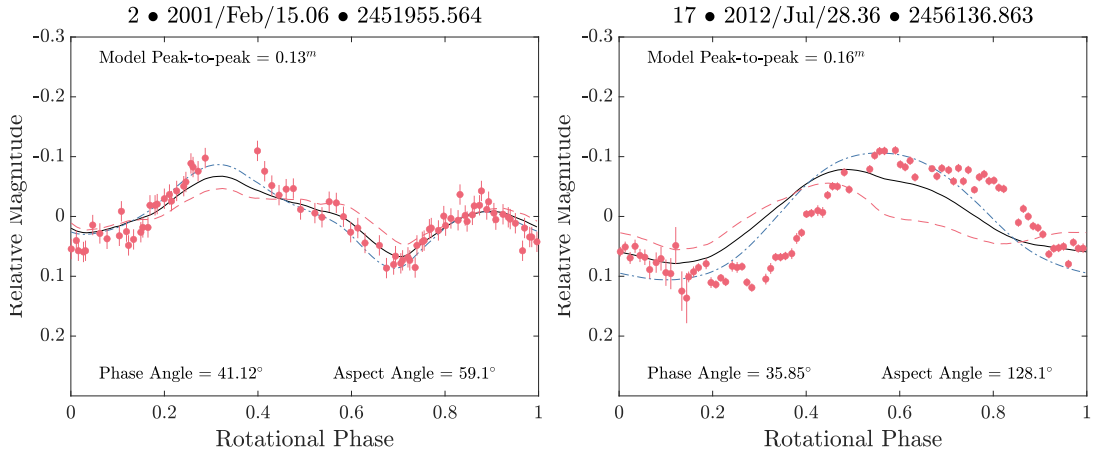

Figure 4.16: Artificial light curves for the best-fit spherical harmonic model of DA using the YORP strength fit in Fig. 4.15, $\nu = (-2.0 \pm 0.1) \times 10^{-5} rad/d^2$. Shown here are the same light curves as shown in Fig. 4.4 for the published models in order to highlight improvement in reproducing the observed light curves. The artificial light curves were produced using a variety of scattering laws. The blue dash dot line is the artificial light curve generated using the Lambertian scattering law. The red dashed line was generated with the Lommel Seeliger scattering law. The black solid line was generated using the Kaasalainen scattering law. Finally, the red dots show the observed light curves.

YORP scan with all light curves using `convexinv`

An additional method to measure a YORP signature is based on the light-curve-only method used in Sect. 4.4.1 to search for the pole orientation. The YORP strength can be included as a fixed parameter, which influences the resulting chi-squared value while the rotation period and shape are optimised in the usual way within `convexinv` (discussed in Sect. 3.1.2). For example, the Fig. 4.7 could be considered as the zero

YORP strength plane in this scan. The value of YORP strengths included in this scan ranged from -2.5×10^{-5} to 1.5×10^{-5}rad/d^2 with a step size of 2×10^{-7}. For each YORP strength a grid of fixed pole orientations was scanned that covered the entire celestial sphere with a resolution of $5° \times 5°$. A best-fit chi squared value is extracted from each YORP plane, which when plotted against the corresponding YORP strength creates a YORPogram (as described in Sect. 3.1.2).

The YORPogram, shown below in Fig. 4.17, was created by performing the YORP scan described above with the complete set of light curves. These light curves included the newly obtained 2019 light curves, giving a total baseline covering 2001 to 2019. The result of the YORPogram shows a distinct preference toward negative YORP strengths with the best-fit chi-squared at a YORP value of $(-3.6 \pm 0.8) \times 10^{-6}$ rad/d^2. Other YORP values, including positive YORP values and zero YORP, are well above the red line marking the global chi-squared minimum plus 10%. Note however, that the resulting value of YORP from this analysis disagrees with the earlier phase-offset analysis and is beyond the range scanned in the YORP scan of Sect. 4.4.1. While both phase-offset analyses indicate a negative YORP solution, the results of Fig. 4.17 favour a significantly smaller negative YORP value.

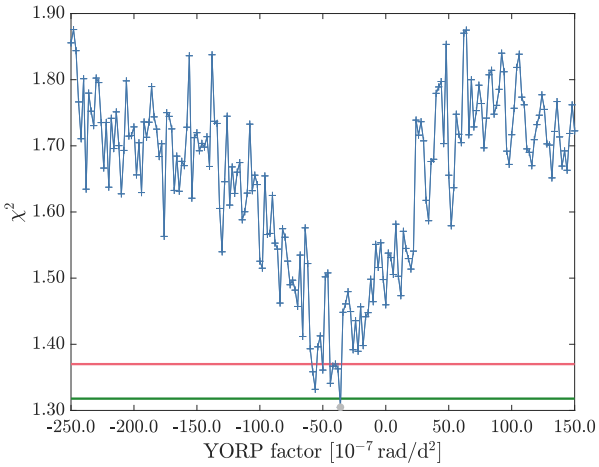

Figure 4.17: YORPogram for asteroid (29075) 1950 DA. Only optical data was utilised in this scan, which includes all of the light curves from 2001 to 2019. For each YORP plane, the entire celestial sphere was scanned with a $5° \times 5°$ resolution with each plane's best chi-squared value recorded and shown here. The global best-fit chi-squared value is marked by a grey circle. The green and red solid lines mark 1% and 10% above the global chi-squared minimum value. This figure shows that a YORP strength of $(-3.6 \pm 0.8) \times 10^{-6}$ rad/d^2 yields the best fit to the light curve data.

Inspection of the -3.6×10^{-6} rad/d^2 YORP plane shows that the pole orientation appears to be in the southern ecliptic hemisphere with the best pole close to the celestial equator. The best-fit pole is located at an ecliptic longitude and latitude of 35° and −25° respectively. This is an additional pole orientation, different to any indicated in earlier analyses. However, like other pole orientations determined within this work, this pole lies close to the celestial equator. This pole also lies almost directly opposite to the (210°, +30°) determined in Sect. 4.4.1. This ambiguity between pole solutions separated by 180° is a result of limited observing geometry (Kaasalainen and Lamberg, 2006).

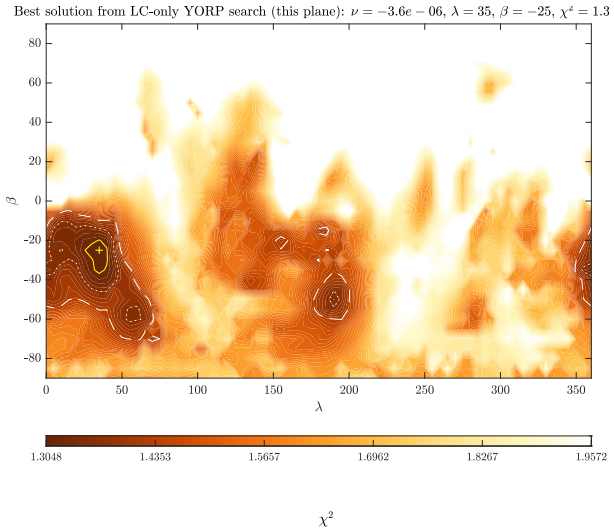

Figure 4.18: Pole scan for the -3.6×10^{-6} rad/d^2 YORP plane. This plane is one of many created during the creation of the YORPogram shown in Fig. 4.17. Shown here is the chi-squared value resulting from the optimisation of the rotation rate and shape at each pole orientation probed. The best solution is marked with a yellow cross. The solid yellow line, dotted white line, and dashed white line indicate solutions within 1%, 5%, and 10% of the best solution. The darker colours indicate a better solution, with all solutions above 50% of the plane's chi-square minimum shown as white. The best pole orientation for this plane is located at (35°, −25°).

The resulting best-fit model from the -3.6×10^{-6}rad/day^2 YORP plane was then used to generate synthetic light curves, in order to access the model's ability to reproduce the light curves. To produce the synthetic light curves the model was propagated from 29 January 2001 (a Julian date of 2451938.7) with a rotation period of 2.121611 hours and a YORP strength of -3.6×10^{-6}rad/day^2. A subset of these synthetic light curves are shown below in Fig. 4.19 with their observed counterparts overlaid. As can be seen in this figure, the model is able to reproduce the observations fairly well. The

entire set of light curves can be found in Fig. A.12 of the appendix.

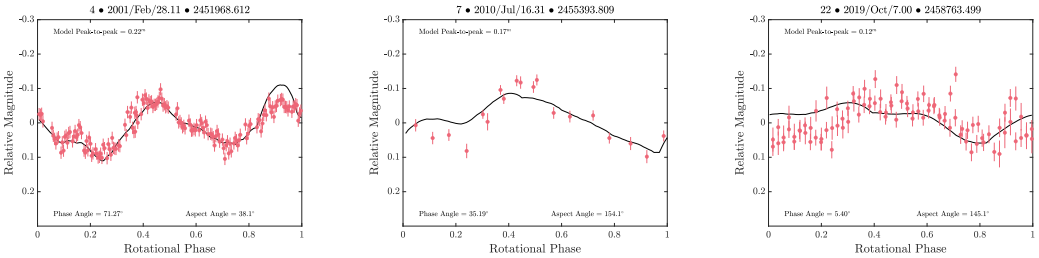

Figure 4.19: Synthetic light curves generated with the best-fit `convexinv` model resulting from the YORP scan of (29075) 1950 DA. The model was propagated forward with a rotation period of 2.121611 hours and a YORP strength of -3.6×10^{-6}rad/d^2 (corresponding to the YORP strength the model was optimised with).

4.5 Summary of main conclusions and discussion

Within this chapter extensive modelling and analysis of the asteroid (29075) 1950 DA have been performed. The data utilised in these include an extensive set of optical light curves obtained as part of the ESO LP and auxiliary programmes. In addition to published radar observations, optical light curves, and shape models (Busch et al., 2007). The main conclusions resulting from this work are listed below:

1. The prograde and retrograde models developed by Busch et al. (2007) were unable to reproduce the new light curves obtained by the ESO LP and auxiliary programmes, even with minor alterations to their shape and pole orientation.

2. Multiple modelling efforts indicated a new pole orientation for DA which lays close to the ecliptic equator. The values obtained for its ecliptic latitude ranged from $-25°$ to $35°$.

3. A deceleration in DA's rotation rate was detected. With multiple analyses: the global scan, phase-offset analysis, and `convexinv` YORP scan, all indicating that

negative YORP is causing the reduction observed its spin-rate. Although, there was difficulty in obtaining a single value.

The asteroid (29075) 1950 DA is an oblate spheroid shaped object with a rotation period close the spin-barrier for cohesionless aggregates. The characterisation of this object was performed by the inversion of a combination of both radar observations and an extensive set of optical light curves. The majority of light curves utilised have a very low amplitude of variation, about 0.1^m, due to the spheroid shape of the asteroid. However, the analysis of these data allowed the investigation of the asteroid's rotation rate, enabling the detection of a reduction in the asteroid's spin-rate.

A strong indication of negative YORP was found through multiple methods during the analysis of DA, see Table 4.3. However, there was difficultly in obtaining a single coherent value for the YORP strength from the different methods. This should not detract from the significance of the results obtained through each method: negative YORP was clearly the preferred solution in contrast to a constant period model or positive YORP. To date, all YORP detections have been positive accelerations (spin-up), when YORP should lead to both positive and negative accelerations for a population of asteroids with random spin-states (Rubincam, 2000). In order to explain this apparent preference for positive YORP, mechanisms such as tangential-YORP have been suggested (Golubov and Krugly, 2012; Golubov et al., 2014; Golubov, 2017). If confirmed, this negative YORP detection could have major implications of the theory of YORP.

Due to the strength of YORP resulting from the phase-offset analysis, the phase-offsets of the 2019 epoch data is equivalent to a approximately 18 full rotations (i.e. $\sim$6480°). A comprehensive confirmation of negative YORP could be obtained with an additional three or four optical light curves taken with a baseline no larger than two years so that the phase offsets are within 360°. A good opportunity to obtain such optical data is coming up in 2023, when DA will be observable in the southern hemisphere at magnitudes brighter than 17^{mag}. There are also northern hemisphere opportunities the years before then, in 2021 and 2022, when the asteroid will be between

$18^{mag} - 19^{mag}$.

DA's orbital geometry over the next five years is shown below in Fig. 4.20, the solar elongation of the asteroid gives an indications of the length of time the asteroid can be observed for each night. As such, a limit on the solar elongation requires that it be larger than 80°, this is reflected in the figure by the bold lines. During 2021 and 2022, the object's declination varies between 0° and 50° and so requires a facility in the northern hemisphere. With a magnitude peaking between $18^{mag} - 19^{mag}$ during these apparitions, a 2.5 m class telescope would be sufficient for the observations. In 2023, the object will be at a declination of −60°, requiring a telescope located in the southern hemisphere. During this apparition, the asteroid will reach magnitudes of 17^{mag}, at this magnitude the asteroid could be observed by a smaller telescope, such as the 1.5 m Danish Telescope in La Silla, Chile.

In order to obtain three/four different epochs of observations, I would aim to observe DA in September 2021, December 2022, late January or early February 2023, and August 2023. For each epoch, I would request three nights of observing time. DA's short rotation period will aid in obtaining light curves covering at least a full rotation period each night.

Finally, the modelling of DA's shape would also benefit from additional delay-Doppler radar imaging covering unseen sections of the object, which would ideally enable the determination of the asteroid's shape purely with radar observations. This would allow the decoupling of the shape model from the optical light curves, which would improve the results from the phase-offset analysis. However, this will not be possible with current facilities for some time, as during the next radar apparition the same geometry of the asteroid will be viewable.

Model	Data range [years]	λ [°]	β [°]	ν $[rad/day^2]$
`convexinv` pole scan	2001-2014	190 ± 5	34 ± 5	N/A
`SHAPE` YORP scan	2001-2014	300 ± 30	0 ± 30	$(-2.1 \pm 0.2) \times 10^{-6}$
Phase-offset analysis	2010-2014	300 ± 30	0 ± 30	$(-1.9 \pm 0.4) \times 10^{-5}$
Revisited phase-offset analysis	2010-2019	300 ± 30	0 ± 30	$(-2.0 \pm 0.1) \times 10^{-5}$
`convexinv` YORP scan	2001-2019	35 ± 10	-25 ± 10	$(-3.6 \pm 0.8) \times 10^{-6}$

Table 4.3: A summary of pole orientations and YORP strengths determined via the various analyses performed within this chapter. Also listed in this table is the range of years covered by the input data. The rotation periods of all of the list models agree with the period of 2.1216 hours listed for the Busch models (Busch et al., 2007).

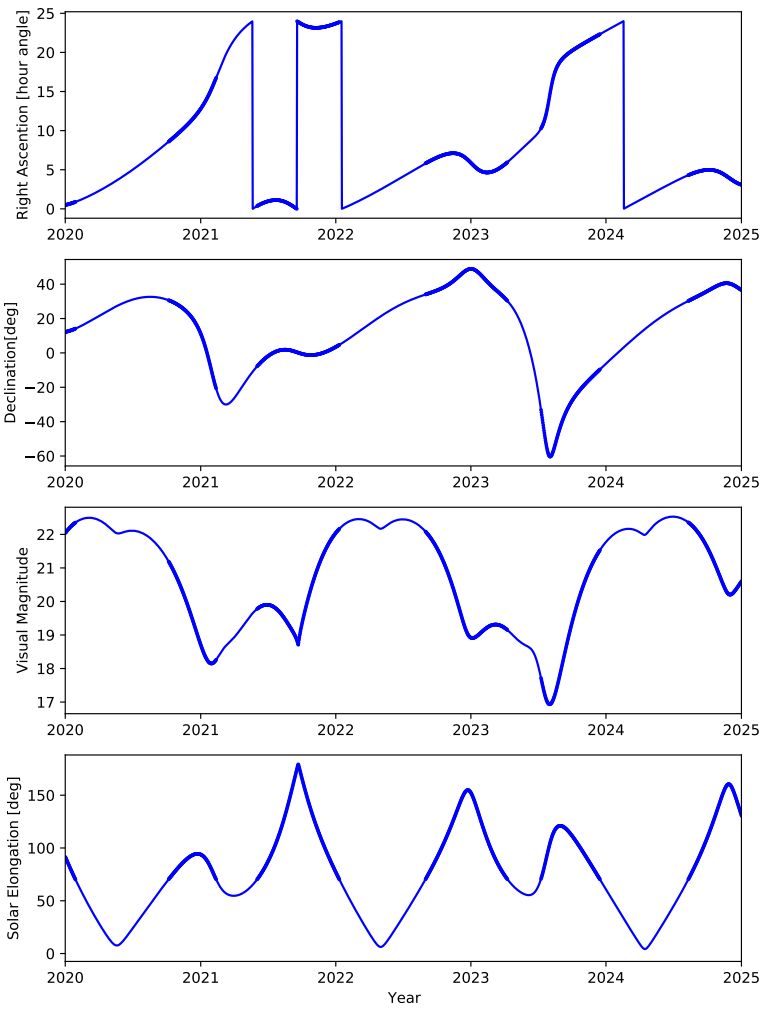

Figure 4.20: Orbital geometry of asteroid (29075) 1950 DA between 2020 and 2025. Shown here is the right ascension, declination, visual magnitude, and solar elongation of the object. The bold lines mark the times when DA's solar elongation is greater than 80°. Based on the object's declination, the majority of the observations would be taken from the northern hemisphere, with the exception of August 2023.

5 | Detection of YORP on the contact-binary (68346) 2001 KZ66 from radar and optical observations

5.1 Introduction

The asteroid (68346) 2001 KZ66 (hereafter referred to as KZ66) is both a Potentiallty Hazardous Asteroid (PHA) and a NEA of the Apollo class, and was discovered on the 29 May 2001 at Haleakala by the Near-Earth Asteroid Tracking programme (Pravdo et al., 1999). It was observed by the NEOWISE survey which determined a geometric albedo of 0.29 ± 0.11. This was used to obtain a diameter of 0.74 ± 0.21 km (Masiero et al., 2017). There have been several measurements of its synodic rotation period. Optical observations from the Palmer Divide Station during May 2016 revealed a large amplitude, 0.63^{mag}, and a rotation period of 4.987 ± 0.005 hours (Warner, 2016). Follow-up observations in July 2016 from the Palmer Divide Station displayed a lower amplitude of 0.35^{mag}, but the rotation period was consistent with the earlier value (Warner, 2017). More recently, the object was observed at the Isaac Aznar Observatory. The lightcurve had an amplitude of 0.77^{mag}, however the synodic rotation period was measured to be

5.633±0.002 hours (Aznar Macias et al., 2017), much larger than earlier measurements.

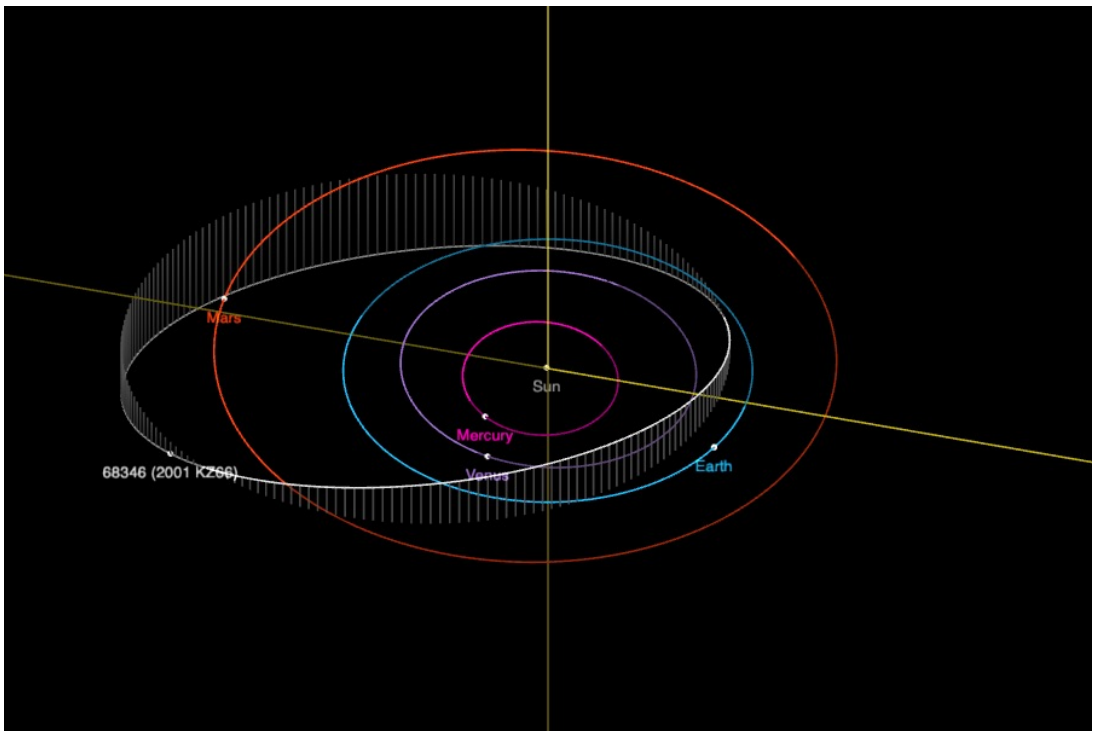

Figure 5.1: Diagram of the orbit of asteroid (68346) 2001 KZ66 also showing the orbits of Mercury, Venus, Earth, and Mars. Positions of all objects are for the date 2020-09-01 00:00 UTC. Image produced using `https://ssd.jpl.nasa.gov/sbdb.cgi`

Nine optical light curves have been obtained throughout the period April 2010 to January 2019 with the 3.6 m NTT. An additional light curve was obtained during a supporting programme on the 2.5 m INT, Spain, in 2012. Included in the dataset are 7 published light curves from the Palmer Divide Station taken between May 2016 and July 2016 (Warner, 2016, 2017). Additionally, radar observations that were taken over two nights in October 2003 from Arecibo Observatory are utilised.

As mentioned in Chapter 1, the Yarkovsky-O'Keefe-Radzievskii-Paddack (YORP) effect is a gentle torque that small asteroids can experience due to the reflection and thermal emission of sunlight from their surfaces (Rubincam, 2000). This torque causes a change the rotation rates and spin-axis obliquities of these bodies. The YORP effect can alter the rotational momentum of NEAs, that is the spin-axis obliquity and rotation period. This process is a major driver in the spin-state evolution of small Solar System

bodies, and can lead to substantial physical changes, including shape and structural changes, binary formation and even mass shedding (Lowry et al., 2019). To date, the YORP effect has been detected on just seven objects. They include: (54509) YORP, (1862) Apollo, (1620) Geographos, (3103) Eger, (25143) Itokawa, (161989) Cacus, and (101955) Bennu (Lowry et al., 2007; Taylor et al., 2007; Kaasalainen et al., 2007; Ďurech et al., 2008, 2012; Lowry et al., 2014; Ďurech et al., 2018; Nolan et al., 2019). Crucially, all of the detections have been rotational accelerations (i.e. in the spin-up sense). For a population of asteroids with randomised shapes and spin-states, YORP should produce both spin-up and spin-down cases. While recent theoretical developments are being proposed to explain the apparent lack of spin-down cases (Golubov and Krugly, 2012; Golubov et al., 2014; Golubov, 2017), to fully understand this important process requires more observational detections of the YORP effect in action.

In this chapter, I will present the results and analysis of a long-term photometric monitoring programme to model the asteroid and to detect changes in the object's rotation rate that could be due to YORP. The format of this chapter is the following: sec. 5.2 describes the observing campaign of KZ66. In sec. 5.3 and 5.4 the analysis of the shape and spin-state modelling is presented, in addition to the approach to detect YORP-induced rotational accelerations. Sec. 5.5 provides a general discussion of the results and their implications, and overall conclusions are drawn in sec. 5.6.

5.2 Observations of (68346) 2001 KZ66

5.2.1 Optical light curves

The optical light curve dataset for KZ66 covers the period from April 2010 to January 2019, spanning a total of nine years. A summary of all of the light curves used in this work are reported in Table 5.2.1, along with details of the observing conditions: observer ecliptic longitude and latitude, geocentric distance, and orbital phase angle. An graphical overview of the observing geometries for all data is given in Fig. 5.2.

When observing the asteroid either sidereal or differential tracking was used, depending on the rate of motion of the object on any given night. If the object was moving slowly enough, sidereal tracking was opted for and the exposure times were kept short enough that the asteroid didn't move by more than the FWHM of the seeing during the exposure. This ensured that the asteroid, and the background comparison stars, were not significantly trailed. To optimize the lightcurve extracted I used circular photometric apertures which varied according to the varying seeing conditions from one exposure to the next. The chosen optimal aperture radius was set to 2 $\times$ FWHM of the profile of the asteroid. This was not required for the comparison stars given their increased brightness so larger apertures were used. The brightness of the asteroid was then compared with the average brightness of the background stars to produce relative light curves. When this condition could not be achieved due to the higher rate of motion, the asteroid was simply tracked at the projected rates of motion to maintain its stellar appearance. Again, an optimal aperture radius of 2 $\times$ FWHM of the profile of the asteroid was chosen. The background stars were now significantly trailed, but the exposure times were limited such that the stars were never trailed by more than 5 arcsecs. In cases where this would result in a low signal-to-noise ratio, multiple images can be co-added. However, this was only necessary for the July 2012 NTT dataset. The light curves which were obtained as a part of the ESO LP programme are those with IDs 1-8 and 16-17 in Table 5.2.1 and are presented with those IDs in Appendix Figs. A.13, A.14, and A.15.

New Technology Telescope – 2010, 2012, 2014, and 2019 The asteroid KZ66 was observed at the ESO 3.6 m NTT telescope in La Silla (Chile), using the EFOSC2. The CCD detector of EFOSC2 has 2048 $\times$ 2048 pixels and a field of view of $4.1' \times 4.1'$. The observations of KZ66 were performed in imaging mode using 2×2 binning on the detector, and with the Bessel R filter in 2010 and 2012, and Bessel V filter in 2014 and 2019. The object was detected at the NTT on two different nights in 2010, three in 2012, two in 2014, and two in 2019 giving a total of nine light curves. The data were

ID	UT Date [*dd/mm/yyyy*]	$R_\odot$ [AU]	$\Delta_\oplus$ [AU]	α [°]	λ_O [°]	β_O [°]	Total [hour]	Filter	Observing facility	Reference	LC-only model
1	04/04/2010	2.134	1.193	12.41	174.4	-18.0	2.0	R	NTT		•
2	05/04/2010	2.133	1.197	12.84	174.0	-17.8	5.3	R	NTT		•
3	26/02/2012	2.125	1.396	22.18	210.1	-13.8	3.3	R	NTT		•
4	27/02/2012	2.124	1.385	21.90	210.0	-13.8	4.7	R	NTT		•
5	24/05/2012	1.949	1.240	27.04	183.3	-4.4	3.1	R	INT		•
6	28/07/2012	1.681	1.723	34.67	196.2	3.3	1.0	R	NTT		•
7	30/03/2014	1.952	1.074	19.06	228.8	-5.3	3.5	V	NTT		•
8	31/03/2014	1.949	1.063	18.63	228.6	-5.2	2.2	V	NTT		•
9	27/05/2016	1.418	0.459	23.53	265.0	29.1	5.8	clear	PDS	1	•
10	28/05/2016	1.412	0.453	23.69	264.7	29.9	5.7	clear	PDS	1	•
11	29/05/2016	1.405	0.446	23.90	264.4	30.7	6.2	clear	PDS	1	•
12	30/05/2016	1.399	0.440	24.15	264.1	31.5	6.2	clear	PDS	1	•
13	17/07/2016	1.095	0.324	67.25	218.6	65.6	5.3	clear	PDS	2	•
14	18/07/2016	1.089	0.323	68.26	217.0	65.9	5.1	clear	PDS	2	•
15	19/07/2016	1.083	0.322	69.24	215.4	66.2	5.2	clear	PDS	2	•
16	27/01/2019	1.835	0.983	20.92	156.8	-31.8	6.1	V	NTT		•
17	28/01/2019	1.839	0.981	20.54	156.3	-31.9	3.1	V	NTT		•

Table 5.1: A log of optical photometry datasets of asteroid (68346) 2001 KZ66 used in this study. Each light curve has a numerical "ID" listed, then the Universal Time (UT) "Date" of the beginning of the night is given, as well as the heliocentric ($R_\odot$) and geocentric ($\Delta_\oplus$) distances measured in AU, the solar phase angle (α), the observer-centred ecliptic longitude (λ_O), the observer-centred ecliptic latitude (β_O), and the "Observing facility" used to obtain the light curve. Where relevant a "Reference" to published work is given. Each line represents a single nightly light curve data set (for some of the nights listed, several light curve segments have been obtained). Circles in the "LC-only model" column indicate which light curves were selected for the light-curve-only shape modelling. These marked light curves were also utilised for the initial radar observation modelling, but are omitted from the subsequent stages. Observing facility key: INT – 2.5 m Isaac Newton Telescope (La Palma, Spain), NTT – European Southern Observatory 3.5 m New Technology Telescope (Chile), PDS – Palmer Divide Station (California, USA). (1) Warner (2016); (2) Warner (2017)

reduced using the standard CCD reduction procedures. The light curve with ID 6 from Table 5.2.1 required co-addition of the images to improve the signal-to-noise ratio.

Isaac Newton Telescope – 2012 KZ66 was also monitored with the 2.5 m INT in La Palma (Spain), using the Wide-Field Camera (WFC). The WFC is an array of four CCD chips, each with 2048×4100 pixels, with a total field of view $34' \times 34'$. However, for these observations, only CCD4 was used with a window of $10' \times 10'$ to reduce readout time between images. The KZ66 observations were performed using the Harris R filter. The target was observed over one night during 2012 on the 24 February for 3.1 hours. The data were reduced using standard CCD reduction procedures.

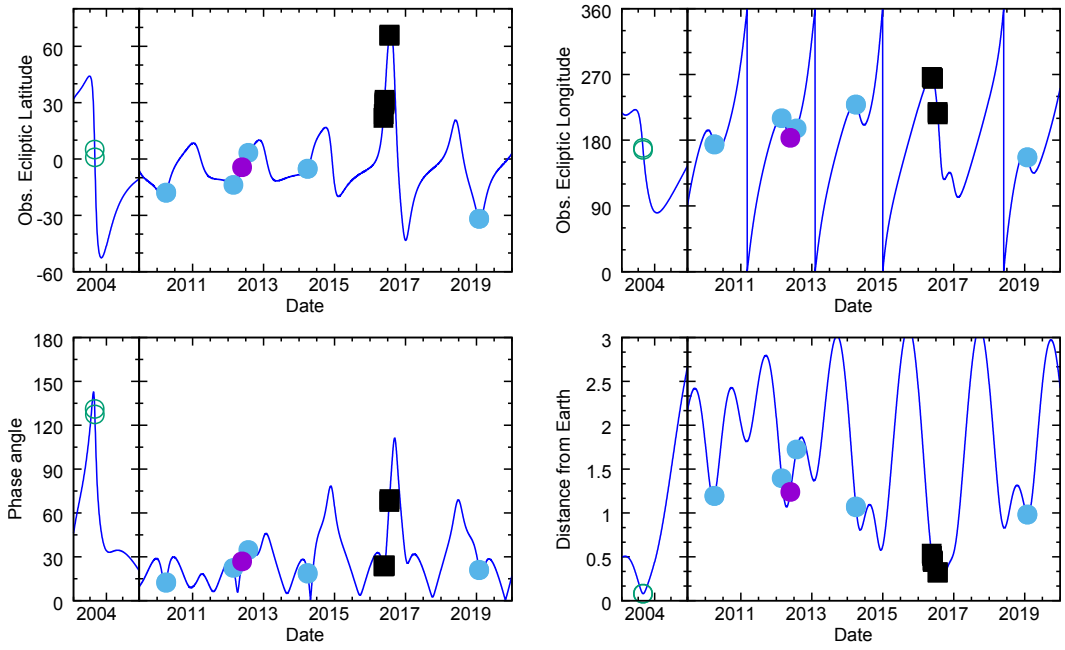

Figure 5.2: Asteroid (68346) 2001 KZ66 observing geometries during the optical and radar observations over the period 2003 to 2019. The top two panels show the position of the object in the ecliptic coordinate system, latitude and longitude, as observed from Earth. The bottom two panels show the phase angle and geocentric distance to the asteroid. Optical light curve data from the NTT are marked with filled blue circles, with lightcurve data from the INT marked with filled purple circles. Black squares represent the published light curve data. The green circles mark when the Arecibo radar data were collected. The blue continuous line represents the object's observational ephemeris.

Published optical light curves – 2016 The previously published photometry data for KZ66 include ten light curves of which seven are used in this study. These light curves have the IDs 9-15 (see Table 5.2.1). The observatory used to obtain these light curves is the Palmer Divide Station in California, USA which hosts several small telescopes with diameters less than 0.5 m. The observations consist of four light curves taken in May 2016 (Warner, 2016) and a further three in July 2016 (Warner, 2017), all of which were taken with a clear filter. These processed light curves were obtained from the Asteroid Lightcurve Data Exchange Format (ALCDEF) database (Warner et al., 2011).

5.2.2 Asteroidal radar observations

Radar observations were also used in this analysis, both delay-Doppler imaging and continuous-wave (cw) spectra. Delay-Doppler images are obtained from a circularly polarized transmitted signal which is phase-modulated with a pseudo-random binary code (Ostro, 1993; Magri et al., 2007). This modulation pattern allows us to determine the distance between the observer and the parts of the object reflecting the signal. The resolution of the delay is determined by the time-resolution of the modulated signal, the baud length. The second axis in a delay-Doppler image is given by the Doppler shift measured in the returning signal. The width of the shifted signal is dependant on a combination of the size of the object and its rotation rate. Unlike the delay-Doppler images, the cw spectra contain no information on the delay of the radar signal, they solely record the Doppler shift of the emitted signal that returns from the object in both circular polarisation orientations.

Arecibo Observatory – 2003 Observations of the asteroid KZ66 with Arecibo Observatory under the Planetary Radar programme (project number R1811) were performed on two consecutive nights: 28 and 29 October 2003. The cw spectra were taken on each night, in addition to imaging with 0.1 μs baud length code corresponding to $\sim$15 m resolution in delay (see the detailed list of radar experiments gathered in Table 5.2).

Modelling radar data is a computationally expensive process. To minimise the computational time required one can either remove datasets with similar geometries or reduce the number of frames within a dataset by co-adding several frames at a time. As only two nights of consecutive data were available with almost identical observing geometry, I opted for the latter. Co-addition of pairs of frames was used in order to maintain maximal rotational coverage. This also had the additional benefit of increasing the signal-to-noise ratio of the delay-Doppler images.

UT Date [*yyyy-mm-dd*]	RTT [s]	Baud [μs]	Resolution [m]	Start-Stop [*hh:mm:ss-hh:mm:ss*]	Runs	Radar model	SC/OC analysis	Ranging
2003-10-28	80	cw		12:21:46-12:36:34	6	•	•	
		cw		12:39:38-12:40:51	1			•
		cw		12:44:45-12:45:58	1			•
		4	600	12:48:22-12:49:35	1			•
		4	600	12:51:38-12:52:51	1			•
		0.1	15	12:57:00-14:37:50	36	•		
2003-10-29	79	cw		12:10:02-12:21:58	5	•	•	
		0.1	15	12:27:18-13:57:37	33	•		
		4	600	14:01:20-14:02:32	1			•
		4	600	14:04:20-14:05:32	1			•
		cw		14:07:19-14:08:31	1			•

Table 5.2: Radar observations of asteroid (68346) 2001 KZ66 obtained at Arecibo in October 2003. "UT Date" is the universal-time date on which the observation began. "RTT" is the round-trip light time to the object. "Baud" is the delay resolution of the pseudo-random code used for imaging; baud does not apply to cw data. The delay "Resolution" is dependant upon the baud and the number of samples taken per baud. For a baud of 0.1 μs and one sample taken per baud this corresponds to a delay resolution of 15 m. The timespan of the received data is listed by the UT *start* and *stop* times. "Runs" is the number of completed transmit-receive cycles. "Radar model" column indicates which radar observations were selected for the shape modelling. "SC/OC analysis" column indicates which cw spectra were utilised to calculate the polarisation ratio. "Ranging" column indicates which observations were taken to refine the ephemeris.

5.3 Modelling shape and spin-state

5.3.1 Period and pole search with light curve data – convex inversion results

The first step in the shape modelling procedure is to define an initial value for the sidereal rotation period of the asteroid, for which I used the method described in Kaasalainen et al. (2001). With this approach six pole orientations are initially spread evenly across the entire celestial sphere. I then set up a range of period values to scan across, and for each period we allow the shape to vary for each of the six selected poles, while each time performing a fit of the model to the observed light curve magnitudes. When this is complete for a given period, I then record the lowest χ^2 value, and the remaining χ^2 values for the other five selected poles are discarded at this stage. The

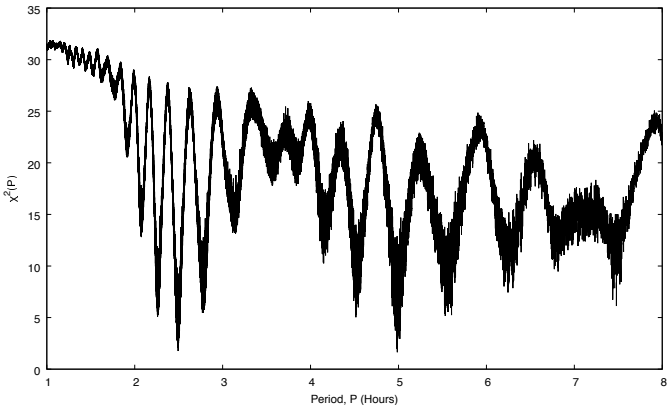

Figure 5.3: Results of the sidereal rotation period scan for asteroid (68346) 2001 KZ66 described in Sect. 5.3.1. The scan resulted in a rotational period of 4.9860 ± 0.0001 hours, which was later refined to 4.985988 ± 0.000020 hours.

period values scanned across ranged from 1–8 hours, which easily encompasses all of the previously reported periods for KZ66 (Benner et al., 2006; Warner, 2016, 2017; Aznar Macias et al., 2017). The result of the period search indicated two potential rotational periods, one at 2.493 hours and the other at 4.980 hours (Fig. 5.3). However, the period of 2.493 h was subsequently eliminated during the pole orientation analysis as the shape models corresponding to the shorter period failed to reproduce the light curves well. Moving forward I will only consider the rotational period of 4.9860 ± 0.0001 h.

To further constrain the asteroid's pole orientation and sidereal rotation period, and to determine a best-fit convex shape for the asteroid, I utilised the convex inversion techniques described by Kaasalainen and Torppa (2001); Kaasalainen et al. (2001) in our customized procedures (discussed in chapter 3). Therefore all shapes obtained from this section of the analysis are convex hulls, meaning that they approximate the real shape of the asteroid.

My approach first involves setting up a grid of pole positions covering the entire celestial sphere with a resolution of $5^\circ \times 5^\circ$. At each pole position, the rotation period and convex shape were optimised to fit the light curves. The sidereal period determined previously is utilised in this step as an optimal starting point for the subsequent optimisation process. The initial epoch, T_0, and the initial rotation phase, φ_0, were held fixed during the optimisation. The T_0 was set to 2455291.0, corresponding to the date

of the first light curve (4 April 2010) and φ_0 set to 0°. The results of the pole search are shown in Fig. 5.4. This model assumes a constant rotation period - a YORP factor is included later in Sect. 5.4.1. Due to the large range of observer-centred ecliptic latitude sampled by the light curve dataset, I was able to tightly constrain the pole to the southern equatorial hemisphere.

The best model's pole is at an ecliptic longitude, λ, of 170° and an ecliptic latitude, β, of $-85°$ with a 1σ error radius of 15°. This pole is marked by a yellow cross in Fig. 5.4. I extracted the best-fit shape model and constant sidereal rotation period at this best-fit pole location. The latter was determined to be 4.985988 ± 0.000020 hours, and the best-fit shape model is shown in Fig. 5.5. The best-fit convex shape can be described as a mix between an elongated ellipsoid and a cylinder. The planar features are the result of the procedure attempting to match the large amplitude of the light curves.

5.3.2 A radar shape model – SHAPE results

The procedure described in Sect. 5.3.1 can only produce convex models, and hence it will not produce the concavities of the neck region of the asteroid which can clearly be seen in the delay-Doppler images. Shape modelling utilising radar data was performed using the SHAPE modelling software (Hudson, 1993; Magri et al., 2007). This process is highly dependant on the starting conditions, hence initial spin-state parameters were set to the values determined from earlier analyses. As for the starting point of the asteroid's shape, the delay-Doppler echoes indicate that this asteroid is bi-lobed. Therefore I took the approach of constructing an initial two-component ellipsoid model comprised of two ellipsoids, with their radii estimated from the delay-Doppler images. Each component is described by three axial lengths, three positional parameters, and three angular parameters. The rotational state of the model is described by five parameters: two angles that describe the model's pole; one angle for the initial rotation phase; the initial UT epoch, T_0; the asteroid is assumed to be a principal-axis rotator with a constant

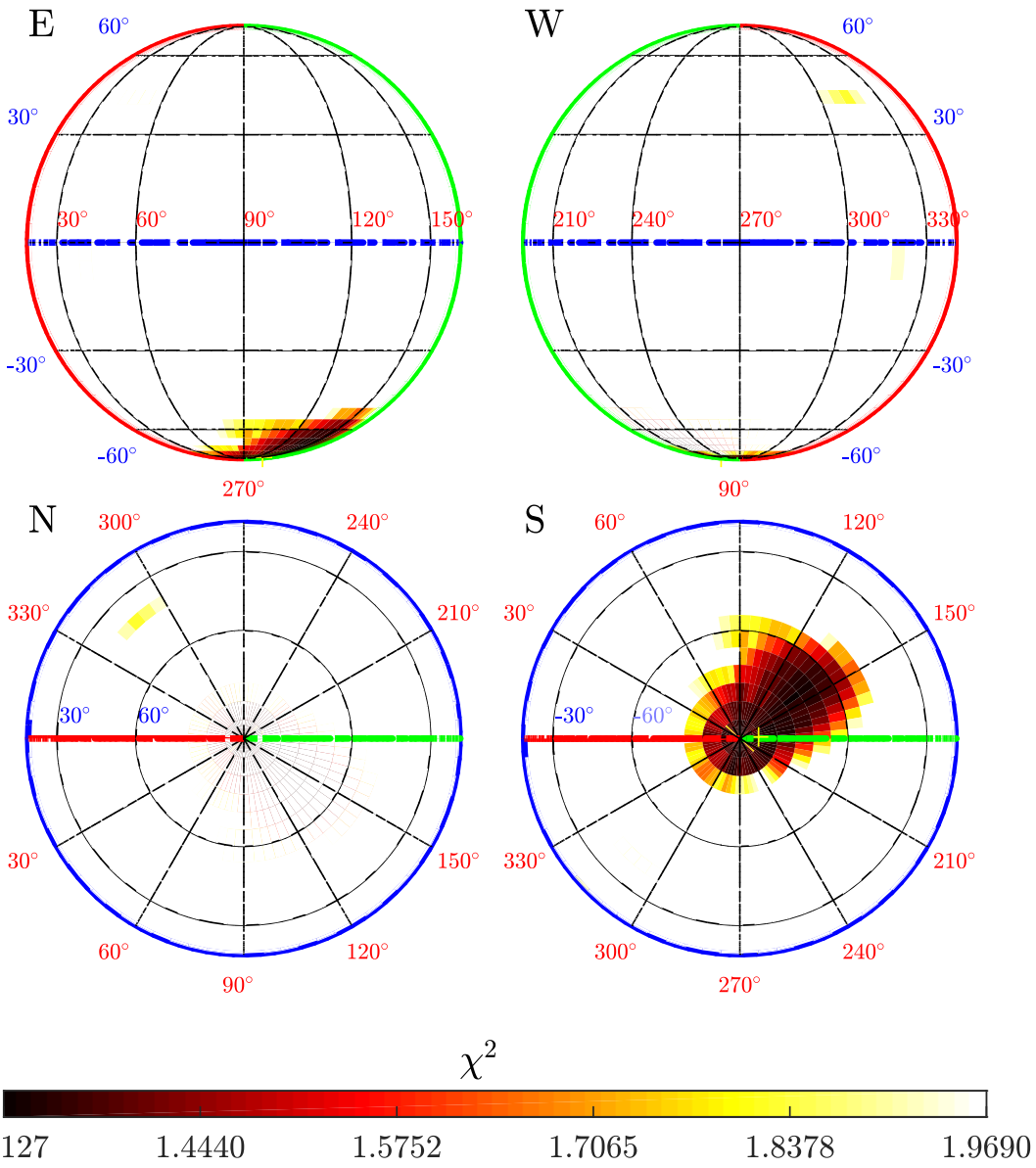

Figure 5.4: Results of the convex inversion pole search for asteroid (68346) 2001 KZ66 projected on the surface of the celestial sphere described in ecliptic coordinates. The blue line marks the ecliptic plane with latitude $\beta = 0°$, additional circles of latitude are marked with black lines and labelled with blue numerals. The red line marks the longitude $\lambda = 0°$ and the green line $\lambda = 180°$, with selected meridians marked with black lines and labelled with red numerals. From top-left clockwise, the projections show the eastern (E), western (W), southern (S) and northern (N) hemispheres of the sky. The colour changes from black at the minimum χ^2, with 1% increments of the minimum χ^2, and the white region representing all the solutions with χ^2 more than 50% above the minimum χ^2. The best period is marked by a yellow '+' which is found at $\lambda = 170°, \beta = -85°$, the pole determination has a 1σ error of radius 15°.

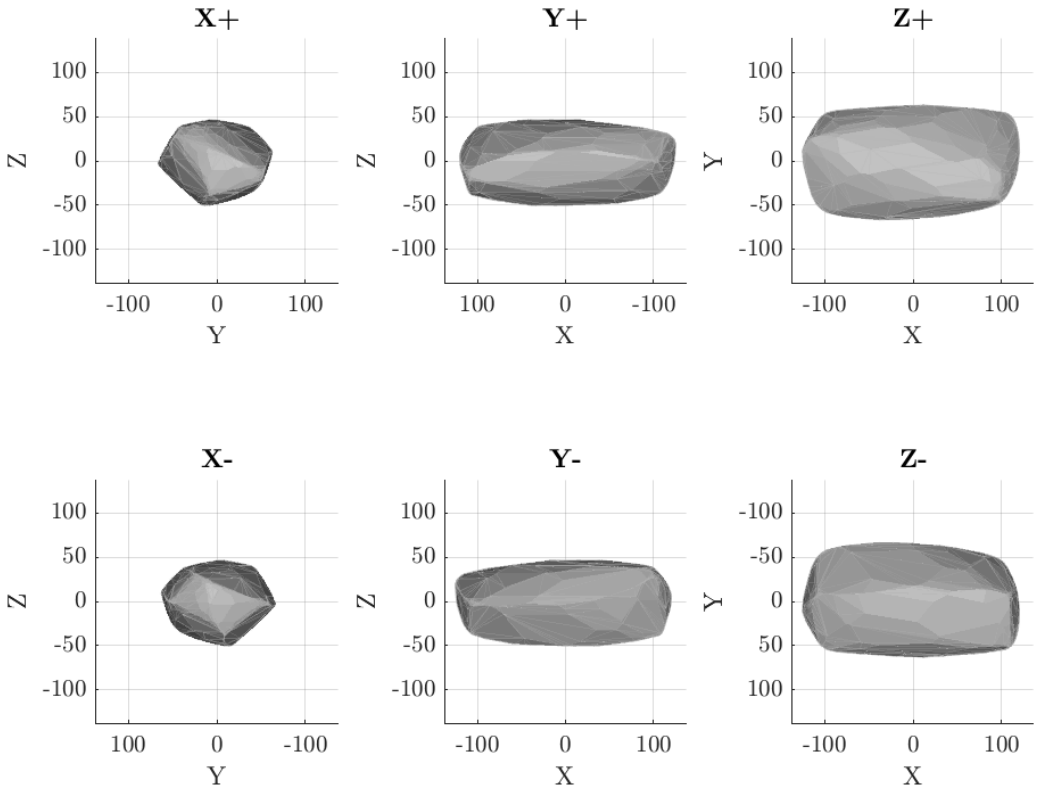

Figure 5.5: The best-fit convex shape model of (68346) 2001 KZ66. The model was produced from a pole search using light curve data only, assuming a constant period, the pole is located at $\lambda = 170°$, $\beta = -85°$. *Top row* (left to right): views along the X, Y and Z axes of the body-centric coordinate frame from the positive end of the axis. *Bottom row* (left to right): views along the X, Y and Z axes from their negative ends. The model's Z axis is aligned with the rotation axis and axis of maximum inertia. The light curve convex inversion model is not scaled and the units shown are arbitrary.

period, therefore the spin is described solely by the period of rotation about the model's z-axis. The initial parameters for the ellipsoid model were manually adjusted by visually matching the synthetic echoes output by SHAPE to a selection of the delay-Doppler images. During this process the origin of the body-fixed coordinate system is overlapped with the model's centre-of-mass. All of the parameters above were optimised during the modelling, except for the pole orientation which is held fixed at the value determined from the convex inversion pole scan. This initial ellipsoidal stage of modelling included both the light curve and radar observations, however, all subsequent modelling relies solely on the radar observations. The resulting model consists of a large ellipsoid and a smaller spheroidal component. The dimensions of the larger component along the

body-centric coordinate axis are $0.85 \times 0.57 \times 0.58$ km. The smaller component has axial lengths of $0.33 \times 0.34 \times 0.34$ km. Both components' centres are separated by a distance of 0.45 km.

The complexity of the shape's description was gradually increased during the fitting procedure. From the initial ellipsoid representation, the model was converted to spherical harmonic form during the intermediate stages before being converted to a vertex model. The final model consists of 1000 vertices giving 1996 facets with a median facet edge length of 57 m. The position of each vertex was optimised individually during the fitting procedure. In addition to the shape, the rotation period and initial rotation phase were also fit for. During the fitting procedure, three penalty functions were applied to discourage certain model features by increasing the numerical value of the goodness-of-fit during the fitting procedure Magri et al. (2007). Since SHAPE attempts to minimise the goodness-of-fit, it follows that the larger these penalties are the more strongly it discourages the features. The first function penalised the deviation of the centre of mass away from the origin of body-fixed coordinates. The second suppressed facet-scale topography, which discourages the appearance of unphysical spikes. The final penalty function attempts to keep the third principal axis aligned with the model's z-axis. The resulting model is shown in Fig. 5.6 (Table 5.3 contains the geometric parameters). The larger component has an ellipsoidal shape and it is joined to the smaller lobe by a tight neck region. The smaller lobe is non-ellipsoidal with a curved body.

Inspection of the model's moments of inertia reveals that the largest axis of inertia is the y-axis opposed to its spin (z) axis. The moment of inertia of the y-axis is 5% larger than that of the z-axis, however, delay-Doppler images suffer from aliasing in their z-axis leading to a worse constraint in the z-axis when compared to the x- and y-axis (Ostro et al., 2002). Due to this ambiguity, KZ66 is likely more compressed in the z-axis than demonstrated by the model, accounting for the difference in the moments of inertia. For a spin-state analysis of this asteroid, this discrepancy is negligible, though this difference would be significant from a dynamical modelling point of view. Table A.1

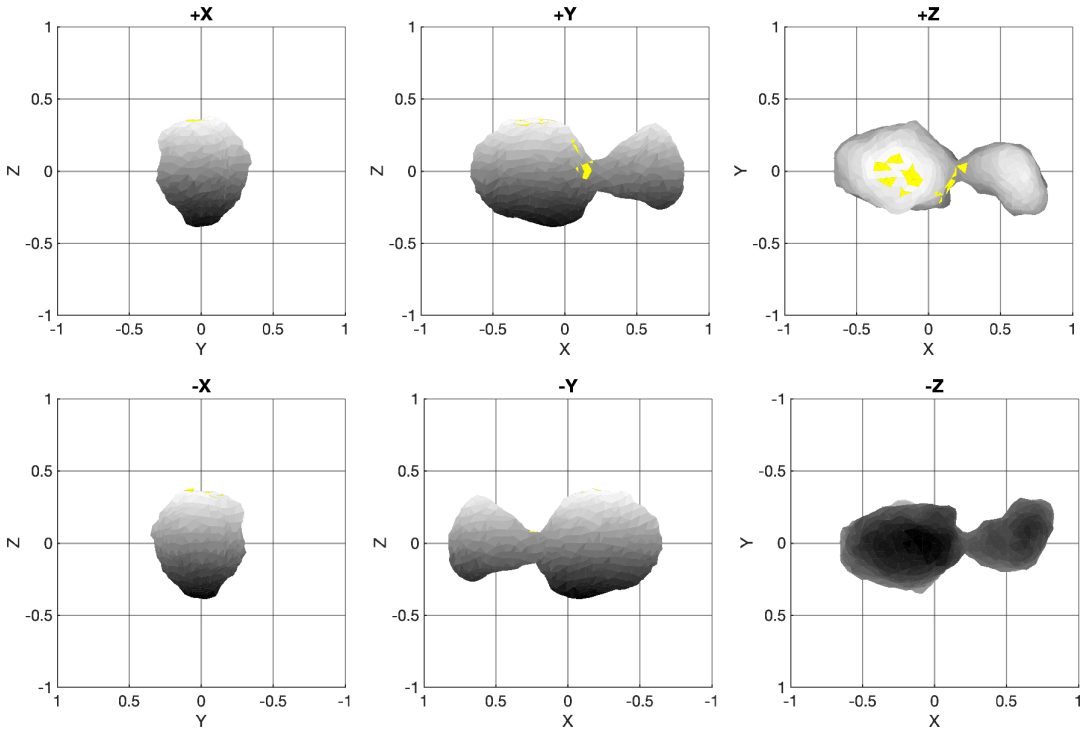

Figure 5.6: Same as Fig. 5.5, but for the best-fit vertex shape model of (68346) 2001 KZ66. The model was derived from cw spectra and delay-Doppler images. The model was given a fixed pole orientation determined during the convex inversion pole search. Yellow facets indicate those not seen in the radar images. The axes scales are shown in kilometres. Details of the alignment between the model's body-centric axes and the principal axes are detailed in Table A.1 of the appendix.

of the appendix contains a full description of the moments of inertia and the alignment of the principal axes to the body-centric axes for this model. The diameter of the model's equivalent-volume sphere has a value of 0.80 km, this is in good agreement with the diameter of 0.74 ± 0.21 km determined in the NEOWISE survey (Masiero et al., 2017). A comparison of the delay-Doppler images, a synthetic echo generated from the shape model, and a plane-of-sky image of the shape model are shown in Figs. 5.7 and 5.8. Using this model it is possible to accurately reproduce all of the data across both nights.

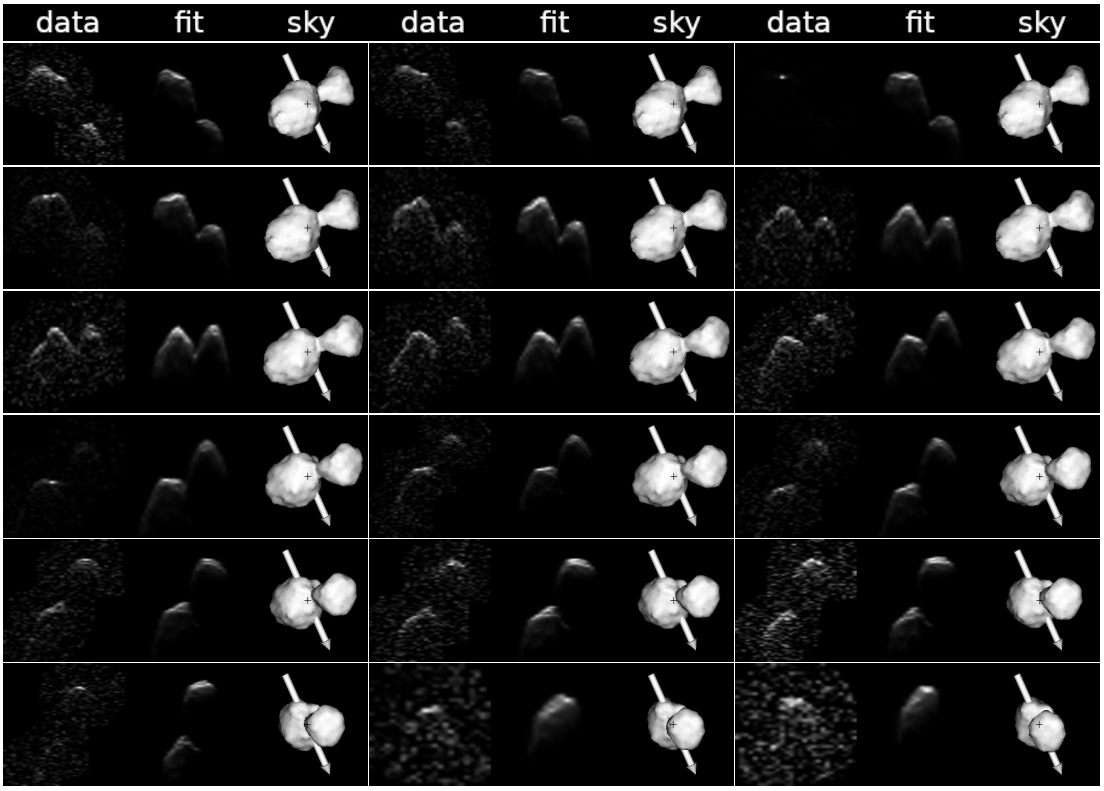

Figure 5.7: Fit of the final radar-derived shape model of asteroid (68346) 2001 KZ66 to the radar data (model summary in Table 5.4). Each three-image sub-panel is comprised of: the observational data (left panel), synthetic echo (middle panel), and plane-of-sky projection of the best-fit model (right panel). On the data and synthetic-echo images the delay increases downwards and the frequency (Doppler) to the right. The plane-of-sky images are orientated with celestial north (in equatorial coordinates) to the top and east to the left. The rotation vector (Z-axis of body-fixed coordinate system) is marked with a white arrow. This sequence of images corresponds to the Arecibo data collected on 28 October 2003.

5.3.3 Surface structure of KZ66

One particularly useful product of radar observations is the circular polarisation ratio. The ratio, SC/OC, is determined from the detection of an asteroid's echo in a cw spectrum. The received signal is recorded in both same circular (SC) polarisation as transmitted and the opposite circular (OC) polarisation. For mirror-like backscattering, the SC component would be zero. These ratios are used as a crude estimate of the near-surface complexity at scales near the wavelength of the observations (Ostro et al., 2002), approximately 13 cm for the observations taken from Arecibo Observatory. The

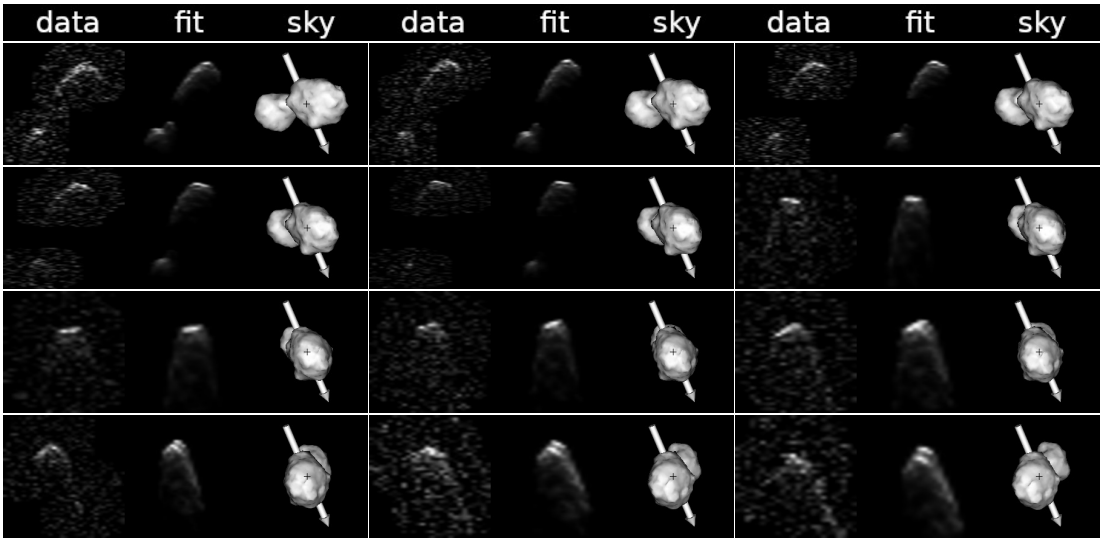

Figure 5.8: Same as Fig. 5.7, but this sequence of images corresponds to the Arecibo data collected on 29 October 2003.

Parameter	Value
DEEVE dimensions (2a, 2b, 2c)	$1.57 \times 0.51 \times 0.63$ km
Max. extent along (x, y, z)	$1.51 \times 0.64 \times 0.78$ km
Surface area	2.70 km^2
Volume	0.27 km^3
D_{eq}	0.80 km

Table 5.3: The geometric parameters for the best fit radar-derived shape model of (68346) 2001 KZ66. DEEVE denotes the dynamically equivalent equal-volume ellipsoid. The maximum extents of the model are measured along the body-centric coordinate axis. The D_{eq} is the diameter of a sphere with volume equal to that of the model.

cw spectra obtained on 28 October 2003 recorded a ratio of 0.218 ± 0.003, and the subsequent night recorded 0.222 ± 0.002 (spectra are shown in Fig. 5.9). This gives a mean polarisation ratio of 0.220 ± 0.003 for KZ66. This value places KZ66 within the mean value for NEAs, 0.34 ± 0.25 (Benner et al., 2008). Compared to the polarisation ratios of other contact-binary asteroids with shape models, KZ66 has the lowest recorded value: Itokawa 0.27 ± 0.04 (Ostro et al., 2004), 1996 HW1 0.29 ± 0.03 (Magri et al., 2011), 1999 JV6 0.37 ± 0.05 (Rożek et al., 2019a). This indicates KZ66's surface roughness is smoother than Itokawa's at the cm-to-m scale.

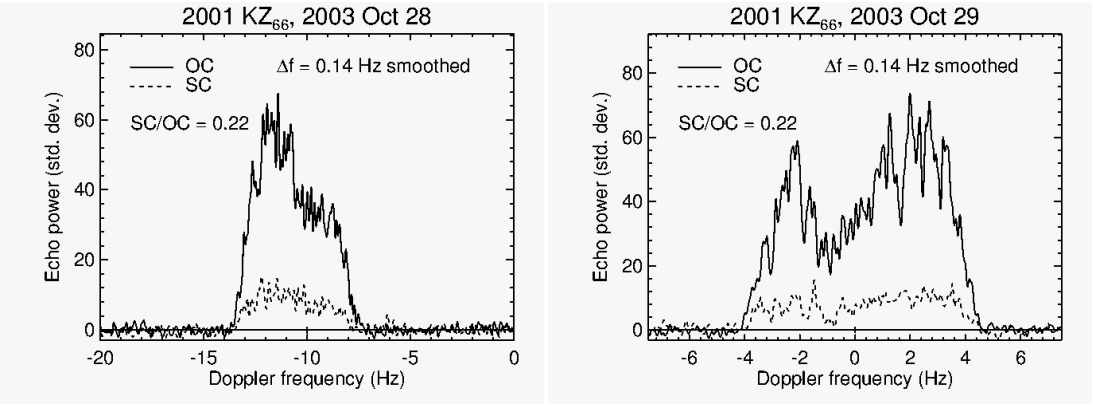

Figure 5.9: Continuous wave (cw) spectra observations of asteroid (68346) 2001 KZ66 observed in October 2003 at Arecibo Observatory (detailed description of the observations given in Table 5.2). The received circularly polarised signal is recorded in both same circular (SC) polarisation as transmitted, shown by the dashed line, and the opposite circular (OC) polarisation, shown by the solid line.

	Convex inversion	Radar inversion
λ	170°	170°
β	−85°	−85°
Pole uncertainty	15°	15°
T_0 [JD]	2455291.0	2455290.98269
P [h]	4.985988	4.985997
ΔP	0.000020	0.000042
$\nu\,[\times 10^{-8}\,\mathrm{rad\,d^{-2}}]$	$7.7^{+3.8}_{-13.2}$	8.43 ± 0.69

Table 5.4: Best-fit spin-state solutions from two approaches to shape modelling: convex light curve inversion, and modelling using the SHAPE software to invert radar data (which utilizes the pole position from light curve inversion). The table lists: the ecliptic coordinates of the rotation pole, longitude (λ) and latitude (β), the model epoch (T_0), the sidereal rotation period (P), and the YORP factor (ν).

5.4 Direct detection of YORP

The constant torque provided by the YORP effect produces a linear change in the rotation rate, which can be measured directly as in Lowry et al. (2007). However, the constant torque also manifests itself as a quadratic change in the rotation phase of an asteroid. To investigate the YORP effect in terms of rotation phase requires light curves with precise timing information and a good shape model and pole solution for

the asteroid asteroid. If the YORP acceleration, ν, is zero the change in rotation phase will be linear. This can clearly be seen in Eq. 3.8 repeated below:

$$\varphi(t) = \varphi\left(T_0\right) + \omega\ \left(t - T_0\right) + \frac{1}{2}\nu\ \left(t - T_0\right)^2 \tag{3.8}$$

5.4.1 Convex inversion

The first approach to detecting a YORP signature was based on the light curve only approach used in Sect. 5.3.1 to determine the pole. This time the pole search was repeated while including a range of YORP strengths, ν, between -1.0×10^{-6} rad/day^2 and 1.0×10^{-6} rad/day^2. Performed in two stages, the first stage step-size in YORP strength was coarse with a resolution of 1.0×10^{-7} rad/day^2. In the second stage, a finer scan between -1.2×10^{-7} rad/day^2 and 2.4×10^{-7} rad/day^2 was performed with a resolution of 1.0×10^{-9} rad/day^2. For each YORP strength, a grid of pole orientations covering the entire celestial sphere with a resolution of $5^\circ \times 5^\circ$ was sampled. The pole and YORP strength were held fixed, while period and convex shape were optimised to fit the light curves. For each ν value a χ^2 map was produced by projecting χ^2 values for each grid point onto the celestial sphere (Fig. 5.4 is an example of such a χ^2 map for $\nu = 0$). These χ^2 maps were examined for each value of ν with the minimum χ^2 extracted from each. The best fit to the light curve dataset is for a YORP value of 7.7×10^{-8} rad/day^2, however, plausible values of YORP range from -5.20×10^{-8} rad/day^2 to 1.15×10^{-7} rad/day^2. It should be noted that the constant period convex inversion model, $\nu = 0$, reproduces the light curves well (a full set of light curves are provided in Fig. A.13).

5.4.2 Phase-offset spin-state analysis

The second approach is to measure the rotational phase offsets, $\Delta\varphi$, between the light curves and the synthetic light curves generated from the radar-derived model (described in Sect. 5.3.2). The radar-derived model was generated independently of the light

curves, with the exception of using the light curve-derived pole position.

First, it is ensured that the rotation phase of the synthetic light curves matches the observations for the first few optical light curves obtained on 4-5 April 2010. This is where T_0 value is set (Table 5.4). To create a synthetic light curve, the model is propagated forward from T_0 to the epoch of each light curve, using the sidereal rotation period. I then determine which facets were illuminated and visible to the observer at each light curve's epoch by using asteroid-centred Sun and Earth vectors from JPL's Horizon service. The software accounts for self-shadowing using ray-tracing. The scattering model employed to produce the synthetic light curves was a combination of the Lambertian and Lommel-Seelinger scattering models (Kaasalainen et al., 2001). At any given rotation phase, the relative flux contribution from each facet was then summed to produce the expected brightness of the asteroid, which was then converted to a relative magnitude. The synthetic light curve and observed light curve were then scaled so that they both oscillate about zero magnitude.

The synthetic and observed light curves may not be aligned at this stage, as a zero YORP strength is assumed initially, and the initial rotation period used may be slightly inaccurate on the first iteration of the fitting procedure. To quantify any phase offsets due to YORP, the phase offsets required in order to align the two light curves is measured. This is done by applying a range of phase offsets from 0° to 360° in steps of 0.5° to the synthetic light curves and recording the phase offset that minimises the χ^2 fit between the light curves. If a constant period model is sufficient to align all synthetic light curves to their associated observed light curves, then a straight line should fit the phase offsets. However, if KZ66 is undergoing a discernable YORP acceleration, then the phase offsets will be fit by a quadratic curve, as seen for (25143) Itokawa (Lowry et al., 2014) and (54509) YORP (Lowry et al., 2007; Taylor et al., 2007). During the initial fittings, the phase offsets may not be purely quadratic. They may also contain a linear component which can be used to refine the rotation period. This process is iterated until the linear component becomes negligible.

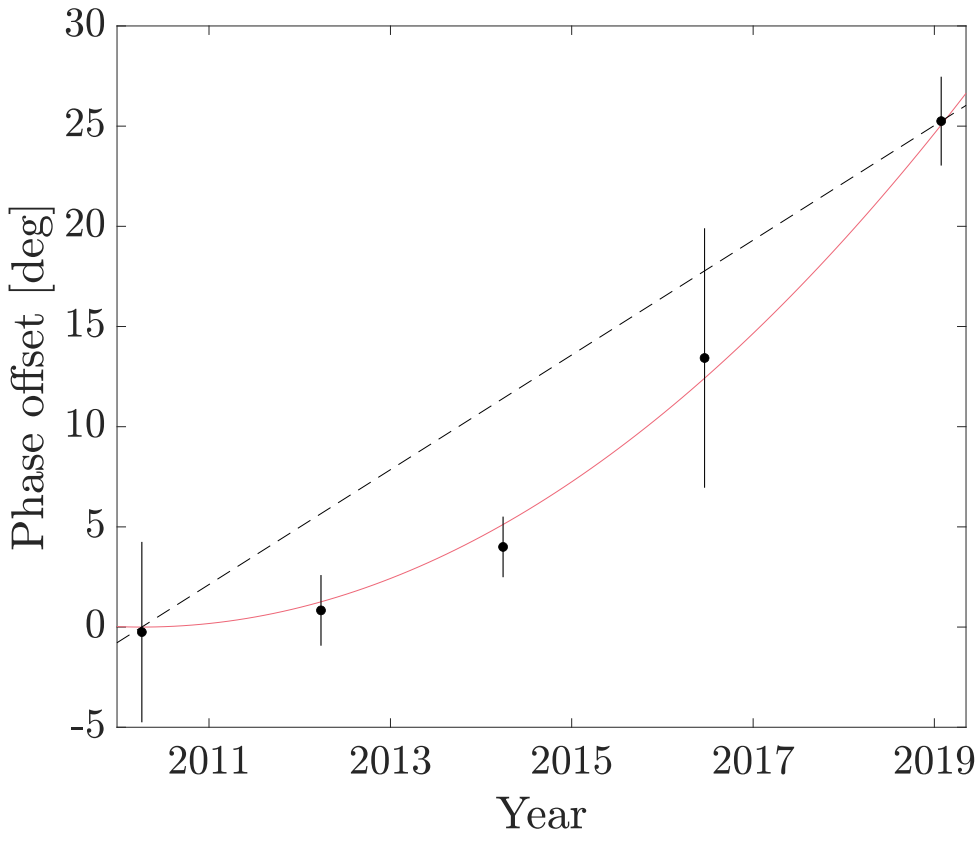

Figure 5.10: Phase offset measurements for the non-convex radar-derived shape model of asteroid (68346) 2001 KZ66, with $\lambda = 170°$, $\beta = -85°$, period $P = 4.985997 \pm 0.000042$ hours, and starting point $T_0 = 2455290.98269$ (April 2010). The black circles represent averaged phase offset measurements for light curves grouped by year, and the associated uncertainties are given by the standard deviation of the individual light curves within each year. The red solid line marks the best-fit YORP solution, $\nu = (8.43 \pm 0.69) \times 10^{-8}$ rad day^{-2} (5.0×10^{-6} deg/day^2. The black dotted line is a straight line between the first and last points to highlight the deviation from a linear trend.

The results of the phase offset measurements are plotted in Fig. 5.10. In this figure the phase offsets have been grouped by similar epochs. The grouped phase offset is given by the mean of the individual light curve phase offsets. The uncertainties of grouped phase offsets are calculated as the standard deviation of the phase offsets within that group. These grouped phase offset measurements result in a clear quadratic trend with a YORP strength of $\nu = (8.43 \pm 0.69) \times 10^{-8}$ rad/day^2, for a rotation period at T_0 of 4.985997 ± 0.000042 h. A figure of a sample light curve comparing the model with and without this YORP acceleration is plotted in Fig. 5.11.

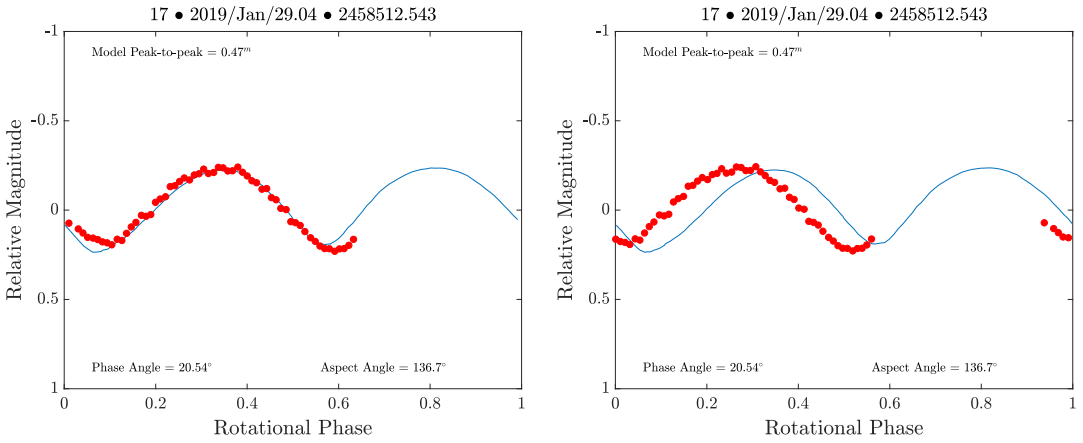

Figure 5.11: Example synthetic light curves generated using the radar-derived shape model of (68346) 2001 KZ66 (blue lines), with YORP (left) and without YORP (right), with the optical data over plotted (red dots). The complete dataset can be found in the Appendix.

5.5 Discussion

5.5.1 Direct detection of YORP spin-up

By combining the detailed shape model with the optical light curves a YORP acceleration of $(8.43 \pm 0.69) \times 10^{-8}$rad/day^2 was measured. This marks the eighth direct detection of YORP to date, and KZ66 is the fourth smallest asteroid of those with YORP detections; it is larger than asteroids YORP (2000 PH5), Itokawa, and Bennu (all detections are in listed Table 1.1). Intriguingly, all YORP detections to date have been positive accelerations (i.e. in the spin-up sense). However, for a population of asteroids with randomized shapes and spin-states, YORP should produce both spin-up and spin-down cases. The probability of eight consecutive spin-up detections is therefore minute. This suggests that there is either a mechanism that favours YORP accelerations or a bias in the sample of YORP detections obtained to date. One such mechanism for the preference of YORP spin-up is 'TYORP', which accounts for the thermal emission tangential to the surface from boulders (Golubov and Krugly, 2012; Golubov et al., 2014; Golubov, 2017). However, while the TYORP process is certainly promising, further YORP detections are required to confirm this model.

There may also be biases in the current sample. To date, the asteroids on which YORP has been detected have all been retrograde rotators; three out of eight of them have pole orientations within 10° of the southern ecliptic pole, and all are within 41°. They all also have obliquities larger than 140° (see Table 1.1). With the exception of YORP and Bennu, all of the asteroids with YORP detections have elongated shapes (Hudson and Ostro, 1999; Ostro et al., 2004; Taylor et al., 2007; Kaasalainen et al., 2007; Nolan et al., 2013; Ďurech et al., 2012, 2018). Under a rotational acceleration, like that of YORP, initially spherical rubble pile asteroids can be disrupted to form various shapes. The end state of this process ranges from ellipsoidal to bilobed shapes (Sánchez and Scheeres, 2018). The magnitude and direction of the rotational torque induced by YORP is dependant on obliquity, but is also highly sensitive to the morphology. The asteroid shapes can roughly be classified into four types (I/II/III/IV) depending on their model response to YORP torque under zero-conductivity assumption. The behaviour of both the spin and obliquity components of YORP for each type of asteroid vary with obliquity differently. In considering type I asteroids, the spin component of YORP is positive outside for obliquities of 0° to ∼60° and ∼120° to 180°, with negative YORP falling in the region ∼60° to ∼120° (Rubincam, 2000; Vokrouhlický and Čapek, 2002; Golubov and Scheeres, 2019).

Asteroids presenting large light curve amplitudes are favoured for direct detection of YORP as their rotation phases can be measured to a greater accuracy. This preference to obtain high-amplitude light curves limits the morphology and observation geometry of asteroids probed, which in turn restricts the type of YORP behaviour detected.

5.5.2 Gravitational slopes and topographic variation on (68346) 2001 KZ66

The bifurcated shape of KZ66 with a small contact area between the two lobes raises questions of how stable its surface is against land sliding and other surface failure events. To investigate this, my collaborator, Ben Rozitis, computed the gravitational

slopes of KZ66 using a polyhedron gravity model (Werner and Scheeres, 1996) that has been modified to account for rotational centrifugal forces (Rozitis et al., 2014). The moderately high geometric albedo and average radar circular polarisation ratio of KZ66 suggests that it is likely to be an S-type asteroid (Benner et al., 2008). Therefore, these calculations were performed assuming uniform bulk density values of 1500, 2000, and 2500 kg m^{-3} to cover the typical bulk density range for rubble-pile asteroids from this spectral class (Carry, 2012). Fig. 5.12a shows the gravitational slopes calculated from the shape model of KZ66, and Fig. 5.12b shows their areal distribution. As shown, there are no large differences in the gravitational slopes between the neck region and the rest of the body. Furthermore, the majority of gravitational slopes are below 40°, particularly for a bulk density of 2500 kg m^{-3}, which indicates that any land sliding occurring on the body would be rather limited in area, even if KZ66 lacked cohesion (Murdoch et al., 2015).

If land sliding did occur on KZ66 then it would cause mobilised material to migrate from areas of high gravitational potential to areas of low gravitational potential. The changes in shape and surface topography resulting from this material migration has the net effect of reducing the topographic variation in gravitational potential across the body. As such, deformable bodies prefer to exist in a state where this topographic variation is minimised (Richardson and Bowling, 2014; Richardson et al., 2019), and the YORP effect can induce migration of material when these bodies stray too far from this preferred state (Scheeres, 2015). To determine what topographic state KZ66 is currently in, Ben Rozitis also computed its topographic variation in gravitational potential as a function of scaled spin (i.e. $\omega/\sqrt{G\pi\rho}$) following the methodology outlined in Richardson et al. (2019). Fig. 5.12c shows the spatial distribution of gravitational potential across the shape model of KZ66, and Fig. 5.12d shows the functional dependence of KZ66's topographic variation with scaled spin. As shown, there are subtle variations in the gravitational potential across KZ66, particularly between its equator and poles, but intriguingly KZ66 currently exists at or near its preferred state where the topographic variation is minimised. However, as the detected YORP effect is causing KZ66 to spin-

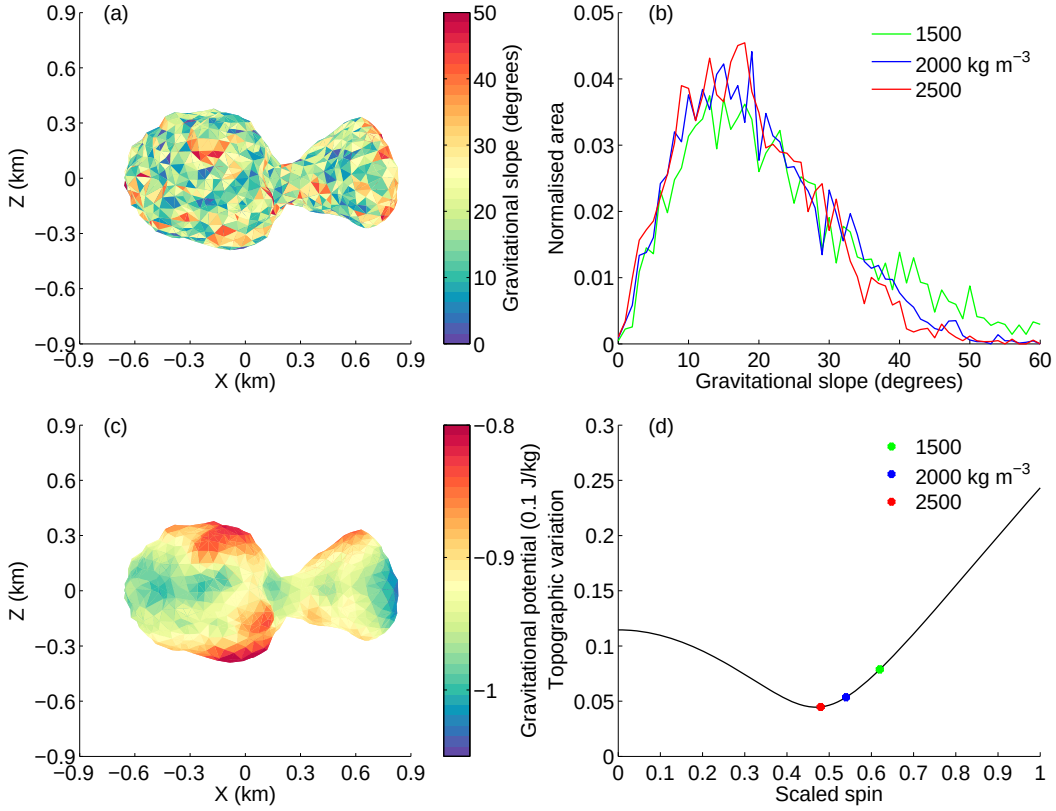

Figure 5.12: Gravitational slopes and topographic variation on asteroid (68346) 2001 KZ66. (a) Gravitational slopes computed with the shape model assuming a bulk density of 2000 kg m^{-3}. (b) Areal distribution of gravitational slope computed for three different values of bulk density. (c) Gravitational potential computed with the shape model assuming a bulk density of 2000 kg m^{-3}. (d) Topographic variation in gravitational potential (i.e. the standard deviation of the gravitational potential variations normalised to the mean gravitational potential) as a function of scaled spin (black line). The current topographic variation of KZ66 is identified for three different assumed values of bulk density (coloured data points).

up, it will not exist in this state permanently. For instance, the scaled spin will be doubled in ∼1Myr at the current rate of YORP spin-up, which would lead to a factor of ∼5 Increase in the amount of topographic variation. Therefore, whilst KZ66 seems to be stable in its current state, the YORP effect will eventually induce changes in its shape and surface topography. It is possible that the induced shape and topography changes would cause the YORP effect to switch from spin-up to spin-down (Cotto-Figueroa et al., 2015), but if spin-up were to continue then KZ66 would ultimately fission to form an unbound asteroid pair (Scheeres, 2007).

5.5.3 Bifurcated shape of (68346) 2001 KZ66

The majority of KZ66's surface was observed during the 2003 approach with Arecibo as shown in Fig 5.6. With a median facet edge length of 57 m, the shape of large-scale topographical features are reported with confidence. KZ66 has a distinct bifurcated shape, which is dissimilar to most other contact binaries with radar shape models such as Kleopatra, Itokawa, and 1999 JV6 as it has a much sharper concavity (Shepard et al., 2018; Ostro et al., 2004; Rożek et al., 2019a). In this regard, KZ66's shape bears more similarity with the NEAs 1996 HW1 (Magri et al., 2011) or 1999 JD6 (Marshall et al., 2015). Other objects such as the Kuiper Belt Object 2014 MU69 (Stern et al., 2019) or comets such as 19P/Borrelly, 67P/Churyumov-Gerasimenko, and 103P/Hartley 2 (Britt et al., 2004; Jorda et al., 2016; Thomas et al., 2013) also have bilobate shapes. The sharp neck line of KZ66 suggests that the formation of this object was not a highly energetic event, and both lobes must have merged gently. There are several mechanisms capable of forming a contact-binary asteroid like KZ66. We will briefly summarise the mechanisms capable of forming a contact-binary asteroid.

One mechanism that can lead to the formation of a contact-binary is the collapse of a binary asteroid system. If this collapse occurred at a low velocity the asteroid would preserve the bilobed shape and avoid the deformation that would occur with a catastrophic collapse. There are several possible processes that lead to the formation of binary asteroids. One is mutual capture which requires the components having relative speeds below their mutual escape velocities which are typically on the order of m/s. However, in present-day conditions for the Main Belt and near-Earth asteroids relative speeds are on the order of km/s. Hence such a scenario is extremely unlikely in today's populations of asteroids (Richardson and Walsh, 2006). Binaries can be formed from a single body rotationally fissioned as rotational acceleration leads the asteroid towards the spin-limit barrier for gravitational aggregates (Pravec and Harris, 2000). Accelerated by YORP, an asteroid would reconfigure its shape before eventually fissioning to form a binary asteroid (Jacobson and Scheeres, 2011). A good example of

this is the NEA 1994 KW4 with its rapidly rotating primary (Ostro et al., 2006). Once the binary had been formed, binary-YORP or BYORP can either expand or contract their mutual orbit. If BYORP decays the orbit, the orbital semi-major axis shrink until the secondary gently collides with the primary and settles (Ćuk and Burns, 2005). It is possible for the contact-binary to experience further fission and re-impact cycles. Presuming each lobe maintains their relative orientation, then the YORP, BYORP, and mutual tides will act similarly during each cycle (McMahon and Scheeres, 2010; Jacobson and Scheeres, 2011). If KZ66 was formed via this mechanism, studying the mass ratio of the lobes could be used to constrain the types of binary system that BYORP is able to produce contact-binaries from.

Collisions between unbound pairs of asteroids are another mechanism that alter their shapes. Studies of catastrophic collisions show that they can form a large spectrum of shapes including contact-binaries (Michel and Richardson, 2013; Sugiura et al., 2018; Schwartz et al., 2018). Far more common, by at least an order of magnitude, are sub-catastrophic collisions in which at least 50% of the impacted asteroid remains gravitationally bound (Jutzi and Benz, 2017). Jutzi (2019) showed that these more frequent sub-catastrophic collisions between an ellipsoidal porous rubble-pile asteroid and a hyper-velocity impactor are able to change the overall structure and shape of the impacted asteroid. If the impactor strikes the centre of an ellipsoid asteroid, it can split into two separate components which during re-accumulation can form Itokawa-like contact-binary asteroids. Collisions between asteroids are also capable of forming binary systems, either by a collisionally induced rotational fission of the parent body due to a glancing impact, or gravitationally bound ejecta resulting from the collision between two asteroids (Walsh and Jacobson, 2015). Although, formation via disruption is far more likely than collisionally induced rotational fission (Merline et al., 2002). A binary asteroid can later form a contact-binary ask discussed above.

An additional mechanism for the formation of a contact-binary is the rotational evolution of a self-gravitating spherical aggregate with a weak core. Sánchez and Scheeres

(2018) consider an inhomogeneous spherical asteroid with a concentric core that is weaker than its outer shell. The inclusion of a weak core means that by the time the shell starts to fail, the core will not provide any resistance. As the spherical asteroid is rotationally accelerated the core and shells start to deform asymmetrically, this is particularly prominent when the radius of the core is equal to half of the total radius of the asteroid. In this case, the shell develops a dent and the core becomes very deformed. When the simulations are continued the asteroid then starts to stretch to form a non-ellipsoidal shape with a distinct "head" and "body". The shape at this stage bears similarities to the asteroid Itokawa and the authors suggest this as a formation mechanism for Itokawa. When advanced further, the concavity between the lobes continues to deepen before finally fissioning to form a binary asteroid. The configurations at each stage are stable and only change when the asteroid is spun-up further. Hence, with the YORP-induced acceleration observed in KZ66 and a more pronounced "neck", it is possible that it has advanced further along this fission process than Itokawa.

For comets it has been suggested that erosion due to out-gassing could play a role in their morphology, and may have contributed to the deep neck region seen on comet 67P/Churyumov-Gerasimenko, by the Rosetta spacecraft (Sierks et al., 2015). However, with a geometric albedo of 0.291 ± 0.110, it is unlikely that KZ66 is an extinct comet. These objects have dark surfaces with geometric albedos generally less than 0.05 (Lamy et al., 2004).

An issue with some of the suggested formation mechanisms is that they require a fast rotation rate, whereas KZ66 has a long rotation period close to five hours. However, asteroids migrate through different spin-states over YORP-cycles caused by structural and small-scale topographical changes (Statler, 2009), presumably caused by YORP torques and perturbations (Scheeres, 2018). Therefore it is possible that KZ66's shape as seen today was formed during a previous YORP cycle where it had a faster rotation period. Recent work by Golubov and Scheeres (2019) in the dynamical evolution of asteroids showed that for an idealised system, ignoring thermal inertia and

tangential YORP (TYORP), the YORP cycle drives the asteroid from the tumbling regime to disruption at high rotation rates, or back to the tumbling regime. Depending on the shape and rotation-state of the asteroid they migrate from obliquities of 0° or 180° to an obliquity of 90°, or from 90° to either 0° or 180° (Golubov and Scheeres, 2019). The inclusion of TYORP allowed stable equilibria states to exist where asteroids would cease to follow these YORP-cycles, although until they encounter these equilibria they continue to migrate between tumbling states or disruption. With an obliquity of 158.5°[1], it is possible that KZ66 has left the tumbling regime and is now in the process of migrating towards an obliquity of 90°.

For now, the formation of KZ66 will remain speculative. More data is needed to determine the composition of the asteroid, which will help deduce whether or not this asteroid was formed by one or more bodies. Future work could involve a thermophysical analysis to determine the theoretical YORP strength, which could lead us to discover the need for heterogeneity to reconcile the theoretical and observed values - a method used by Lowry et al. (2014) to determine the density inhomogeneity for the asteroid Itokawa. In the meantime, the shape model developed here can be used to further study the formation mechanisms of binary asteroids.

5.6 Conclusions

The Apollo PHA (68346) 2001 KZ66 was monitored for nine years during the period 2010 to 2019, obtaining ten optical light curves. Additionally, two nights of radar observations are available from the Arecibo Observatory taken in 2003. With these data and published optical light curves I have derived a robust shape model of KZ66. KZ66 has a distinct bifurcated shape comprising of a large ellipsoidal component joined by a sharp concavity to a smaller non-ellipsoidal curved component. I have discussed four different formation mechanisms that could have played a role in the evolution of KZ66 - collapse of a binary system, rotational deformation, re-formation after collision,

[1]JPL solution number 206 from the Horizons ephemeris system (`https://ssd.jpl.nasa.gov/`)

erosion. One of the mechanisms was ruled out by considering the geometric albedo of KZ66. It is unlikely that out-gassing was responsible for the morphology that is seen today. The stability of KZ66's shape has also been discussed by calculating its gravitational slopes and investigating the topographic variation. KZ66 was found to currently exist at or near its preferred state with minimised topographic variation.

Using the radar-derived shape model an acceleration of the asteroid's rotation rate was detected which can be attributed to YORP. Using nine years of light curve data, the light-curve-only analysis resulted in a large range of possible YORP strengths with the best value at $(7.7^{+3.8}_{-13.2}) \times 10^{-8}$rad/day^2. However, by combining the optical light-curves with the radar-derived shape model, it was found that the model required a YORP strength of $(8.43 \pm 0.69) \times 10^{-8}$rad/day^2 with an initial rotation period of 4.985997 ± 0.000042 h to fit all of the data. This detection marks the eighth direct detection of YORP, all of which are positive accelerations.

The SC/OC polarisation ratio of 0.220 ± 0.003 determined for KZ66 from the Arecibo cw spectra shows that it is a typical representative of the NEA population. Compared to other contact binaries with shape models, KZ66 has the lowest recorded value indicating that its surface roughness is smoother than Itokawa's at the cm-to-m scale.

6 | Optical observing campaign and modelling of asteroid (89830) 2002 CE

6.1 Introduction

The asteroid (89830) 2002 CE was discovered on the 1 February 2002 at Socorro by the Lincoln Near-Earth Asteroid Research project (Stokes et al., 2000). This object is an NEA with a semi-major axis of 2.08 AU and an eccentricity of 0.51. Its orbit is entirely outside of that of Earth, making it a member of the Amor classification. (89830) 2002 CE is also classified as a Potentiallty Hazardous Asteroid (PHA) due to its absolute magnitude and the proximity of its orbit to Earth's (see Fig. 6.1).

Since the asteroid's discovery, it has been observed by Pravec from the Ondrejov Observatory who determined a rotation period of 2.6149 ± 0.0008 h (Warner et al., 2009). The asteroid was also observed on 7 October 2010 with the 2.2 m telescope at Calar Alto, Spain, when Sanchez et al. (2013) used visible wavelength observations in order to measure its spectral slope. Determining the asteroid to be an S-class asteroid within the Bus taxonomic classification system (Bus and Binzel, 2002). The object was later revisited as part of the MIT-Hawaii Near-Earth Object Spectroscopic Survey which also determined (89830) 2002 CE to be an S-class object (Binzel et al., 2019).

In addition, the NEOWISE survey has also observed this object in the infrared wavelengths, determining a geometric albedo of 0.08 ± 0.08 and a diameter of 5.07 ± 2.16 km (Mainzer et al., 2012; Mainzer et al., 2019).

Over the period covering 2010 to 2019, 25 optical light curves were collected as part of our European Southern Observatory Large Programme (ESO LP) and auxiliary campaigns. From our main programme, eight light curves were obtained from the New Technology Telescope taken over 2010, 2012, and 2013. An additional 11 light curves were obtained from the Table Mountain Observatory, four from the Isaac Newton Telescope, and one from both the Nordic Optical Telescope and 200-inch Hale Telescope.

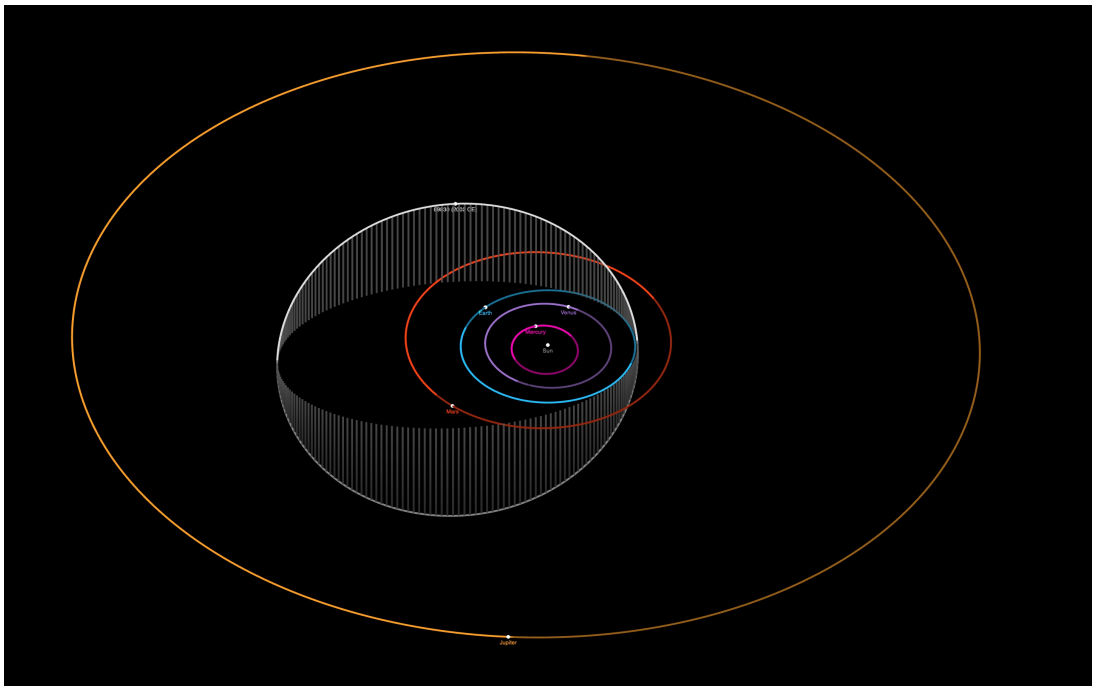

Figure 6.1: Diagram of the orbit of asteroid (89830) 2002CE also showing the orbits of Mercury, Venus, Earth, Mars, and Jupiter. Positions of all objects are for the date 2020-02-21 00:00 UTC. Image produced using `https://ssd.jpl.nasa.gov/sbdb.cgi`

In this chapter, I will present the results and analysis of the investigation of (89830) 2002 CE. In which, the aim was to develop a physical model of the asteroid describing its shape and spin-state, in order to search for a possible influence of a YORP acceleration. Our long-term photometric observing campaign monitored this asteroid over the period

2010 to 2019 and a description of this is given in Sect. 6.2. In the following sections a description of the modelling of the asteroid's shape and spin-state is described in Sect. 6.3, including the search for a signature of a change in the spin-state. Finally, a discussion of the results is given in Sect. 6.4.

6.2 Optical datasets obtained from the observing campaign of (89830) 2002 CE

The optical dataset for (89830) 2002 CE was obtained as part of the ESO LP, it covers a period of nine years from 2010 to 2019. The observations were obtained at a range of observing geometries, particular with respect to the ecliptic latitude. Our light curves cover a large range of ecliptic latitudes from $-50°$ to $70°$. Such a large range of observing geometries will aid in accurately determining the asteroid's pole orientation and constraining its shape. A summary of the light curves including information such as the asteroid's distance from the Sun and Earth, the orbital phase angle, the observer centric ecliptic longitude and latitude, and more is listed in Table 6.1. The observing geometries of the light curves are also displayed in Fig. 6.2.

The data reduction process for all of our observations are similar no matter what facility they were obtained from. It includes the steps outlined in Sect. 2.1.4: bias and flat-field corrections. Additional steps are sometimes required, but these can be dependant on the configurations of the instrumentation. These steps are the correction of bad pixels that are persistent artefacts of a particular CCD's images and the removal of fringes that appear due to interference of light within the CCD. Furthermore, after inspection, some frames also require steps to remove any cosmic ray incident with the CCD during the image's exposure.

All of the light curves utilised in this work have been extracted from the processed images obtained from various facilities listed below. The steps performed in order to extract an asteroid's light curve are described in detail in Sect. 2.1.4 of this thesis.

To summarise the process briefly here, the brightness of the asteroid is measured by counting the flux within an aperture. The size of the aperture is related to the FWHM of the image. To account for the changing circumstances of the images throughout the night, non-variable background stars are used as reference to measure the frame-to-frame changes in instrumental magnitude. This can be used to correct temporal changes in the brightness of the asteroid due changing observing conditions. The light curves obtained with this method are relative light curves, as they are not calibrated against the catalogued magnitudes of reference stars. From our dataset, the reduction and light curve extraction of the NTT, TMO, and PAL datasets for this object were handled by Sam Jackson of the University of Kent.

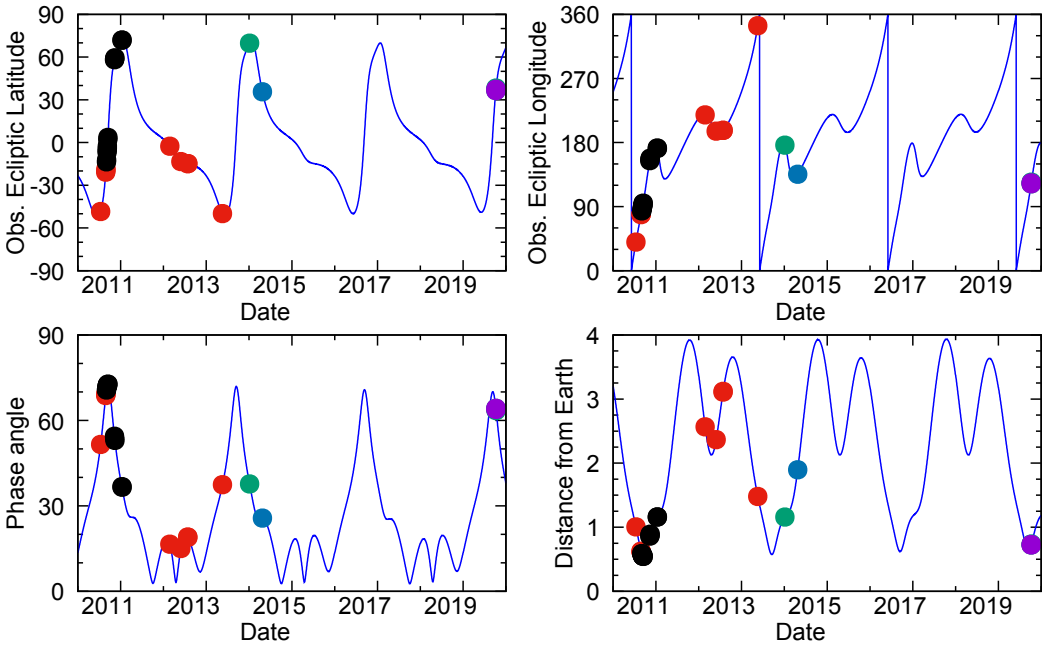

Figure 6.2: Asteroid (89830) 2002 CE observing geometries during the optical observations over the period 2010 to 2019. The top two panels show the position of the object in the ecliptic coordinate system, latitude and longitude, as observed from Earth. The bottom two panels show the phase angle and geocentric distance to the target. Optical light curve data from the NTT are marked with filled red circles, with lightcurve data from the INT marked with filled blue circles, data from the TMO are marked by filled black circles, data from PAL are shown by green circles. The blue continuous line represents the object's observational ephemeris.

New Technology Telescope – 2010, 2012, and 2013

All of the observations obtained with the NTT were taken with the EFOSC2 instrument (Buzzoni et al., 1984). The instrument CCD has 2048x2048 pixels and a 4.1' x 4.1' field of view. A comprehensive description of the telescope and its instruments are given in Sect. 2.1.2. Observations of (89830) 2002 CE were taken in imaging mode with a binning of 2x2 of the CCD's pixels. The images obtained with EFOSC2 were performed using the Bessel R filter, the only exception to this is the set of observations taken in 2013 which were performed using the Bessel V filter. In total, eight light curves of 89830 were obtained from the NTT. Four were obtained in 2010, three in 2012, and one in 2013. Of the eight light curves, four required stacking of the images to improve their signal-to-noise ratio, those with IDs 1, 17, 18, and 19 in Table 6.1.

Table Mountain Observatory – 2010 and 2011

Images of the asteroid were also obtained from the one-metre telescope at Table Mountain Observatory over 2010 and 2011. All observations were performed using a R-band filter and utilised the full 4096 x 4096 pixel array of the CCD. A total of 11 light curves were captured over a four-month period between 3 September 2010 and 12 January 2011.

200-inch Hale Telescope – 2014

The asteroid was observed during 2014 from the 200-inch Hale Telescope using the LFC (Gunn et al., 1987). Images were taken with the CCD unbinned and utilising the instrument's full 24' x 9' field of view. The filter selected for these images was a broadband R filter. A single light curve was obtained from this facility on the night of 25 April 2014.

Isaac Newton Telescope – 2014 and 2019

Observations from the INT were made utilising the telescope's WFC instrument (Ives et al., 1996). In 2014, the entire 23' x 12' field of field of CCD 4 was utilised for

the observations. These observations were performed on the 6 January 2014 using the Sloan-Gunn r filter. For the 2019 observations however, the WFC was windowed to use a small section of CCD 4 covering 15' x 10', this has the benefit of reducing the readout time required between images. During these observations, the asteroid was observed on three nights between the 7 and 9 October 2019. The images taken on these nights were taken using the Harris V filter.

Nordic Optical Telescope – 2019

The final telescope used to observe (89830) 2002 CE was the NOT with the instrument ALFOSC. The instrument was used in imaging mode with the CCD un-windowed to give a field of view of 6.4' x 6.4'. The asteroid was imaged in the Bessel V filter for a single night on 7 October 2019.

6.3 Shape modelling of (89830) 2002 CE

6.3.1 Determination of the sidereal rotation period

The first stage of the analysis of 2002 CE involved determining the asteroid's sidereal rotation period. Although the asteroid already has a reported rotation period in the Asteroid Lightcurve Database, this is a synodic rotation period which is dependant on viewing geometry and the asteroid's rate of motion across the sky. To determine the asteroid's sidereal rotation period, `convexinv` is utilised to probe a range of fixed rotation periods (Kaasalainen et al., 2001). This approach uses six different models with predefined pole orientations spread over the celestial sphere for each of the fixed rotation periods. Both the shapes of these models and their pole orientations are optimised to fit the optical light curves. However, at the end of the optimisation, only the chi-squared value of the best-fit model is recorded for each of the probed rotation periods.

With data covering the epochs from July 2010 to October 2019, our dataset has a

ID	UT Date [*dd/mm/yyyy*]	$R_\odot$ [AU]	$\Delta_\oplus$ [AU]	α [°]	λ_O [°]	β_O [°]	Total [hour]	Filter	Observing facility	Reference	LC-only model
1	15/07/2010	1.268	1.005	51.58	40.3	-48.4	2.4	R	NTT		•
2	28/08/2010	1.052	0.627	68.74	78.7	-20.8	0.7	R	NTT		•
3	29/08/2010	1.049	0.620	69.09	79.5	-19.7	1.3	R	NTT		
4	30/08/2010	1.047	0.613	69.43	80.4	-18.5	0.7	R	NTT		
5	03/09/2010	1.037	0.589	70.67	83.9	-13.5	1.8	R	TMO		•
6	04/09/2010	1.035	0.583	70.95	84.8	-12.2	2.3	R	TMO		
7	08/09/2010	1.029	0.564	71.88	88.4	-6.8	2.2	R	TMO		
8	09/09/2010	1.028	0.560	72.07	89.3	-5.3	2.7	R	TMO		•
9	10/09/2010	1.027	0.557	72.23	90.2	-3.9	2.8	R	TMO		
10	11/09/2010	1.026	0.553	72.38	91.2	-2.4	2.2	R	TMO		
11	14/09/2010	1.023	0.546	72.68	94.0	2.1	1.4	R	TMO		
12	15/09/2010	1.023	0.544	72.74	94.9	3.6	1.0	R	TMO		
13	10/11/2010	1.201	0.860	54.47	154.5	58.1	1.7	R	TMO		•
14	13/11/2010	1.225	0.890	52.98	158.2	59.5	1.5	R	TMO		•
15	12/01/2011	1.626	1.159	36.75	172.3	71.8	3.3	R	TMO		
16	25/02/2012	3.128	2.567	16.53	218.9	-2.5	2.9	R	NTT		•
17	28/05/2012	3.091	2.367	15.05	195.9	-13.4	2.4	R	NTT		•
18	27/07/2012	2.998	3.109	19.03	197.2	-14.8	2.0	R	NTT		
19	20/05/2013	1.638	1.479	37.45	344.1	-49.9	1.0	V	NTT		•
20	06/01/2014	1.599	1.160	37.69	176.4	69.8	2.0	r	INT		•
21	25/04/2014	2.287	1.895	25.70	135.4	35.7	2.2	R	PAL		
22	07/10/2019	1.073	0.725	64.22	122.2	36.5	2.0	V	INT		•
23	08/10/2019	1.076	0.731	63.85	123.3	37.4	2.1	V	INT		
24	09/10/2019	1.080	0.737	63.47	124.4	38.2	2.1	V	INT		•
25	07/10/2019	1.073	0.725	64.22	122.2	36.5	1.7	V	NOT		

Table 6.1: A chronological list of optical lightcurves of asteroid (89830) 2002 CE used in this study. Each light curve has a numerical "ID" listed, then the Universal Time (UT) "Date" of the beginning of the night is given as well as the heliocentric ($R_\odot$) and geocentric ($\Delta_\oplus$) distances measured in AU, the solar phase angle (α), the observed ecliptic longitude (λ_O), the observed ecliptic latitude (β_O), and the "Observing facility" used to obtain the light curve. Where relevant, a "Reference" to published work is given. Each line represents a single light curve (sometimes a few segments were observed on a single night). Circles in the "LC-only model" columns indicate which light curves were selected for the light-curve-only shape modelling. The subset of data used is representative of the full variation in observing geometry captured. It was necessary to select a subset due to issues encountered during the modelling process, this is described more in detail in Sect. 6.3.2. Observing facility key: INT – 2.5 m Isaac Newton Telescope (La Palma, Spain), NTT – European Southern Observatory 3.5 m New Technology Telescope (Chile), TMO – Table Mountain Observatory (California, USA). NOT – Nordic Optical Telecope (La Palma, Spain) PAL – Palomar Observatory, 200-inch Hale Telescope (California, USA).

baseline of 1380 days. Using an initial period of 2.6149 hours taken from the literature (Warner et al., 2009) and with this baseline, the smallest separation of local minima that can be distinguished is 0.000103 hours (given by applying Eqn. 3.6). To obtain the step size utilised between periods this separation is multiplied by a coefficient of 0.8. Initially, 100 periods were probed surrounding the starting period of 2.6149 hours,

ranging from 2.610771 to 2.6190289 hours. However, upon inspection of the results, an additional 100 periods were added to extend this range down to a period of 2.602525 hours as the minima was positioned close to the lower boundary. For more details regarding how the period scan functions, please refer to Sect. 3.1.2

The results of this period scan are displayed in Fig. 6.3. This figure indicates that the sidereal rotation period that best fits the optical data is 2.6135 ± 0.0011 hours. The rotation period reported here is close to the literature period for this asteroid – 2.6149 ± 0.0008 hours. However, although there is a disagreement, this is expected since this figure illustrates a sidereal rotation period rather than a synodic period.

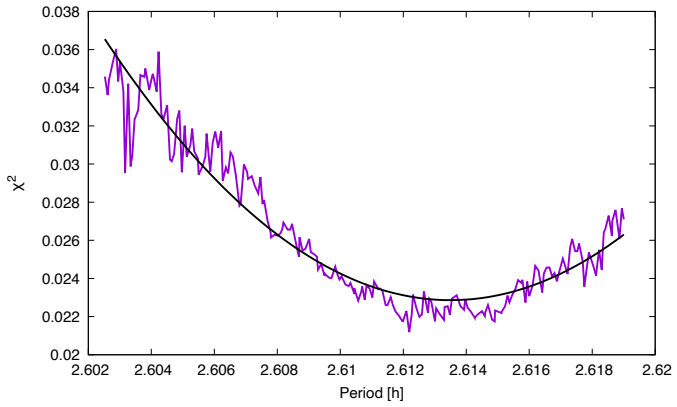

Figure 6.3: Results of the period scan for asteroid (89830) 2002 CE. For each fixed rotation period displayed within these results, six models were optimised to fit the data. These models have different pole orientations which were optimised, in addition to their shape. However, only the chi-squared value of the best-fit model for each period was recorded. A quadratic curve was fit to the results, which indicates a best-fit sidereal rotation period of 2.6135 ± 0.0011 hours.

6.3.2 Grid search for the pole orientation using `convexinv`

The next step of the analysis of 89830 probed the pole orientation of the asteroid by using `convexinv`. This process involved setting up a grid of pole orientations covering the entire celestial sphere. The poles were separated by 5° in both ecliptic longitude and latitude, giving a total of 2,592 models to be optimised. For each model, both the shape and rotation period were optimised while the pole was held constant. The resulting best-fit chi-squared value of the optimisation is recorded and used to plot a

chi-squared plane for the pole scan.

Initially, the grid search was attempted using all of the light curves listed in Table 6.1. In doing so, it was possible to perform the optimisation with `convexinv` and obtain chi-square values for each of the optimised pole orientations. However, whilst converting the plane's best-fit model from `convexinv`'s internal description to a polyhedral model for further investigation, the author repeatedly encountered software errors in this process; the procedure used was unable to convert the shape's description, which prohibited the inspection of the model's shape to assess the feasibility of its morphology.

In order to resolve this issue, a subset of light curves were chosen which represented the full variation in observing geometry captured by the complete dataset. The subset was also selected to include light curves that display clear turning points in their brightness and avoid including those with a poor signal-to-noise ratio. This selection of light curves is shown in Table 6.1 by bullet points under the column "LC-only model". Although a subset of light curves are used in the model's optimisation, it should be noted that all light curves are compared to their synthetic counterparts for the models discussed below.

The results of this pole search using subset of light curves is shown in Fig. 6.4. From this figure, it is shown that the resulting best-fit pole orientation is located at an ecliptic longitude of $80^\circ \pm 5^\circ$ and a latitude of $45^\circ \pm 5^\circ$. This pole is tightly constrained to this region such that the white dashed contour, representing solution +10% from the minimum, is barely visible around the yellow cross. In order to better probe the region containing the pole solution, a higher resolution scan was performed. This scan bracketed the region containing all pole solutions within +10% of the chi-squared minimum or within the dashed white line, ranging from 70° to 120° in ecliptic longitude and 30° to 60° in latitude. This subsequent scan was performed with a resolution of $1^\circ \times 1^\circ$ with the results presented in Fig. 6.5. This figure show that the best-fit pole orientation is actually located near a longitude of $94^\circ \pm 5^\circ$ and a latitude of $47^\circ \pm 5^\circ$, this is labelled as Model A. Although, there is also an additional pole orientation within

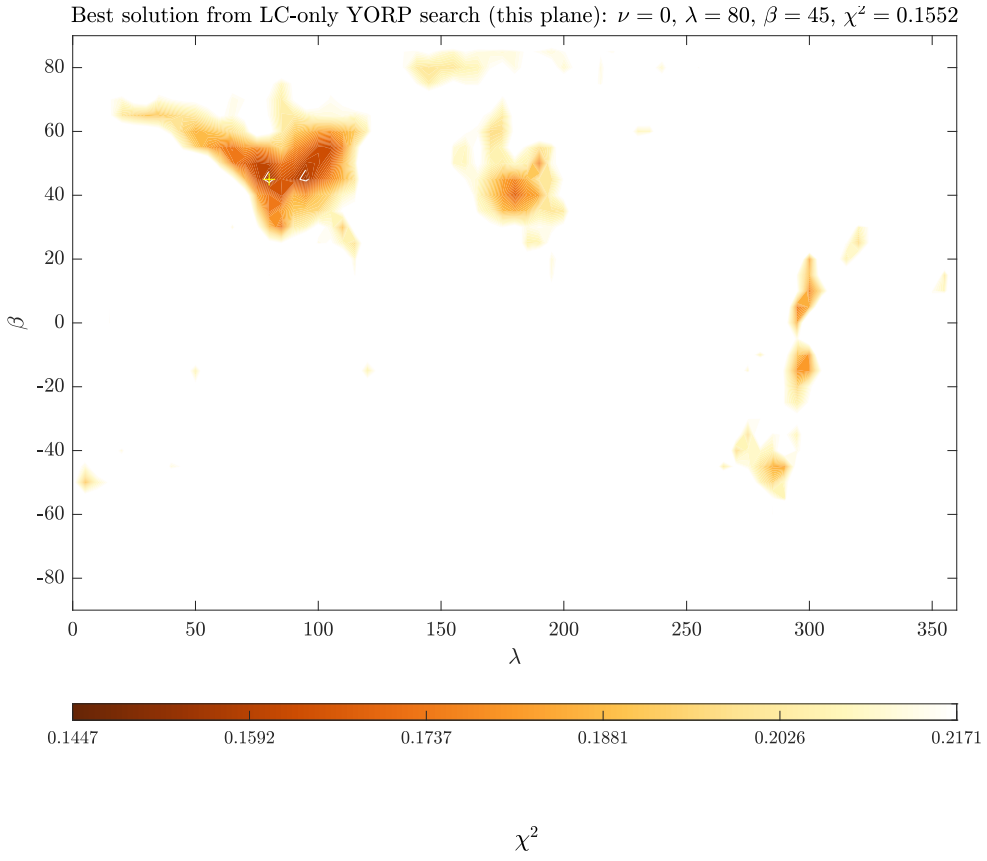

Figure 6.4: Results of a $5° \times 5°$ pole search covering the entire celestial sphere. Pole orientations are described in ecliptic longitude λ and latitude β. Both the shape and rotation period of the model were optimised for each pole orientation. Displayed here is the resulting chi-squared value indicating the goodness-of-fit, darker colours indicate a better fit to the data. Only pole orientations with a chi-squared value within +50% of the best-fit chi-squared value (marked by the yellow cross) are displayed here, those above are display as white. The dashed white contour represents a 10% increase in chi-square.

1% of the chi-squared minimum located at $(81°, 44°)$ labelled Model B.

At each of the probed pole orientations, the asteroid's shape was also optimised; therefore for both Models A and B, a shape model can be extracted for each. Both models are output in the form of triangulated polyhedrons, which can be visually examined and used to generate synthetic light curves, using the method described in Sect. 3.3.1. Inspection of the models' shapes reveals quasi-triangular appearances when viewed along the y-axis, although the two models diverge in appearance when viewed from the x-axis. Particularly, Model B retains the quasi-triangular appearance, while

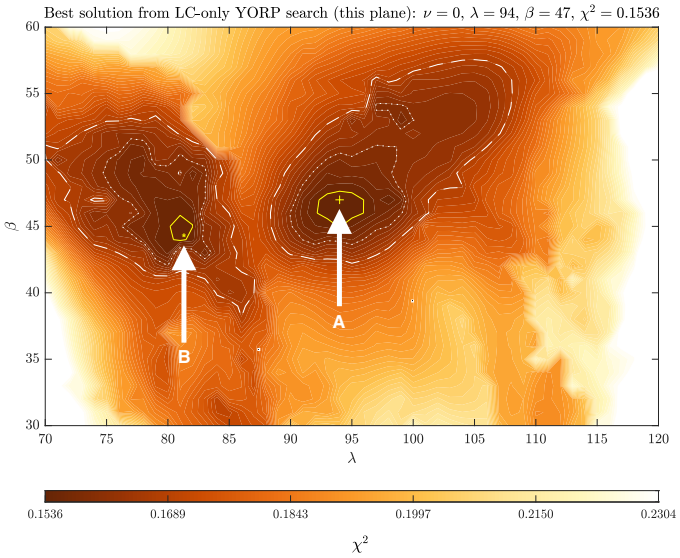

Figure 6.5: Results of a $1° \times 1°$ pole search about the pole solution of Fig. 6.3. Only pole orientations with a chi-squared value within +50% of the best-fit chi-squared value (marked by the yellow cross) are displayed here, those above are display as white. The yellow solid contour indicates a 1% increase from the best-fit value, the dotted white and dashed white contours represent a 5% and 10% increase respectively.

Model A appears more rounded (see Figs. 6.6 and 6.7). The shape of Model B bears similarities to both asteroid (1917) Cuyo and (2867) Steins (Rożek et al., 2019b; Jorda et al., 2012), the latter of which was observed by the Rosetta mission during a fly-by. Synthetic light curves were created using both Model A and B using the method described in Sect. 3.3.1. Upon assessment of the synthetic light curves of both shape models, a very good fit to the rotational light curves collected between 2010 and 2019 was revealed, as shown by Figs. A.16 and A.17 of the appendix. As both models reproduce the light curves and neither of the models appear unphysical or excessively flattened, neither of the shape models can be discarded at this stage.

6.3.3 Spin-state modelling of (89830) 2002 CE

Phase-offset analysis of convex inversion models

Now that shape models of the asteroid have been obtained, these can be utilised to search for indications that the spin-state of the asteroid is changing. The YORP effect produces a constant torque on the asteroid due to the anisotropic radiation of thermal photons (Rubincam, 2000). This constant torque leads to a linear change in the asteroid's rotation rate, which, when described in terms of rotation phase becomes

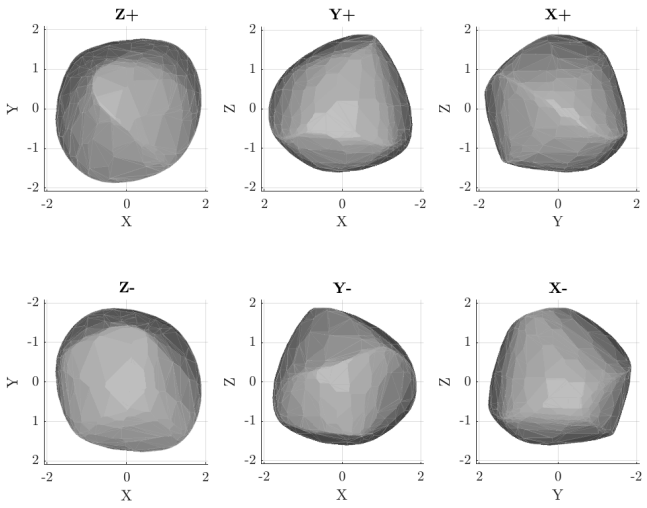

Figure 6.6: Model A - The best-fit convex shape model of asteroid (89830) 2002 CE. The model has a pole orientation located at ecliptic longitude 94° and latitude 47°, and a constant rotation period of 2.6135 hours. *Left to right*: views along the Z, Y and X axes of the body-centric coordinate frame from the positive (top row) or negative (bottom) end of the axis. The light curve convex inversion model is not scaled and the units shown are arbitrary.

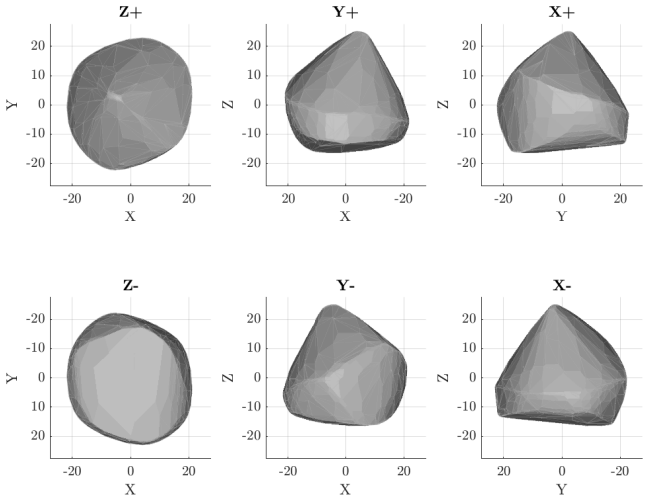

Figure 6.7: Model B - An alternative best-fit convex shape model of asteroid (89830) 2002 CE. The model has a pole orientation located at ecliptic longitude 81° and latitude 44°, and a constant rotation period of 2.6135 hours. Views are along the axes of the body-centric coordinate frame. The light curve convex inversion model is not scaled and the units shown are arbitrary.

a quadratic change of the form shown in Eqn. 3.22. Due to YORP's quadratic influence on rotation phase, this is the preferred domain in which to measure YORP accelerations.

As discussed in the previous section, the models can be used to produce synthetic light curves. By comparing the synthetic light curves with the observations, any changes in the spin-state can be determined by measuring the phase-offset required to align the two. This is done by applying a range of phase-offsets to the artificial light curves, these phase-offsets are chosen to cover an entire rotation. The best-fit phase-offset that aligns the two is determined by finding the phase-offset which minimises the recorded chi-

squared value. For a detailed description of the phase-offset measurement please revisit Sect. 3.3.2. The phase-offsets are then plotted against the epoch of their respective light curves.

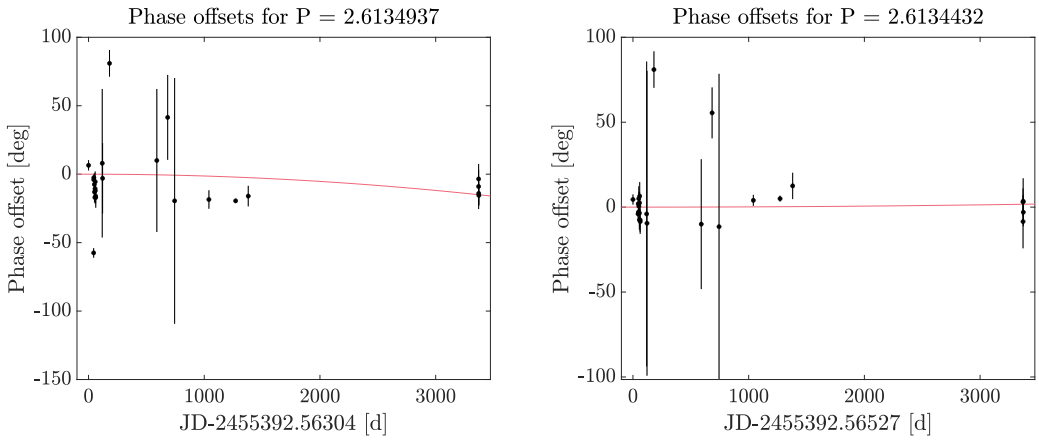

Figure 6.8: Shown here are the phase offset measurements required to align the synthetic light curves generated with both Models A (left) and B (right) to the observations. The solid red line represents a quadratic curve that has been fit to the measured phase offsets. The YORP coefficient of the fits are $\nu = (-0.54 \pm 1.30) \times 10^{-7}$ rad/d^2 and $(0.88 \pm 6.40) \times 10^{-8}$ rad/d^2 for Models A and B respectively. Note that zero YORP is included within the uncertainty of both fits.

Fig. 6.8 displays the results for the phase offset analysis of both Model A and B shown separately in two panels, the left panel for Model A and the right for Model B. It can be seen in the figure that the majority of the phase-offsets reside about 0°. The red solid line represents a weighted best-fit quadratic curve for the phase-offsets. Note that in both cases, that although the curve suggests a small YORP acceleration, the uncertainty includes a constant period solution or zero YORP. Therefore, it appears that a constant period solution is able to reproduce the light curves using either model.

Generating YORPogram with convex inversion

An additional approach to modelling the observations is to include YORP strength in the modelling process. Thus far, while modelling, the assumption was made that 2002 CE rotates with constant rotation period. However, in order to determine if the asteroid's rotation rate is changing due to a YORP-induced acceleration, YORP must be included in the modelling procedure. This is achieved by including YORP as fixed

parameter that is scanned over as described in Sect. 3.1.2.

Like the previous analysis, pole orientations covering the entire celestial sphere are probed at a resolution of $5° \times 5°$. However, this is now performed for multiple YORP values, creating 'YORP-planes'. For each of the possible pole orientations, both the rotation period and shape are optimised and the chi-squared value of the fit is recorded. Initially, the selection of YORP strengths scanned ranged from -1×10^{-7} rad/day^2 to 1×10^{-7} rad/day^2 with a resolution of 1×10^{-8} rad/day^2. This range was chosen as it covered the range of YORP strengths most common amongst the current direct detections of YORP as listed in Table 1.1. From each YORP-plane, the best-fit chi-squared is extracted and plotted against its corresponding YORP strength to create a YORPogram. Which allows the identification of the global best-fit solution and assessment of the possibility of a YORP detection.

Upon inspection of the results, there was no clearly bracketed minimum chi-squared value and so the range of YORP values was extended in both the positive and negative direction. The subsequent extension of YORP values occurred twice. First, extending the scan from $\pm 1 \times 10^{-7}$ rad/day^2 to $\pm 1 \times 10^{-6}$ rad/day^2 in steps of 1×10^{-7} rad/day^2. Then, finally, extending the scan again from $\pm 1 \times 10^{-6}$ rad/day^2 to $\pm 5 \times 10^{-6}$ rad/day^2 in steps of 2×10^{-7} rad/day^2. The results of the final scan are shown below in Fig. 6.9. The best fit to the light curve dataset is the model with a YORP strength of

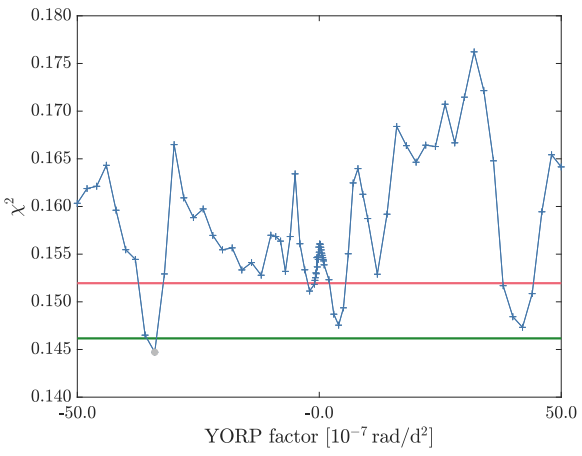

Figure 6.9: YORPogram for asteroid (89830) 2002 CE. Each cross in this figure represents the best-fit chi-squared value from a pole scan with a corresponding YORP strength. The YORP-plane containing the lowest chi-squared value is marked with a grey circle. The green and red solid lines mark +1% and +10% increases to the minimum chi-squared value.

-3.4×10^{-6} rad/day^2. However, there are additional solutions that should also be investigated further at 4×10^{-7} rad/day^2 and 4.2×10^{-6} rad/day^2.

Inspection of the -3.4×10^{-6} rad/day^2 model and other solutions

Within the -3.4×10^{-7} rad/day^2 YORP plane, the pole orientation was found to be tightly constrained to the same region as found in the pole scan. The resulting best-fit pole orientation is located at an ecliptic longitude of 105° and a latitude of 55°. Inspection of the morphology of this model reveals that the shape is only similar to that of Fig. 6.6 when viewed parallel to the spin-axis. However, when viewed perpendicular to the spin-axis the model appears more irregular and has lost the quasi-triangular appearance of the zero-YORP models.

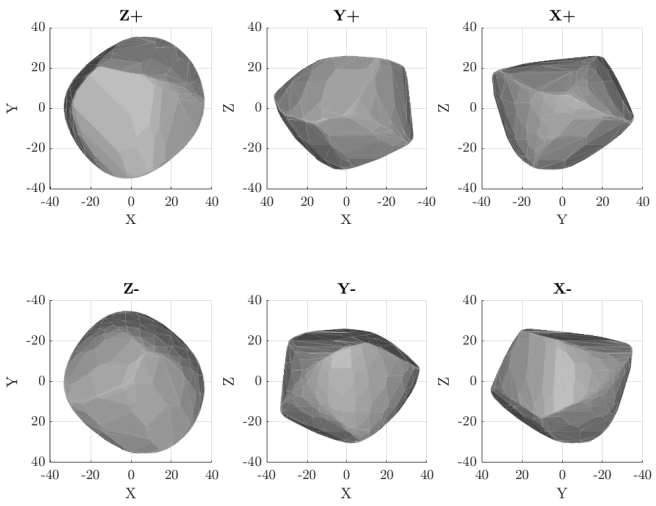

Figure 6.10: The best-fit convex shape model of asteroid (89830) 2002 CE from the -3.4×10^{-6} rad/day^2 YORP-plane. The model has a pole orientation located at ecliptic longitude 105° ± 5° and latitude 55° ± 5°, and an initial rotation period of 2.6119 hours. Views are along the Z, Y and X axes of the body-centric coordinate frame from both the positive and negative ends of the axis. The light curve convex inversion model is not scaled and the units shown are arbitrary.

Synthetic light curves generated using the shape model with a rotation period of 2.6119 hours and a YORP strength of -3.4×10^{-6} rad/day^2 provide a good fit to the observed light curves. Mathematically, this model provides a better fit to the data. However, when compared with the zero-YORP Model A's ability to reproduce the light curves, both models appear equal in their ability to reproduce the observations. A comparison of both models' ability to reproduce light curve number 22 from Table 6.1 is shown in Fig. 6.11.

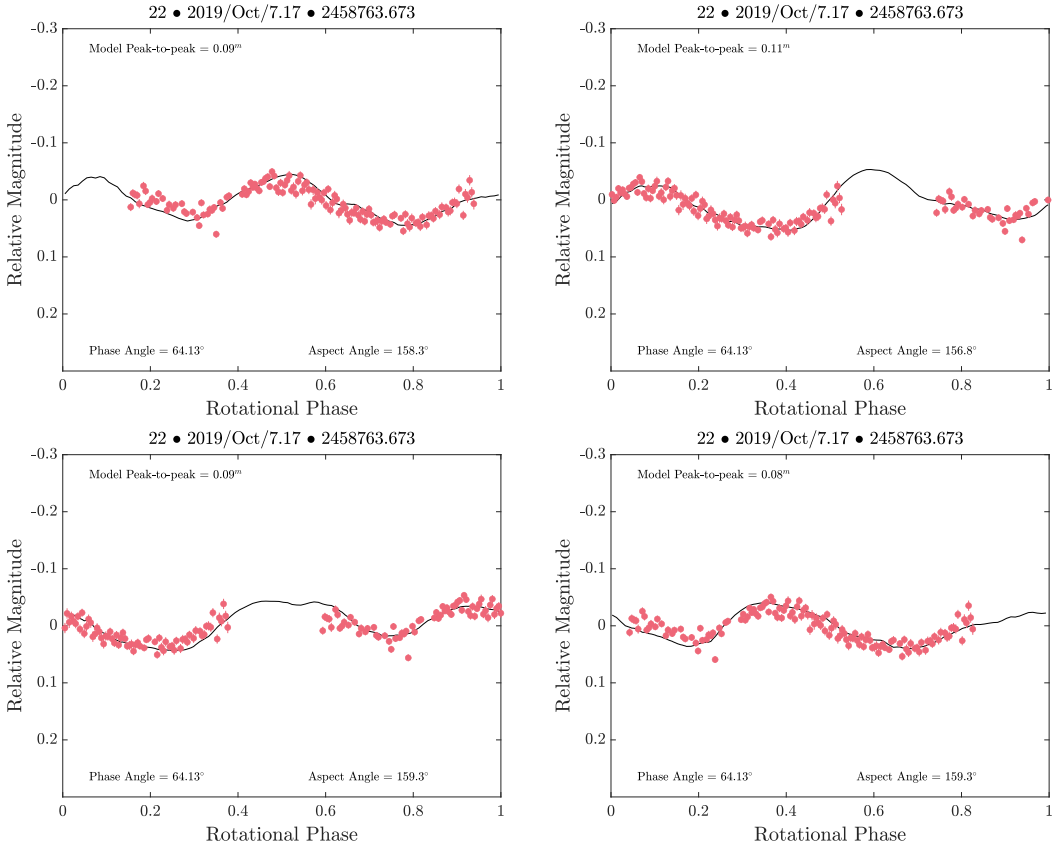

Figure 6.11: Comparison between several models' ability to reproduce the observations. Shown here is the comparison for light curve number 22 from Table 6.1. From the top left proceeding clockwise, the synthetic light curves are from the: -3.4×10^{-6}rad/day^2 YORP model, zero-YORP's Model A, 4×10^{-7}rad/day^2 YORP model and 4.2×10^{-6}rad/day^2 YORP model.

Similarly, inspection of the models produced by both positive YORP planes: 4×10^{-7}rad/day^2 and 4.2×10^{-6}rad/day^2, reveals that they too have pole orientations close to that of Model A. Both positive YORP planes' pole orientations are located at $(100°, 50°)$. Additionally, they are also able to reproduce the observed optical light curves. This is shown for light curve number 22 in Fig. 6.11, synthetic light curves for all other observations can be found in Figs. A.19 and A.20 of the appendix. Therefore, considering that each of these models are able to reproduce these light curves with such a similar level of success, and that their shapes are all physically feasible with pole orientations all tightly constrained to the same region of the ecliptic sphere. Discarding any of the models discussed in this chapter, including the zero-YORP models, was not

possible.

6.4 Summary and discussion of the analysis of (89830) 2002 CE

Light curve observations of the near-Earth asteroid (89830) 2002 CE have been collected over a duration of nine years, obtaining a total of 25 optical light curves. These observations were obtained at a wide variety of observing geometries, which was crucial in enabling the robust determination of the asteroid's pole orientation and rotation period. The asteroid was found to be spinning about its principal axis with a period of 2.6135 ± 0.0011 hours. It was also found to be a prograde rotator, with a pole orientation located at $(94^\circ \pm 5^\circ, 47^\circ \pm 5^\circ)$ in ecliptic coordinates. With an orbital inclination of 43.6° and longitude of ascending node of 19.9°, the object has an obliquity of 85.6°. An asteroid with an obliquity close to 90°, considering only Normal-YORP (N-YORP), would be expected to be experiencing zero acceleration of the object's pole orientation, but either a positive or negative acceleration of the rotation spin rate depends on the asteroid's 'Type' as defined in Vokrouhlický and Čapek (2002); Čapek and Vokrouhlický (2004). However, when the influence of Tangential-YORP (T-YORP) is also included, this places the asteroid close to a 'YORP sink', where both the spin and obliquity components of YORP torque are zero (Golubov and Scheeres, 2019). Implying that the asteroid is close to reaching an equilibria point, where the asteroid's spin-state evolution will cease to be influenced by YORP. Therefore, a YORP detection or lack thereof could be used to constrain the asteroid's surface roughness.

With the application of convex inversion techniques the asteroid's shape was also constrained. Although this work has produce several variations of the asteroid's shape, they have a common feature among them. All of the models bear a ridge feature that passes through their equator when viewed perpendicular to the spin-axis. Interestingly, their shapes seem to morph in a similar fashion as the magnitude of YORP increases.

Starting as quasi-triangular in appearance and transitioning to a quasi-rhomboid appearance as the magnitude of YORP increases, all while maintaining their ability to reproduce the observations.

Finally, attempts were made to detect signatures of a YORP acceleration acting on the asteroid. The first attempt involved measuring the phase-offsets between the synthetic light curves and their observed counterparts. Due to YORP's continuous torque, an acceleration caused by YORP would manifest itself as a quadratic curve in the phase-offsets. However, for both Models A and B, the uncertainty of the fitted quadratic curve was such that a constant period solution couldn't be excluded. An additional attempt to detect YORP signatures was also performed by including YORP as a fixed parameter in the convex inversion of the light curves. YORP strengths between $\pm 5 \times 10^{-6}$rad/day^2 were probed by producing 'YORP-planes'. These YORP-planes are in essence pole scans with non-constant rotation periods, as such, the rotation period is accelerated by a fixed YORP strength while the model is propagated to the epochs of the input light curves. Within these planes for each pole orientation probed, both the model's rotation period and shape are optimised to fit the observed light curves. The chi-squared value of each plane's best-fit model was then recorded and used to create the YORPogram seen in Fig. 6.9. From the YORPogram, three non-zero values of YORP appeared to best reproduce the light curves. However, upon further inspection, it was found that these models were no better than Models A and B, produced from the zero YORP plane, at reproducing the light curves.

As such, the conclusion drawn from this work regarding YORP is ultimately inconclusive. To reach a definitive conclusion and resolve this would require either more light curves covering an unseen observing geometry. Shown in Fig. 6.12 are the upcoming periods that CE will be observable from new observer ecliptic latitudes. Observations taken during these times will be valuable in breaking the degeneracy between the models discussed in this chapter. Alternatively, radar observations of the asteroid would enable the creation of a robust shape model that is independent from the light curves.

Either of these would in turn will allow a renewed investigation into the possible YORP evolution of this asteroid's spin-state.

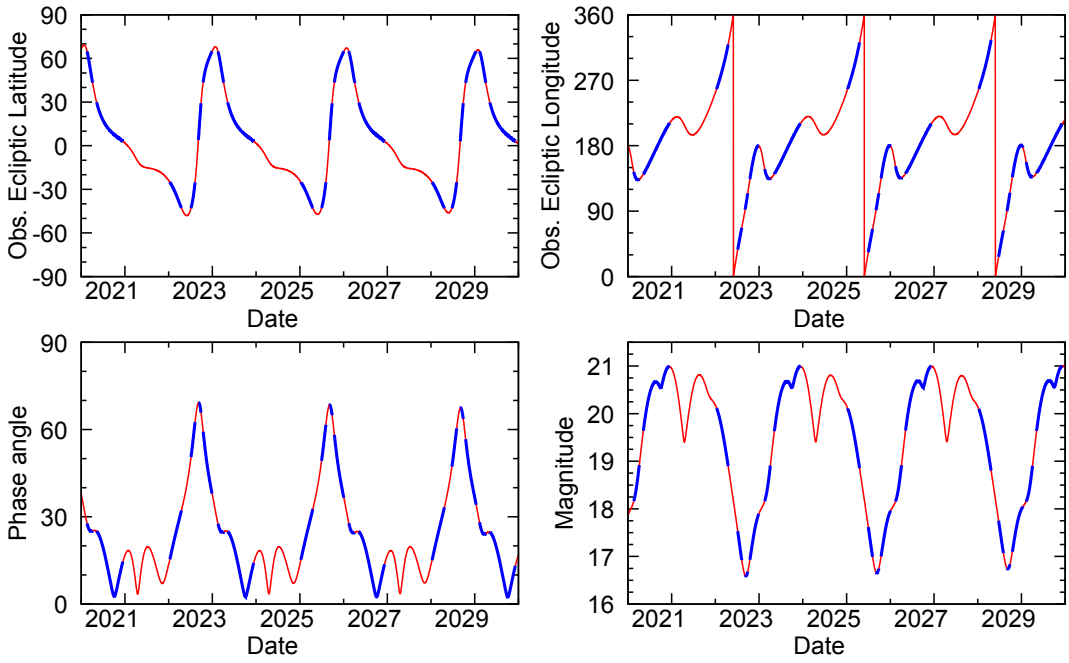

Figure 6.12: Future observing geometry of asteroid (89830) 2002 CE between 2020 and 2030. Shown here are: the position of the object in ecliptic latitude and longitude - as observed from Earth, orbital phase angle, and visual magnitude. The bold blue lines mark the periods of unobserved sub-observer latitudes, greater than 5° of those observed and shown in Fig. 6.2, which are the red lines here.

7 | Final conclusions and future work

7.1 Final comments on the modelling results

The aim of this thesis was to characterise near-Earth asteroids with the goal of detecting YORP-induced changes in their spin-state. The YORP effect is a rotational torque due to both incident solar radiation and the recoil of anisotropically emitted thermal photons, which is able to alter the rotation rate and obliquities of small bodies in the Solar System. By discovering more asteroid accelerated by YORP, we hope to further the understanding and development of YORP theories. It is important to understand YORP as it plays a significant role in the evolution of small asteroids throughout the Solar System. The research performed here was undertaken as part of the European Southern Observatory Large Programme (ESO LP), a dedicated programme contributing to the improvement of YORP-related theory by providing ground-truth for YORP modelling efforts. The programme has been monitoring over 40 asteroids photometrically since 2010. Of those asteroids, three were investigated in this thesis: (29075) 1950 DA (Chapter 4), (68346) 2001 KZ66 (Chapter 5), and (89830) 2002 CE (Chapter 6).

Utilising the independently derived radar shape model obtained for asteroid (68346) 2001 KZ66, a clear direct detection of YORP acting on the object was discovered. A YORP acceleration of $(8.50 \pm 0.11) \times 10^{-8}\text{rad/day}^2$ was derived, which is yet another

spin-up - marking the eighth such detection of positive YORP (see Table 1.1 for all detections to date). However, YORP should produce both cases of spin-up and spin-down for a population of asteroids with randomised spin-states and shapes (Rubincam, 2000; Vokrouhlický and Čapek, 2002). One mechanism that could explain this apparent bias for YORP spin-up cases is T-YORP. T-YORP results from the anisotropic emission of thermal radiation from surface boulders (Golubov and Krugly, 2012; Golubov et al., 2014; Golubov, 2017). These boulders must be large enough, or have a heat conductivity, such that they are not in thermal equilibrium. The differential thermal radiation emitted from the eastern and western sides of these boulders will create a force that acts tangentially to the surface of the asteroid. Though, there are circumstances in which the tangential component of YORP is zero. For example, if the boulder is small enough and the heat conductivity is sufficient to make both the east and west sides of the boulder isothermal, then the torque produced on both sides will be equal and the net T-YORP force will be zero (Golubov and Krugly, 2012).

An additional explanation for the lack of negative YORP detections to date may be due to an observational bias. The asteroids that have been observed to be influenced by YORP accelerations are all retrograde rotators with obliquities larger than 140°. YORP is dependant upon not only an asteroid's shape, but also its spin-state, particularly its obliquity (Rubincam, 2000). Investigations into the pole orientation distribution of asteroids shows that NEAs are dominated by retrograde rotators; the $\sin(\beta)$ of the vast majority of those retrograde rotators are smaller than -0.8, as shown by Fig. 7.1. Note, although the figure doesn't show obliquity but $\sin(\beta)$, the majority of asteroids have an orbital inclination lower than 5° and so there would not be a significant shift in the plot's distribution. The disparity in the pole orientation of NEAs is due to retrograde rotation offering a better chance of migration into near-Earth space (La Spina et al., 2004), as both the diurnal and seasonal Yarkovsky effects will act to shrink the object's orbit. The two major resonances that supply Main Belt asteroids to near-Earth space, the secular ν_6 and the 3:1 mean motion resonance, are also more likely to be reached by asteroids with shrinking orbits (Bottke et al., 2002;

Morbidelli and Vokrouhlický, 2003). Additionally, prograde rotators can be caught in spin-orbit resonances, which slow their orbital evolution (Slivan, 2002; Vokrouhlický et al., 2006d). This discrepancy propagates to the pole orientations of the YORP detections to date, ie. that all detections have a $\sin(\beta)$ larger than -0.75 and seven out of eight are larger than -0.8. In order to better understand the YORP effect, a wider range of pole orientations should be sampled covering a larger span of ecliptic latitudes. Equally important in understanding the YORP effect, are the non-detections of YORP as these asteroids could have reached the end of their YORP-cycle. They could be resting in an equilibrium state, where the torques from N-YORP and T-YORP are equal and opposite (Golubov and Scheeres, 2019). This constant-rotation-period equilibrium state has implications for our understanding of an asteroid's spin-state evolution as well as its physical evolution. Non-detections are an important piece of the puzzle, and as such should be consolidated in a manner similar to the YORP detections listed in Table 1.1.

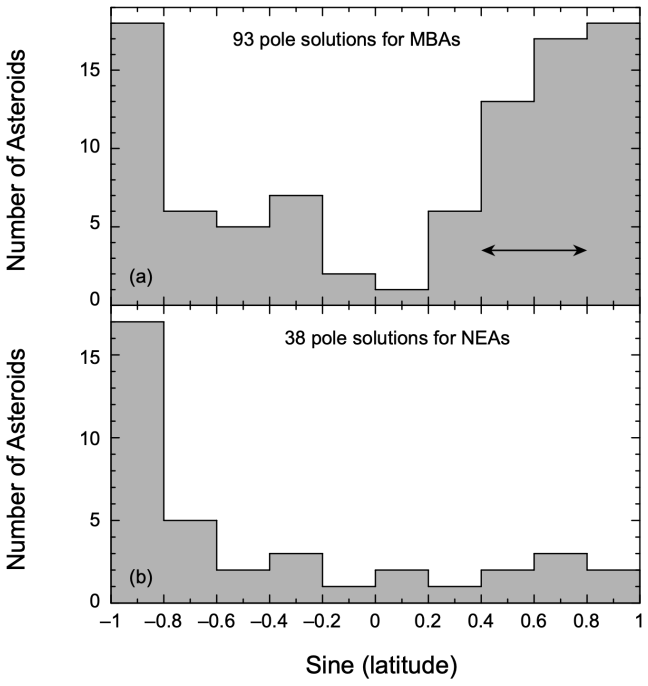

Figure 7.1: Distribution of ecliptic latitudes for: **(a)** 93 small main-belt asteroids (smaller than 30 km in diameter), **(b)** 38 small near-Earth asteroids. The pole solutions of the NEAs are dominated by retrograde-rotating objects (∼73% of cases). This lack of prograde-rotators entering near-Earth space is due to the preference that Yarkovsky provides retrograde rotators in the migration from the main belt (La Spina et al., 2004). *Reprinted from Vokrouhlický et al. (2015).*

Asteroid (29075) 1950 DA is an interesting target, which I plan to monitor in the future, due to the strong indications of negative YORP. Several different analytical

techniques indicate that the detected deceleration is due to negative YORP. However, there was difficultly in extracting a single value when measuring the strength of the YORP deceleration. Similarly, there was difficultly in determining the asteroid's pole orientation, but it was constrained close to the ecliptic equator, between an ecliptic latitude of $-25°$ to $35°$ or $\sin(\beta)$ of -0.42 to 0.57. If this indication of negative YORP is confirmed, this would be the first detection of this unseen mode of YORP. A direct detection of negative YORP would constitute a major-breakthrough in the study of this non-gravitational effect. Further studies would be conducted to determine what characteristics of this object drive the YORP deceleration. Particularly of interest would be to study the surface structure and determine the strength, if consequential, of tangential-YORP.

In order to strengthen the detection of negative YORP acting on 1950 DA, we have planned an observing campaign which aims to measure the YORP strength from phase offset measurements that are no larger than $360°$. This observing campaign, focusing on 1950 DA, has already begun. In January 2021, two nights were awarded to our programme to observe the object from the Isaac Newton Telescope (INT) using the Wide Field Camera. However, unfortunately due to bad weather the first night was lost. On the second night (19 January) though, 1950 DA was monitored for three-hours at a visual magnitude of 18.2. In addition to the January 2021 light curve, two runs on the NTT during Period 108 are scheduled to occur in early August and September of 2021. Each of these runs will last for three-nights, and 1950 DA will be observable for approximately five-hours each night - allowing coverage of multiple rotations per night. During the August run, the object will move slowly across the sky at a rate of 20 arcseconds per hour. Accordingly, for these observations, we would track at sidereal rates with exposure times under two minutes. However, in September the object will be moving at a rate of 100 arcseconds per hour, which will require differential tracking at the asteroid's rates of motion. Additionally, an application for three nights on the INT during semester 2021B will be submitted. From the INT, I hope to observe 1950 DA during its brightest period (18.7 magnitude) during the late 2021 apparition. These

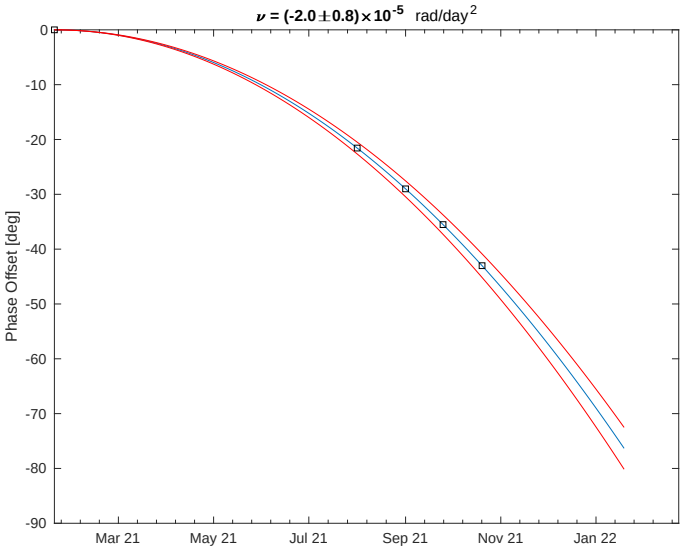

Figure 7.2: Theoretical phase-offset values for the asteroid (29075) 1950 DA using the largest of the measured YORP strengths from Table 4.3. The curve begins on the 19 January 2021 and is propagated forward one-year. The solid blue curve shows the phase-offsets expected for a YORP strength of 2.0×10^{-5}rad/day^2, and the red curves indicates the uncertainty. The black squares mark the phase-offsets expected for each of the new datasets we hope to obtain.

observations will likely require the telescope to track at differential rates, as 1950 DA will move across the sky at a rate of 71 arcseconds per hour but will ultimately depend on the seeing conditions of the nights. Finally, in Period 109, another proposal is being drafted to observe 1950 DA for the last time in 2021 from the NTT. These observations will take place over three nights in the first half of October.

If successful in these applications, four new epochs of observations will be used, in addition to the fifth epoch obtained in January 2021, to confirm the detection of negative YORP discovered in this thesis. The predicted phase-offsets for these observations are shown below in Fig. 7.2. Additionally, during these observations, the observational geometry from which the asteroid will be observed is similar over the year, particularly between August and October. Although, observing the same geometry is a hindrance when modelling an asteroid's shape, it is advantageous when measuring YORP strength. This is because the variation in the light curve's shape will be minimised, which makes it easier to measure the phase-offsets. During 2021, the observer-centred ecliptic latitude of DA only fluctuates between 15° and −5° (see Fig. 7.3).

Given the values of YORP strength presented in Chapter 4 (see Table 4.3 for a

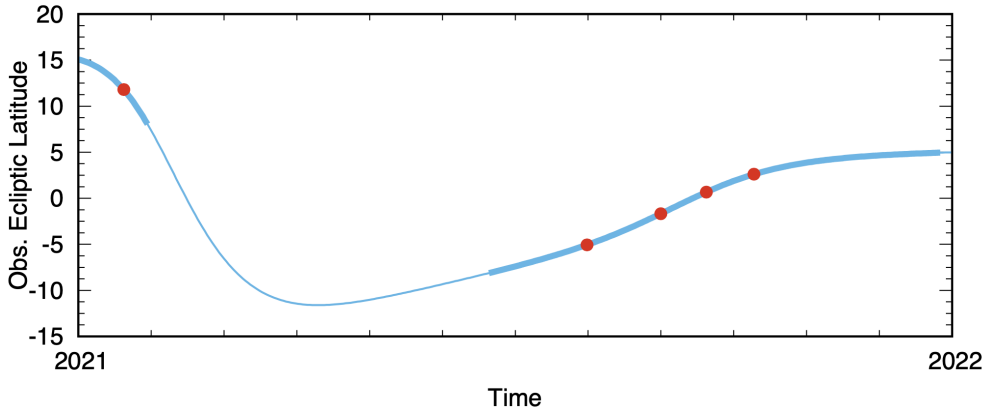

Figure 7.3: Observer ecliptic latitude of the asteroid (29075) 1950 DA over the year 2021. This is shown by solid blue line, which is bold during the periods where the solar elongation for the object is greater than 80°. The red circles mark the dates at which I plan to observe DA.

summary), in the case of the strongest deceleration, these dates are such that the observation campaign can be extended if needed, for example, if we are unsuccessful in obtaining all of the required time from the time-allocation committees, or our efforts are frustrated by bad weather. Additional observing opportunities in December 2022, and late January or early February 2023 could be used to obtain any extra required phase-offset measurements. The dates of these observations are such that they will fall within 360°, see Fig. 7.4 for the predicted phase-offsets of these two dates.

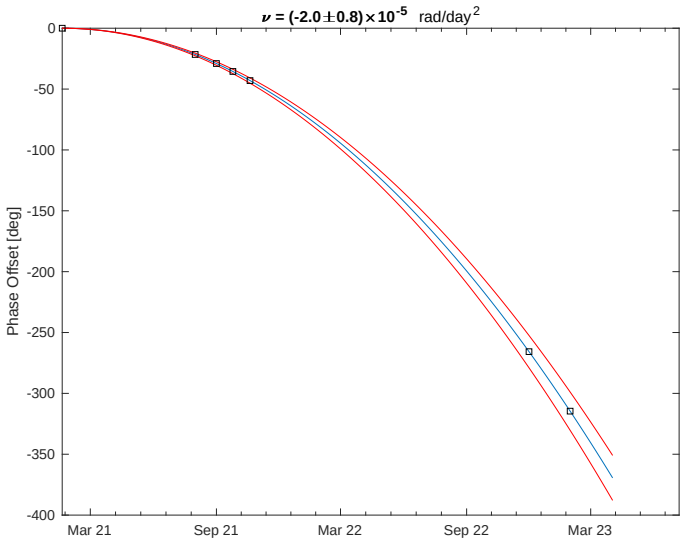

Figure 7.4: Same as Fig. 7.2, but the theoretical phase-offset values for the 1950 DA have been extended into 2023. This extension shows two additional opportunities to observe 1950 DA: one in December 2022, and the other in late January or early February 2023.

The shapes of both the asteroids (29075) 1950 DA and (68346) 2001 KZ66 suggest

that they are both YORP evolved objects. Across the various shapes generated for asteroid (29075) 1950 DA, a spinning top-shape - like that of (101955) Bennu, was prevalent. This is a characteristic feature of fast rotating gravitationally-bound aggregates (Sánchez and Scheeres, 2016). This YORPoid shape is typical of a YORP-evolved system, indicating that (29075) 1950 DA has in the past undergone YORP acceleration (Walsh et al., 2008). However, 1950 DA has passed this stage of its YORP-cycle with present analysis suggesting that it is now experiencing a deceleration of its rotation rate, which could eventually lead 1950 DA's spin-state into a tumble.

The shape of asteroid (68346) 2001 KZ66 is highly bifurcated, more so than similar asteroids such as Itokawa. With a rotation period of 4.985997h 2001 KZ66 rotates more than twice as fast as Itokawa; an analysis of the gravitational slopes of 2001 KZ66's shape shows that the asteroid is currently in a stable configuration (see Sect. 5.5.2). However, 2001 KZ66 is experiencing a YORP acceleration, which eventually shall result in changes to the asteroids morphology and may have already played a role in the asteroid's present shape (Sánchez and Scheeres, 2018). Continued acceleration of this object will cause the two lobes of the asteroid to move apart, which could result in a reconfiguration of the asteroid's shape, or fission of the two lobes creating a binary system. The radar-derived shape model of the asteroid could be used to derive a theoretical value of the YORP strength. If this differs from the value derived in this thesis, it could be used to probe for any inhomogeneity between the two lobes using an analysis similar to that performed on Itokawa by Lowry et al. (2014). In Lowry et al. (2014), they used the ATPM to derive a theoretical YORP value for Itokawa, which for a homogeneous model, is the YORP torque about the centre-of-figure, $\vec{T}_{CF}$. In contrast, the measured YORP torque, $\vec{T}_{CM}$, is about the centre-of-mass. Possible new locations of the centre-of-mass in the xy-plane are defined by $\vec{T}_{CM} = \vec{T}_{CF} - \vec{R} \times \vec{F}_{CM}$, where $\vec{R}$ is the offset from the centre-of-figure and $\vec{F}_{CM}$ is the overall photon force acting on the asteroid. Once the offset from the centre-of-figure has been calculated, the two lobes of the asteroid can be approximated by ellipsoids to determine the required density heterogeneity to reproduce the centre-of-mass location. For more discussion about this

technique see Scheeres and Gaskell (2008); Lowry et al. (2014).

In the future, I plan to periodically monitor this asteroid via optical light curves, in order to search for indications that the lobes of the asteroid are undergoing a rotational fission. The orbit of KZ66 is such that the object is observable approximately every two years, predominantly from the southern hemisphere. This monitoring campaign will be launched in the first half of 2023, with biennial observations of the target. Below in Fig. 7.5 the visual magnitude of KZ66 is shown over a decade, the asteroid will regularly reach 19 magnitude or brighter. The figure also illustrates when the asteroid is observable, which is shown by the bold segments of the curve, indicating when the solar elongation is larger than 80°. Under the acceleration of YORP, this asteroid will eventually undergo a fission. To observe indications of the asteroid going through this process would be a priceless insight into the formation of binary asteroids. Furthermore, any additional observations of 2001 KZ66 could be used to refine the YORP detection presented in this thesis. Fig. 7.6 shows where the potential future phase-offsets of these observations would be placed.

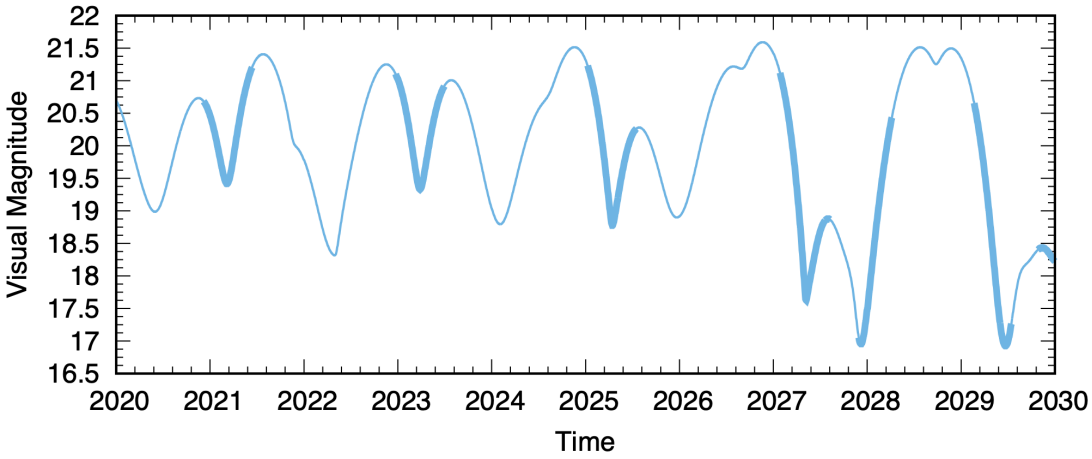

Figure 7.5: Visual magnitude of the asteroid (68346) 2001 KZ66 over the next decade. This is shown by solid blue line, which is bold during the periods where the solar elongation for the object is greater than 80°.

The robust shapes and spin-states developed within this thesis were utilised for the purpose of detecting YORP accelerations. However, the models that were produced can also be used to inform theories regarding the formation mechanisms that produce these

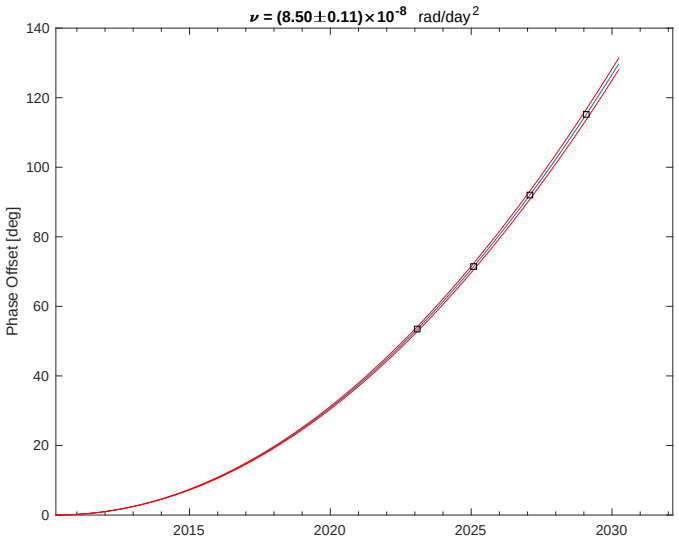

Figure 7.6: Same as Fig. 7.2, but the theoretical phase-offset values are for the asteroid 2001 KZ66. The additional phase-offsets span the 2020s, opportunities to observe 2001 KZ66 are biennial starting from early 2023.

objects. Additionally, the detailed shape models play an important role in thermophysical modelling of asteroids, by using tools such as the Advanced Thermophysical Model (ATPM) (Rozitis and Green, 2011, 2012, 2013). The ATPM describes the thermal emission from small atmosphereless bodies, accounting for self-shadowing, self-heating, and thermal beaming. With a detailed shape model, the ATPM can predict the thermal-infrared emission for a range of surface properties by solving the one-dimensional heat conduction equation. When given thermal light curves, thermophysical modelling can then be used to place constraints on the physical characteristics of asteroids. These physical characteristics include their size, thermal inertia, and surface roughness. Although, it should be noted that the size derived from this method is the diameter of an equivalent volume sphere. With these physical parameters and a shape model, the ATPM is also able to derive theoretical estimates of the strength of both the YORP and Yarkovsky effects.

7.2 Thoughts to the future of asteroidal studies and YORP theory

Over the duration of my doctoral studies, recent developments in YORP theory have been focused on T-YORP - the tangential manifestation of YORP. This variant of YORP appears when boulders on the surface of an asteroid emit thermal radiation anisotropically between their eastern-western hemispheres, which results in a recoil force tangential to the surface (Golubov and Krugly, 2012; Golubov et al., 2014; Golubov, 2017). Numerical studies of T-YORP have been performed for simple geometries including: a one-dimensional wall (Golubov and Krugly, 2012), and a spherical boulder (Golubov et al., 2014; Ševeček et al., 2016). However, the model is being continually developed to tackle more complex and realistic scenarios. These include modelling the torque produced from irregular boulders, and the effects of shadowing and self-heating for various arrangements of boulders (Golubov et al., 2019). Additionally, studies are analysing the interplay between normal YORP and T-YORP which can produce equilibria points where the torques produced by each cancel out, which in turn interrupts the YORP cycle (Golubov and Scheeres, 2019; Golubov et al., 2020).

Another development in the field of YORP was the recent indication of B-YORP influencing the mutual orbit of the binary asteroid (88710) 2001 SL9 (Scheirich et al., 2021). The authors obtained photometric observations of the binary covering the period from 2001 to 2015. Using this dataset, they were able to model the mutual orbit of (88710), finding that the semi-major axis of the mutual orbit was drifting by -2.8 ± 0.2 or -5.1 ± 0.2cm/yr. Gravitational influence from close planetary encounters were investigated and ruled out as the cause of this decrease, leaving B-YORP as the only known physical mechanism that could shrink the semi-major axis at this rate. Understanding B-YORP is important in order to understand the long-term evolution of binary asteroids, as B-YORP will heavily influence the lifetime and formation rate of binary systems.

Looking to the future, I believe that the rate of discovery of YORP detections will increase, influenced by the growing amount of data that is being collected and the ease by which it is accessible. Survey telescopes will likely contribute significantly, for example, the Transiting Exoplanet Survey Satellite (TESS) released 9,912 light curves of Main-Belt Asteroids and Jovian Trojans (Pál et al., 2020). Their intention is also to expand on the object classes that they process, which will include near-Earth objects. Investigations into the capabilities for emerging next-generation telescopes to survey and characterise Near-Earth Objects (NEOs) show that they will significantly increase the number of asteroid light curves available (Milam et al., 2019).

In order to calibrate and verify the predictions made by YORP theory, it is important to continue to increase the number of direct YORP detections. Continued effort is required in producing YORP detections across an increased range of rotation periods and pole orientations. However, equally important is the publication of YORP null-detections on asteroids and their robust physical models. As these asteroids could be in a state of equilibria, this also helps to constrain YORP theory and inform us of the end-states of YORP-influenced rotational evolution. Below in Table 7.1, I have compiled the non-detections of YORP resulting from our ESO LP.

Asteroid	Period [h]	d [km]	Pole [°]	Obliquity [°]	Reference
(89830) 2002 CE	2.6122(1)	5.067	(94, 47)	85.6	(This work)
(8567) 1996 HW1	8.76243(4)	2.02	(281, -31)	129.2	(Magri et al., 2011)
(6053) 1993 BW3	2.57386	3.720	(357, -12)	114.7	(Ďurech et al., 2010)

Table 7.1: Non-detections of YORP recorded as part of the ESO LP. The table lists: Asteroid's name, rotation period (with uncertainty given in parenthesis), diameter of a sphere of equivalent volume, pole orientation (λ, β), orbital obliquity, and reference to published work. All obliquities were calculated using the pole orientations determined by the authors and the best orbital solution from JPL Horizons as of Feb 2021.

Within the first chapter of this thesis, I discussed the motivations behind the study of near-Earth asteroids. To briefly summarise, those reasons included: understanding the formation and history of the Solar System via these planetary building-blocks,

explorations of the Solar System through manned and unmanned missions, mitigating the threat posed to humanity by asteroidal impacts, and interest in mining asteroids for their resources. Accordingly, the conclusion of this thesis will end by framing the future of asteroidal studies through the lens of these four motivations.

During the last thirty years, optical observations, Earth-based radar observations, and spacecraft missions have revolutionised our understanding of asteroids and comets. Spacecraft, although few in number, have provided the most detailed advances in our knowledge of specific targets. The recently completed mission, Hayabusa 2 (Yoshikawa et al., 2014), to asteroid (162173) Ryugu to collect a sample from the C-type asteroid has not only returned precious surface samples, but also extensive data on the asteroid's morphology, surface structure, and spectral characteristics (Watanabe et al., 2019; Michikami and Hagermann, 2021; Riu et al., 2021). The data collected during this mission will likely continue to provide insights long passed the lifetime of the mission.

Upcoming approved ambitious space missions will further advance our knowledge of the history of the Solar Systems and its formation. The missions all aim to be the first in their respective objectives. The Psyche mission is visiting the asteroid (16) Psyche (Polanskey et al., 2020), and it will be the first mission to visit a metallic asteroid - which could be the nickel-iron core of an early planet. Launching in 2022, the mission is expected to arrive at the asteroid in the year 2026 when it will orbit and observe the asteroid for 21 months. During this time, the mission aims to determine whether Psyche is a core, or if it is unmelted material. If it is a core, it will allow a look inside the terrestrial planets which otherwise cannot be seen. Furthermore, the Lucy mission is the first mission to study the Trojans (Levison et al., 2019), which are thought to be remnants of the primordial material that formed the Jovian planets. Launching in October 2021, the mission will journey for 12-years, visiting eight different asteroids: one main-belt and seven Trojans, four of which are binaries. The path of Lucy will allow the mission to perform close-up observations of three major types of bodies: the C-, P-, and D-types. While space missions are inherently about exploration, for the

missions mentioned up to now, their main objectives have focused on the first of the motivations: understanding the formation of these bodies and their place in the Solar System.

The next mission, while it will undoubtedly encompass the same motivations as the first two missions, has a different primary aim. The Asteroid Impact and Deflection Assessment (AIDA) is a double-spacecraft mission that will test the efficiency of orbital deflection with a kinetic impactor. This planetary defence mission is a collaboration between ESA and NASA, contributing one craft each. The first spacecraft to launch will be NASA's DART (Cheng et al., 2016, 2018), which is planned to depart in July 2021. In September 2022, the craft will impact the secondary of the binary asteroid (65803) Didymos at a velocity of $\sim 7 km/s$ and it is expected to alter the binary orbit period by approximately four minutes. In 2024, the second spacecraft, ESA's Hera (Michel et al., 2018) will depart aiming to rendezvous with the asteroid in January 2027, five-years after the impact, to perform a detailed characterisation of the secondary. The craft will survey the impact crater produced by DART, and also measure the impact's effect on the binary system's orbit.

With regards to the mining of asteroids, interest in this topic in the past decade has promoted it from a fantasy into near-reality. A recent study of this topic probed the economics of utilising these space-based resources in orbit opposed to launching them in to orbit from Earth (Colvin et al., 2020). Deciding to focus on water, due its versatility and demand in a range of space activities, Colvin et al. (2020) found that, within the next decade, water derived from asteroids could become an economically competitive alternative to delivering it from Earth. Besides the economic considerations, others have begun to ponder the ethical factors involved with opening up the Solar System to human exploitation. To which Rivkin et al. (2020) question if it is ethical to leave a trove of likely lifeless resources untouched while continuing to mine the only body with known life in the Solar System. However, although the Solar System is big, it is ultimately finite. As such, these resources should be managed in a way that ensures that

they are not over-exploited or depleted. This has lead to proposals recommending that an agreement on the limit to which the Solar System's resources should be developed is reached before the activity becomes mainstream (Elvis and Milligan, 2019). Within the next decade, while the technology required is developed, the focus of research supporting asteroid mining will likely focus on the identification of water-rich near-Earth asteroids and the extraction of water (Elvis, 2014; Rivkin and DeMeo, 2019).

An important requirement throughout all of the motivations to study asteroids, is the need for characterisation of these objects. This is also true when studying the YORP effect; a quasi-independent shape model derived from high quality data is a valuable asset when attempting to measure phase-offsets. This can be achieved by using radar observations to generate a robust model of the targets shape, as done for (68346) 2001 KZ66 (Chapter 5) and other asteroids (Taylor et al., 2007; Lowry et al., 2014). The ESO LP has a rich optical dataset with a decade's worth of optical light curves for dozens of near-Earth asteroids that are good candidates for YORP detection. Determining which objects within the ESO LP also have radar observations, in order to derive independent shape models for them, could result in new direct YORP detections. At the very least, it would result in robust shape models.

Sadly, towards the end of 2020, the Arecibo radar telescope collapsed ending its 57 years of service. However, there remains a trove of archived data from this facility yet to be analysed. The reconstruction of an asteroid's shape and spin-state resulting from the inversion of radar data is a computationally expensive process. Though, the largest bottle-neck in the analysis of these radar observations is the extensive human oversight required in the process to ensure that the results are physical. Exciting work in the production of machine learning tools aim to aid in the development of these shape models by training neural networks to recognise features in radar images and link them to the surface features that produce them (Rożek et al., 2019c). If accomplished, this would lead to a boom in the number of robust shape models published, which would have a widespread effect across the field.

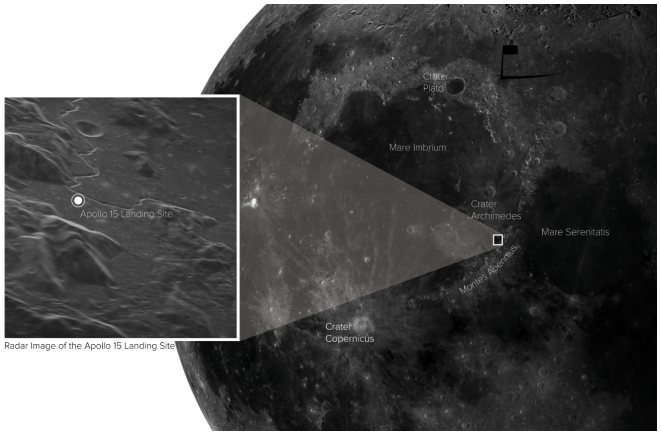

Figure 7.7: Radar image of the Apollo 15 landing site captured during proof-of-concept test. A high-powered transmitter on the Green Bank Telescope transmitted a signal which was reflected off the Moon and captured using the Very Long Baseline Array. *Credit: Sophia Dagnello, NRAO/GBO/Ratheon/AUI/ NSF/USGS.*

A new generation of planetary radar is also under development. The recent proof-of-concept test utilising a 700 W transmitter operating at a frequency of 13.9 GHz that was installed on the Green Bank Telescope, a 100 metre fully steerable radio telescope, produced a high resolution image of the Apollo 15 landing site on the Moon - this image is shown in Fig. 7.7. This novel method used bistatic observations with the signal being received by the Very Long Baseline Array (VLBA) interferometer. Future plans in the testing of this new method include the observation of asteroid 2001 FO32 and the Jovian moons. Higher power observations aim to achieve a high resolution ($\sim$1.25m) view of asteroid 2001 FO32, if achieved this would enable large boulders on the asteroid's surface to be resolved. This new radar system has the potential to open up previously unseen features of the Solar System to observation from Earth. Until this transmitter is fully operational at the Green Bank Telescope, only one planetary radar system on Earth is functional, the Goldstone Observatory. Perhaps now, in the wake of this new generation of planetary radar and the loss of Arecibo, it is time to revive the call for a purpose built European NEO Radar facility (Zaitsev, 2002).

Bibliography

Daniel R. Altschuler and Christopher J. Salter. The Arecibo Observatory: Fifty astronomical years. *Physics Today*, 66(11):43–49, November 2013. ISSN 0031-9228, 1945-0699. doi: 10.1063/PT.3.2179. URL `http://physicstoday.scitation.org/doi/10.1063/PT.3.2179`.

Colin Aspin. *Future Instrumentation for the Nordic Optical Telescope*, volume 228, page 55. 1998. doi: 10.1007/978-94-011-5262-4_8.

A Aznar Macias, M Predatu, O Vaduvescu, and J Oey. EURONEAR - First Light Curves and Physical Properties of Near Earth Asteroids. *Romanian Journal of Physics*, 62(904):arXiv:1801.09420, February 2017.

C M Bardwell. 1950DA Rediscovery. *Minor Planet Electronic Circulars*, A26, 2001.

M A Barucci, A Cellino, C De Sanctis, M Fulchignoni, K Lumme, V Zappalà, and P Magnusson. Ground-based Gaspra modelling - Comparison with the first Galileo image. *Astronomy & Astrophysics*, 266:385–394, December 1992.

Lance Benner, Michael C Nolan, Steven J Ostro, Jon D Giorgini, Donald P Pray, Alan W Harris, Christopher Magri, and Jean-Luc Margot. Near-Earth Asteroid 2005 CR37: Radar images and photometry of a candidate contact binary. *Icarus*, 182(2):474–481, June 2006.

Lance Benner, Steven J Ostro, Christopher Magri, Michael C Nolan, Ellen S Howell, Jon D Giorgini, Raymond F Jurgens, Jean-Luc Margot, Patrick A Taylor, Michael W

Busch, and Michael K Shepard. Near-Earth asteroid surface roughness depends on compositional class. *Icarus*, 198(2):294–304, December 2008.

Richard Berry and James Burnell. *The Handbook of Astronomical Image Processing*. Willmann-Bell, Inc., January 2005.

R P Binzel, F E DeMeo, E V Turtelboom, S J Bus, A Tokunaga, T H Burbine, C Lantz, D Polishook, B Carry, A Morbidelli, M Birlan, P Vernazza, B J Burt, N Moskovitz, S M Slivan, C A Thomas, A S Rivkin, M D Hicks, T Dunn, V Reddy, J A Sanchez, M Granvik, and T Kohout. Compositional distributions and evolutionary processes for the near-Earth object population. *Icarus*, 324:41–76, May 2019.

Richard P. Binzel, Paolo Farinella, Vincenzo Zappala, and Alberto Cellino. Asteroid rotation rates: distributions and statistics. In Richard P. Binzel, Tom Gehrels, and Mildred Shapley Matthews, editors, *Asteroids II*, pages 416–441, January 1989.

Bryce T Bolin, Marco Delbo, Alessandro Morbidelli, and Kevin J Walsh. Yarkovsky V-shape identification of asteroid families. *Icarus*, 282(C):290–312, January 2017.

William F Bottke, Alessandro Morbidelli, Robert Jedicke, Jean-Marc Petit, Harold F Levison, Patrick Michel, and Travis S Metcalfe. Debiased Orbital and Absolute Magnitude Distribution of the Near-Earth Objects. *Icarus*, 156(2):399–433, April 2002.

William F Bottke, Daniel D Durda, David Nesvorný, Robert Jedicke, Alessandro Morbidelli, David Vokrouhlický, and Hal Levison. The fossilized size distribution of the main asteroid belt. *Icarus*, 175(1):111–140, May 2005.

William F Jr Bottke, David Vokrouhlický, David P Rubincam, and David Nesvorný. The Yarkovsky and Yorp Effects: Implications for Asteroid Dynamics. *Annual Review of Earth and Planetary Sciences*, 34(1):157–191, May 2006.

D T Britt, D C Boice, B J Buratti, H Campins, R M Nelson, J Oberst, B R Sandel, S A Stern, L A Soderblom, and N Thomas. The morphology and surface processes of Comet 19/P Borrelly. *Icarus*, 167(1):45–53, January 2004.

Peter Brown. A Preliminary Report on the Chelyabinsk Fireball/Airburst. *WGN*, 41: 22–, February 2013.

Schelte J Bus and Richard P Binzel. Phase II of the Small Main-Belt Asteroid Spectroscopic Survey. The Observations. *Icarus*, 158(1):106–145, July 2002.

Michael W Busch, Jon D Giorgini, Steven J Ostro, Lance Benner, Raymond F Jurgens, Randy Rose, Michael D Hicks, Petr Pravec, Peter Kušnirák, Michael J Ireland, Daniel J Scheeres, Stephen B Broschart, Christopher Magri, Michael C Nolan, Alice A Hine, and Jean-Luc Margot. Physical modeling of near-Earth Asteroid (29075) 1950 DA. *Icarus*, 190(2):608–621, October 2007.

B. Buzzoni, B. Delabre, H. Dekker, S. Dodorico, D. Enard, P. Focardi, B. Gustafsson, W. Nees, J. Paureau, and R. Reiss. The ESO Faint Object Spectrograph and Camera / EFOSC. *The Messenger*, 38:9, December 1984.

B Buzzoni, B Delabre, H Dekker, S Dodorico, D Enard, P Focardi, B Gustafsson, W Nees, J Paureau, and R Reiss. The ESO Faint Object Spectrograph and Camera (EFOSC). *ESO Messenger (ISSN 0722-6691)*, 38:9–13, December 1984.

D Čapek and D Vokrouhlický. The YORP effect with finite thermal conductivity. *Icarus*, 172(2):526–536, December 2004.

V Carruba and A Morbidelli. On the first $\nu 6$ anti-aligned librating asteroid family of Tina. *Monthly Notices of the Royal Astronomical Society*, 412(3):2040–2051, January 2011.

B Carry. Density of asteroids. *Planetary and Space Science*, 73(1):98–118, December 2012.

A Cellino, V Zappalà, and P Farinella. Asteroid shapes and lightcurve morphology. *Icarus (ISSN 0019-1035)*, 78(2):298–310, April 1989.

A F Cheng, P Michel, M Jutzi, A S Rivkin, A Stickle, O Barnouin, C Ernst, J Atchison, P Pravec, D C Richardson, and AIDA team. Asteroid Impact & Deflection Assess-

ment mission: Kinetic impactor. *Planetary and Space Science*, 121:27–35, February 2016.

Andrew F Cheng, Andrew S Rivkin, Patrick Michel, Justin Atchison, Olivier Barnouin, Lance Benner, Nancy L Chabot, Carolyn Ernst, Eugene G Fahnestock, Michael Kueppers, Petr Pravec, Emma Rainey, Derek C Richardson, Angela M Stickle, and Cristina Thomas. AIDA DART asteroid deflection test: Planetary defense and science objectives. *Planetary and Space Science*, 157:104–115, August 2018.

Steven R Chesley, Steven J Ostro, David Vokrouhlický, David Čapek, Jon D Giorgini, Michael C Nolan, Jean-Luc Margot, Alice A Hine, Lance Benner, and Alan B Chamberlin. Direct Detection of the Yarkovsky Effect by Radar Ranging to Asteroid 6489 Golevka. *Science*, 302(5):1739–1742, December 2003.

Thomas J Colvin, Keith Crane, and Bhavya Lal. Assessing the economics of asteroid-derived water for propellant. *Acta Astronautica*, 176:298–305, November 2020.

Desireé Cotto-Figueroa, Thomas S Statler, Derek C Richardson, and Paolo Tanga. Coupled Spin and Shape Evolution of Small Rubble-pile Asteroids: Self-limitation of the YORP Effect. *The Astrophysical Journal*, 803(1):25, April 2015.

Matija Ćuk and Joseph A Burns. Effects of thermal radiation on the dynamics of binary NEAs. *Icarus*, 176(2):418–431, August 2005.

Matija Ćuk and David Nesvorný. Orbital evolution of small binary asteroids. *Icarus*, 207(2):732–743, June 2010.

Gennaro D'Angelo and Francesco Marzari. Outward Migration of Jupiter and Saturn in Evolved Gaseous Disks. *The Astrophysical Journal*, 757(1):50, September 2012.

Donald R. Davis, Stuart J. Weidenschilling, Paolo Farinella, Paolo Paolicchi, and Richard P. Binzel. Asteroid collisional history: effects on sizes and spins. In Richard P. Binzel, Tom Gehrels, and Mildred Shapley Matthews, editors, *Asteroids II*, pages 805–826, January 1989.

Marco Delbo, Kevin Walsh, Bryce Bolin, Chrysa Avdellidou, and Alessandro Morbidelli. Identification of a primordial asteroid family constrains the original planetesimal population. *Science*, 357(6):1026–1029, September 2017.

J Ďurech, D Vokrouhlický, M Kaasalainen, D Higgins, Yu N Krugly, N M Gaftonyuk, V G Shevchenko, V G Chiorny, H Hamanowa, H Hamanowa, V Reddy, and R R Dyvig. Detection of the YORP effect in asteroid (1620) Geographos. *Astronomy & Astrophysics*, 489(2):L25–L28, September 2008.

J Ďurech, V Sidorin, and M Kaasalainen. DAMIT: a database of asteroid models. *Astronomy & Astrophysics*, 513:A46–13, April 2010.

J Ďurech, D Vokrouhlický, A R Baransky, S Breiter, O A Burkhonov, W Cooney, V Fuller, N M Gaftonyuk, J Gross, R Ya Inasaridze, M Kaasalainen, Yu N Krugly, O I Kvaratshelia, E A Litvinenko, B Macomber, F Marchis, I E Molotov, J Oey, D Polishook, J Pollock, P Pravec, K Sárneczky, V G Shevchenko, I Slyusarev, R Stephens, Gy Szabó, D Terrell, F Vachier, Z Vanderplate, M Viikinkoski, and B D Warner. Analysis of the rotation period of asteroids (1865) Cerberus, (2100) Ra-Shalom, and (3103) Eger – search for the YORP effect. *Astronomy & Astrophysics*, 547:A10–9, October 2012.

J Ďurech, D Vokrouhlický, P Pravec, J Hanuš, D Farnocchia, Yu N Krugly, R Y Inasaridze, V R Ayvazian, P Fatka, V G Chiorny, N Gaftonyuk, A Galád, R Groom, K Hornoch, H Kucakova, P Kušnirák, M Lehký, O I Kvaratskhelia, G Masi, I E Molotov, J Oey, J T Pollock, V G Shevchenko, J Vraštil, and B D Warner. YORP and Yarkovsky effects in asteroids (1685) Toro, (2100) Ra-Shalom, (3103) Eger, and (161989) Cacus. *Astronomy & Astrophysics*, 609:A86, January 2018.

Martin Elvis. How many ore-bearing asteroids? *Planetary and Space Science*, 91: 20–26, February 2014.

Martin Elvis and Tony Milligan. How much of the Solar System should we leave as wilderness? *Acta Astronautica*, 162:574–580, September 2019.

Paolo Farinella, David Vokrouhlický, and William K Hartmann. Meteorite Delivery via Yarkovsky Orbital Drift. *Icarus*, 132(2):378–387, April 1998.

D Farnocchia and S R Chesley. Assessment of the 2880 impact threat from Asteroid (29075) 1950 DA. *Icarus*, 229(C):321–327, February 2014.

D Farnocchia, S R Chesley, D Vokrouhlický, A Milani, F Spoto, and W F Bottke. Near Earth Asteroids with measurable Yarkovsky effect. *Icarus*, 224(1):1–13, May 2013.

A Fujiwara, J Kawaguchi, and S Sasaki. HAYABUSA Mission to Asteroid Itokawa: In-Situ Observation and Sample Return. In *Dust in Planetary Systems*, page 50, 2005.

J D Giorgini, S J Ostro, L A M Benner, P W Chodas, S R Chesley, R S Hudson, M C Nolan, A R Klemola, E M Standish, R F Jurgens, R ROSE, A B Chamberlin, D K Yeomans, and J L Margot. Asteroid 1950 DA's Encounter with Earth in 2880: Physical Limits of Collision Probability Prediction. *Science*, 296(5):132–136, April 2002.

B J Gladman, F Migliorini, A Morbidelli, V Zappalà, P Michel, A Cellino, C Froeschlé, H F Levison, M Bailey, and M Duncan. Dynamical lifetimes of objects injected into asteroid belt resonances. *Science*, 277(5323):197–201, 1997.

O Golubov, D J Scheeres, and Yu N Krugly. A Three-dimensional Model of Tangential YORP. *The Astrophysical Journal*, 794(1):22, October 2014.

Oleksiy Golubov. Analytic Model for Tangential YORP. *The Astronomical Journal*, 154(6):0–0, November 2017.

Oleksiy Golubov and Yurij N Krugly. TANGENTIAL COMPONENT OF THE YORP EFFECT. *The Astrophysical Journal*, 752(1):L11–5, May 2012.

Oleksiy Golubov and Daniel J Scheeres. Systematic Structure and Sinks in the YORP Effect. *The Astronomical Journal*, 157(3):0–0, February 2019.

Oleksiy Golubov, Nathan Myhrvold, Pavel Ševeček, Cem Özen, and Dhileep Sivam. Sensitivity of Tangential YORP Effect to Shapes and Arrangement of Boulders. *EPSC-DPS Joint Meeting 2019*, 13:EPSC–DPS2019–969, September 2019.

Oleksiy Golubov, Daniel J Scheeres, and Yurij N Krugly. YORP equilibria: ways out of YORP cycles. *Astronomy in Focus XXX*, 30(A30):15–15, March 2020.

Mikael Granvik, Alessandro Morbidelli, Robert Jedicke, Bryce Bolin, William F Bottke, Edward Beshore, David Vokrouhlický, Marco Delbo, and Patrick Michel. Super-catastrophic disruption of asteroids at small perihelion distances. *Nature*, 530(7): 303–306, February 2016.

Mikael Granvik, Alessandro Morbidelli, David Vokrouhlický, William F Bottke, David Nesvorný, and Robert Jedicke. Escape of asteroids from the main belt. *Astronomy & Astrophysics*, 598:A52–13, January 2017.

Mikael Granvik, Alessandro Morbidelli, Robert Jedicke, Bryce Bolin, William F Bottke, Edward Beshore, David Vokrouhlický, David Nesvorný, and Patrick Michel. Debiased orbit and absolute-magnitude distributions for near-Earth objects. *Icarus*, 312:181–207, September 2018.

Peter M. Gray. Assembly and integration to first light of the four VLT telescopes. In Thomas A. Sebring and Torben Andersen, editors, *Telescope Structures, Enclosures, Controls, Assembly/Integration/Validation, and Commissioning*, volume 4004, pages 2 – 13. International Society for Optics and Photonics, SPIE, 2000. doi: 10.1117/12.393913. URL `https://doi.org/10.1117/12.393913`.

Adam H Greenberg, Jean-Luc Margot, Ashok K Verma, Patrick A Taylor, and Susan E Hodge. Yarkovsky Drift Detections for 247 Near-Earth Asteroids. *The Astronomical Journal*, 159(3):0–0, February 2020.

James E Gunn, Michael Carr, G Edward Danielson, Ernest O Lorenz, Richard Lucinio, Victor E Nenow, J Devere Smith, James A Westphal, Donald P Schneider, and Barbara A Zimmerman. Four-shooter - A large format charge-coupled device camera

for the Hale telescope. *Optical Engineering (ISSN 0091-3286)*, 26(8):779–787, August 1987.

Stephen D J Gwyn, Norman Hill, and J J Kavelaars. SSOS: A Moving-Object Image Search Tool for Asteroid Precovery. *Publications of the Astronomical Society of the Pacific*, 124(9):579–, June 2012.

Karl E Jr Haisch, Elizabeth A Lada, and Charles J Lada. Disk Frequencies and Lifetimes in Young Clusters. *The Astrophysical Journal*, 553(2):L153–L156, June 2001.

J K Harmon. Planetary delay-Doppler radar and the long-code method. *IEEE Transactions on Geoscience and Remote Sensing*, 40(9):1904–1916, September 2002.

A W Harris. The Rotation Rates of Very Small Asteroids: Evidence for 'Rubble Pile' Structure. *Lunar and Planetary Science*, 27, March 1996.

A W Harris, J W Young, E Bowell, L J Martin, R L Millis, M Poutanen, F Scaltriti, V Zappalà, H J Schober, H Debehogne, and K W Zeigler. Photoelectric observations of asteroids 3, 24, 60, 261, and 863. *Icarus (ISSN 0019-1035)*, 77(1):171–186, January 1989.

Alan W Harris, Eugene G Fahnestock, and Petr Pravec. On the shapes and spins of "rubble pile" asteroids. *Icarus*, 199(2):310–318, February 2009.

Masatoshi Hirabayashi and Daniel J Scheeres. Rotationally induced failure of irregularly shaped asteroids. *Icarus*, 317:354–364, January 2019.

Keith A. Holsapple. Spin limits of solar system bodies: From the small fast-rotators to 2003 el61. *Icarus*, 187(2):500–509, Apr 2007. ISSN 00191035. doi: 10.1016/j.icarus.2006.08.012.

R S Hudson and S J Ostro. Physical Model of Asteroid 1620 Geographos from Radar and Optical Data. *Icarus*, 140(2):369–378, August 1999.

R Scott Hudson and Steven J Ostro. Shape of Asteroid 4769 Castalia (1989 PB) from Inversion of Radar Images. *Science*, 263(5):940–943, February 1994.

Scott Hudson. Three-dimensional reconstruction of asteroids from radar observations. *Remote Sensing Reviews*, 8(1-3):195–203, January 1993.

Derek J Ives, Simon Tulloch, and John Churchill. INT prime focus mosaic camera. *Proc. SPIE Vol. 2654*, 2654:266–276, March 1996.

Seth A Jacobson and Daniel J Scheeres. Dynamics of rotationally fissioned asteroids: Source of observed small asteroid systems. *Icarus*, 214(1):161–178, July 2011.

Peter Jenniskens, Olga P Popova, Dmitry O Glazachev, Elena D Podobnaya, and Anna P Kartashova. Tunguska eyewitness accounts, injuries, and casualties. *Icarus*, 327:4–18, July 2019.

D Jewitt, H Hsieh, and J Agarwal. The Active Asteroids. *Asteroids IV*, pages 221–241, 2015.

A Johansen, E Jacquet, J N Cuzzi, A Morbidelli, and M Gounelle. New Paradigms for Asteroid Formation. *Asteroids IV*, pages 471–492, 2015.

L Jorda, P L Lamy, R W Gaskell, M Kaasalainen, O Groussin, S Besse, and G Faury. Asteroid (2867) Steins: Shape, topography and global physical properties from OSIRIS observations. *Icarus*, 221(2):1089–1100, December 2012.

L Jorda, R Gaskell, C Capanna, S Hviid, P Lamy, J Ďurech, G Faury, O Groussin, P Gutierrez, C Jackman, S J Keihm, H U Keller, J Knollenberg, E Kührt, S Marchi, S Mottola, E Palmer, F P Schloerb, H Sierks, J B Vincent, M F A'Hearn, C Barbieri, R Rodrigo, D Koschny, H Rickman, M A Barucci, J L Bertaux, I Bertini, G Cremonese, V Da Deppo, B Davidsson, S Debei, M De Cecco, S Fornasier, M Fulle, C Güttler, W H Ip, J R Kramm, M Küppers, L M Lara, M Lazzarin, J J Lopez Moreno, F Marzari, G Naletto, N Oklay, N Thomas, C Tubiana, and K P Wenzel. The global shape, density and rotation of Comet 67P/Churyumov-Gerasimenko from preperihelion Rosetta/OSIRIS observations. *Icarus*, 277:257–278, October 2016.

M Jutzi and W Benz. Formation of bi-lobed shapes by sub-catastrophic collisions. *Astronomy & Astrophysics*, 597:A62–10, January 2017.

Martin Jutzi. The shape and structure of small asteroids as a result of sub-catastrophic collisions. *Planetary and Space Science*, 177:104695, November 2019.

M Kaasalainen and J Torppa. Optimization Methods for Asteroid Lightcurve Inversion I. Shape Determination. *Icarus*, 153(1):24–36, September 2001.

M Kaasalainen, L Lamberg, and K Lumme. Interpretation of lightcurves of atmosphereless bodies. II - Practical aspects of inversion. *Astronomy and Astrophysics (ISSN 0004-6361)*, 259(1):333–340, June 1992a.

M Kaasalainen, L Lamberg, K Lumme, and E Bowell. Interpretation of lightcurves of atmosphereless bodies. I - General theory and new inversion schemes. *Astronomy and Astrophysics (ISSN 0004-6361)*, 259(1):318–332, June 1992b.

M Kaasalainen, J Torppa, and K Muinonen. Optimization Methods for Asteroid Lightcurve Inversion II. The Complete Inverse Problem. *Icarus*, 153(1):37–51, September 2001.

Mikko Kaasalainen and Lars Lamberg. Inverse problems of generalized projection operators. *Inverse Problems*, 22(3):749–769, April 2006.

Mikko Kaasalainen, Josef Ďurech, Brian D Warner, Yurij N Krugly, and Ninel M Gaftonyuk. Acceleration of the rotation of asteroid 1862 Apollo by radiation torques. *Nature*, 446(7134):420–422, March 2007.

Sascha Kempf, Susanne Pfalzner, and Thomas K Henning. N-Particle-Simulations of Dust Growth. I. Growth Driven by Brownian Motion. *Icarus*, 141(2):388–398, October 1999.

A La Spina, P Paolicchi, A Kryszczyńska, and P Pravec. Retrograde spins of near-Earth asteroids from the Yarkovsky effect. *Nature*, 428(6981):400–401, March 2004.

P. O. Lagage, J. W. Pel, M. Authier, J. Belorgey, A. Claret, C. Doucet, D. Dubreuil, G. Durand, E. Elswijk, P. Girardot, H. U. Käufl, G. Kroes, M. Lortholary, Y. Lussignol, M. Marchesi, E. Pantin, R. Peletier, J. F. Pirard, J. Pragt, Y. Rio, T. Schoenmaker, R. Siebenmorgen, A. Silber, A. Smette, M. Sterzik, and C. Veyssiere. Successful Commissioning of VISIR: The Mid-Infrared VLT Instrument. *The Messenger*, 117:12–16, September 2004.

P L Lamy, I Toth, Y R Fernandez, and H A Weaver. The sizes, shapes, albedos, and colors of cometary nuclei. *Comets II*, pages 223–264, 2004.

D S Lauretta, S S Balram-Knutson, E Beshore, W V Boynton, C Drouet Aubigny, D N DellaGiustina, H L Enos, D R Golish, C W Hergenrother, E S Howell, C A Bennett, E T Morton, M C Nolan, B Rizk, H L Roper, A E Bartels, B J Bos, J P Dworkin, D E Highsmith, D A Lorenz, L F Lim, R Mink, M C Moreau, J A Nuth, D C Reuter, A A Simon, E B Bierhaus, B H Bryan, R Ballouz, O S Barnouin, R P Binzel, W F Bottke, V E Hamilton, K J Walsh, S R Chesley, P R Christensen, B E Clark, H C Connolly, M K Crombie, M G Daly, J P Emery, T J McCoy, J W McMahon, D J Scheeres, S Messenger, K Nakamura-Messenger, K Righter, and S A Sandford. OSIRIS-REx: Sample Return from Asteroid (101955) Bennu. *Space Sci Rev*, pages 1–60, October 2017.

Oliver Le Fèvre, Michel Saisse, Dario Mancini, Sylvie Brau-Nogue, Oreste Caputi, Louis Castinel, Sandro D'Odorico, Bianca Garilli, Markus Kissler-Patig, Christian Lucuix, Guido Mancini, Alain Pauget, Giovanni Sciarretta, Marco Scodeggio, Laurence Tresse, and Gianpaolo Vettolani. Commissioning and performances of the VLT-VIMOS instrument. In Masanori Iye and Alan F. M. Moorwood, editors, *Instrument Design and Performance for Optical/Infrared Ground-based Telescopes*, volume 4841 of *Society of Photo-Optical Instrumentation Engineers (SPIE) Conference Series*, pages 1670–1681, March 2003. doi: 10.1117/12.460959.

H F Levison, C Olkin, K S Noll, and S Marchi. Lucy - First to the Trojans. *American Geophysical Union*, 54, December 2019.

LONEOS. 2000 YK66 Discovery. *Minor Planet Electronic Circulars*, A22, 2001.

S C Lowry, P R Weissman, S R Duddy, B Rozitis, A Fitzsimmons, S F Green, M D Hicks, C Snodgrass, S D Wolters, S R Chesley, J Pittichová, and P van Oers. The internal structure of asteroid (25143) Itokawa as revealed by detection of YORP spin-up. *Astronomy & Astrophysics*, 562:A48–9, February 2014.

Stephen Lowry, Agata Rozek, Benjamin Rozitis, Simon Green, Colin Snodgrass, Alan Fitzsimmons, Paul Weissman, Eloise Brown, Tarik Zegmott, Lord Dover, Michael Hicks, Kenneth Lawrence, Guido Roberts-Borsani, Raoul Behrend, and Federico Manzini. Physical Model of Near-Earth Asteroid (1917) Cuyo and Detection of a Mass-Lofting Event. In *EPSC-DPS Joint Meeting 2019*, volume 2019, pages EPSC–DPS2019–1561, September 2019.

Stephen C Lowry, Alan Fitzsimmons, Petr Pravec, David Vokrouhlický, Hermann Boehnhardt, Patrick A Taylor, Jean-Luc Margot, Adrian Galád, Mike Irwin, Jonathan Irwin, and Peter Kušnirák. Direct Detection of the Asteroidal YORP Effect. *Science*, 316(5):272–, April 2007.

W Lyra, A Johansen, A Zsom, H Klahr, and N Piskunov. Planet formation bursts at the borders of the dead zone in 2D numerical simulations of circumstellar disks. *Astronomy & Astrophysics*, 497(3):869–888, March 2009.

P Magnusson, M A Barucci, J D Drummond, K Lumme, S J Ostro, J Surdej, R C Taylor, and V Zappalà. Determination of pole orientations and shapes of asteroids. *Asteroids II*, pages 66–97, 1989.

Christopher Magri, Steven J Ostro, Daniel J Scheeres, Michael C Nolan, Jon D Giorgini, Lance Benner, and Jean-Luc Margot. Radar observations and a physical model of Asteroid 1580 Betulia. *Icarus*, 186(1):152–177, January 2007.

Christopher Magri, Ellen S Howell, Michael C Nolan, Patrick A Taylor, Yanga R Fernández, Michael Mueller, Ronald J Vervack Jr, Lance Benner, Jon D Giorgini, Steven J Ostro, Daniel J Scheeres, Michael D Hicks, Heath Rhoades, James M

Somers, Ninel M Gaftonyuk, Vladimir V Kouprianov, Yurij N Krugly, Igor E Molotov, Michael W Busch, Jean-Luc Margot, Vladimir Benishek, Vojislava Protitch-Benishek, Adrian Galád, David Higgins, Peter Kušnirák, and Donald P Pray. Radar and photometric observations and shape modeling of contact binary near-Earth Asteroid (8567) 1996 HW1. *Icarus*, 214(1):210–227, July 2011.

A. Mainzer, T. Grav, J. Bauer, J. Masiero, R. S. McMillan, R. M. Cutri, R. Walker, E. Wright, P. Eisenhardt, D. J. Tholen, and et al. Neowise observations of near-earth objects: Preliminary results. *The Astrophysical Journal*, 743(2):156, Dec 2011. ISSN 0004-637X, 1538-4357. doi: 10.1088/0004-637X/743/2/156.

A Mainzer, T Grav, J Masiero, J Bauer, R M Cutri, R S McMillan, C R Nugent, D Tholen, R Walker, and E L Wright. PHYSICAL PARAMETERS OF ASTEROIDS ESTIMATED FROM THE WISE3-BAND DATA AND NEOWISE POST-CRYOGENIC SURVEY. *The Astrophysical Journal*, 760(1):L12–6, November 2012.

Amy K. Mainzer, James M. Bauer, Roc M. Cutri, Tommy Grav, Emily A. Kramer, Joseph R. Masiero, Sarah Sonnett, and Edward L. Wright. NEOWISE Diameters and Albedos V2.0. *NASA Planetary Data System*, January 2019. doi: 10.26033/18S3-2Z54.

Sean E Marshall, Ellen S Howell, Marina Brozovic, Patrick A Taylor, Donald B Campbell, L A M Benner, Shantanu P Naidu, Jon D Giorgini, Joseph S Jao, Clement G Lee, James E Richardson, Linda A Rodriguez-Ford, E G Rivera-Valentín, F D Ghigo, Adam Kobelski, Michael W Busch, Petr Pravec, Brian D Warner, Vishnu Reddy, Michael D Hicks, Jenna L Crowell, Y R Fernandez, Ronald J Vervack, Michael C Nolan, Christopher Magri, Benjamin Sharkey, and Brandon Bozek. Potentially Hazardous Asteroid (85989) 1999 JD6: Radar, Infrared, and Lightcurve Observations and a Preliminary Shape Model. In *American Astronomical Society, DPS*, page id.204.09, November 2015.

K Marti and T Graf. COSMIC-RAY EXPOSURE HISTORY OF ORDINARY CHONDRITES. *Annual Review of Earth and Planetary Sciences*, pages 221–243, 1992.

Joseph R Masiero, C Nugent, A K Mainzer, E L Wright, J M Bauer, R M Cutri, T Grav, E Kramer, and S Sonnett. NEOWISE Reactivation Mission Year Three: Asteroid Diameters and Albedos. *The Astronomical Journal*, 154(4):0–0, September 2017.

Jay McMahon and Daniel Scheeres. Detailed prediction for the BYORP effect on binary near-Earth Asteroid (66391) 1999 KW4 and implications for the binary population. *Icarus*, 209(2):494–509, October 2010.

W J Merline, S J Weidenschilling, D D Durda, J L Margot, P Pravec, and A D Storrs. Asteroids Do Have Satellites. *Asteroids III*, pages 289–312, March 2002.

P Michel and D C Richardson. Collision and gravitational reaccumulation: Possible formation mechanism of the asteroid Itokawa. *Astronomy & Astrophysics*, 554:L1–4, May 2013.

P Michel, R L Ballouz, O S Barnouin, M Jutzi, K J Walsh, B H May, C Manzoni, D C Richardson, S R Schwartz, S Sugita, S Watanabe, H Miyamoto, M Hirabayashi, W F Bottke, H C Connolly, M Yoshikawa, and D S Lauretta. Collisional formation of top-shaped asteroids and implications for the origins of Ryugu and Bennu. *Nature Communications*, 11(1):268–11, May 2020.

Patrick Michel, Willy Benz, Paolo Tanga, and Derek C Richardson. Collisions and Gravitational Reaccumulation: Forming Asteroid Families and Satellites. *Science*, 294(5):1696–1700, November 2001.

Patrick Michel, Michael Kueppers, Holger Sierks, Ian Carnelli, Andy F Cheng, Karim Mellab, Mikael Granvik, Antti Kestilä, Tomas Kohout, Karri Muinonen, Antti Näsilä, Antti Penttila, Tuomas Tikka, Paolo Tortora, Valérie Ciarletti, Alain Hérique, Naomi Murdoch, Erik Asphaug, Andy Rivkin, Olivier Barnouin, Adriano Campo Bagatin, Petr Pravec, Derek C Richardson, Stephen R Schwartz, Kleomenis Tsiganis, Stephan Ulamec, and Ozgür Karatekin. European component of the AIDA mission to a binary

asteroid: Characterization and interpretation of the impact of the DART mission. *Advances in Space Research*, 62(8):2261–2272, October 2018.

Tatsuhiro Michikami and Axel Hagermann. Boulder sizes and shapes on asteroids: A comparative study of Eros, Itokawa and Ryugu. *Icarus*, 357(2083):114282–16, March 2021.

S N Milam, H B Hammel, J Bauer, M Brozović, T Grav, B J Holler, C Lisse, A Mainzer, V Reddy, M E Schwamb, T Spahr, C A Thomas, and D Woods. Combined Emerging Capabilities for Near-Earth Objects (NEOs). *arXiv.org*, page arXiv:1907.08972, July 2019.

Thierry Montmerle, Jean-Charles Augereau, Marc Chaussidon, Mathieu Gounelle, Bernard Marty, and Alessandro Morbidelli. 3. Solar System Formation and Early Evolution: the First 100 Million Years. *Earth, Moon, and Planets*, 98(1-4):39–95, October 2006.

A Morbidelli and D Vokrouhlický. The Yarkovsky-driven origin of near-Earth asteroids. *Icarus*, 163(1):120–134, May 2003.

Alessandro Morbidelli, William F Bottke, David Nesvorný, and Harold F Levison. Asteroids were born big. *Icarus*, 204(2):558–573, December 2009.

N Murdoch, P Sánchez, S R Schwartz, and H Miyamoto. Asteroid Surface Geophysics. *Asteroids IV*, pages 767–792, 2015.

David Nesvorný and William F Bottke. Detection of the Yarkovsky effect for main-belt asteroids. *Icarus*, 170(2):324–342, August 2004.

David Nesvorný, William F Jr Bottke, Luke Dones, and Harold F Levison. The recent breakup of an asteroid in the main-belt region. *Nature*, 417(6):720–771, June 2002.

M C Nolan, E S Howell, D J Scheeres, J W McMahon, O Golubov, C W Hergenrother, J P Emery, K S Noll, S R Chesley, and D S Lauretta. Detection of Rotational

Acceleration of Bennu Using HST Light Curve Observations. *Geophysical Research Letters*, 46(4):1956–1962, February 2019.

Michael C Nolan, Christopher Magri, Ellen S Howell, Lance Benner, Jon D Giorgini, Carl W Hergenrother, R Scott Hudson, Dante S Lauretta, Jean-Luc Margot, Steven J Ostro, and Daniel J Scheeres. Shape model and surface properties of the OSIRIS-REx target Asteroid (101955) Bennu from radar and lightcurve observations. *Icarus*, 226(1):629–640, September 2013.

E. J. Opik. Collision probability with the planets and the distribution of planetary matter. *Proc. R. Irish Acad. Sect. A*, 54:165–199, January 1951.

S J Ostro, R Connelly, and L Belkora. Asteroid shapes from radar echo spectra - A new theoretical approach. *Icarus*, 73(1):15–24, January 1988.

S J Ostro, K D Rosema, and R F Jurgens. The shape of Eros. *Icarus*, 84(2):334–351, April 1990.

S J Ostro, K D Rosema, R S Hudson, R F Jurgens, J D Giorgini, R Winkler, D K Yeomans, D Choate, R ROSE, M A Slade, S D Howard, and D L Mitchell. Extreme elongation of asteroid 1620 Geographos from radar images. *Nature*, 375(6):474–477, June 1995.

S J Ostro, R S Hudson, L A M Benner, J D Giorgini, C Magri, J L Margot, and M C Nolan. Asteroid Radar Astronomy. *Asteroids III*, pages 151–168, 2002.

Steven J Ostro. Planetary radar astronomy. *Reviews of Modern Physics*, 65(4):1235–1279, October 1993.

Steven J. Ostro. Chapter 40 - planetary radar. In Lucy-Ann McFadden, Paul R. Weissman, and Torrence V. Johnson, editors, *Encyclopedia of the Solar System (Second Edition)*, pages 735 – 764. Academic Press, San Diego, second edition edition, 2007. ISBN 978-0-12-088589-3. doi: https://doi.org/10.1016/B978-012088589-3/50044-X. URL `http://www.sciencedirect.com/science/article/pii/B978012088589350044X`.

Steven J Ostro, Lance Benner, Michael C Nolan, Christopher Magri, Jon D Giorgini, Daniel J Scheeres, Stephen B Broschart, Mikko Kaasalainen, David Vokrouhlický, Steven R Chesley, Jean-Luc Margot, Raymond F Jurgens, Randy Rose, Donald K Yeomans, Shigeru Suzuku, and Eric M de Jong. Radar observations of asteroid 25143 Itokawa (1998 SF36). *Meteoritics & Planetary Science*, 39(3):407–424, March 2004.

Steven J Ostro, Jean-Luc Margot, Lance Benner, Jon D Giorgini, Daniel J Scheeres, Eugene G Fahnestock, Stephen B Broschart, Julie Bellerose, Michael C Nolan, Christopher Magri, Petr Pravec, Petr Scheirich, Randy Rose, Raymond F Jurgens, Eric M de Jong, and Shigeru Suzuki. Radar Imaging of Binary Near-Earth Asteroid (66391) 1999 KW4. *Science*, 314(5):1276–1280, November 2006.

András Pál, Róbert Szakáts, Csaba Kiss, Attila Bódi, Zsófia Bognár, Csilla Kalup, László L Kiss, Gábor Marton, László Molnár, Emese Plachy, Krisztián Sárneczky, Gyula M Szabó, and Róbert Szabó. Solar System Objects Observed with TESS—First Data Release: Bright Main-belt and Trojan Asteroids from the Southern Survey. *The Astrophysical Journal Supplement Series*, 247(1):26, March 2020.

Paolo Paolicchi and Zoran Knežević. Footprints of the YORP effect in asteroid families. *Icarus*, 274:314–326, August 2016.

Paolo Paolicchi, F Spoto, Z Knežević, and A Milani. Ages of asteroid families estimated using the YORP-eye method. *Monthly Notices of the Royal Astronomical Society*, 484(2):1815–1828, December 2018.

Jean-Marc Petit, Alessandro Morbidelli, and John Chambers. The Primordial Excitation and Clearing of the Asteroid Belt. *Icarus*, 153(2):338–347, October 2001.

G. H. Pettengill and R. F. Jurgens. *Radar observations of asteroids.*, pages 206–211. 1979.

Carol Polanskey, Linda Elkins-Tanton, James Bell, Richard Binzel, David Lawrence, Jose Merayo, Ryan Park, Benjamin Weiss, and David Williams. Mission to (16) Psyche. *14th Europlanet Science Congress 2020*, 14:EPSC2020–988, September 2020.

Olga P Popova, Peter Jenniskens, Vacheslav Emel'yanenko, Anna Kartashova, Eugeny Biryukov, Sergey Khaibrakhmanov, Valery Shuvalov, Yurij Rybnov, Alexandr Dudorov, Victor I Grokhovsky, Dmitry D Badyukov, Qing-Zhu Yin, Peter S Gural, Jim Albers, Mikael Granvik, Läslo G Evers, Jacob Kuiper, Vladimir Kharlamov, Andrey Solovyov, Yuri S Rusakov, Stanislav Korotkiy, Ilya Serdyuk, Alexander V Korochantsev, Michail Yu Larionov, Dmitry Glazachev, Alexander E Mayer, Galen Gisler, Sergei V Gladkovsky, Josh Wimpenny, Matthew E Sanborn, Akane Yamakawa, Kenneth L Verosub, Douglas J Rowland, Sarah Roeske, Nicholas W Botto, Jon M Friedrich, Michael E Zolensky, Loan Le, Daniel Ross, Karen Ziegler, Tomoki Nakamura, Insu Ahn, Jong Ik Lee, Qin Zhou, Xian-Hua Li, Qiu-Li Li, Yu Liu, Guo-Qiang Tang, Takahiro Hiroi, Derek Sears, Ilya A Weinstein, Alexander S Vokhmintsev, Alexei V Ishchenko, Phillipe Schmitt-Kopplin, Norbert Hertkorn, Keisuke Nagao, Makiko K Haba, Mutsumi Komatsu, Takashi Mikouchi, and aff34. Chelyabinsk Airburst, Damage Assessment, Meteorite Recovery, and Characterization. *Science*, 342 (6):1069–1073, November 2013.

Steven H Pravdo, David L Rabinowitz, Eleanor F Helin, Kenneth J Lawrence, Raymond J Bambery, Christopher C Clark, Steven L Groom, Steven Levin, Jean Lorre, Stuart B Shaklan, Paul Kervin, John A Africano, Paul Sydney, and Vicki Soohoo. The Near-Earth Asteroid Tracking (NEAT) Program: An Automated System for Telescope Control, Wide-Field Imaging, and Object Detection*. *The Astronomical Journal*, 117(3):1616–1633, March 1999.

P Pravec and A W Harris. Fast and Slow Rotation of Asteroids. *Icarus*, 148(1):12–20, November 2000.

P Pravec and A W Harris. Binary asteroid population. *Icarus*, 190(1):250–259, September 2007.

P Pravec, A W Harris, and T Michalowski. Asteroid Rotations. *Asteroids III*, pages 113–122, 2002.

Petr Pravec, Marek Wolf, and Lenka Šarounová. Lightcurves of 26 Near-Earth Asteroids. *Icarus*, 136(1):124–153, November 1998.

Sean N Raymond and Alessandro Morbidelli. The Grand Tack model: a critical review. *arXiv.org*, (S310):194–203, September 2014.

Sean N Raymond, David P O'Brien, Alessandro Morbidelli, and Nathan A Kaib. Building the terrestrial planets: Constrained accretion in the inner solar system. *Icarus*, 203(2):644–662, October 2009.

Derek C Richardson and Kevin J Walsh. Binary Minor Planets. *Annual Review of Earth and Planetary Sciences*, 34(1):47–81, May 2006.

James E Richardson and Timothy J Bowling. Investigating the combined effects of shape, density, and rotation on small body surface slopes and erosion rates. *Icarus*, 234(C):53–65, May 2014.

James E Richardson, Kevin J Graves, Alan W Harris, and Timothy J Bowling. Small body shapes and spins reveal a prevailing state of maximum topographic stability. *Icarus*, 329:207–221, September 2019.

Lucie Riu, Cédric Pilorget, Ralph Milliken, Kohei Kitazato, Tomoki Nakamura, Yuichiro Cho, Moe Matsuoka, Seiji Sugita, Masanao Abe, Shuji Matsuura, Makiko Ohtake, Shingo Kameda, Naoya Sakatani, Eri Tatsumi, Yasuhiro Yokota, and Takahiro Iwata. Spectral characterization of the craters of Ryugu as observed by the NIRS3 instrument on-board Hayabusa2. *Icarus*, 357:114253, March 2021.

A S Rivkin, R P Binzel, and S J Bus. Constraining near-Earth object albedos using near-infrared spectroscopy. *Icarus*, 175(1):175–180, May 2005.

A S Rivkin, H Campins, J P Emery, E S Howell, J Licandro, D Takir, and F Vilas. Astronomical Observations of Volatiles on Asteroids. *Asteroids IV*, pages 65–87, 2015.

Andrew S Rivkin and Francesca E DeMeo. How Many Hydrated NEOs Are There? *Journal of Geophysical Research: Planets*, 124(1):128–142, January 2019.

Andrew S Rivkin, Moses Milazzo, Aparna Venkatesan, Elizabeth Frank, Monica R Vidaurri, Phil Metzger, and Chris Lewicki. Asteroid Resource Utilization: Ethical Concerns and Progress. *arXiv.org*, November 2020.

A Rożek, S C Lowry, M C Nolan, P A Taylor, L A M Benner, A Fitzsimmons, T J Zegmott, P R Weissman, S F Green, B Rozitis, C Snodgrass, W D Smythe, M D Hicks, E S Howell, A K Virkki, B Aponte-Hernandez, E G Rivera-Valentín, L A Rodriguez-Ford, L F Zambrano-Marin, M Brozović, S P Naidu, J D Giorgini, L G Snedeker, J S Jao, and F D Ghigo. Shape model and spin-state analysis of PHA contact binary (85990) 1999 JV6 from combined radar and optical observations. *Astronomy & Astrophysics*, 631:A149–28, November 2019a.

A Rożek, S C Lowry, B Rozitis, S F Green, C Snodgrass, P R Weissman, A Fitzsimmons, M D Hicks, K J Lawrence, S R Duddy, S D Wolters, G Roberts-Borsani, R Behrend, and F Manzini. Physical model of near-Earth asteroid (1917) Cuyo from ground-based optical and thermal-IR observations. *Astronomy & Astrophysics*, 627: A172–18, July 2019b.

Agata Rożek, Michael W Busch, Sean E Marshall, Grace C Young, Adam D Cobb, Chedy Raïssi, Yarin Gal, Lance Benner, Patrick A Taylor, and Stephen C Lowry. Machine learning tools to develop 3D shape models of near Earth asteroids from radar observations. *EPSC-DPS Joint Meeting 2019*, 13:EPSC–DPS2019–2074, September 2019c.

B Rozitis and S F Green. Directional characteristics of thermal-infrared beaming from atmosphereless planetary surfaces - a new thermophysical model. *Monthly Notices of the Royal Astronomical Society*, 415(3):2042–2062, July 2011.

B Rozitis and S F Green. The influence of rough surface thermal-infrared beaming

on the Yarkovsky and YORP effects. *Monthly Notices of the Royal Astronomical Society*, 423(1):367–388, April 2012.

B Rozitis and S F Green. The influence of global self-heating on the Yarkovsky and YORP effects. *Monthly Notices of the Royal Astronomical Society*, 433(1):603–621, May 2013.

Ben Rozitis, Eric MacLennan, and Joshua P Emery. Cohesive forces prevent the rotational breakup of rubble-pile asteroid (29075) 1950 DA. *Nature*, 512(7513):174–176, August 2014.

D Rubincam. Radiative Spin-up and Spin-down of Small Asteroids. *Icarus*, 148(1): 2–11, November 2000.

H N Russell. On the light variations of asteroids and satellites. *Astrophysical Journal*, 24:1–18, July 1906.

Diego Paul Sánchez and Daniel J Scheeres. DEM simulation of rotation-induced reshaping and disruption of rubble-pile asteroids. *Icarus*, 218(2):876–894, April 2012.

Juan A Sanchez, René Michelsen, Vishnu Reddy, and Andreas Nathues. Surface composition and taxonomic classification of a group of near-Earth and Mars-crossing asteroids. *Icarus*, 225(1):131–140, July 2013.

Paul Sánchez and Daniel J Scheeres. Disruption patterns of rotating self-gravitating aggregates: A survey on angle of friction and tensile strength. *Icarus*, 271:453–471, June 2016.

Paul Sánchez and Daniel J Scheeres. Rotational evolution of self-gravitating aggregates with cores of variable strength. *Planetary and Space Science*, 157:39–47, August 2018.

D J Scheeres. Rotational fission of contact binary asteroids. *Icarus*, 189(2):370–385, August 2007.

D J Scheeres. Landslides and Mass shedding on spinning spheroidal asteroids. *Icarus*, 247(C):1–17, February 2015.

D J Scheeres. Disaggregation of small, cohesive rubble pile asteroids due to YORP. *Icarus*, 304:183–191, April 2018.

D J Scheeres and R W Gaskell. Effect of density inhomogeneity on YORP: The case of Itokawa. *Icarus*, 198(1):125–129, November 2008.

P Scheirich, P Pravec, P Kušnirák, K Hornoch, J McMahon, D J Scheeres, D Čapek, D P Pray, H Kucakova, A Galád, J Vraštil, Yu N Krugly, N Moskovitz, L D Avner, B Skiff, R S McMillan, J A Larsen, M J Brucker, A F Tubbiolo, W R Cooney, J Gross, D Terrell, O Burkhonov, K E Ergashev, Sh A Ehgamberdiev, P Fatka, R Durkee, E Lilly Schunova, R Ya Inasaridze, V R Ayvazian, G Kapanadze, N M Gaftonyuk, J A Sanchez, V Reddy, L McGraw, M S Kelley, and I E Molotov. A satellite orbit drift in binary near-Earth asteroids (66391) 1999 KW4 and (88710) 2001 SL9 - Indication of the BYORP effect. *Icarus*, 360:114321, May 2021.

Stephen R Schwartz, Patrick Michel, Martin Jutzi, Simone Marchi, Yun Zhang, and Derek C Richardson. Catastrophic disruptions as the origin of bilobate comets. *Nature Astronomy*, 2(5):379–382, March 2018.

P Ševeček, O Golubov, D J Scheeres, and Yu N Krugly. Obliquity dependence of the tangential YORP. *Astronomy & Astrophysics*, 592:A115–6, August 2016.

Michael K Shepard, Bradley Timerson, Daniel J Scheeres, Lance Benner, Jon D Giorgini, Ellen S Howell, Christopher Magri, Michael C Nolan, Alessondra Springmann, Patrick A Taylor, and Anne Virkki. A revised shape model of asteroid (216) Kleopatra. *Icarus*, 311:197–209, September 2018.

Holger Sierks, Cesare Barbieri, Philippe L Lamy, Rafael Rodrigo, Detlef Koschny, Hans Rickman, Horst Uwe Keller, Jessica Agarwal, Michael F A'Hearn, Francesco Angrilli, Anne-Thérèse Auger, M Antonella Barucci, Jean-Loup Bertaux, Ivano Bertini, Sebastien Besse, Dennis Bodewits, Claire Capanna, Gabriele Cremonese, Vania Da Deppo, Björn Davidsson, Stefano Debei, Mariolino De Cecco, Francesca Ferri, Sonia Fornasier, Marco Fulle, Robert Gaskell, Lorenza Giacomini, Olivier Groussin,

Pablo Gutierrez-Marques, Pedro J Gutiérrez, Carsten Güttler, Nick Hoekzema, Stubbe F Hviid, Wing-Huen Ip, Laurent Jorda, Jörg Knollenberg, Gabor Kovacs, J Rainer Kramm, Ekkehard Kührt, Michael Küppers, Fiorangela La Forgia, Luisa M Lara, Monica Lazzarin, Cédric Leyrat, Josè J Lopez Moreno, Sara Magrin, Simone Marchi, Francesco Marzari, Matteo Massironi, Harald Michalik, Richard Moissl, Stefano Mottola, Giampiero Naletto, Nilda Oklay, Maurizio Pajola, Marco Pertile, Frank Preusker, Lola Sabau, Frank Scholten, Colin Snodgrass, Nicolas Thomas, Cecilia Tubiana, Jean-Baptiste Vincent, Klaus-Peter Wenzel, Mirco Zaccariotto, and Martin Pätzold. On the nucleus structure and activity of comet 67P/Churyumov-Gerasimenko. *Science*, 347(6):aaa1044–aaa1044, January 2015.

M A Slade, L A M Benner, and A Silva. Goldstone Solar System Radar Observatory: Earth-Based Planetary Mission Support and Unique Science Results. *Proceedings of the IEEE*, 99(5):757–769, May 2011. ISSN 0018-9219, 1558-2256. doi: 10.1109/JPROC.2010.2081650. URL `http://ieeexplore.ieee.org/document/5643090/`.

Stephen M Slivan. Spin vector alignment of Koronis family asteroids. *Nature*, 419 (6902):49–51, September 2002.

Stephen M Slivan, Richard P Binzel, Lucy D Crespo da Silva, Mikko Kaasalainen, Mariah M Lyndaker, and Marko Krčo. Spin vectors in the Koronis family: comprehensive results from two independent analyses of 213 rotation lightcurves. *Icarus*, 162(2):285–307, April 2003.

C Snodgrass and B Carry. Automatic Removal of Fringes from EFOSC Images. *The Messenger*, 152:14–16, June 2013.

Donald L. Snyder. Delay-doppler radar imaging. Semiannual Progress Report, November 1987.

Thomas S Statler. Extreme sensitivity of the YORP effect to small-scale topography. *Icarus*, 202(2):502–513, August 2009.

I. A. Steele. The Liverpool Telescope. *Astronomische Nachrichten*, 322:307–310, December 2001. doi: 10.1002/1521-3994(200112)322:5/6\textless{}307::AID-ASNA307\textgreater{}3.0.CO;2-2.

S A Stern, H A Weaver, J R Spencer, C B Olkin, G R Gladstone, W M Grundy, J M Moore, D P Cruikshank, H A Elliott, W B McKinnon, J Wm Parker, A J Verbiscer, L A Young, D A Aguilar, J M Albers, T Andert, J P Andrews, F Bagenal, M E Banks, B A Bauer, J A Bauman, K E Bechtold, C B Beddingfield, N Behrooz, K B Beisser, S D Benecchi, E Bernardoni, R A Beyer, S Bhaskaran, C J Bierson, R P Binzel, E M Birath, M K Bird, D R Boone, A F Bowman, V J Bray, D T Britt, L E Brown, M R Buckley, M W Buie, B J Buratti, L M Burke, S S Bushman, B Carcich, A L Chaikin, C L Chavez, A F Cheng, E J Colwell, S J Conard, M P Conner, C A Conrad, J C Cook, S B Cooper, O S Custodio, C M Dalle Ore, C C Deboy, P Dharmavaram, R D Dhingra, G F Dunn, A M Earle, A F Egan, J Eisig, M R El-Maarry, C Engelbrecht, B L Enke, C J Ercol, E D Fattig, C L Ferrell, T J Finley, J Firer, J Fischetti, W M Folkner, M N Fosbury, G H Fountain, J M Freeze, L Gabasova, L S Glaze, J L Green, G A Griffith, Y Guo, M Hahn, D W Hals, D P Hamilton, S A Hamilton, J J Hanley, A Harch, K A Harmon, H M Hart, J Hayes, C B Hersman, M E Hill, T A Hill, J D Hofgartner, M E Holdridge, M Horányi, A Hosadurga, A D Howard, C J A Howett, S E Jaskulek, D E Jennings, J R Jensen, M R Jones, H K Kang, D J Katz, D E Kaufmann, J J Kavelaars, J T Keane, G P Keleher, M Kinczyk, M C Kochte, P Kollmann, S M Krimigis, G L Kruizinga, D Y Kusnierkiewicz, M S Lahr, T R Lauer, G B Lawrence, J E Lee, E J Lessac-Chenen, I R Linscott, C M Lisse, A W Lunsford, D M Mages, V A Mallder, N P Martin, B H May, D J McComas, R L McNutt, D S Mehoke, T S Mehoke, D S Nelson, H D Nguyen, J I Núñez, A C Ocampo, W M Owen, G K Oxton, A H Parker, M Pätzold, J Y Pelgrift, F J Pelletier, J P Pineau, M R Piquette, S B Porter, S Protopapa, E Quirico, J A Redfern, A L Regiec, H J Reitsema, D C Reuter, D C Richardson, J E Riedel, M A Ritterbush, S J Robbins, D J Rodgers, G D Rogers, D M Rose, P E Rosendall, K D Runyon, M G Ryschkewitsch, M M Saina, M J Salinas, P M

Schenk, J R Scherrer, W R Schlei, B Schmitt, D J Schultz, D C Schurr, F Scipioni, R L Sepan, R G Shelton, M R Showalter, M Simon, K N Singer, E W Stahlheber, D R Stanbridge, J A Stansberry, A J Steffl, D F Strobel, M M Stothoff, T Stryk, J R Stuart, M E Summers, M B Tapley, A Taylor, H W Taylor, R M Tedford, H B Throop, L S Turner, O M Umurhan, J Van Eck, D Velez, M H Versteeg, M A Vincent, R W Webbert, S E Weidner, G E Weigle, J R Wendel, O L White, K E Whittenburg, B G Williams, K E Williams, S P Williams, H L Winters, A M Zangari, and T H Zurbuchen. Initial results from the New Horizons exploration of 2014 MU69, a small Kuiper Belt object. *Science*, 364(6):aaw9771, May 2019.

Grant H Stokes, Jenifer B Evans, Herbert E M Viggh, Frank C Shelly, and Eric C Pearce. Lincoln Near-Earth Asteroid Program (LINEAR). *Icarus*, 148(1):21–28, November 2000.

K Sugiura, H Kobayashi, and S Inutsuka. Toward understanding the origin of asteroid geometries. *Astronomy & Astrophysics*, 620:A167–11, December 2018.

M. Tarenghi and R. N. Wilson. The ESO NTT (New Technology Telescope): The First Active Optics Telescope. In Francois J. Roddier, editor, *Active Telescope Systems*, volume 1114, pages 302 – 313. International Society for Optics and Photonics, SPIE, 1989. doi: 10.1117/12.960835. URL `https://doi.org/10.1117/12.960835`.

Patrick A Taylor, Jean-Luc Margot, David Vokrouhlický, Daniel J Scheeres, Petr Pravec, Stephen C Lowry, Alan Fitzsimmons, Michael C Nolan, Steven J Ostro, Lance Benner, Jon D Giorgini, and Christopher Magri. Spin Rate of Asteroid (54509) 2000 PH5 Increasing Due to the YORP Effect. *Science*, 316(5):274–, April 2007.

P C Thomas, Michael F A'Hearn, Joseph Veverka, Michael J S Belton, Jochen Kissel, Kenneth P Klaasen, Lucy A McFadden, H Jay Melosh, Peter H Schultz, Sebastien Besse, Brian T Carcich, Tony L Farnham, Olivier Groussin, Brendan Hermalyn, Jian-Yang Li, Don J Lindler, Carey M Lisse, Karen Meech, and James E Richardson. Shape, density, and geology of the nucleus of Comet 103P/Hartley 2. *Icarus*, 222(2): 550–558, February 2013.

Doug Tody. The Iraf Data Reduction And Analysis System. In David L Crawford, editor, *1986 Astronomy Conferences*, pages 733–17. SPIE, October 1986.

Dimitri Veras and Daniel J Scheeres. Post-main-sequence debris from rotation-induced YORP break-up of small bodies – II. Multiple fissions, internal strengths, and binary production. *Monthly Notices of the Royal Astronomical Society*, 492(2):2437–2445, December 2019.

P Vernazza, L Jorda, B Carry, J Hanuš, M Marsset, M Viikinkoski, F Marchis, M Brož, A Drouard, T Fusco, R Fetick, M Ferrais, and Harissa Team. SPHERE Unveils the True Face of the Largest Main Belt Asteroids. *The Messenger*, 179:13–16, March 2020.

D Vokrouhlický and D Čapek. YORP-Induced Long-Term Evolution of the Spin State of Small Asteroids and Meteoroids: Rubincam's Approximation. *Icarus*, 159(2):449–467, October 2002.

D Vokrouhlický, M Brož, W F Bottke, D NESVORNY, and A Morbidelli. The peculiar case of the Agnia asteroid family. *Icarus*, 183(2):349–361, August 2006a.

D Vokrouhlický, M Brož, W F Bottke, D NESVORNY, and A Morbidelli. Yarkovsky/YORP chronology of asteroid families. *Icarus*, 182(1):118–142, May 2006b.

D Vokrouhlický, M Brož, A Morbidelli, W F Bottke, D NESVORNY, D Lazzaro, and A S Rivkin. Yarkovsky footprints in the Eos family. *Icarus*, 182(1):92–117, May 2006c.

D Vokrouhlický, D NESVORNY, and W BOTTKE. Secular spin dynamics of inner main-belt asteroids. *Icarus*, 184(1):1–28, September 2006d.

D Vokrouhlický, W F Bottke, S R Chesley, D J Scheeres, and T S Statler. The Yarkovsky and YORP Effects. *Asteroids IV*, pages 509–531, 2015.

David Vokrouhlický, David Nesvorný, and William F Bottke. The vector alignments of asteroid spins by thermal torques. *Nature*, 425(6954):147–151, September 2003.

K J Walsh and S A Jacobson. Formation and Evolution of Binary Asteroids. *Asteroids IV*, pages 375–393, 2015.

Kevin J Walsh. Rubble Pile Asteroids. *Annual Review of Astronomy and Astrophysics*, 56(1):593–624, September 2018.

Kevin J Walsh, Derek C Richardson, and Patrick Michel. Rotational breakup as the origin of small binary asteroids. *Nature*, 454(7201):188–191, July 2008.

Kevin J. Walsh, Alessandro Morbidelli, Sean N. Raymond, David P. O'Brien, and Avi M. Mandell. A low mass for Mars from Jupiter's early gas-driven migration. *Nature*, 475(7355):206–209, July 2011. doi: 10.1038/nature10201.

Brian D Warner. Near-Earth Asteroid Lightcurve Analysis at CS3-Palmer Divide Station: 2016 April-July. *Minor Planet Bulletin*, 43(4):311–319, October 2016.

Brian D Warner. Near-Earth Asteroid Lightcurve Analysis at CS3-Palmer Divide Station: 2016 July-September. *Minor Planet Bulletin*, 44(1):22–36, January 2017.

Brian D Warner, Alan W Harris, and Petr Pravec. The asteroid lightcurve database. *Icarus*, 202(1):134–146, July 2009.

Brian D Warner, Robert D Stephens, and Alan W Harris. Save the Lightcurves! *The Minor Planet Bulletin*, 38(3):172–174, July 2011.

S Watanabe, M Hirabayashi, N Hirata, Na Hirata, R Noguchi, Y Shimaki, H Ikeda, E Tatsumi, M Yoshikawa, S Kikuchi, H Yabuta, T Nakamura, S Tachibana, Y Ishihara, T Morota, K Kitazato, N Sakatani, K Matsumoto, K Wada, H Senshu, C Honda, T Michikami, H Takeuchi, T Kouyama, R Honda, S Kameda, T Fuse, H Miyamoto, G Komatsu, S Sugita, T Okada, N Namiki, M Arakawa, M Ishiguro, M Abe, R Gaskell, E Palmer, O S Barnouin, P Michel, A S French, J W McMahon, D J Scheeres, P A Abell, Y Yamamoto, K Shirai, M Matsuoka, M Yamada,

Y Yokota, H Suzuki, K Yoshioka, Y Cho, S Tanaka, N Nishikawa, T Sugiyama, H Kikuchi, R Hemmi, T Yamaguchi, N Ogawa, G Ono, Y Mimasu, K Yoshikawa, T Takahashi, Y Takei, A Fujii, C Hirose, T Iwata, M Hayakawa, S Hosoda, O Mori, H Sawada, T Shimada, S Soldini, H Yano, R Tsukizaki, M Ozaki, Y Iijima, K Ogawa, M Fujimoto, T M Ho, A Moussi, R Jaumann, J P Bibring, C Krause, F Terui, T Saiki, S Nakazawa, and Y Tsuda. Hayabusa2 arrives at the carbonaceous asteroid 162173 Ryugu—A spinning top–shaped rubble pile. *Science*, 364(6):268–272, April 2019.

Robert A Werner and Daniel J Scheeres. Exterior gravitation of a polyhedron derived and compared with harmonic and mascon gravitation representations of asteroid 4769 Castalia. *Celestial Mechanics and Dynamical Astronomy*, 65(3):313–344, September 1996.

C. A. Wirtanen. 1950 DA Discovery. *Minor Planet Circulars*, 416, 1950.

Makoto Yoshikawa, Sei-ichiro Watanabe, Yuichi Tsuda, and Hitoshi Kuninaka. Hayabusa2 - The Next Asteroid Sample Return Mission of Japan. *Transactions of the Japan Society for Aeronautical and Space Sciences, Aerospace Technology Japan*, 12(29):29–33, 2014.

P S Zain, G C de Elía, and R P Di Sisto. New multi-part collisional model of the main belt: the contribution to near-Earth asteroids. *Astronomy & Astrophysics*, 639:A9–13, July 2020.

Alexander L Zaitsev. European near-Earth object radar. In *In: Proceedings of Asteroids, Comets, Meteors*, pages 879–882, November 2002.

A Zsom, C W Ormel, C Güttler, J Blum, and C P Dullemond. The outcome of protoplanetary dust growth: pebbles, boulders, or planetesimals? *Astronomy & Astrophysics*, 513:A57–22, April 2010.

B Zuckerman, C Melis, B Klein, D Koester, and M Jura. Ancient Planetary Systems are Orbiting a Large Fraction of White Dwarf Stars. *The Astrophysical Journal*, 722 (1):725–736, October 2010.

A | Supplementary figures and tables

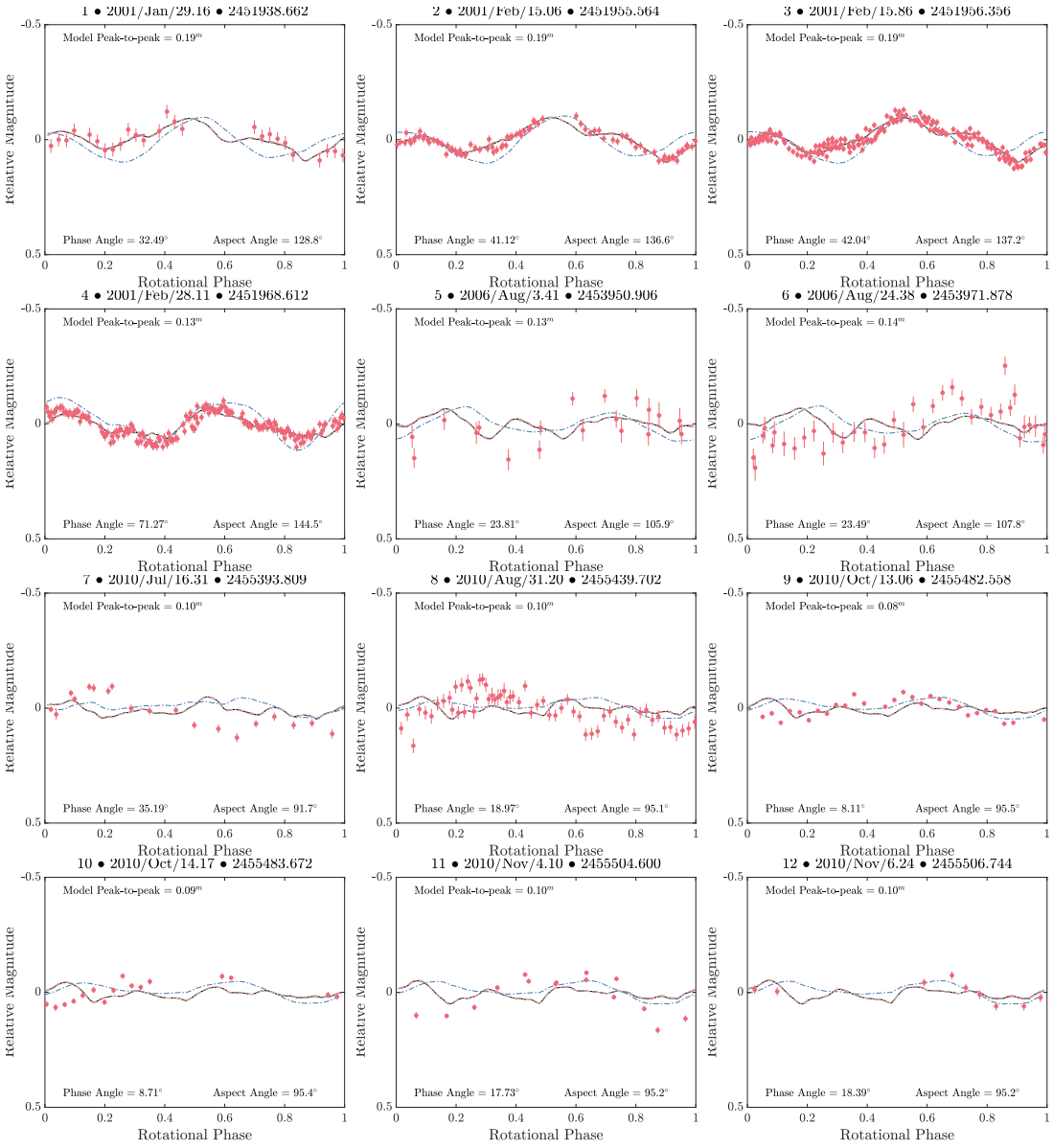

Figure A.1: Light curves of asteroid (29075) 1950 DA compared to synthetic light curves generated with the Busch prograde model. T_0 was set the epoch of the 2001 light curves and propagated forward using a constant period of 2.1216 hours. The numbered light curves correspond to those listed in Table 4.1. The blue dash dot line is the artificial light curve generated using the Lambertian scattering law. The red dashed line was generated with the Lommel Seeliger scattering law. The black solid line was generated using the Kaasalainen scattering law. Finally, the red dots show the observed light curves.

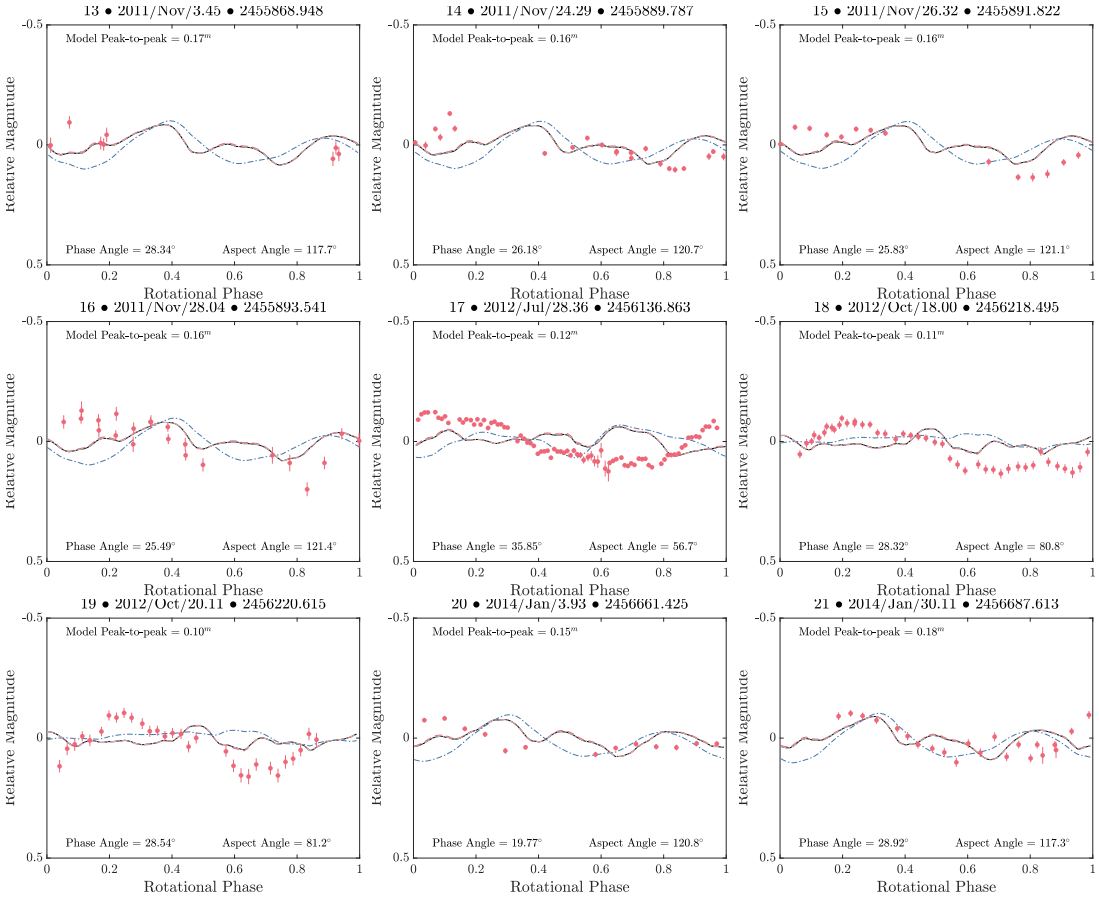

Figure A.1: (Continued.)

Direction cosines of PAs with respect to body axes				Ratio of moments of inertia to maximum moment of inertia
	x	y	z	
PA1	0.996415	-0.084589	-0.001556	0.226285
PA2	0.084601	0.996352	0.011208	1.000000
PA3	0.000602	-0.011300	0.999936	0.951949
Angular offset between PA and body axes [deg]				
PA1 & x = 4.853186		PA2 & y = 4.895571		PA3 & z = 0.648350

Table A.1: A summary of the vertex shape model's moments of inertia and the alignment of the PAs to the model's body-centric axes. This table contains a description of: the direction of the cosines of each PA to each body-centric axis, this matrix transforms the body-centric axes to PAs (if these were perfectly aligned: PA1 = 1, 0, 0; PA2 = 0, 1, 0; PA3 = 0, 0, 1); the ratio of the moment of inertia for each axis to the axis with the maximum moment of inertia; and the angular offset between each PA and its closest body-centric axes. A interpretation of the moments of inertia is discussed in Sect. 5.3.2.

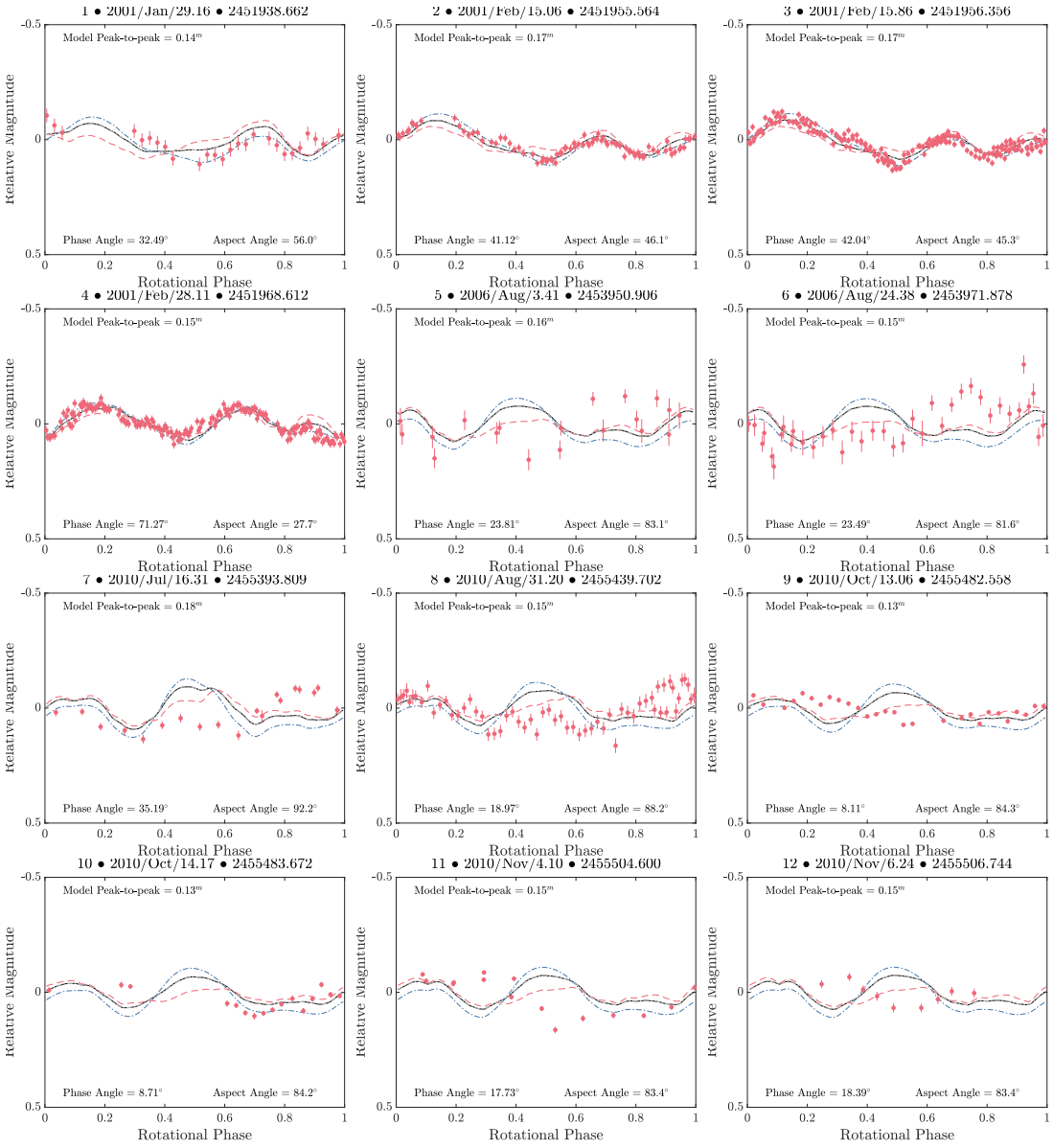

Figure A.2: Light curves of asteroid (29075) 1950 DA compared to synthetic light curves generated with the Busch retrograde model. T_0 was set the epoch of the 2001 light curves and propagated forward using a constant period of 2.1216 hours. The numbered light curves correspond to those listed in Table 4.1. The blue dash dot line is the artificial light curve generated using the Lambertian scattering law. The red dashed line was generated with the Lommel Seeliger scattering law. The black solid line was generated using the Kaasalainen scattering law. Finally, the red dots show the observed light curves.

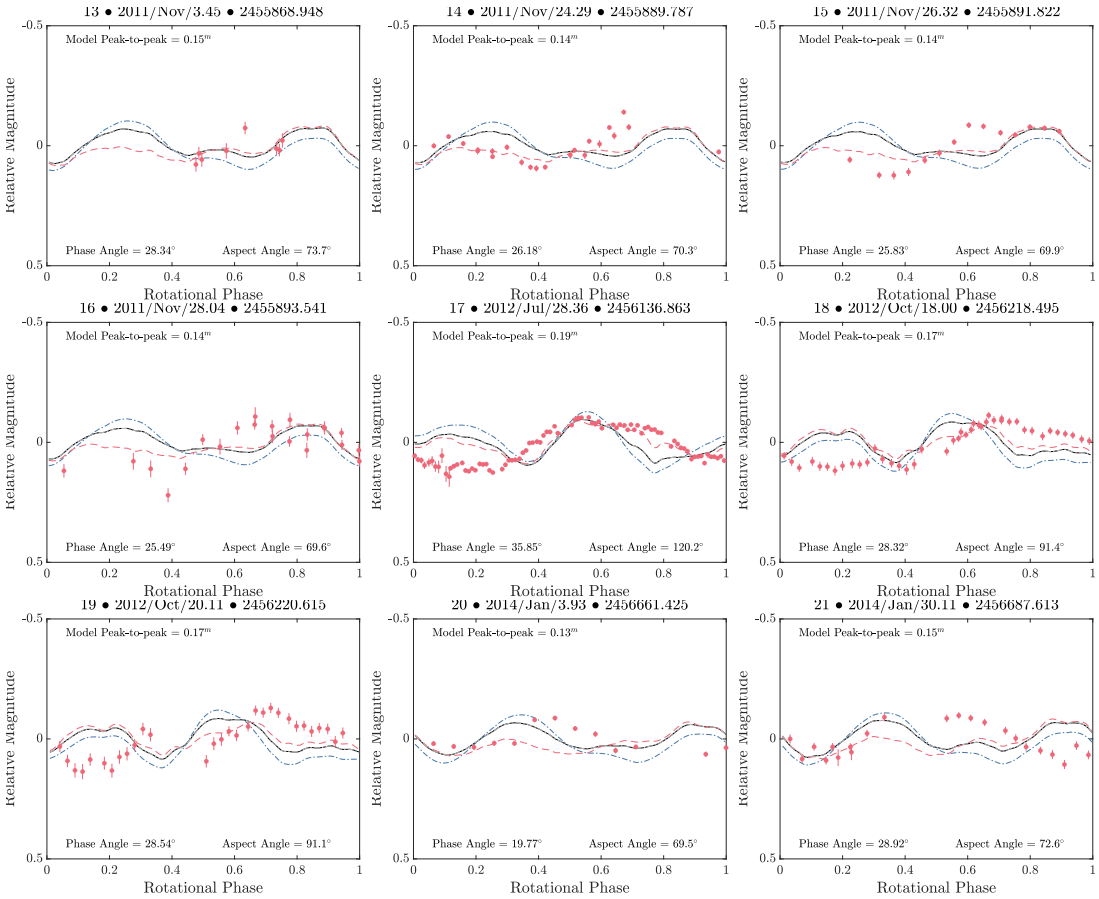

Figure A.2: (Continued.)

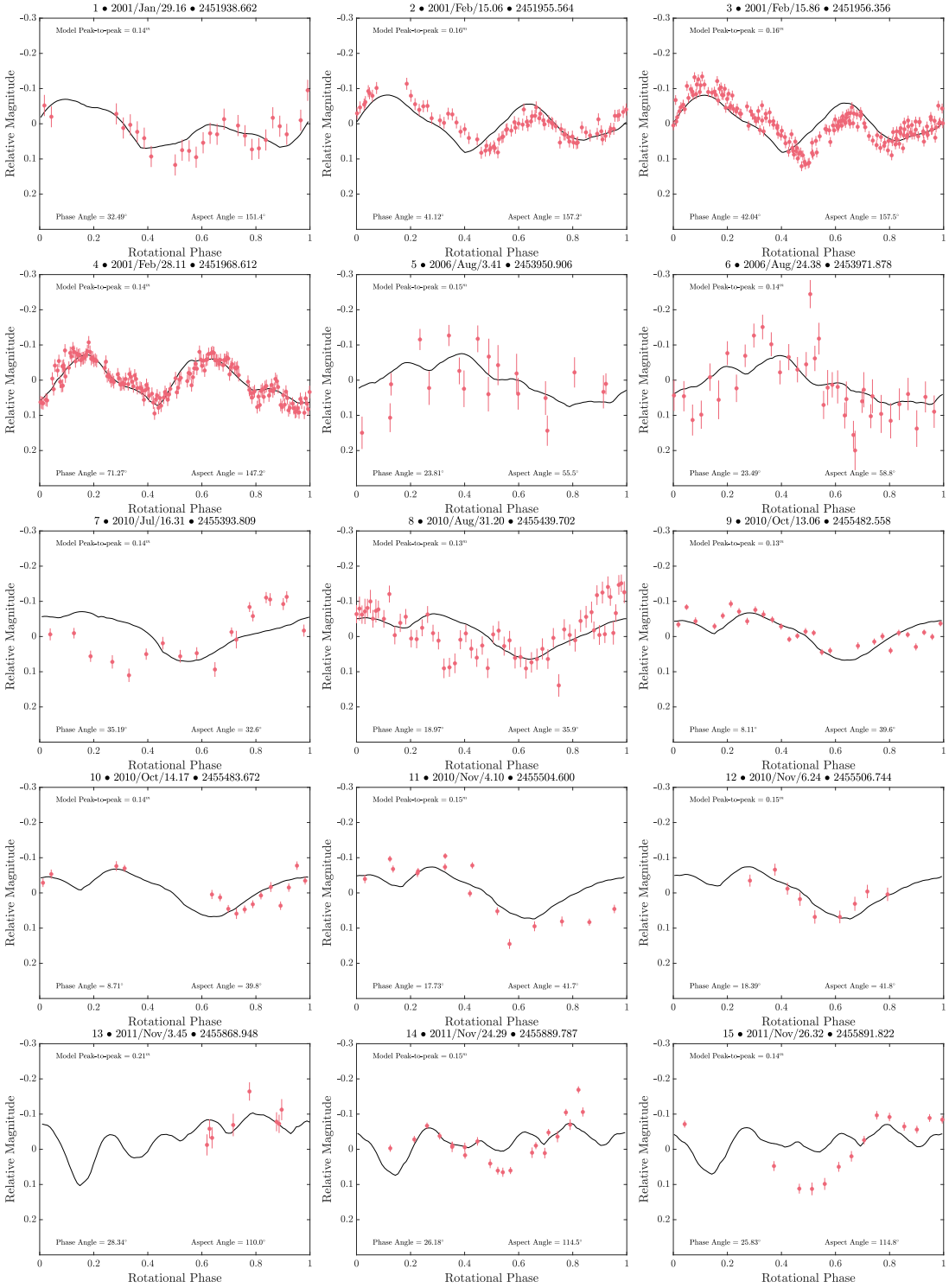

Figure A.3: Light curves of asteroid (29075) 1950 DA compared to synthetic light curves generated with the `convexinv` model (see Fig. 4.9). The numbered light curves correspond to those listed in Table 4.1. The black solid line was generated using the Kaasalainen scattering law and the red dots show the observed light curves.

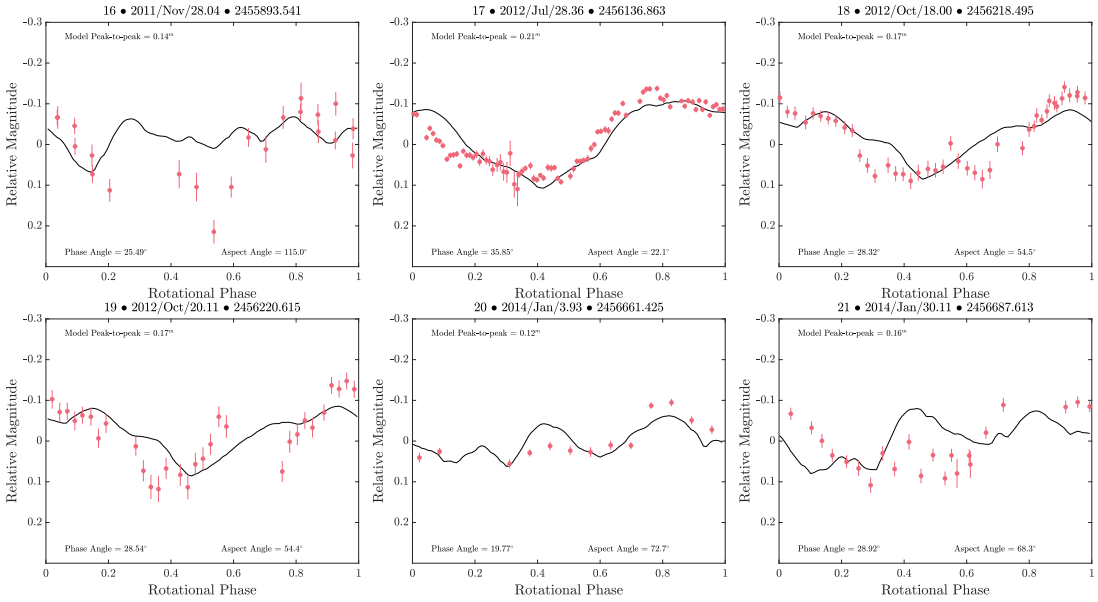

Figure A.3: (Continued.)

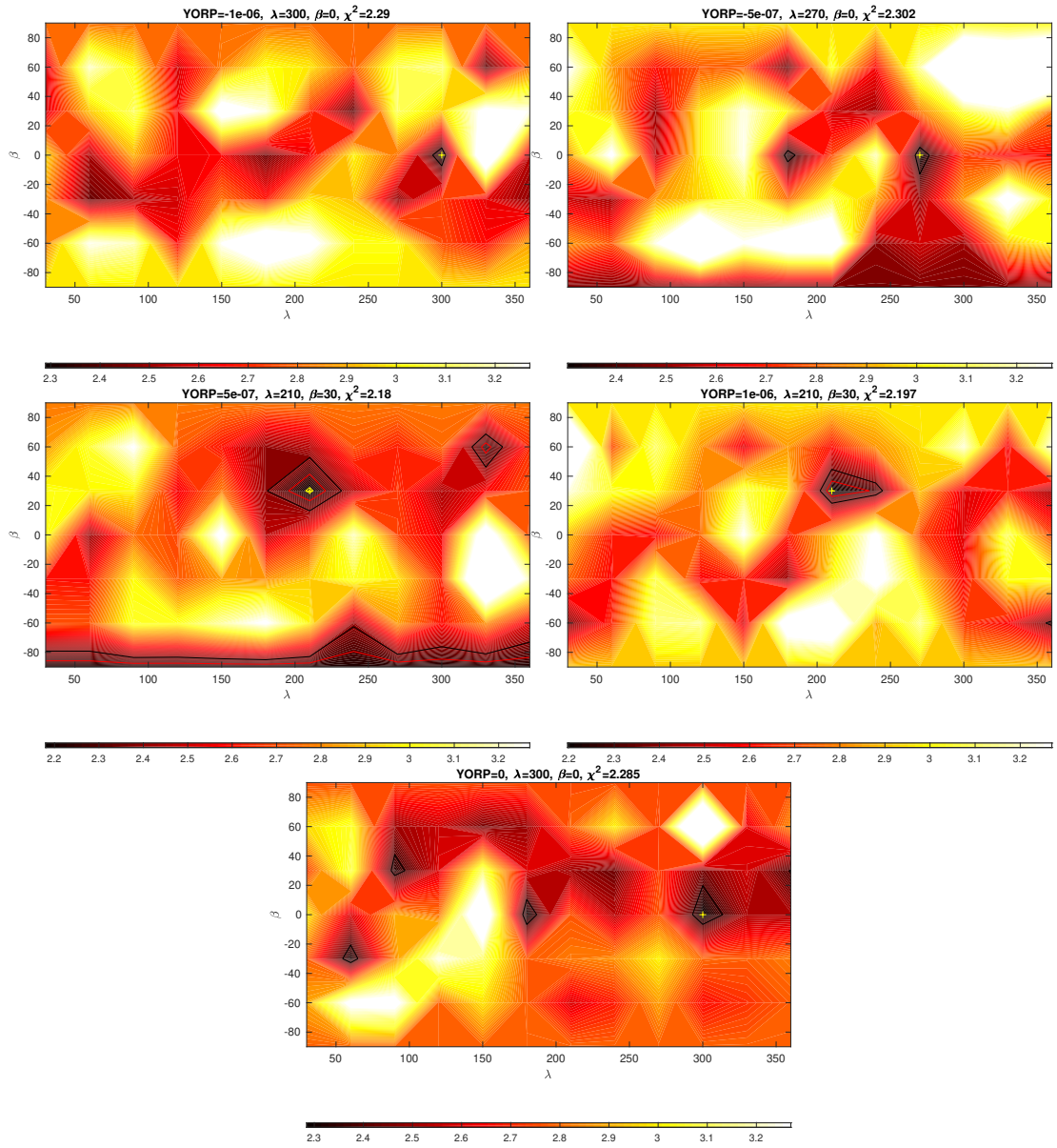

Figure A.4: Results from the SHAPE global scan for asteroid (29075) 1950 DA. The scan convered the entire celestial sphere with a resolution of 30° × 30°. The scan was performed utilising both radar data and optical light curves from 2001 to 2014. Displayed is the chi-squared value from the optimisation of the asteroid's shape, rotation period, and initial rotation phase. Darker colours indicate a better fit to the data, as shown by the colour bar at the bottom, and the best solution is marked by a yellow cross.

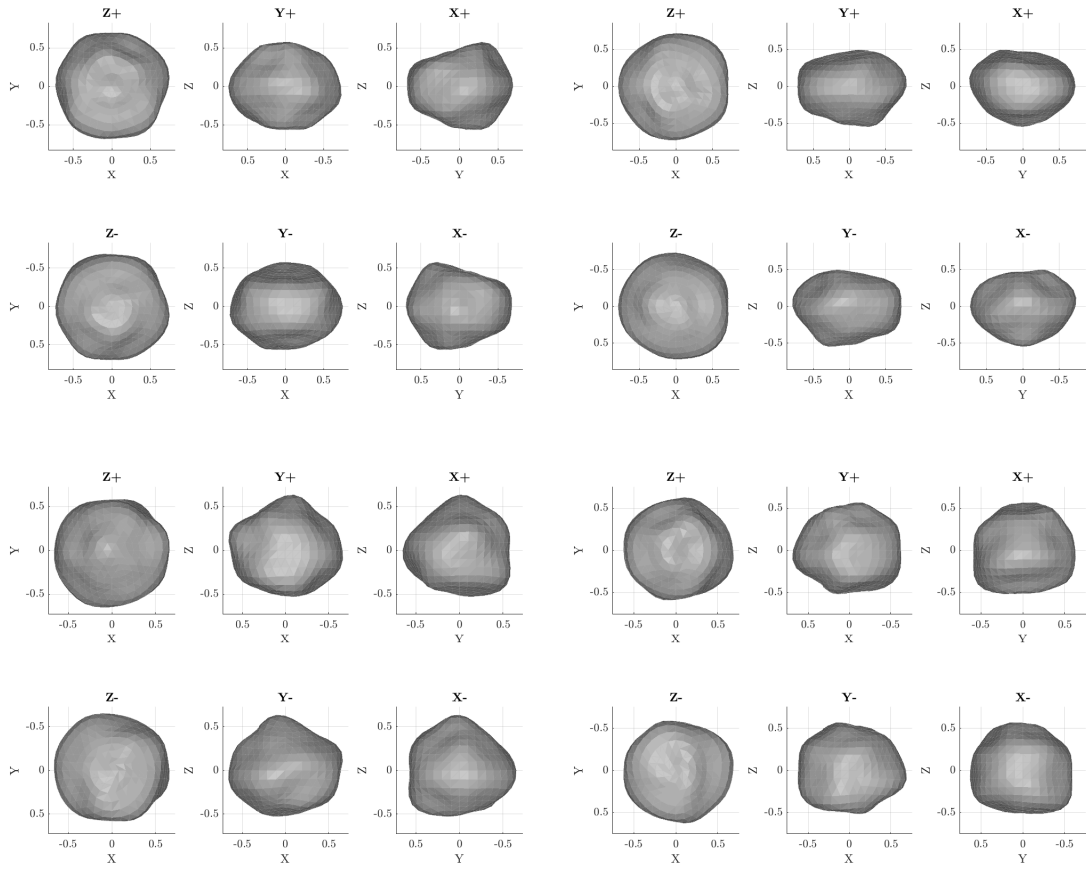

Figure A.5: Additional YORP plane models from the extended YORP scan of (29075) 1950 DA. These figures the best-fit shape model for four YORP planes: 9.75×10^{-7}, 5.00×10^{-7}, -1.203×10^{-6}, and -1.541×10^{-6}rad/d^2 (respectively from left to right, top to bottom).

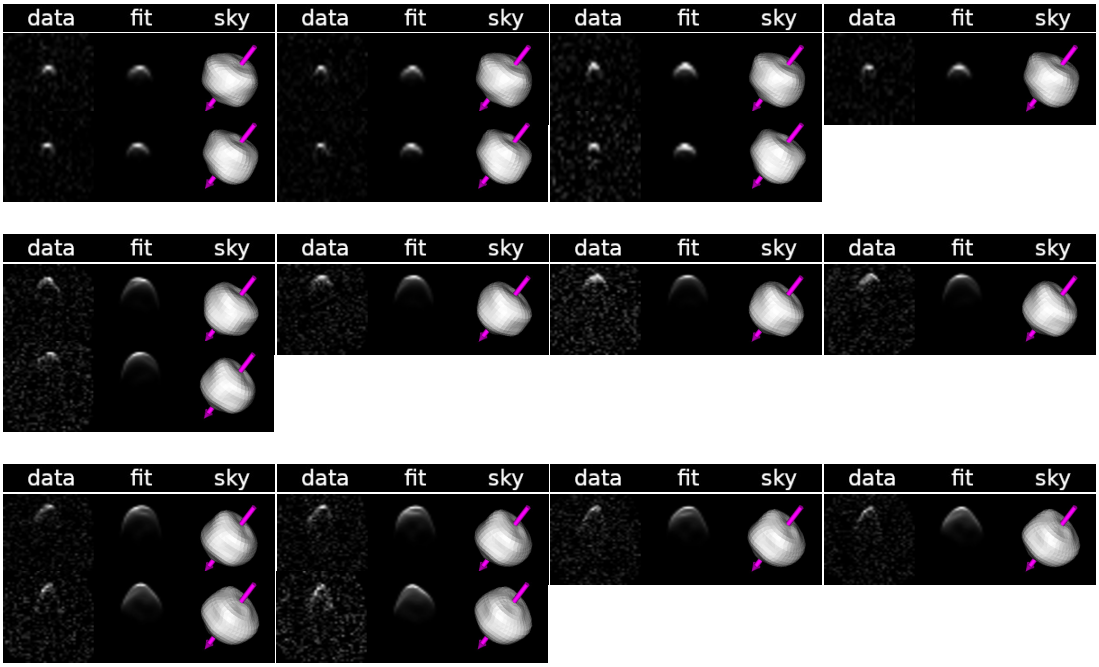

Figure A.6: Fit of the best-fit spherical harmonic model of asteroid (29075) 1950 DA to the radar data. Each three-image sub-panel is comprised of: the observational data (left panel), synthetic echo (middle panel), and plane-of-sky projection of the best-fit model (right panel). On the data and synthetic-echo images the delay increases downwards and the frequency (Doppler) to the right. The plane-of-sky images are orientated with celestial north (in equatorial coordinates) to the top and east to the left. The rotation vector (Z-axis of body-fixed coordinate system) is marked with a pink arrow. This sequence of images corresponds to multiple sets of Goldstone data collected on 3 March 2001.

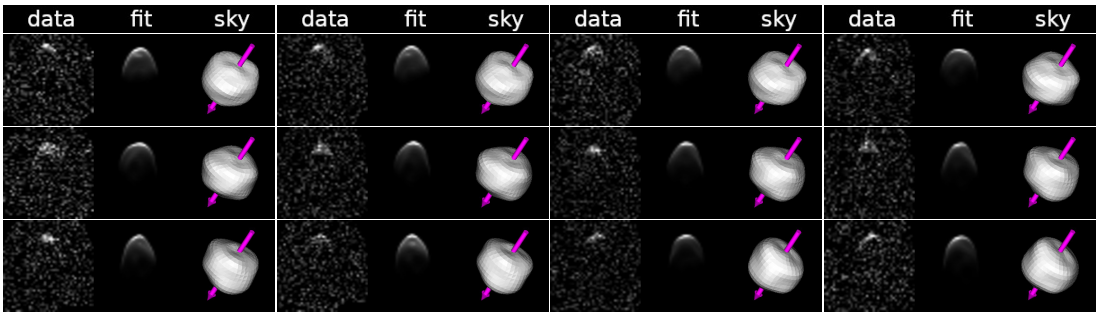

Figure A.7: Same as Fig. A.6 for the night of 4 March 2001.

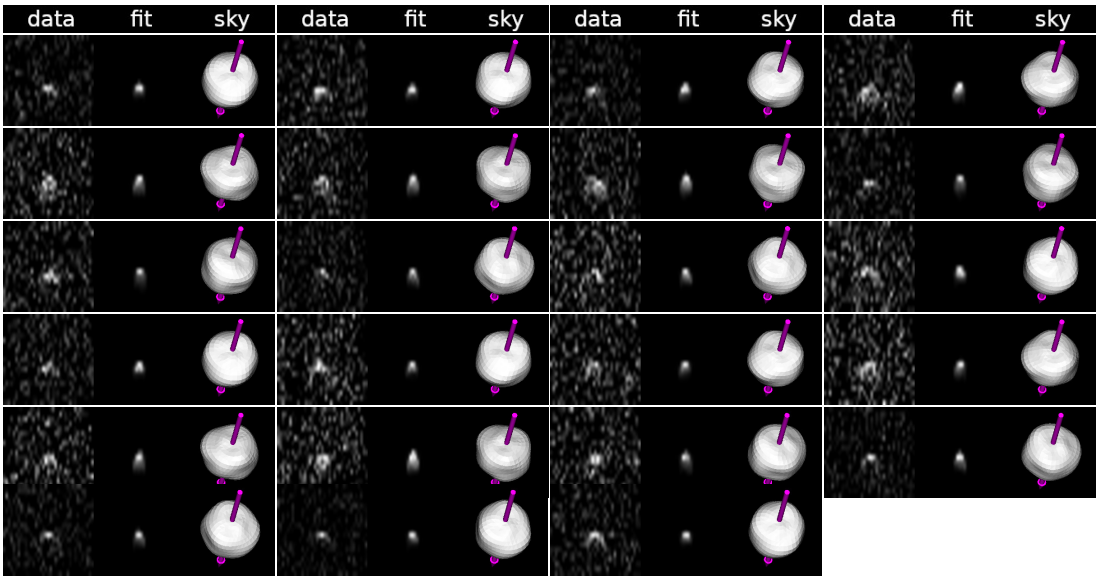

Figure A.8: Same as Fig. A.6 for the night of 7 March 2001.

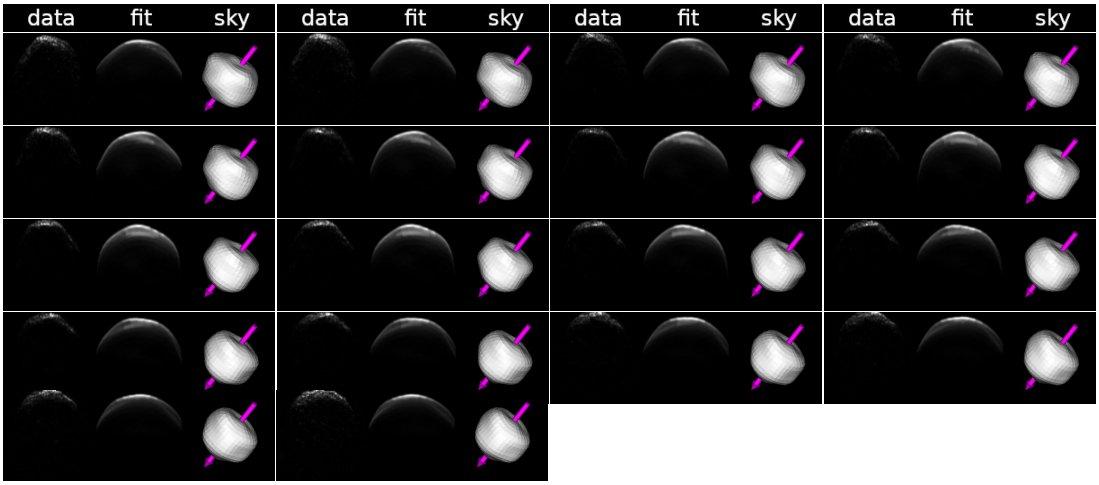

Figure A.9: Same as Fig. A.6, but for Arecibo data taken on the night of 3 March 2001.

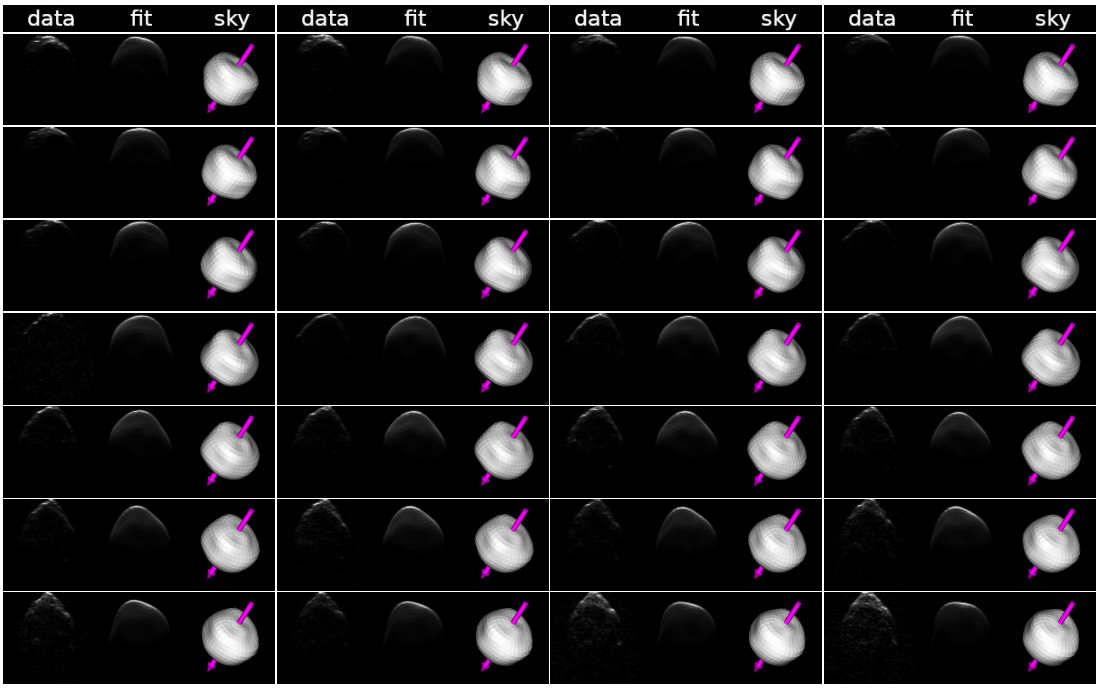

Figure A.10: Same as Fig. A.6, but for Arecibo data taken on the night of 4 March 2001.

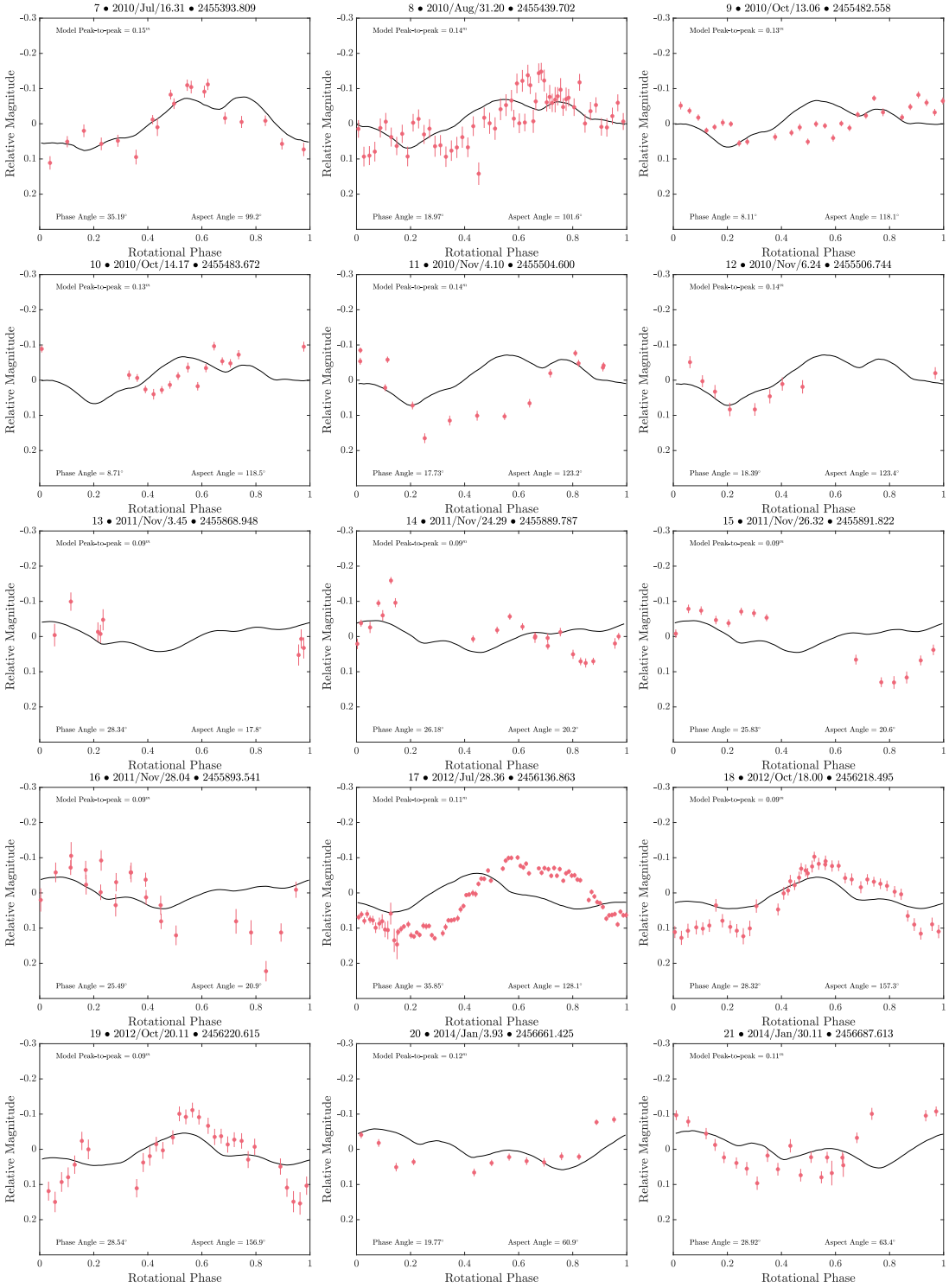

Figure A.11: Light curves of asteroid (29075) 1950 DA compared to synthetic light curves generated with the spherical harmonic model with a YORP strength $\nu = (-2.0 \pm 0.1) \times 10^{-5} rad/d^2$. The light curves generated are the post 2010, with the numbering starting at 7 to align with Table 4.1.

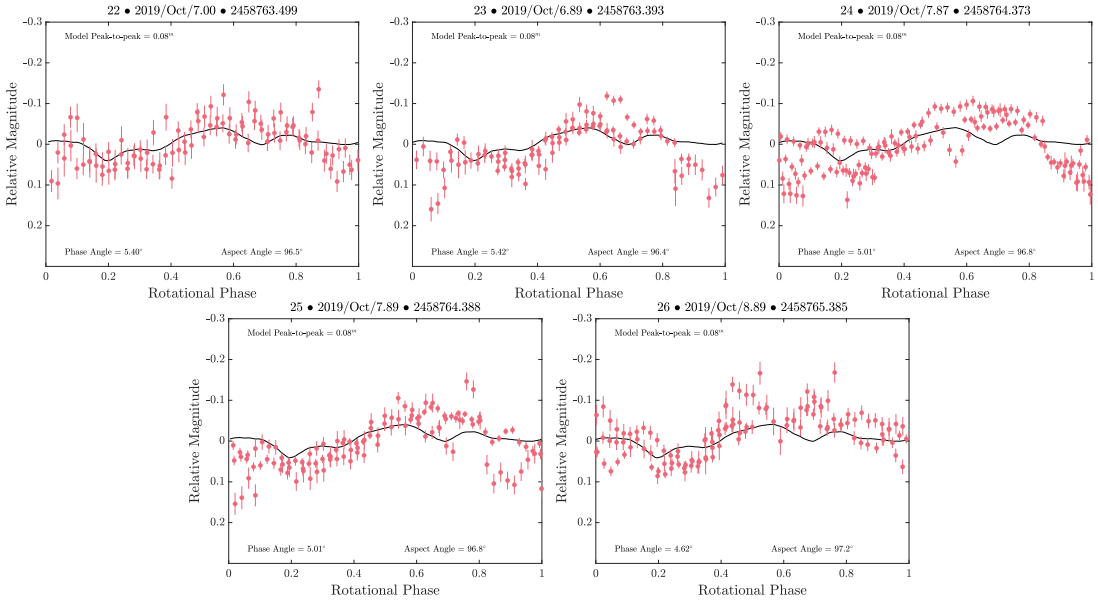

Figure A.11: (Continued.)

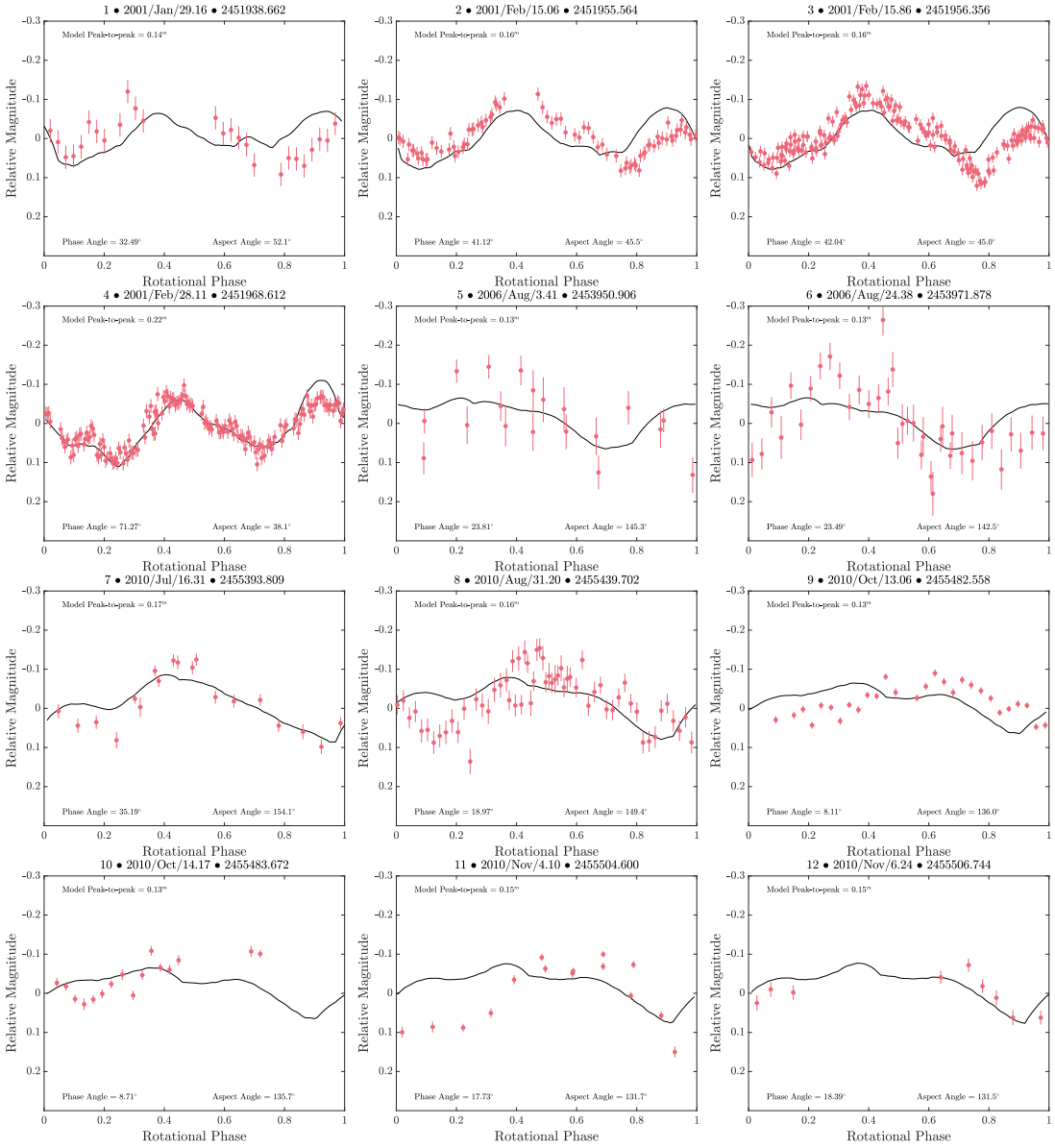

Figure A.12: Light curves of asteroid (29075) 1950 DA compared to synthetic light curves generated with the Busch prograde model. T_0 was set the epoch of the 2001 light curves and propagated forward using a constant period of 2.1216 hours. The numbered light curves correspond to those listed in Table 4.1. The blue dotted line is the artificial light curve generated using the Lambertian scattering law. The green dashed line was generated with the Lommel Seeliger scattering law. The black/red solid line was generated using the Kaasalainen scattering law. Finally, the red dots show the observed light curves.

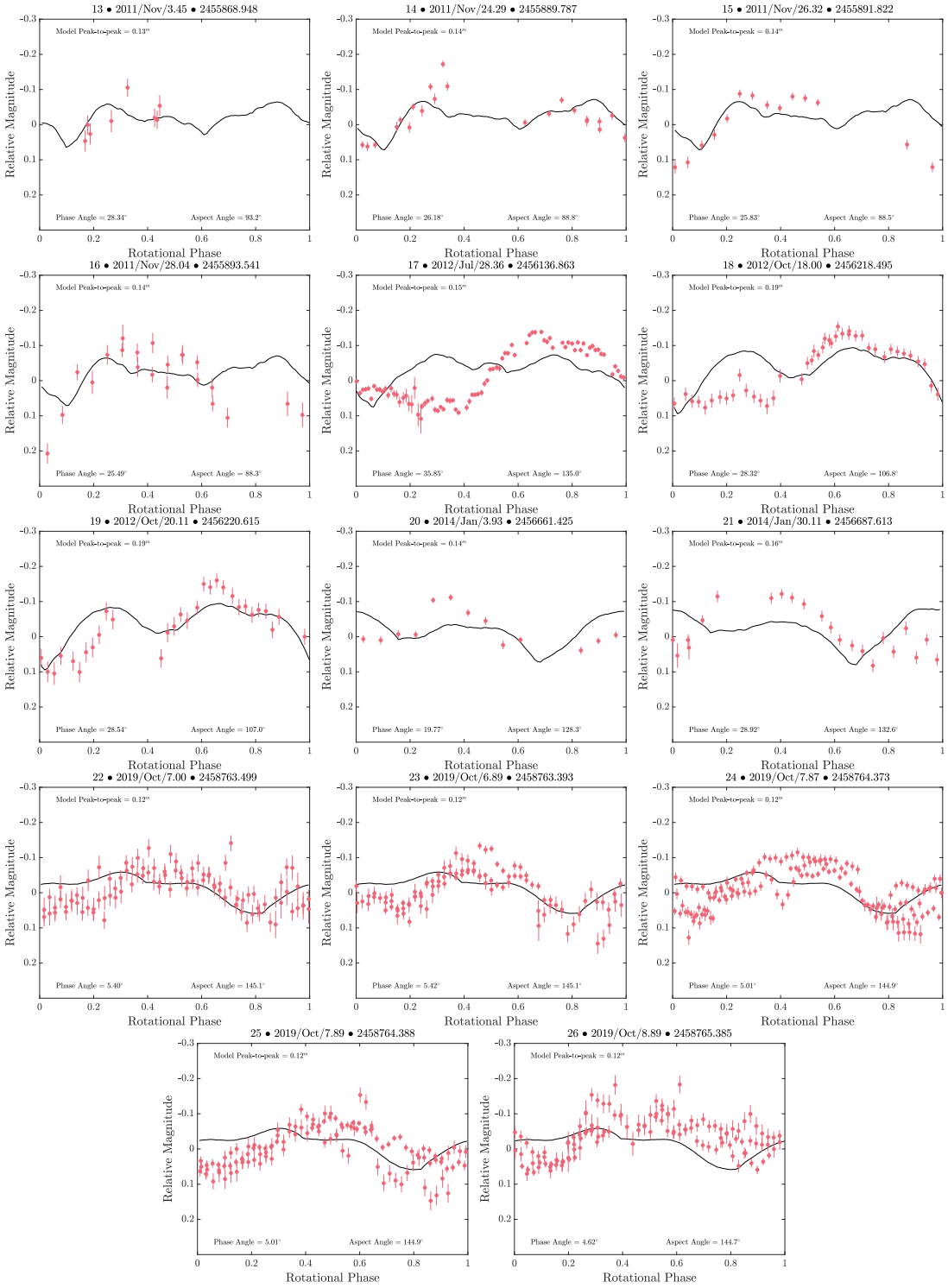

Figure A.12: (Continued.)

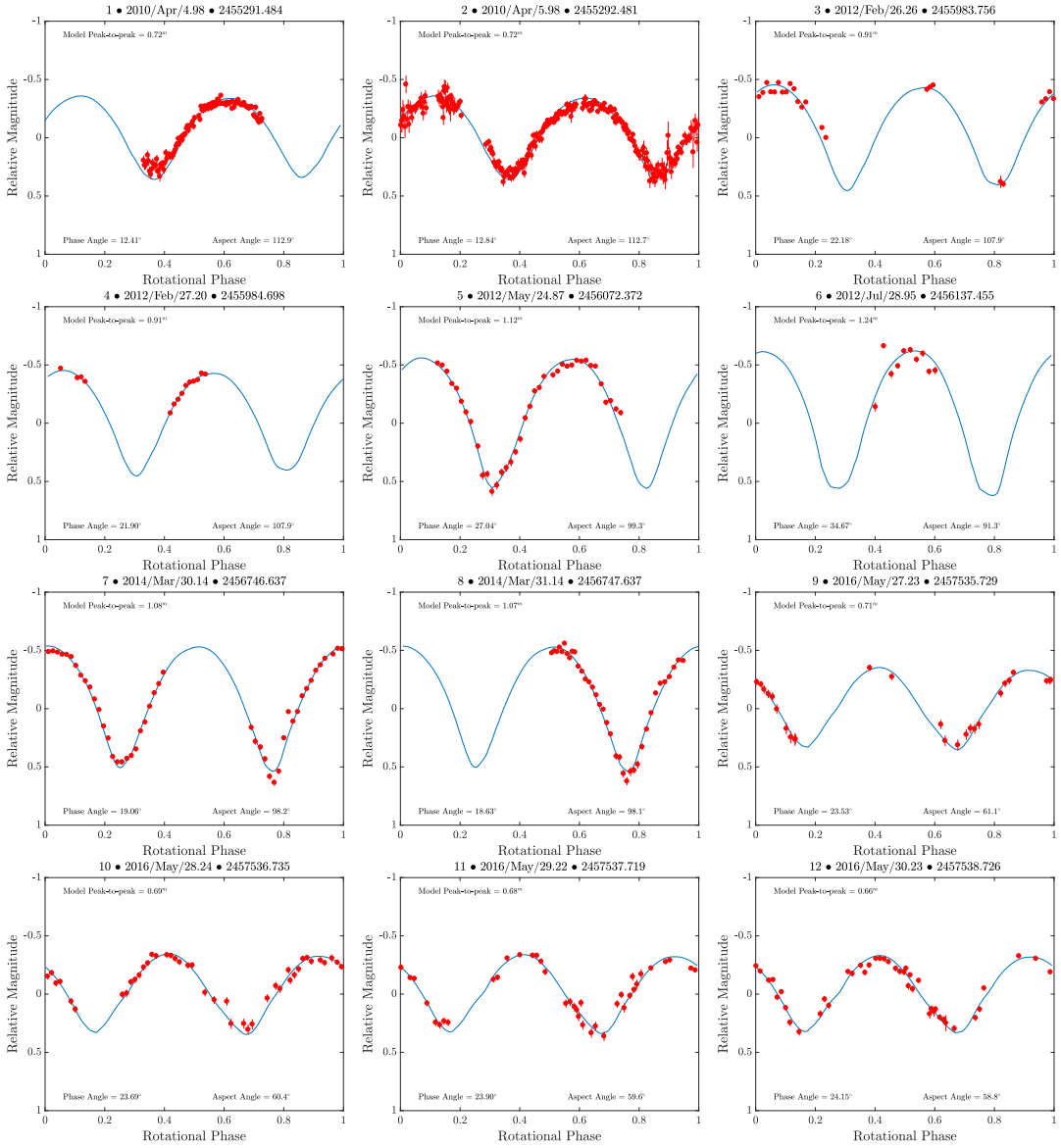

Figure A.13: Synthetic lightcurves generated with the convex-inversion shape model of asteroid (68346) 2001 KZ66 (blue lines) plotted over all available lightcurve data (red dots). Lightcurve details can be found in Table 5.2.1. The model summary is given in Table 5.4.

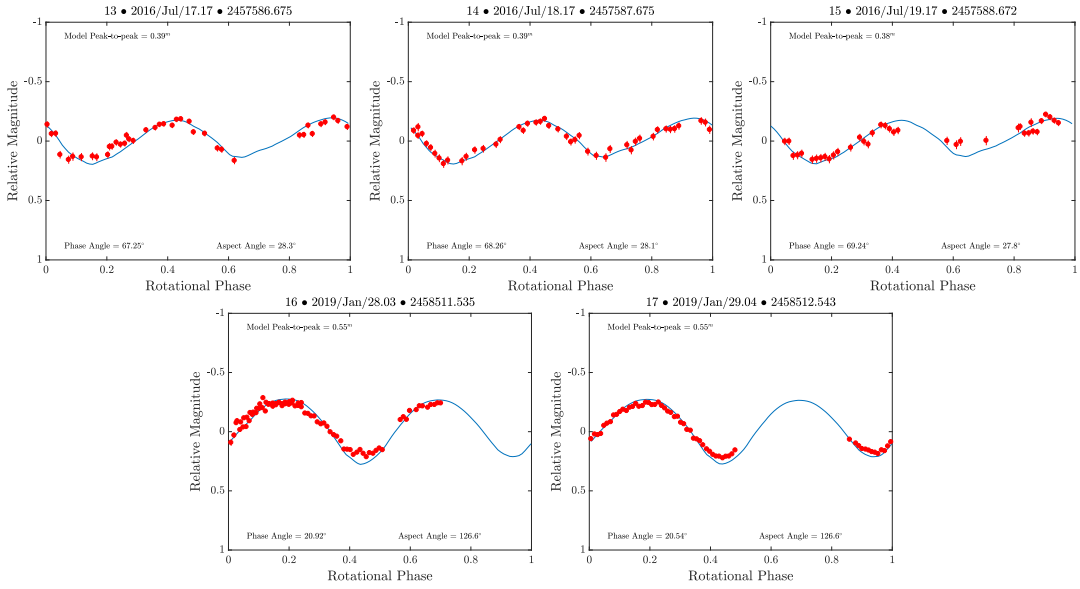

Figure A.13: (Continued.)

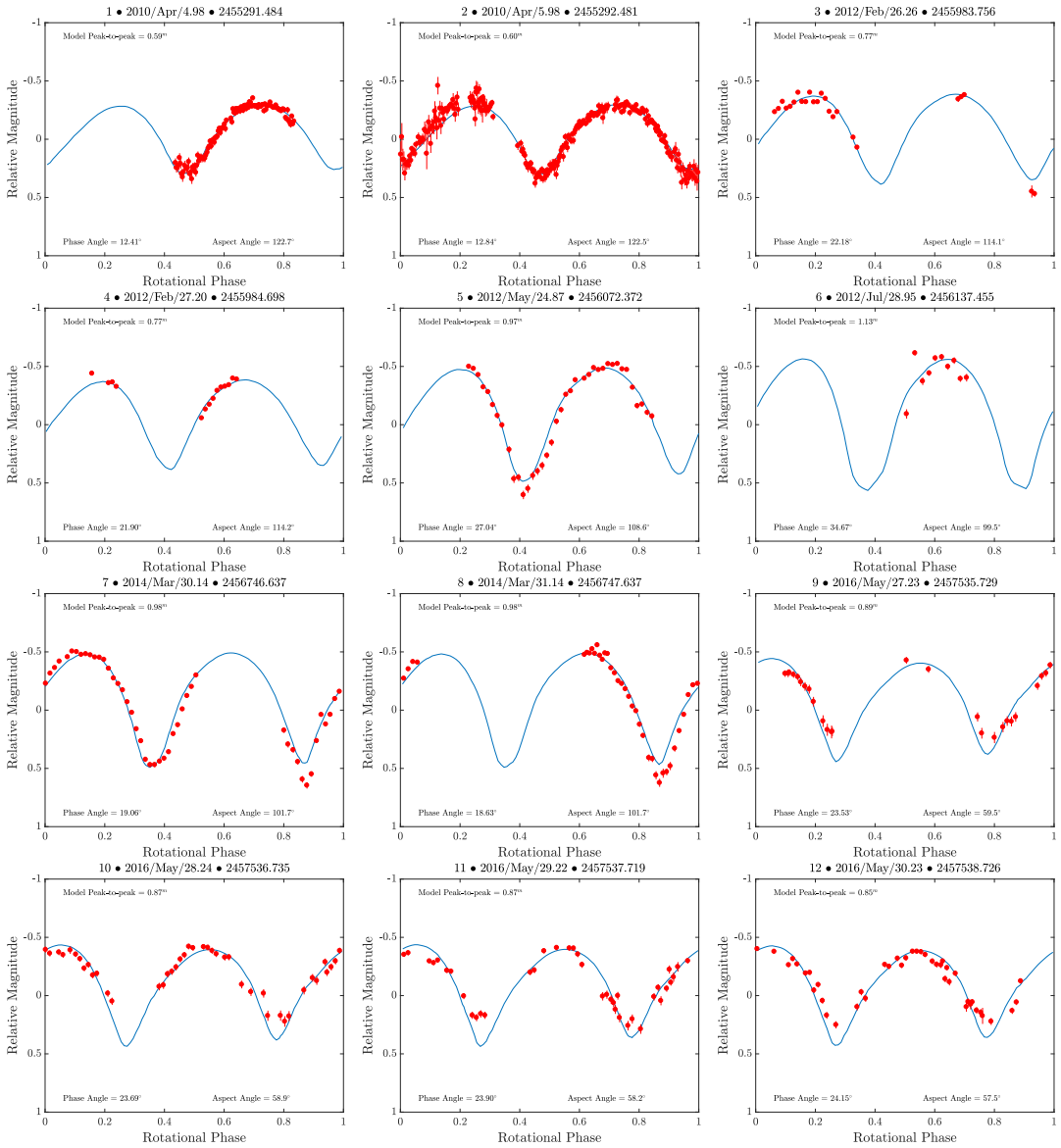

Figure A.14: Same as Fig. A.13, but for the radar-derived shape model with a YORP acceleration of 8.50×10^{-8}rad/day^2.

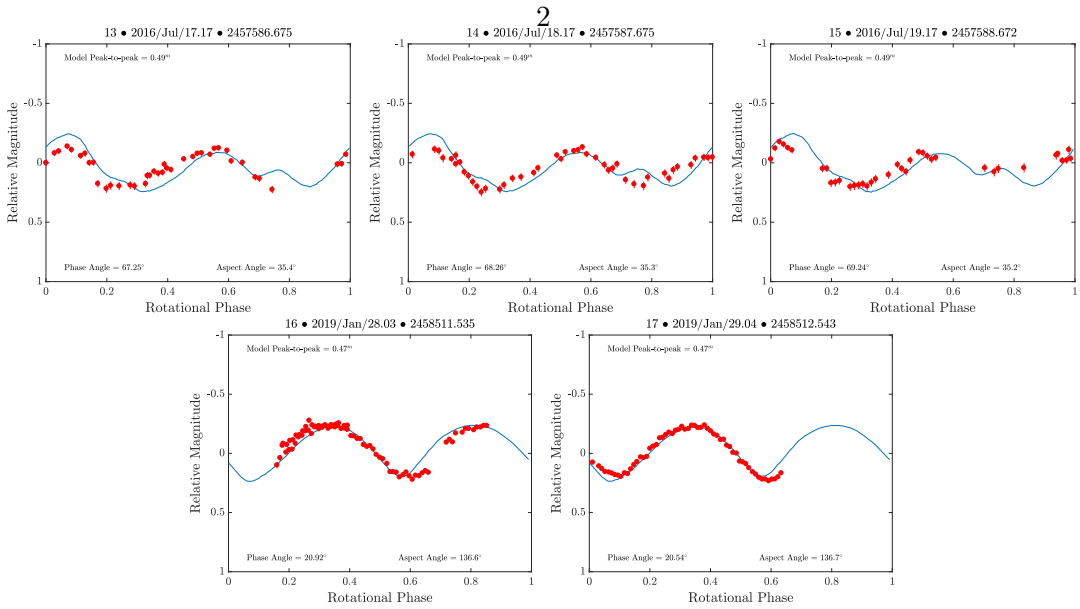

Figure A.14: (Continued.)

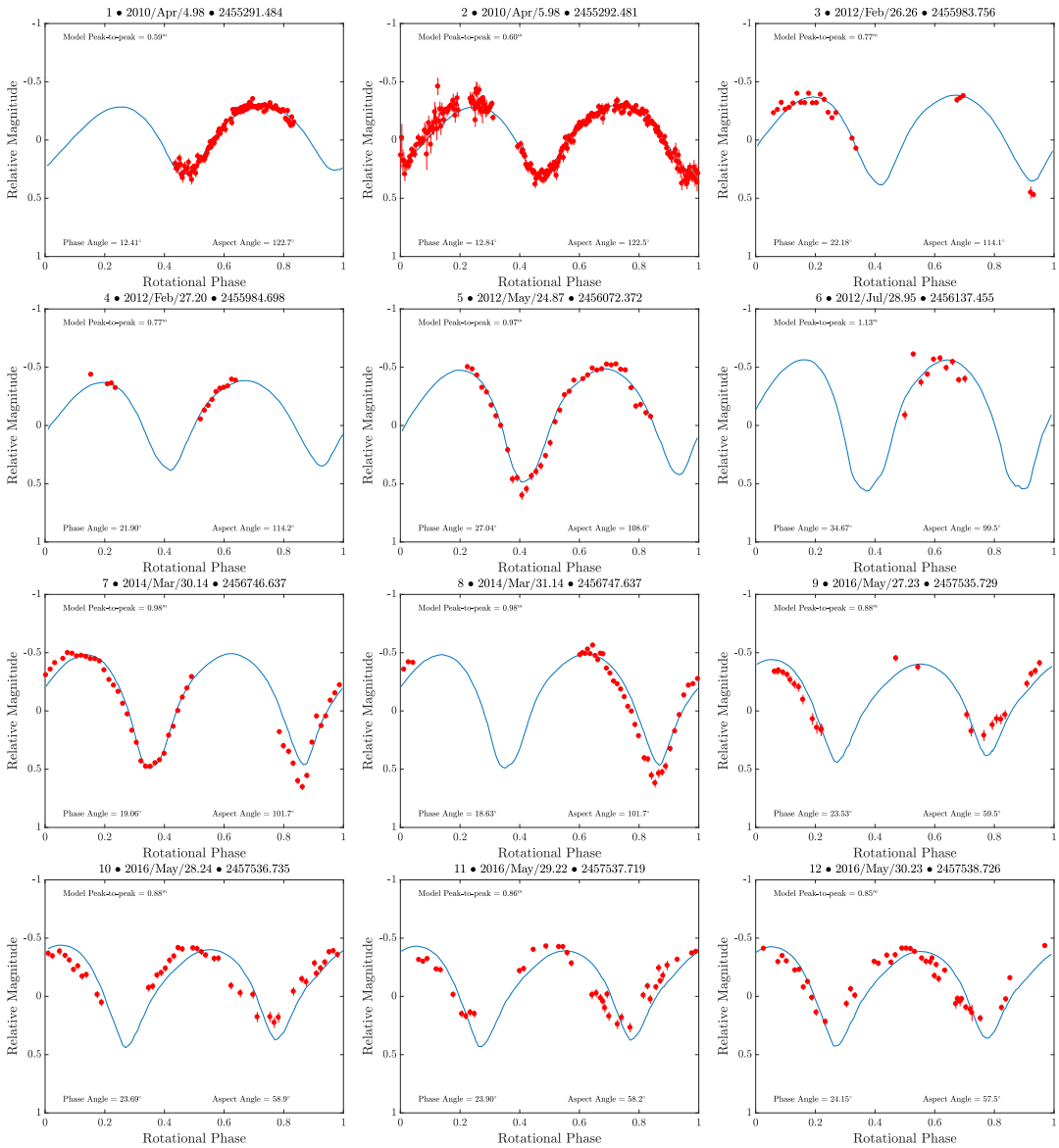

Figure A.15: Same as Fig. A.13, but for the radar-derived shape model with a constant period.

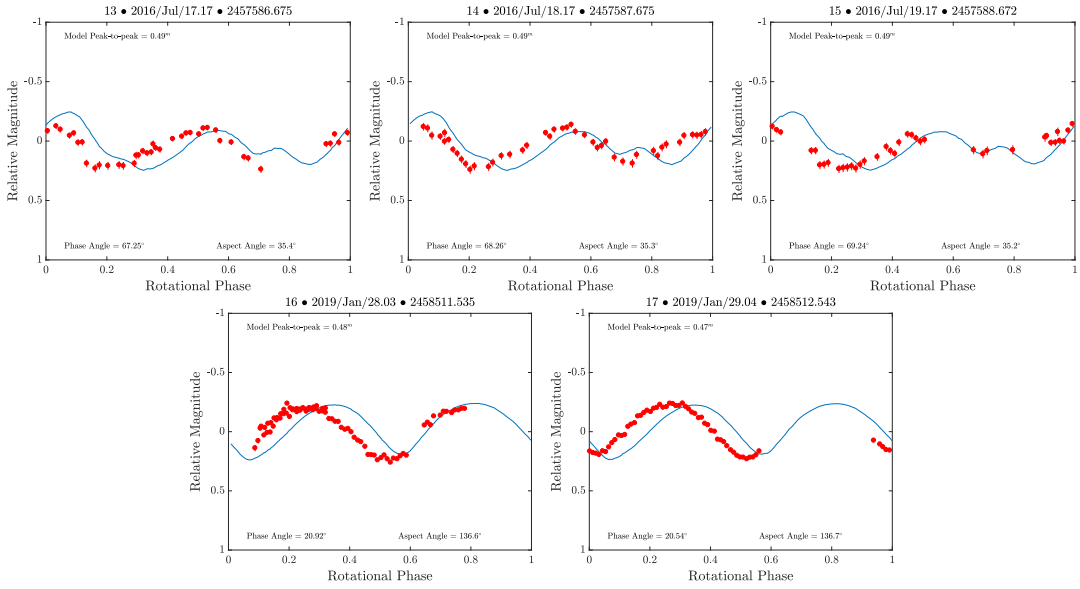

Figure A.15: (Continued.)

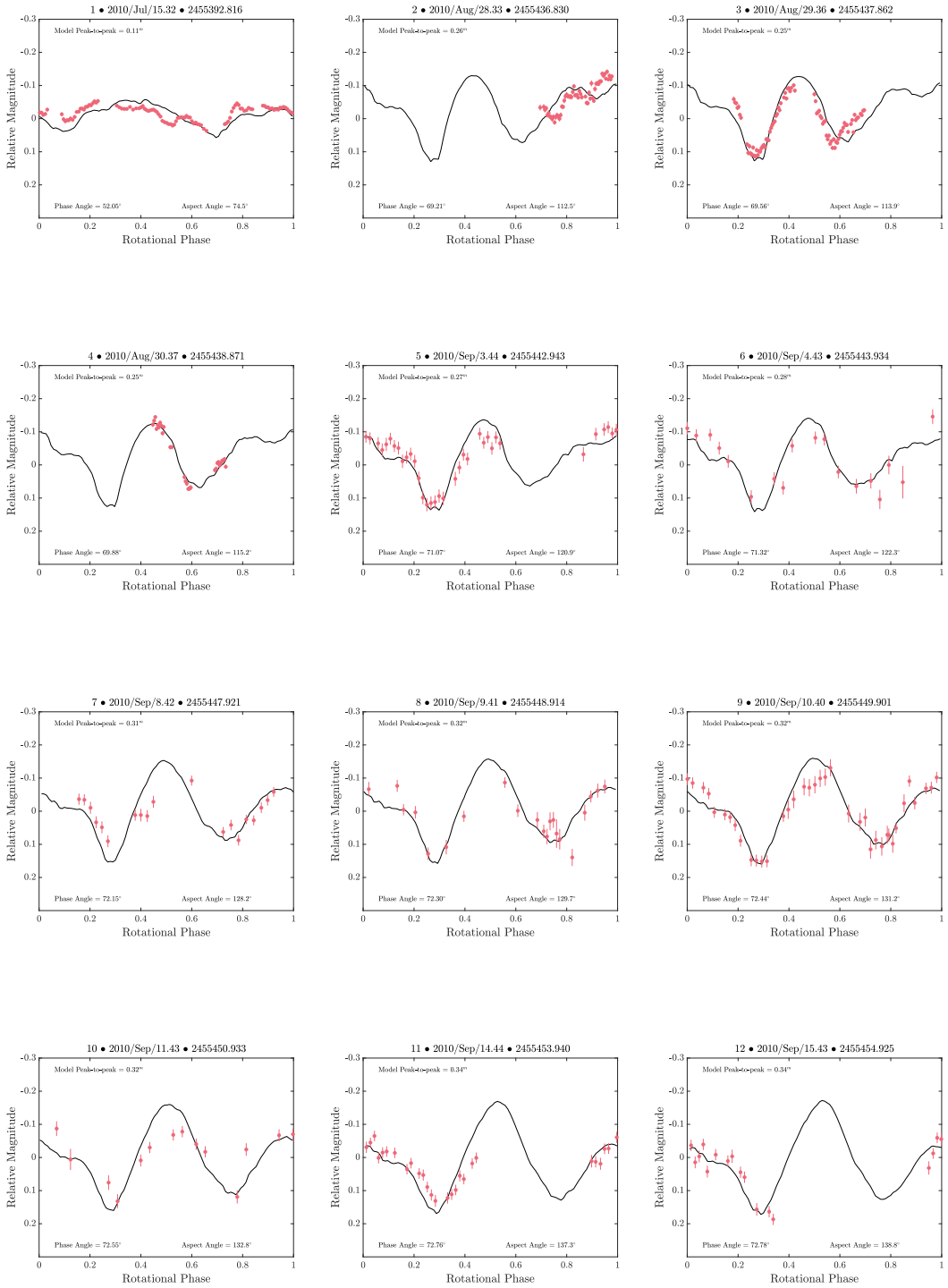

Figure A.16: Synthetic light curves from the `convexinv` Model A of (89830) 2002 CE with constant period.

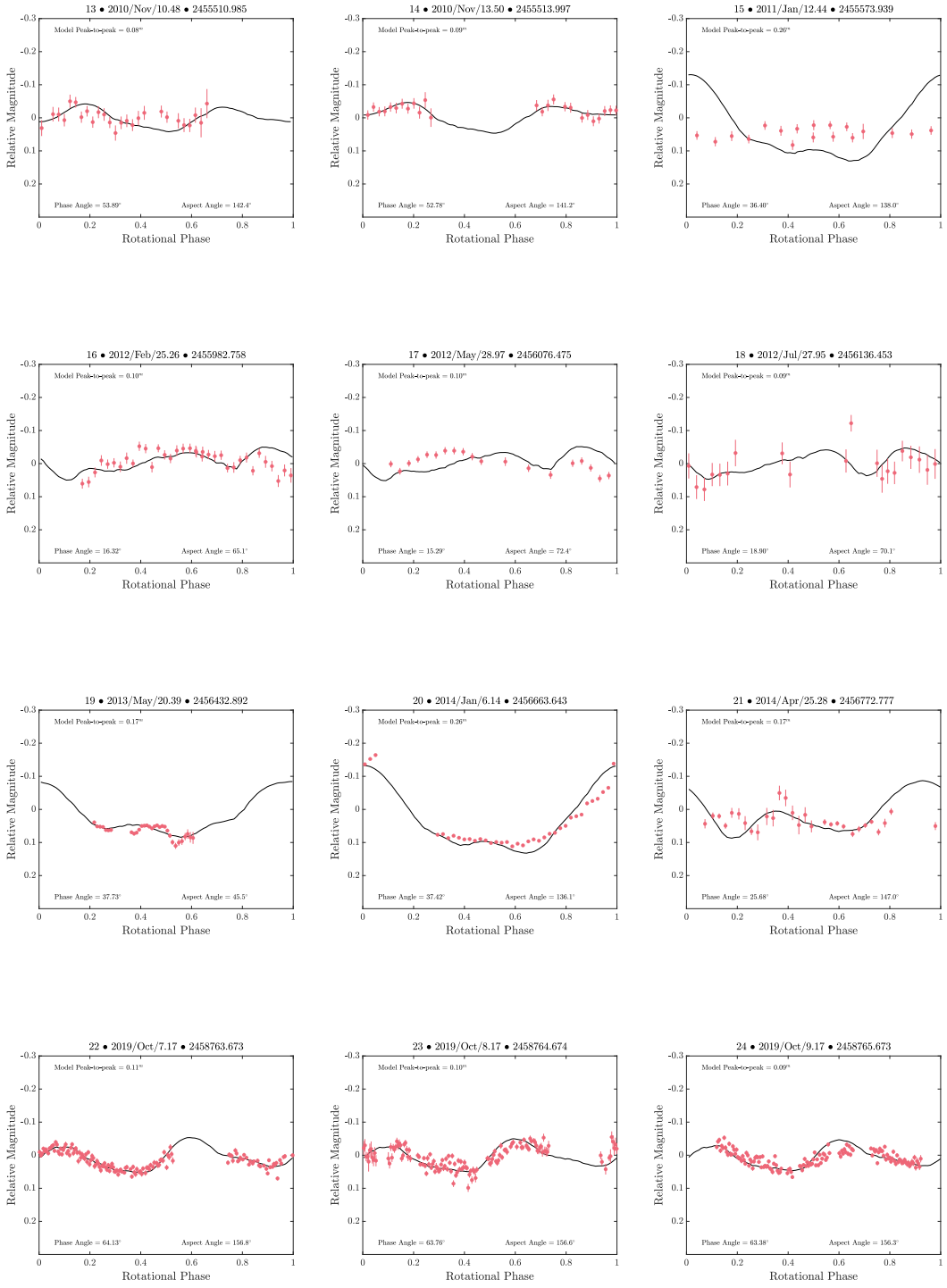

Figure A.16: (Continued.)

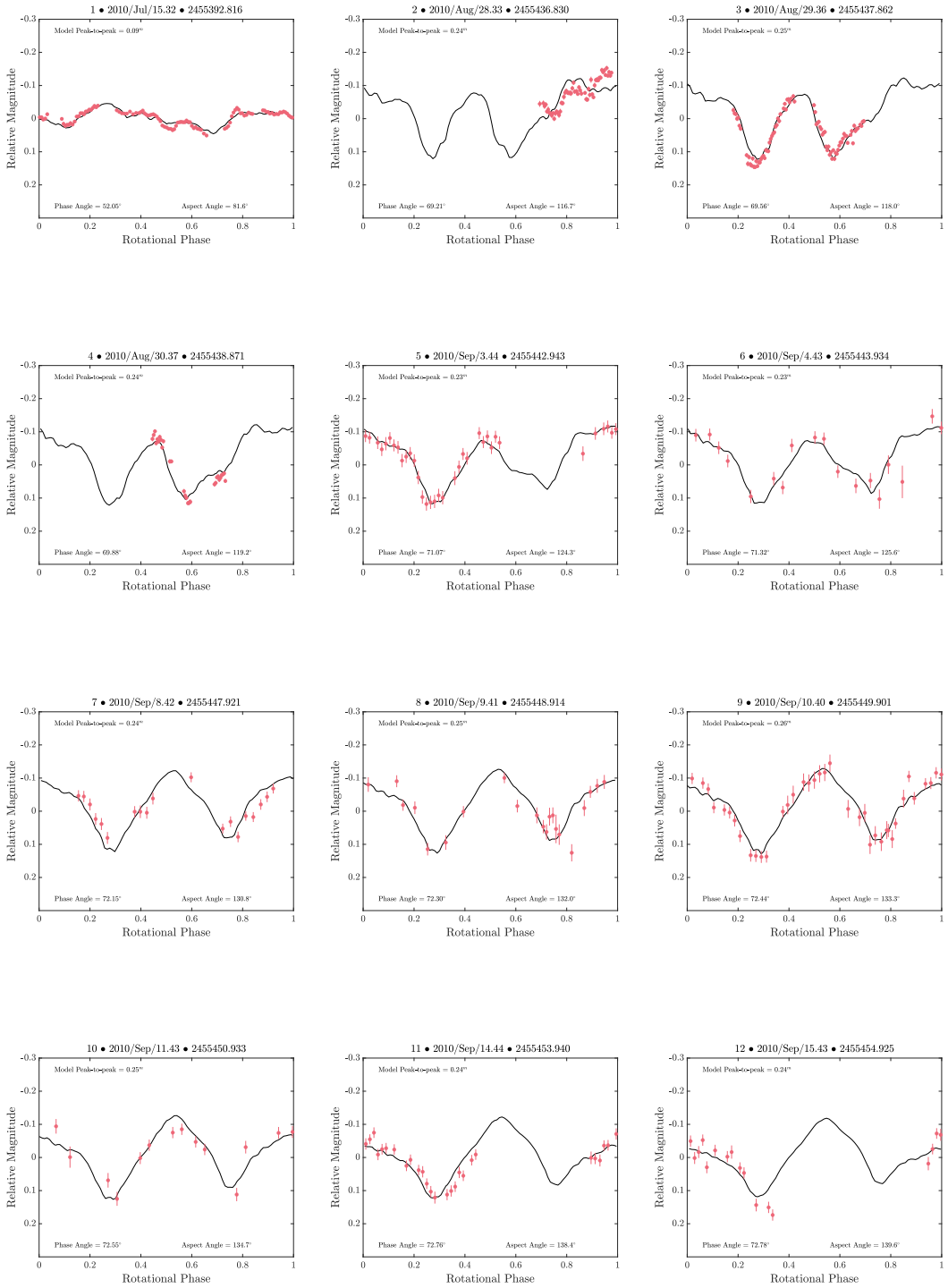

Figure A.17: Synthetic light curves from the `convexinv` Model B of (89830) 2002 CE with constant period.

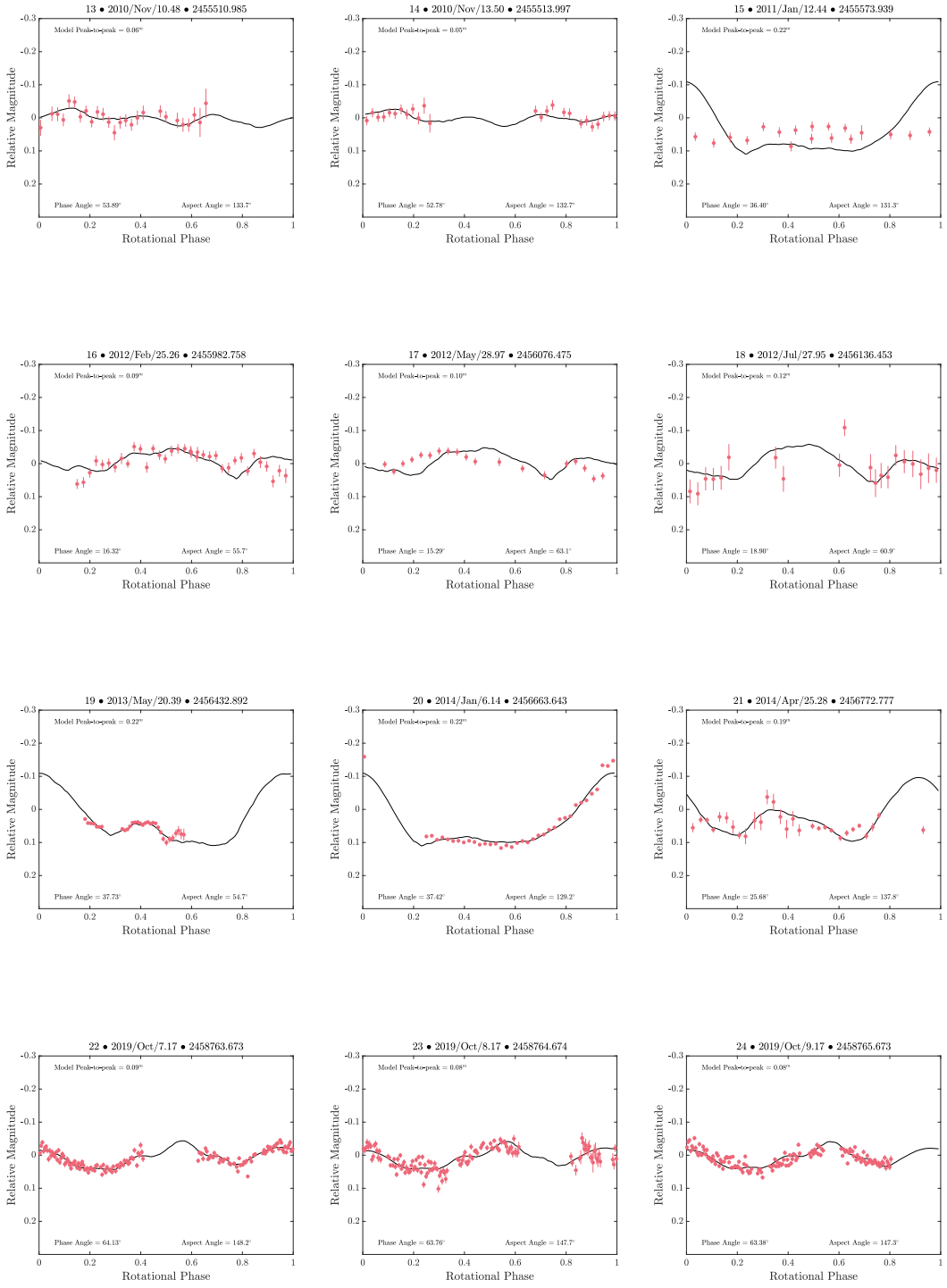

Figure A.17: (Continued.)

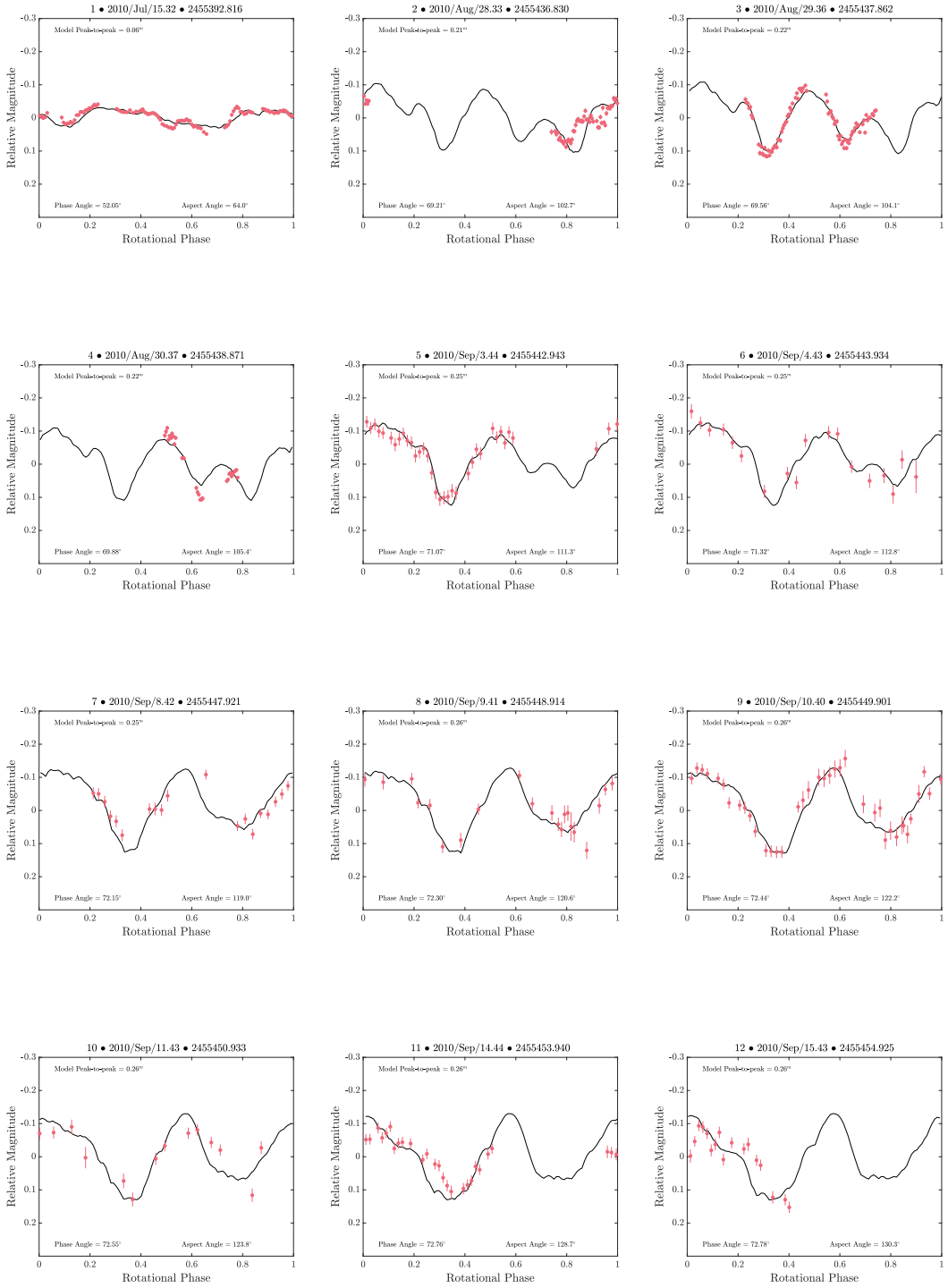

Figure A.18: Synthetic light curves from `convexinv` model of (89830) 2002 CE with YORP strength of -3.4×10^{-6}rad/day^2.

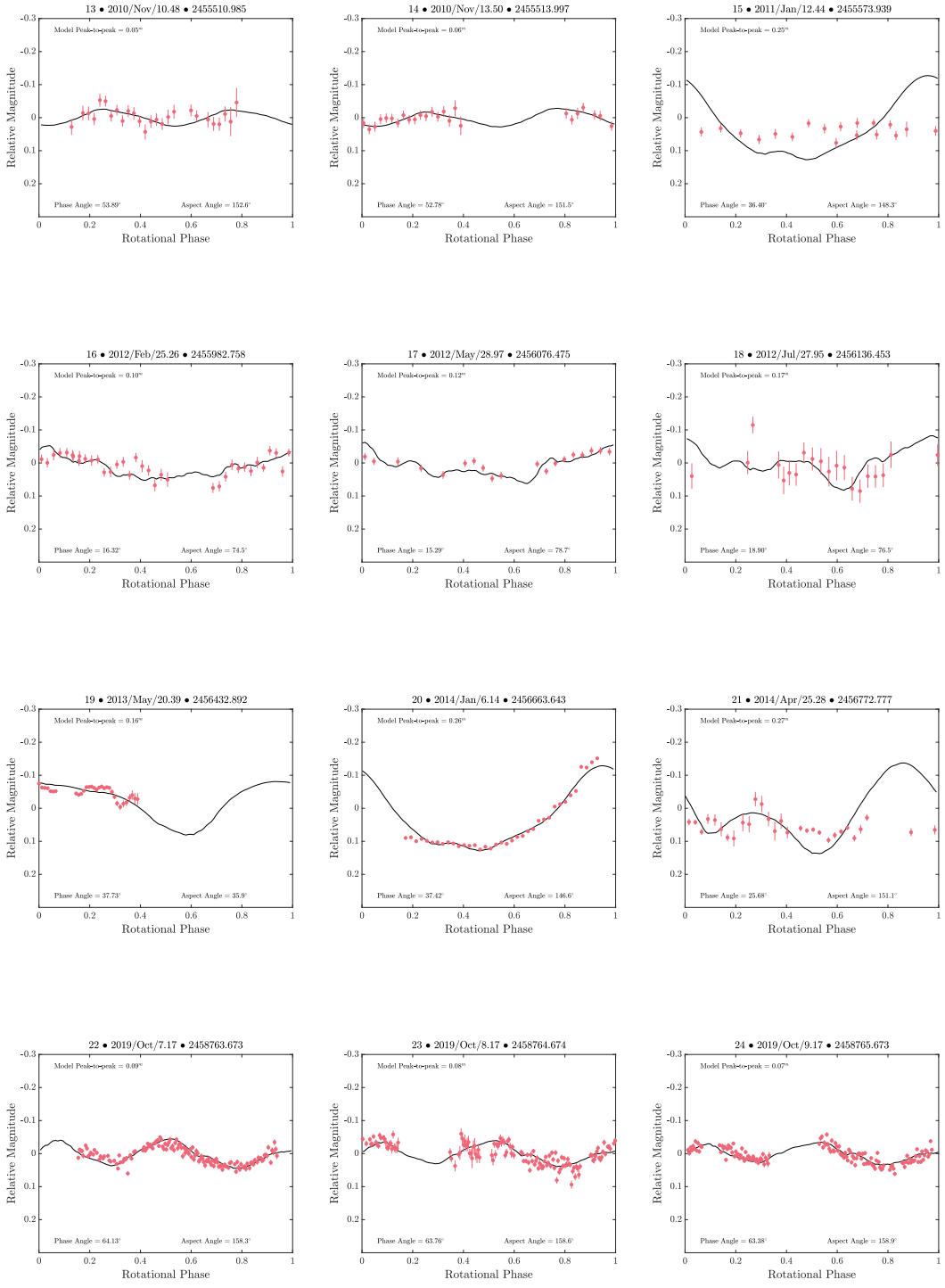

Figure A.18: (Continued.)

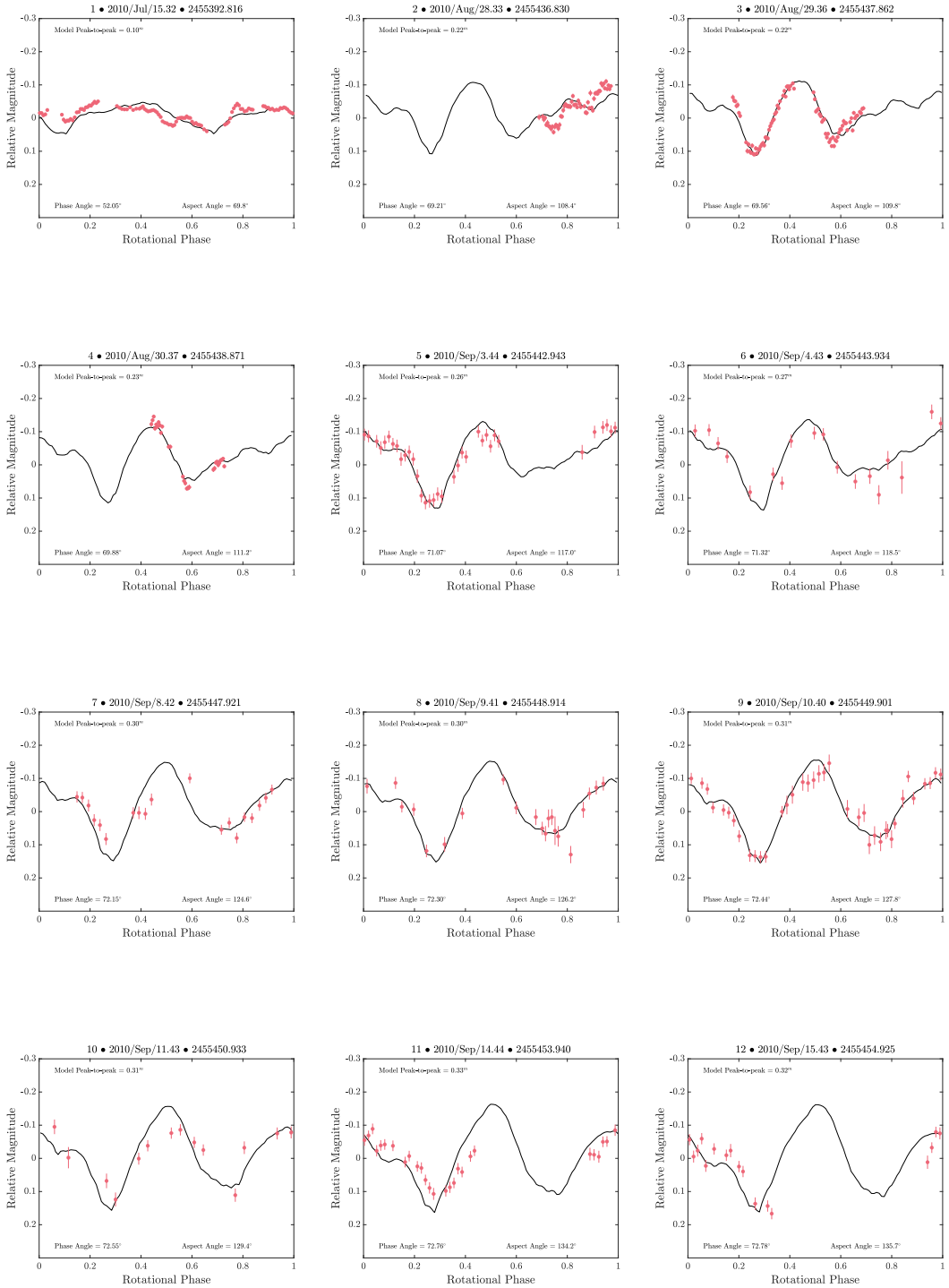

Figure A.19: Synthetic light curves from `convexinv` model of (89830) 2002 CE with YORP strength of 4×10^{-7}rad/day^2.

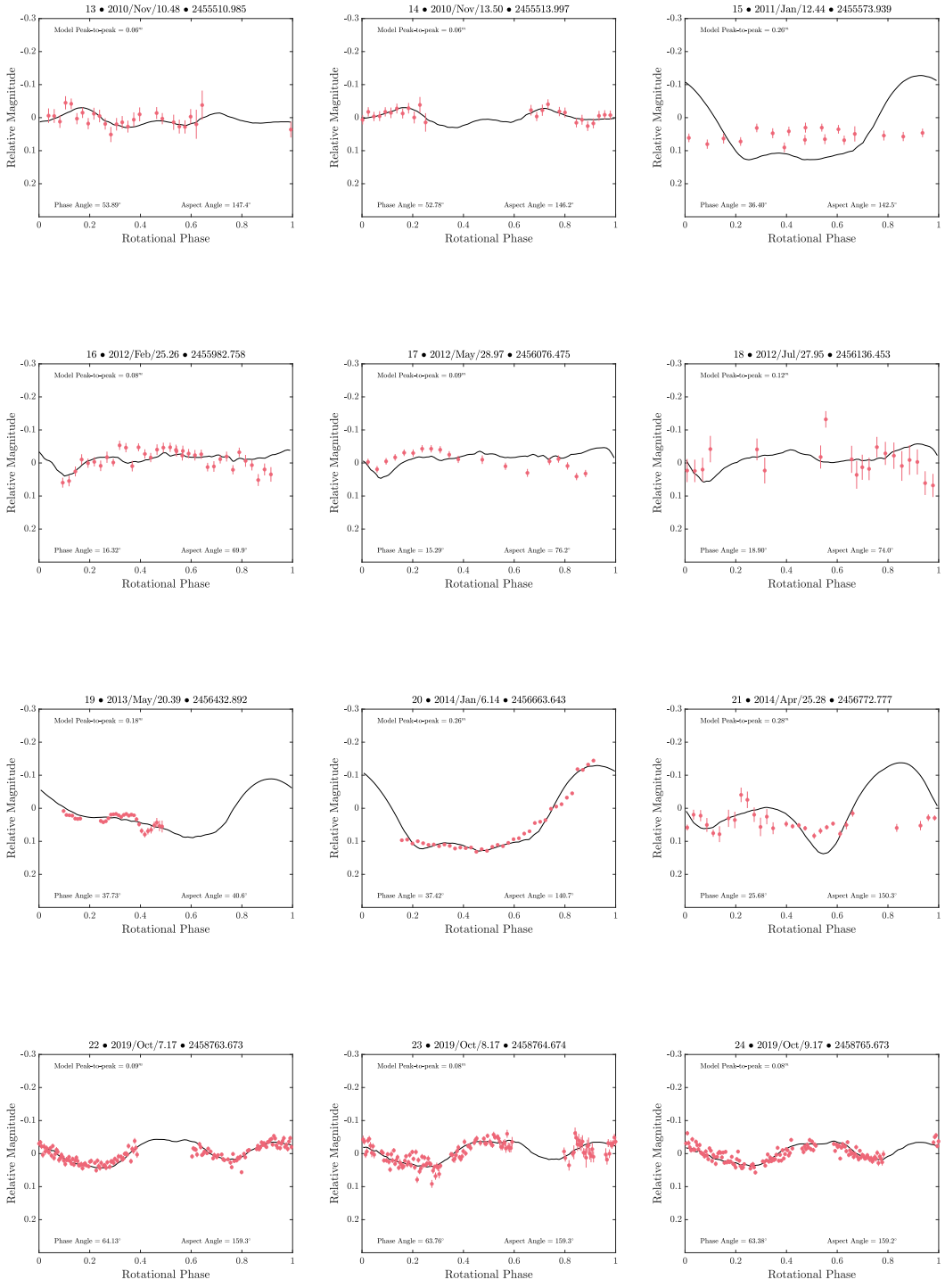

Figure A.19: (Continued.)

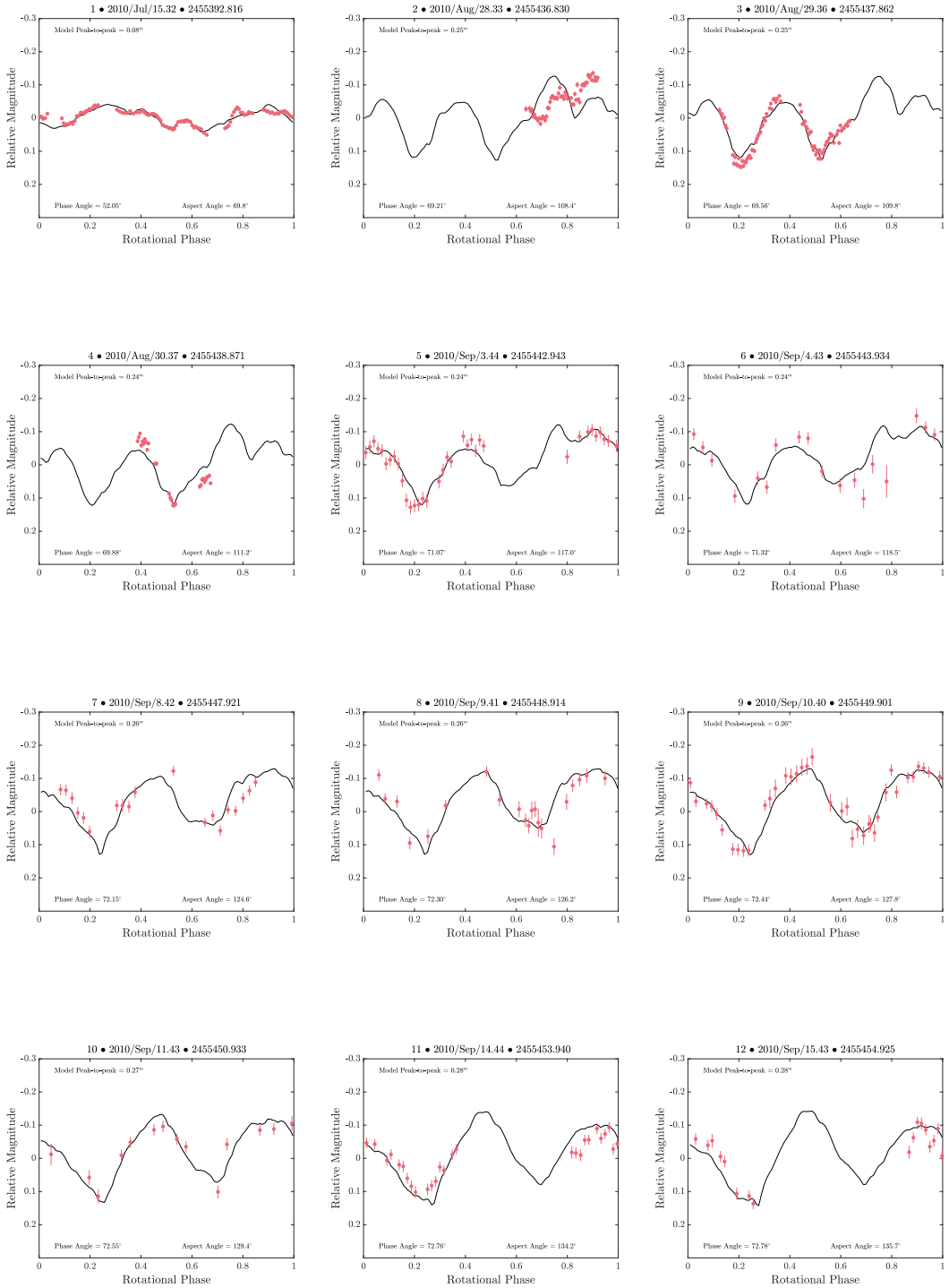

Figure A.20: Synthetic light curves from `convexinv` model of (89830) 2002 CE with YORP strength of 4.2×10^{-6}rad/day^2.

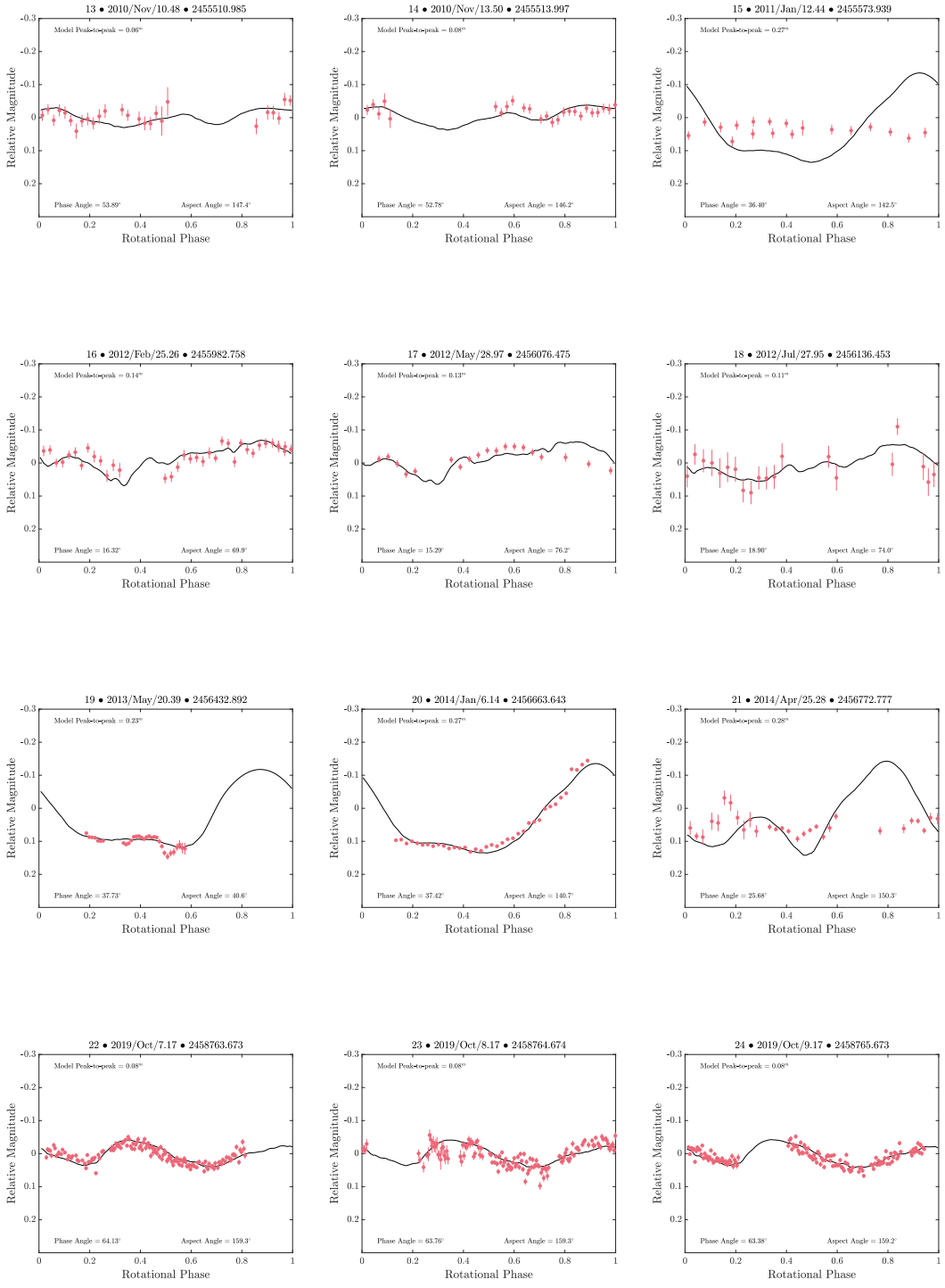

Figure A.20: (Continued.)

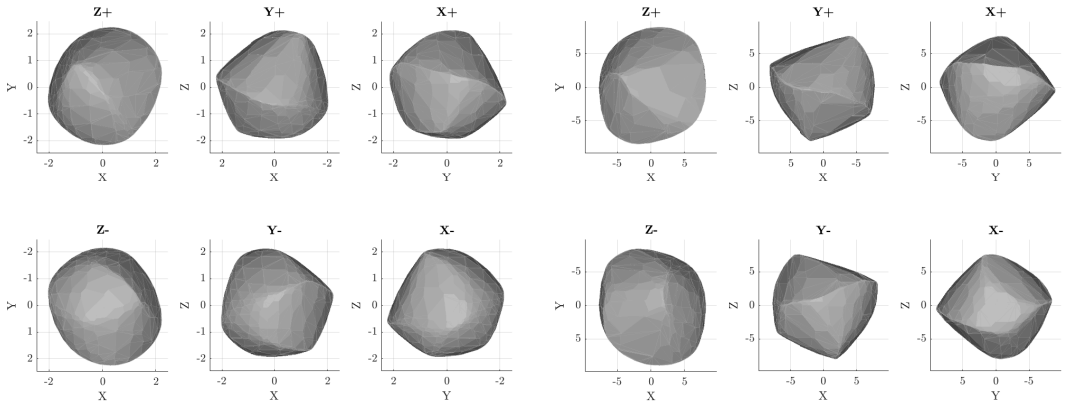

Figure A.21: Best-fit convex inversion shape models of (89830) 2002 CE for the 4×10^{-7}rad/day^2 (left) and4.2×10^{-6}rad/day^2 (right) YORP planes. Views are along the Z, Y and X axes of the body-centric coordinate frame from both the positive and negative ends of the axis. The light curve convex inversion model is not scaled and the units shown are arbitrary.

B Formatting of the input data files

Formatting data for `Convexinv` and `MATLAB` input

The `convexinv` and `MATLAB` input files are plain text data files. All of the input light curves are collected together in a single input file. The formatting required for `convexinv` input starts with a single column on the first line, this column is an integer number that signifies the number of light curves contained within this data file. Following the first line, the light curve data begins. Each light curve begins with a two column line that comprises of an integer that gives the total number of light curve data points and a 0/1 code to flag to the software that the light curve is relative (0) or calibrated (1). Where a relative light curve shows how the brightness varies compared to the reference stars within the image, and calibrated light curves utilise photometric-standard stars to determine the exact brightness of objects. The subsequent lines after this are comprised of eight columns, these contain: the Julian date corrected for the light travel time between scattering from the asteroid and arrival at the telescope, brightness of the asteroid in intensity units, ecliptic Cartesian coordinates describing the vector from the asteroid to the Sun, and ecliptic Cartesian coordinates describing the vector from the asteroid to the Earth. Following the end of a light curve, the next light curve starts immediately after. Once all light curves have been listed the end of file is reached.

```
19
110 0
2455291.484097573 2.471 2.097130e+00 1.401301e-01 3.670652e-01 1.130701e+00 -1.179045e-01 3.670433e-01
2455291.484809459 2.374 2.097130e+00 1.401363e-01 3.670637e-01 1.130704e+00 -1.179103e-01 3.670419e-01
2455291.485527145 2.378 2.097129e+00 1.401426e-01 3.670622e-01 1.130706e+00 -1.179161e-01 3.670404e-01
2455291.486233932 2.420 2.097129e+00 1.401488e-01 3.670607e-01 1.130708e+00 -1.179218e-01 3.670389e-01
2455291.486950418 2.572 2.097128e+00 1.401550e-01 3.670591e-01 1.130711e+00 -1.179275e-01 3.670374e-01
2455291.487656704 2.455 2.097128e+00 1.401612e-01 3.670576e-01 1.130713e+00 -1.179332e-01 3.670359e-01
2455291.488362790 2.266 2.097128e+00 1.401674e-01 3.670561e-01 1.130716e+00 -1.179389e-01 3.670345e-01
2455291.489068576 2.206 2.097127e+00 1.401735e-01 3.670546e-01 1.130718e+00 -1.179446e-01 3.670330e-01
2455291.489774563 2.298 2.097127e+00 1.401797e-01 3.670531e-01 1.130720e+00 -1.179503e-01 3.670315e-01
2455291.490492549 2.419 2.097126e+00 1.401860e-01 3.670516e-01 1.130723e+00 -1.179561e-01 3.670300e-01
2455291.491902322 2.361 2.097126e+00 1.401983e-01 3.670486e-01 1.130728e+00 -1.179675e-01 3.670271e-01
2455291.492610307 2.373 2.097125e+00 1.402045e-01 3.670471e-01 1.130730e+00 -1.179732e-01 3.670256e-01
2455291.493327794 2.493 2.097125e+00 1.402107e-01 3.670456e-01 1.130733e+00 -1.179790e-01 3.670241e-01
2455291.494045380 2.263 2.097124e+00 1.402170e-01 3.670440e-01 1.130735e+00 -1.179848e-01 3.670226e-01
2455291.494762965 2.291 2.097124e+00 1.402233e-01 3.670425e-01 1.130737e+00 -1.179905e-01 3.670212e-01
2455291.495469652 2.174 2.097124e+00 1.402294e-01 3.670410e-01 1.130740e+00 -1.179962e-01 3.670197e-01
2455291.496175238 2.388 2.097123e+00 1.402356e-01 3.670395e-01 1.130742e+00 -1.180019e-01 3.670182e-01
2455291.496880924 2.354 2.097123e+00 1.402418e-01 3.670380e-01 1.130745e+00 -1.180076e-01 3.670168e-01
2455291.497587011 2.411 2.097122e+00 1.402479e-01 3.670365e-01 1.130747e+00 -1.180133e-01 3.670153e-01
2455291.498304396 2.288 2.097122e+00 1.402542e-01 3.670350e-01 1.130749e+00 -1.180191e-01 3.670138e-01
2455291.499010683 2.418 2.097122e+00 1.402604e-01 3.670335e-01 1.130752e+00 -1.180248e-01 3.670123e-01
2455291.499719669 2.619 2.097121e+00 1.402666e-01 3.670320e-01 1.130754e+00 -1.180306e-01 3.670109e-01
2455291.500434755 2.504 2.097121e+00 1.402728e-01 3.670304e-01 1.130757e+00 -1.180363e-01 3.670094e-01
2455291.501140041 2.547 2.097120e+00 1.402790e-01 3.670289e-01 1.130759e+00 -1.180420e-01 3.670079e-01
2455291.501846027 2.584 2.097120e+00 1.402851e-01 3.670274e-01 1.130762e+00 -1.180477e-01 3.670065e-01
2455291.502552113 2.557 2.097120e+00 1.402913e-01 3.670259e-01 1.130764e+00 -1.180534e-01 3.670050e-01
2455291.503258200 2.563 2.097119e+00 1.402975e-01 3.670244e-01 1.130766e+00 -1.180591e-01 3.670035e-01
2455291.503975685 2.554 2.097119e+00 1.403037e-01 3.670229e-01 1.130769e+00 -1.180649e-01 3.670020e-01
2455291.504682372 2.560 2.097118e+00 1.403099e-01 3.670214e-01 1.130771e+00 -1.180706e-01 3.670006e-01
2455291.505388158 2.628 2.097118e+00 1.403161e-01 3.670199e-01 1.130774e+00 -1.180763e-01 3.669991e-01
```

Figure B.1: An excerpt of a data file formatted for the `convexinv` modelling software. This file contains fragments of a light curve of asteroid (68346) 2001 KZ66, the format of the file is described in depth above.

```
19
110 0
2455291.484097573 2.471 2.097130e+00 1.401301e-01 3.670652e-01 1.130701e+00 -1.179045e-01 3.670433e-01 0.038
2455291.484809459 2.374 2.097130e+00 1.401363e-01 3.670637e-01 1.130704e+00 -1.179103e-01 3.670419e-01 0.039
2455291.485527145 2.378 2.097129e+00 1.401426e-01 3.670622e-01 1.130706e+00 -1.179161e-01 3.670404e-01 0.038
2455291.486233932 2.420 2.097129e+00 1.401488e-01 3.670607e-01 1.130708e+00 -1.179218e-01 3.670389e-01 0.041
2455291.486950418 2.572 2.097128e+00 1.401550e-01 3.670591e-01 1.130711e+00 -1.179275e-01 3.670374e-01 0.039
2455291.487656704 2.455 2.097128e+00 1.401612e-01 3.670576e-01 1.130713e+00 -1.179332e-01 3.670359e-01 0.041
2455291.488362790 2.266 2.097128e+00 1.401674e-01 3.670561e-01 1.130716e+00 -1.179389e-01 3.670345e-01 0.040
2455291.489068576 2.206 2.097127e+00 1.401735e-01 3.670546e-01 1.130718e+00 -1.179446e-01 3.670330e-01 0.040
2455291.489774563 2.298 2.097127e+00 1.401797e-01 3.670531e-01 1.130720e+00 -1.179503e-01 3.670315e-01 0.036
2455291.490492549 2.419 2.097126e+00 1.401860e-01 3.670516e-01 1.130723e+00 -1.179561e-01 3.670300e-01 0.040
2455291.491902322 2.361 2.097126e+00 1.401983e-01 3.670486e-01 1.130728e+00 -1.179675e-01 3.670271e-01 0.037
2455291.492610307 2.373 2.097125e+00 1.402045e-01 3.670471e-01 1.130730e+00 -1.179732e-01 3.670256e-01 0.034
2455291.493327794 2.493 2.097125e+00 1.402107e-01 3.670456e-01 1.130733e+00 -1.179790e-01 3.670241e-01 0.036
2455291.494045380 2.263 2.097124e+00 1.402170e-01 3.670440e-01 1.130735e+00 -1.179848e-01 3.670226e-01 0.034
2455291.494762965 2.291 2.097124e+00 1.402233e-01 3.670425e-01 1.130737e+00 -1.179905e-01 3.670212e-01 0.034
2455291.495469652 2.174 2.097124e+00 1.402294e-01 3.670410e-01 1.130740e+00 -1.179962e-01 3.670197e-01 0.042
2455291.496175238 2.388 2.097123e+00 1.402356e-01 3.670395e-01 1.130742e+00 -1.180019e-01 3.670182e-01 0.036
2455291.496880924 2.354 2.097123e+00 1.402418e-01 3.670380e-01 1.130745e+00 -1.180076e-01 3.670168e-01 0.036
2455291.497587011 2.411 2.097122e+00 1.402479e-01 3.670365e-01 1.130747e+00 -1.180133e-01 3.670153e-01 0.032
2455291.498304396 2.288 2.097122e+00 1.402542e-01 3.670350e-01 1.130749e+00 -1.180191e-01 3.670138e-01 0.034
2455291.499010683 2.418 2.097122e+00 1.402604e-01 3.670335e-01 1.130752e+00 -1.180248e-01 3.670123e-01 0.032
2455291.499719669 2.619 2.097121e+00 1.402666e-01 3.670320e-01 1.130754e+00 -1.180306e-01 3.670109e-01 0.034
2455291.500434755 2.504 2.097121e+00 1.402728e-01 3.670304e-01 1.130757e+00 -1.180363e-01 3.670094e-01 0.031
2455291.501140041 2.547 2.097120e+00 1.402790e-01 3.670289e-01 1.130759e+00 -1.180420e-01 3.670079e-01 0.032
2455291.501846027 2.584 2.097120e+00 1.402851e-01 3.670274e-01 1.130762e+00 -1.180477e-01 3.670065e-01 0.032
2455291.502552113 2.557 2.097120e+00 1.402913e-01 3.670259e-01 1.130764e+00 -1.180534e-01 3.670050e-01 0.034
2455291.503258200 2.563 2.097119e+00 1.402975e-01 3.670244e-01 1.130766e+00 -1.180591e-01 3.670035e-01 0.031
2455291.503975685 2.554 2.097119e+00 1.403037e-01 3.670229e-01 1.130769e+00 -1.180649e-01 3.670020e-01 0.030
2455291.504682372 2.560 2.097118e+00 1.403099e-01 3.670214e-01 1.130771e+00 -1.180706e-01 3.670006e-01 0.032
2455291.505388158 2.628 2.097118e+00 1.403161e-01 3.670199e-01 1.130774e+00 -1.180763e-01 3.669991e-01 0.029
```

Figure B.2: An excerpt of a data file formatted for the `MATLAB` spin-state modelling software. This file contains fragments of a light curve of asteroid (68346) 2001 KZ66, the format of the file is described in depth above.

The input format for Kent's MATLAB software is the same as that for convexinv, the only exception being that the light curve data points contain an additional ninth column that gives the uncertainty of the brightness measurement in magnitude units. An example of both a convexinv and MATLAB input file can be see in Figs. B.1 and B.2.

Formatting data for SHAPE input

Unlike convexinv, SHAPE allows the input of multiple data types which complicates the structure of the input file. The SHAPE input file is called an observation (obs) file, it contains metadata describing the data and the paths to the actual data files. The observation file starts by stating how many datasets are contained within it. A dataset here is a set of observations taken with identical observing parameters. In the context of light curves, a single dataset represents a single light curve through a series of points taken typically over one night. For delay-Doppler images, a dataset has the same baud length, same image dimensions, and taken using the same ephemeris solution. For example, images taken over one night, but which change baud length need to be split up into multiple dataset each with the same baud length. The same applies to Doppler spectra. Each dataset starts with two lines containing three parameters: the first line is three angular offsets that can be applied to the initial orientation of the model, the second line is another three angular offsets that are applied to the evolved spin vector at the time of the dataset. A detailed description of what is contained within a dataset is described below for each of the observation types used in this thesis.

Light curves – These datasets start with a parameter to describe the type of data contained in the dataset, this is adequately set to 'lightcurve'. Following this is a zero-based number to select which optical scattering law to apply to the light curve if multiple scattering laws are utilised. Then an asteroid ephemeris is listed, followed by a solar ephemeris, these are given at intervals of time, typically an hour, that encompass

```
{DATA FILE FOR SHAPE.C VERSION 2.10.4 BUILD Wed 25 Jul 2018 15:39:03 WEST}

           19 {number of sets}


{SET 0}

-1 {is mpi node responsible for this set}

 c   0.000000e+00 c   0.000000e+00 c   0.000000e+00 {Euler angle offsets}
 c   0.000000e+00 c   0.000000e+00 c   0.000000e+00 {spin vector offsets}

    lightcurve {set type}

            0 {optical scattering law for this set}

            5 {number of asteroid ephemeris points}
{ yr mo dd hh mm ss        ra       dec      dist}
2010  4  4 22  0  0 167.34830 -14.06299 1.19438538
2010  4  4 23  0  0 167.33676 -14.05079 1.19452338
2010  4  5  0  0  0 167.32512 -14.03858 1.19466307
2010  4  5  1  0  0 167.31341 -14.02634 1.19480495
2010  4  5  2  0  0 167.30165 -14.01408 1.19494943

            5 {number of solar ephemeris points}
{ yr mo dd hh mm ss        ra       dec      dist}
2010  4  4 22  0  0 179.50267 -10.59722 2.13364742
2010  4  4 23  0  0 179.51275 -10.59902 2.13363335
2010  4  5  0  0  0 179.52283 -10.60083 2.13361923
2010  4  5  1  0  0 179.53290 -10.60263 2.13360506
2010  4  5  2  0  0 179.54298 -10.60443 2.13359085

           -1 {number of calculated points}

1    1.000 center {smearing: # views per point, view interval (s), mode}

          110 {number of samples in lightcurve}
/Volumes/DATA/Data/68346/68346SHAPELC_20100404_NTT.txt f 1.000000e+00 1.000000e+00 {name, calfact, weight}
```

Figure B.3: An excerpt of an obs file used by `SHAPE`. This figure displays the format required when describing light curve observations. This file describes light curve observations of asteroid (68346) 2001 KZ66, the format of the file is described in depth above.

the total duration of the light curve. These list the time, right ascension, declination, and distance to the object. Ephemeris for the exact time of each data point are obtained by interpolating between these intervals. Finally the last two lines relate to the light curve itself. The first is a number indicating the number of data point that the light curve contains. Followed by a line containing the name of the data file, a flag for the calibration factor (either a 'f' allowing the value to be fitted, or a 'c' if it is already calibrated), the calibration factor itself that adjusts the level of the light curve, and a weighting factor for the dataset's statistical contribution. The light curve file format itself is a simple three column plain text file: the first column is the Julian date of the data point without a light-time correction, the brightness of the asteroid in magnitude units, and its uncertainty also in magnitude. For excerpts, see Figs. B.3 and B.4.

```
2455291.49524   19.061   0.0111
2455291.50421   19.052   0.0099
2455291.51284   18.920   0.0085
2455291.52141   18.759   0.0075
2455291.53049   18.618   0.0079
2455291.53890   18.541   0.0061
2455291.54739   18.523   0.0056
2455291.55541   18.532   0.0058
2455291.56400   18.564   0.0054
2455291.57180   18.652   0.0085
```

Figure B.4: An excerpt of a light curve data file used by `SHAPE`. This figure displays the format required when listing light curve data points, this file lists the data points for asteroid (68346) 2001 KZ66, the format of the file is described above.

Delay-Doppler images – Similar to the light curve datasets, these start by indicating that they are of the 'delay-doppler' type. They also list the applied radar scattering law, as well as an ephemeris which lists the asteroid's location. Following this, the transmitted frequency is stated in MHz. Given next are details of the delay dimension listing: the number of image rows, the pixel height in micro-seconds, the number of samples per baud, the number of samples per pixel - referred to as 'stride', and the signal encoding method. Then details of the Doppler dimension listing: the number of image columns, the pixel width in Hz, the column of the centre-of-mass echo predicted by the ephemeris, the DC column which accounts for the offset applied to the signal from the standard frequency, and the length of the fast Fourier-transform used. Since the predictions of the asteroid's location in the observing ephemeris are likely not perfect, there is also the ability to apply a delay correction. A Doppler scaling factor can be used to alter the Doppler bandwidth in the synthetic images. The final part of the dataset details the data itself; it starts with a line listing the directory that the data is stored in and how many frames there are. This is followed by a line for each frame, each line list: the name of the file, the date and time of mid-observation, the radar cross-section - 'sdev', a calibration factor, the number of 'looks' - analogous to frames in photometry, the row of the centre-of-mass in delay, a statistical weight that is applied to the frame's contribution to chi squared when modelling, and a flag to indicate whether or not to apply a mask to the frame. An excerpt of this file is given in Fig. B.5.

```
{DATA FILE FOR SHAPE.C VERSION 2.10.4 BUILD Wed Sep 13 11:47:26 BST 2017}

            2 {number of sets}


{SET 0}

-1 {is mpi node responsible for this set}

 c   0.000000e+00 c   0.000000e+00 c   0.000000e+00 {Euler angle offsets}
 c   0.000000e+00 c   0.000000e+00 c   0.000000e+00 {spin vector offsets}

 delay-doppler {set type}

            0 {radar scattering law for this set}

            5 {number of ephemeris points}
{ yr mo dd hh mm ss        ra       dec      dist}
2003 10 28 11  0  0 172.52993   8.92140 0.08029907
2003 10 28 12  0  0 172.34507   8.81090 0.08025342
2003 10 28 13  0  0 172.15939   8.69988 0.08021143
2003 10 28 14  0  0 171.97341   8.58835 0.08017330
2003 10 28 15  0  0 171.78769   8.47632 0.08013904

   2380.000000 {transmitter frequency (MHz)}

150 0.100000 1 1 short {delay: # rows, pixel height (usec), spb, stride, code method}

200 0.298028 116.776962 100.000000 512 {dop: # cols, pixel width (Hz), COM col, DC col, fftlen}

2003 10 28 11  0  0 {t0 of delcor poly}
            1 {order of polynomial}
 f  0.000000e+00 {coefficient 0}
 f  0.000000e+00 {coefficient 1}

 c  1.000000e+00 {Doppler scaling factor}

1    1.000 center {smearing: # views per frame, view interval (s), mode}

/data/tjz2/68346/data/radar/2003/oct28/pfs {data directory}

           36 {number of frames}
{                   name year mo dd hh mm ss         sdev        calfact   looks COM delay row       weight mask}
   run20031028125700.fits 2003 10 28 12 57 37 1.000000e+00 f 1.000000e+00    22.0  -3250.051270 1.000000e+00    0
   run20031028125942.fits 2003 10 28 13  0 19 1.000000e+00 f 1.000000e+00    22.0  -3249.872803 1.000000e+00    0
   run20031028130224.fits 2003 10 28 13  3  1 1.000000e+00 f 1.000000e+00    22.0  -3249.325684 1.000000e+00    0
   run20031028130506.fits 2003 10 28 13  5 43 1.000000e+00 f 1.000000e+00    22.0  -3249.319580 1.000000e+00    0
```

Figure B.5: An excerpt of an obs file used by `SHAPE`. This figure displays the format required when describing delay-Doppler observations. This file describes delay-Doppler observations of asteroid (68346) 2001 KZ66, the format of the file is described in depth above.

cw spectra – Again, like all other datasets, this also starts by listing the data type - 'doppler', the radar scattering law, and an ephemeris for the asteroid. The rest of this dataset follows a very similar format to the delay-Doppler dataset, there are only a couple differences: first, there is no line detailing the delay dimensions, only the line describing the Doppler dimension. This contains the number of Doppler bins in the spectrum and their width in Hz, and the predicted centre-of-mass bin. Secondly, the lines detailing the data itself do not contain the row of the centre-of-mass in delay and so these lines only contain seven values opposed to the eight for delay-Doppler data. See Fig. B.6 for an excerpt of this file.

```
{DATA FILE FOR SHAPE.C VERSION 2.10.4 BUILD Wed Sep 13 11:47:26 BST 2017}

            5 {number of sets}


{SET 0}

-1 {is mpi node responsible for this set}

 c   0.000000e+00 c   0.000000e+00 c   0.000000e+00 {Euler angle offsets}
 c   0.000000e+00 c   0.000000e+00 c   0.000000e+00 {spin vector offsets}

       doppler {set type}

            0 {radar scattering law for this set}

            3 {number of ephemeris points}
{ yr mo dd hh mm ss        ra       dec      dist}
2003 10 28 11  0  0 172.52993   8.92140 0.08029907
2003 10 28 12  0  0 172.34507   8.81090 0.08025342
2003 10 28 13  0  0 172.15939   8.69988 0.08021143

   2380.000000 {transmitter frequency (MHz)}

146001 0.013699 73001.000000 {dop: # bins, bin width (Hz), COM bin}

2003 10 28 11  0  0 {t0 of delcor poly}
            1 {order of polynomial}
 c  0.000000e+00 {coefficient 0}
 f  0.000000e+00 {coefficient 1}

 c  1.000000e+00 {Doppler scaling factor}

1    1.000 center {smearing: # views per frame, view interval (s), mode}

/data/tjz2/68346/data/radar/2003/oct28/cw/1set {data directory}

            6 {number of frames}
{                          name year mo dd hh mm ss         sdev        calfact   looks       weight mask}
2001KZ66.2003Oct28.p0137Hz.rdf 2003 10 28 12 22 23 5.235496e-05 c 1.000000e+00     1.0 1.000000e+00    0
2001KZ66.2003Oct28.p0137Hz.rdf 2003 10 28 12 25  5 4.743157e-05 c 1.000000e+00     1.0 1.000000e+00    0
2001KZ66.2003Oct28.p0137Hz.rdf 2003 10 28 12 27 48 4.371812e-05 c 1.000000e+00     1.0 1.000000e+00    0
2001KZ66.2003Oct28.p0137Hz.rdf 2003 10 28 12 30 32 4.089433e-05 c 1.000000e+00     1.0 1.000000e+00    0
2001KZ66.2003Oct28.p0137Hz.rdf 2003 10 28 12 33 14 3.879240e-05 c 1.000000e+00     1.0 1.000000e+00    0
```

Figure B.6: An excerpt of an obs file used by `SHAPE`. This figure displays the format required when describing Doppler spectra. This file describes Doppler spectra of asteroid (68346) 2001 KZ66, the format of the file is described in depth above.

Model (mod) file

This file describes the 'model' which includes the shape of the asteroid, its spin-state and photometric parameters. The description of this file here supplements the description in Sect. 3.2.2. Each parameter's value is preceded by a single character flag that indicates its state: 'f' indicates a floating parameter (the value will be optimised), 'c' specifies a constant parameter, or '=' which will set the parameter equal to the value of a preceding parameter (this can only be done for a few parameters). The description of a model's shape can be comprised of multiple components, as described earlier. The shape of each component can be described using one of three types: ellipsoid, spherical harmonic, or vertex. The first two of the three available types are described in the

following paragraphs. An excerpt of a mod file can be found below in Fig. B.7.

Ellipsoid components – These are the simplest descriptions of the model components available within the software, and so the initial stages of the modelling process are usually carried out with this component type. Ellipsoidal components are described by three parameters: the longest diameter (2a), the elongation (a/b), and the flattening (b/c). For a principal axis rotator, the third diameter should be the smallest; both $b/c < 1$ and $a/b \cdot b/c < 1$. Although `SHAPE` describes the components in terms of these three parameters, when the software produces synthetic data to be compared against the observations, it converts the model into a polyhedron that approximates the ellipsoid shape to do so. Therefore, the 'number of theta steps' is also included in this component type below the axial ratios. This parameter describes the angular resolution of the polyhedron, with a higher value leading to a better approximation of the ellipsoidal shape, but also requires a longer time to compute the synthetic data which the polyhedron is used to generate.

Spherical harmonic components – This component type starts with the maximum harmonic degree L_{max}, which determines the complexity of the component's shape. This is followed by scaling factors for the x, y, and z dimensions of the component. Listed below the scaling factors are the sine and cosine coefficients of the spherical harmonic series. The number of these coefficients is dependant on L_{max}, giving a total of $(L_{max} + 1)^2$ parameters. Like the ellipsoid components, for the calculation of the synthetic data spherical harmonic components are internally converted to a polyhedron, therefore these too have the 'number of theta steps' parameter to determine the angular resolution.

The final section of the model file details the spin state. The first line of this section gives the initial epoch t_0 (UT) in the format (yyyy mm dd hh mm ss). Any epoch is acceptable, but often a round number just before the start of the observations is used. The next three numbers are Euler angles giving the model's orientation at this epoch in ecliptic coordinates. The first two angles relate to the longitude and latitude of the

asteroids pole, defined in the right hand sense: 'angle 0' = $\lambda + 90°$ and 'angle 1' = $90° - \beta$. 'angle 2' is the initial rotation around the body-fixed z-axis, this value must be fit as it cannot be determined *a priori*. Next are the x, y, and z components of the initial sidereal spin in deg/day these are given in the body-fixed coordinates. So for the example of a principal-axis rotation, the first two (x and y) components are held constant at zero and the spin axis, the body-fixed z-axis (labelled 'spin 2'), is set to the rotation period. The next three values are the principal moments of inertia again in body-fixed coordinates. After these come three parameters that represent the YORP effect by defining linear rates of change for the three spin rates. Three parameters are also available to include librations in the asteroid's spin state.

Parameter (par) file

This file contains not only the action to be performed by `SHAPE`, but also a list of parameter values required in order to run. Additionally, this file contains weighting factors for any penalty functions that may have been applied. The parameter file is split into two headings: 'PARAMETERS' and 'PENALTIES'. The Parameters are discussed below and the Penalties were described in Sect. 3.2.2.

Under the former, each parameter occupies a single line and the value assigned to each parameter is separated by white-space. The most important is the 'action' parameter, this dictates to `SHAPE` what to do. The actions available to `SHAPE` are: 'fit', 'write', 'moments', and many others that can be found within the software's documentation. The 'fit' action tells `SHAPE` to optimise any parameters in the model file (described later) that have been set to the floating state. 'write' is used to output synthetic data that can be used to manually assess the quality of the fit between the model and observations. 'moments' is another important action which outputs physical properties of the model such as its dimensions, moments of inertia, and the alignment between the principal axes and body-fixed axes. Below the 'action' parameter, a number of additional parameters are listed. Two important parameters are: 'pos_pixels' and 'pos_width', as these determine the plane-of-sky view of our model. It is crucial that these parameters are set

```
{MODEL FILE FOR SHAPE.C VERSION 2.10.4 BUILD Thu 6 Jul 18:09:25 PDT 2017}

{SHAPE DESCRIPTION}
               2 {number of components}
{COMPONENT 0}
 c -1.050000e-01 {linear offset 0}
 c  0.000000e+00 {linear offset 1}
 c  0.000000e+00 {linear offset 2}
 c  0.000000e+00 {rotational offset 0}
 c  0.000000e+00 {rotational offset 1}
 c  0.000000e+00 {rotational offset 2}
        ellipse {component type}
 f      0.800000 {2a}
 f      1.500000 {a/b}
 f      1.000000 {b/c}
              45 {number of theta steps}
{COMPONENT 1}
 c  3.450000e-01 {linear offset 0}
 c  0.000000e+00 {linear offset 1}
 c  0.000000e+00 {linear offset 2}
 c  0.000000e+00 {rotational offset 0}
 c  0.000000e+00 {rotational offset 1}
 c  0.000000e+00 {rotational offset 2}
        ellipse {component type}
 f      0.350000 {2a}
 f      1.000000 {a/b}
 f      1.000000 {b/c}
              45 {number of theta steps}


{PHOTOMETRIC FUNCTIONS}
               1 {number of radar scattering laws}
{RADAR SCATTERING LAW 0}
  hagfors+cosine {type}
 c      0.099223 {R_qs}
 c      6.622733 {C_qs}
       25.000000 {qs cutoff angle}
 c      0.120642 {R_diff}
 c      0.846530 {C_diff}
               1 {number of optical scattering laws}
{OPTICAL SCATTERING LAW 0}
     kaasalainen {type}
 c      0.061153 {R}
 c      0.455806 {wt}
 c      0.000000 {A0}
 c      5.314868 {D}
 c      0.000000 {k}


{SPIN STATE}
2003 10 27  0  0  0 {yyyy mo dd hh mm ss of t0}
 c   260.0000000000 {angle 0 (deg) lambda=170.000000}
 c   48.0000000000 {angle 1 (deg) beta=-42.000000}
 f   60.0000000000 {angle 2 (deg)}
 c     0.0000000000 {spin 0 (deg/day)}
 c     0.0000000000 {spin 1 (deg/day)}
 c  3200.0000000000 {spin 2 (deg/day) P=2.700000}
 c     0.7736280000 {moment of inertia 0}
 c     0.9772080000 {moment of inertia 1}
 c     1.0000000000 {moment of inertia 2}
 c     0.0000000000 {spin 0 dot (deg/day/day)}
 c     0.0000000000 {spin 1 dot (deg/day/day)}
 c     0.0000000000 {spin 2 dot (deg/day/day)}
 c     0.0000000000 {Libration Amplitude (degrees)}
 c     0.0000000000 {Libration Frequency (degrees/day)}
 c     0.0000000000 {Libration Phase (degrees)}
                 0 {number of spin impulses}

{
volume  = 0.086287 km^3
com     = 0.000711 0.000000 -0.000000 km
inertia =  0.214909  0.000000  0.000003
           0.000000  0.999924  0.000003
           0.000003  0.000003  1.000000
}
```

Figure B.7: An excerpt of a mod file used by `SHAPE`. This figure displays the format of a model comprised of ellipsoid components. The format of the file is described in depth above and in Sect. 3.2.2.

```
PARAMETERS

action          write
pos_pixels      201
pos_width       1.7 {0.8}
nsinc2          2
sinc2width      6
dd_scaling      none
dd_maxsides     bottom-right
scalefitobs     separate {separate}
plot_com        yes
plot_pa         yes yes yes
plot_spinvec    yes
listfit         yes
maskdir         /Volumes/DATA/Data/68346/data/radar/2003/masks/sum2+cw/
mark_unseen     no
maxangle_seen   35

PENALTIES       0
```

Figure B.8: An excerpt of a par file used by `SHAPE`. This figure displays the format to list `SHAPE` parameters and penalties. The format of the file is described in depth above and in Sect. 3.2.2.

correctly, such that the plane-of-sky projection of the asteroid does not extend outside of these bounds. Several triples of values are also given, each of these comprise of a parameter step-size, a fractional tolerance, and an absolute tolerance. These triples are for the model's length, spin, angular orientation, and photometric parameters. Finally, there are also parameters to determine the termination point of the model's fitting. This can be given as either a maximum iteration number or a fractional termination precision. See Fig. B.8 for an excerpt.

C | Acronyms

NEA Near-Earth Asteroid

NEO Near-Earth Object

PHA Potentiallty Hazardous Asteroid

LCDB Asteroid Lightcurve Database

ALCDEF Asteroid Lightcurve Data Exchange Format

CCD Charge Coupled Device

PSF Point Spread Function

FWHM Full Width at Half Maximum

ESO LP European Southern Observatory Large Programme

ORM Observatorio del Roque de los Muchachos

INT Isaac Newton Telescope

WFC Wide Field Camera

IDS Intermediate Dispersion Spectrograph

NTT New Technology Telescope

EFOSC2 ESO Faint Object Spectrograph and Camera - version 2

VLT Very Large Telescope

UT Unit Telescope

VISIR VLT Imager and Spectrometer for mid-Infrared

VIMOS VIsible MultiObject Spectrograph

NOT Nordic Optical Telescope

ALFOSC Alhambra Faint Object Spectrograph and Camera

LT Liverpool Telescope

TMO Table Mountain Observatory

PAL200 200-inch Hale Telescope

LFC Large Format Camera

FAST Five hundred metre Aperture Spherical Telescope

LINEAR Lincoln Near-Earth Asteroid Research

VLBA Very Long Baseline Array

TESS Transiting Exoplanet Survey Satellite